Update to the Technical Design Report

for the

$\overline{\text{P}}$ANDA Electromagnetic Calorimeter

(AntiProton Annihilations at Darmstadt)

Strong Interaction Studies with Antiprotons

$\overline{\text{P}}$ANDA Collaboration

October 8, 2020

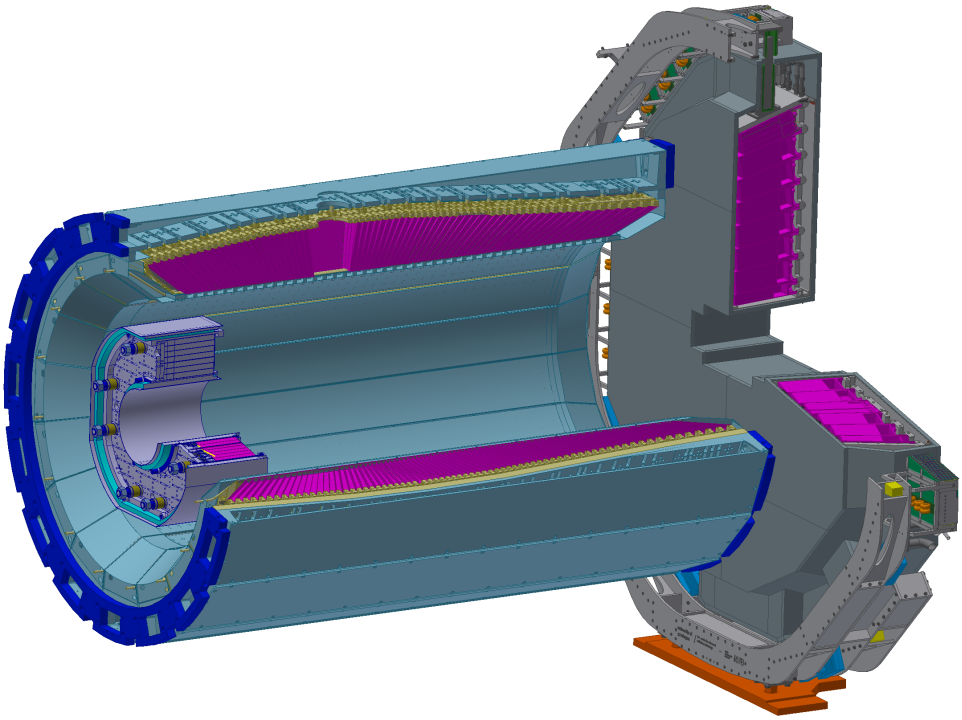

The $\overline{\text{P}}$ANDA Collaboration

Università Politecnica delle Marche-Ancona, **Ancona**, Italy
G. Barucca, F. Davì, G. Lancioni, P. Mengucci, L. Montalto, P. P. Natali, N. Paone, D. Rinaldi, L. Scalise

Universität Basel, **Basel**, Switzerland
W. Erni, B. Krusche, M. Steinacher, N. Walford

Institute of High Energy Physics, Chinese Academy of Sciences, **Beijing**, China
N. Cao, Z. Liu, C. Liu, B. Liu, X. Shen, S. Sun, J. Tao, X. A. Xiong, G. Zhao, J. Zhao

Ruhr-Universität Bochum, Institut für Experimentalphysik I, **Bochum**, Germany
M. Albrecht, W. Alkakhi, S. Bökelmann, S. Coen, F. Feldbauer, M. Fink, J. Frech, V. Freudenreich, M. Fritsch, J. Grochowski, R. Hagdorn, F.H. Heinsius, T. Held, T. Holtmann, I. Keshk, H. Koch, B. Kopf, M. Kuhlmann, M. Kümmel, M. Küßner, J. Li, L. Linzen, J. Oppotsch, S. Pankonin, M. Pelizäus, A. Pitka, J. Reher, G. Reicherz, C. Schnier, M. Steinke, T. Triffterer, C. Wenzel, U. Wiedner

Department of Physics, Bolu Abant Izzet Baysal University, **Bolu**, Turkey
H. Denizli, N. Er, U. Keskin

Rheinische Friedrich-Wilhelms-Universität Bonn, **Bonn**, Germany
R. Beck, V. Chauhan, C. Hammann, J. Hartmann, B. Ketzer, J. Müllers, M. Rossbach, B. Salisbury, C. Schmidt, T. Seifen, U. Thoma, M. Urban

Università di Brescia, **Brescia**, Italy
A. Bianconi

Institutul National de C&D pentru Fizica si Inginerie Nucleara "Horia Hulubei", **Bukarest-Magurele**, Romania
M. Bragadireanu, D. Pantea

University of Technology, Institute of Applied Informatics, **Cracow**, Poland
M. Domagala, G. Filo, E. Lisowski, F. Lisowski, M. Michałek, P. Poznański, J. Płażek

IFJ, Institute of Nuclear Physics PAN, **Cracow**, Poland
K. Korcyl, A. Kozela, P. Lebiedowicz, K. Pysz, W. Schäfer, A. Szczurek

AGH, University of Science and Technology, **Cracow**, Poland
M. Firlej, T. Fiutowski, M. Idzik, J. Moron, K. Swientek, P. Terlecki

Instytut Fizyki, Uniwersytet Jagiellonski, **Cracow**, Poland
G. Korcyl, R. Lalik, A. Malige, P. Moskal, K. Nowakowski, W. Przygoda, N. Rathod, Z. Rudy, P. Salabura, J. Smyrski

FAIR, Facility for Antiproton and Ion Research in Europe, **Darmstadt**, Germany
I. Augustin, R. Böhm, I. Lehmann, L. Schmitt, V. Varentsov

GSI Helmholtzzentrum für Schwerionenforschung GmbH, **Darmstadt**, Germany
M. Al-Turany, A. Belias, H. Deppe, R. Dzhygadlo, H. Flemming, A. Gerhardt, K. Götzen, A. Heinz, P. Jiang, R. Karabowicz, S. Koch, U. Kurilla, D. Lehmann, J. Lühning, U. Lynen, H. Orth, K. Peters, J. Rieger, T. Saito, G. Schepers, C. J. Schmidt, C. Schwarz, J. Schwiening, A. Täschner, M. Traxler, B. Voss, P. Wieczorek

Joint Institute for Nuclear Research, **Dubna**, Russia
V. Abazov, G. Alexeev, V. A. Arefiev, V. Astakhov, M. Yu. Barabanov, B. V. Batyunya, V. Kh. Dodokhov, A. Efremov, A. Fechtchenko, A. Galoyan, G. Golovanov, E. K. Koshurnikov, Y. Yu. Lobanov, A. G. Olshevskiy, A. A. Piskun, A. Samartsev, S. Shimanski, N. B. Skachkov, A. N. Skachkova, E. A. Strokovsky, V. Tokmenin, V. Uzhinsky, A. Verkheev, A. Vodopianov, N. I. Zhuravlev

University of Edinburgh, **Edinburgh**, United Kingdom
D. Branford, D. Watts

Friedrich-Alexander-Universität Erlangen-Nürnberg, **Erlangen**, Germany
M. Böhm, W. Eyrich, A. Lehmann, D. Miehling, M. Pfaffinger

Northwestern University, **Evanston**, U.S.A.
N. Quin, L. Robison, K. Seth, T. Xiao

Università di Ferrara and INFN Sezione di Ferrara, **Ferrara**, Italy
D. Bettoni

Goethe-Universität, Institut für Kernphysik, **Frankfurt**, Germany
A. Ali, A. Hamdi, M. Himmelreich, M. Krebs, S. Nakhoul, F. Nerling

Frankfurt Institute for Advanced Studies, **Frankfurt**, Germany
A. Belousov, I. Kisel, G. Kozlov, M. Pugach, M. Zyzak

INFN Laboratori Nazionali di Frascati, **Frascati**, Italy
N. Bianchi, P. Gianotti, V. Lucherini

Dept of Physics, University of Genova and INFN-Genova, **Genova**, Italy
G. Bracco

Justus-Liebig-Universität Gießen II. Physikalisches Institut, **Gießen**, Germany
Y. Bettner, S. Bodenschatz, K.T. Brinkmann, L. Brück, S. Diehl, V. Dormenev, M. Düren, T. Erlen, K. Föhl, C. Hahn, A. Hayrapetyan, J. Hofmann, S. Kegel, M. Kesselkaul, I. Köseoglu, A. Kripko, W. Kühn, J. S. Lange, V. Metag, M. Moritz, M. Nanova, R. Novotny, P. Orsich, J. Pereira-de-Lira, M. Peter, M. Sachs, M. Schmidt, R. Schubert, H. Stenzel, M. Straube, M. Strickert, U. Thöring, T. Wasem, B. Wohlfahrt, H.G. Zaunick

IRFU, CEA, Université Paris-Saclay, **Gif-sur-Yvette Cedex**, France
E. Tomasi-Gustafsson

University of Glasgow, **Glasgow**, United Kingdom
D. Glazier, D. Ireland, B. Seitz

Birla Institute of Technology and Science, Pilani, K K Birla Goa Campus, **Goa**, India
P.N. Deepak, A. Kulkarni

KVI-Center for Advanced Radiation Technology (CART), University of Groningen, **Groningen**, Netherlands
R. Kappert, M. Kavatsyuk, H. Loehner, J. Messchendorp, V. Rodin, P. Schakel, S. Vejdani

Gauhati University, Physics Department, **Guwahati**, India
K. Dutta, K. Kalita

University of Science and Technology of China, **Hefei**, China
G. Huang, D. Liu, H. Peng, H. Qi, Y. Sun, X. Zhou

Universität Heidelberg, **Heidelberg**, Germany
M. Kunze

Department of Physics, Dogus University, **Istanbul**, Turkey
K. Azizi

Forschungszentrum Jülich, Institut für Kernphysik, **Jülich**, Germany
A. Derichs, R. Dosdall, W. Esmail, A. Gillitzer, F. Goldenbaum, D. Grunwald, L. Jokhovets, J. Kannika, P. Kulessa, S. Orfanitski, G. Pérez Andrade, D. Prasuhn, E. Prencipe, J. Pütz, J. Ritman, E. Rosenthal, S. Schadmand, R. Schmitz, A. Scholl, T. Sefzick, V. Serdyuk, T. Stockmanns, D. Veretennikov, P. Wintz, P. Wüstner, H. Xu, Y. Zhou

Chinese Academy of Science, Institute of Modern Physics, **Lanzhou**, China
X. Cao, Q. Hu, Z. Li, H. Li, Y. Liang, X. Ma

INFN Laboratori Nazionali di Legnaro, **Legnaro**, Italy
V. Rigato

Lunds Universitet, Department of Physics, **Lund**, Sweden
L. Isaksson

Johannes Gutenberg-Universität, Institut für Kernphysik, **Mainz**, Germany
P. Achenbach, O. Corell, A. Denig, M. Distler, M. Hoek, W. Lauth, H. H. Leithoff, Z. Liu, H. Merkel, U. Müller, J. Pochodzalla, S. Schlimme, C. Sfienti, M. Thiel, M. Zambrana

Helmholtz-Institut Mainz, **Mainz**, Germany
S. Ahmed , S. Bleser, M. Bölting, L. Capozza, A. Dbeyssi, A. Ehret, R. Klasen, R. Kliemt, F. Maas, S. Maldaner, C. Motzko, O. Noll, S. Pflüger, D. Rodríguez Piñeiro, F. Schupp, M. Steinen, S. Wolff, I. Zimmermann

Research Institute for Nuclear Problems, Belarus State University, **Minsk**, Belarus
A. Fedorov, D. Kazlou, M. Korzhik, O. Missevitch

Moscow Power Engineering Institute, **Moscow**, Russia
A. Balashoff, A. Boukharov, O. Malyshev

Institute for Theoretical and Experimental Physics named by A.I. Alikhanov of National Research Centre "Kurchatov Institute", **Moscow**, Russia
P. Balanutsa, V. Chernetsky, A. Demekhin, A. Dolgolenko, P. Fedorets, A. Gerasimov, A. Golubev, V. Goryachev, A. Kantsyrev, D. Y. Kirin, N. Kristi, E. Ladygina, E. Luschevskaya, V. A. Matveev, V. Panjushkin, A. V. Stavinskiy

Nuclear Physics Division, Bhabha Atomic Research Centre, **Mumbai**, India
K. N. Basant, H. Kumawat, B. Roy, A. Saxena, S. Yogesh

Westfälische Wilhelms-Universität Münster, **Münster**, Germany
D. Bonaventura, P. Brand, C. Fritzsch, S. Grieser, C. Hargens, A.K. Hergemöller, B. Hetz, N. Hüsken, J. Kellers, A. Khoukaz, C. Mannweiler

Suranaree University of Technology, **Nakhon Ratchasima**, Thailand
D. Bumrungkoh, C. Herold, K. Khosonthongkee, C. Kobdaj, A. Limphirat, K. Manasatitpong, T. Nasawad, S. Pongampai, T. Simantathammakul, P. Srisawad, N. Wongprachanukul, Y. Yan

Nankai University, **Nankai**, China
C. Yu, X. Zhang, W. Zhu

Novosibirsk State University, **Novosibirsk**, Russia
A. E. Blinov, S. Kononov, E. A. Kravchenko

Budker Institute of Nuclear Physics, **Novosibirsk**, Russia
E. Antokhin, A. Yu. Barnyakov, K. Beloborodov, V. E. Blinov, I. A. Kuyanov, S. Pivovarov, E. Pyata, Y. Tikhonov

Institut de Physique Nucléaire, CNRS-IN2P3, Univ. Paris-Sud, Université Paris-Saclay, 91406, **Orsay cedex**, France
R. Kunne, B. Ramstein

University of Wisconsin Oshkosh, **Oshkosh**, U.S.A.
G. Hunter, M. Lattery, H. Pace

Dipartimento di Fisica, Università di Pavia, INFN Sezione di Pavia, **Pavia**, Italy
G. Boca

University of West Bohemia, **Pilsen**, Czech
D. Duda

Charles University, Faculty of Mathematics and Physics, **Prague**, Czech Republic
M. Finger, M. Finger, Jr., A. Kveton, M. Pesek, M. Peskova, I. Prochazka, M. Slunecka, M. Volf

Czech Technical University, Faculty of Nuclear Sciences and Physical Engineering, **Prague**, Czech Republic
P. Gallus, V. Jary, O. Korchak, M. Marcisovsky, G. Neue, J. Novy, L. Tomasek, M. Tomasek, M. Virius, V. Vrba

A.A. Logunov Institute for High Energy Physics of the National Research Centre "Kurchatov Institute",

Protvino, Russia
V. Abramov, S. Bukreeva, S. Chernichenko, A. Derevschikov, V. Ferapontov, Y. Goncharenko, A. Levin, E. Maslova, Y. Melnik, A. Meschanin, N. Minaev, V. Mochalov, V. Moiseev, D. Morozov, L. Nogach, S. Poslavskiy, A. Ryazantsev, S. Ryzhikov, P. Semenov, I. Shein, A. Uzunian, A. Vasiliev, A. Yakutin

Sikaha-Bhavana, Visva-Bharati, WB, **Santiniketan**, India
U. Roy

University of Sidney, School of Physics, **Sidney**, Australia
B. Yabsley

National Research Centre "Kurchatov Institute" B. P. Konstantinov Petersburg Nuclear Physics Institute, Gatchina, **St. Petersburg**, Russia
S. Belostotski, G. Fedotov, G. Gavrilov, A. Izotov, S. Manaenkov, O. Miklukho, A. Zhdanov

Kungliga Tekniska Högskolan, **Stockholm**, Sweden
A. Atac, T. Bäck, B. Cederwall

Stockholms Universitet, **Stockholm**, Sweden
K. Makonyi, M. Preston, P.E. Tegner, D. Wölbing

Sardar Vallabhbhai National Institute of Technology, Applied Physics Department, **Surat**, India
K. Gandhi, A. K. Rai

Veer Narmad South Gujarat University, Department of Physics, **Surat**, India
S. Godre

Florida State University, **Tallahassee**, U.S.A.
V. Crede, S. Dobbs, P. Eugenio, D. Lersch

INFN Sezione di Torino, **Torino**, Italy
D. Calvo, P. De Remigis, A. Filippi, G. Mazza, A. Rivetti, R. Wheadon

Università di Torino and INFN Sezione di Torino, **Torino**, Italy
M. P. Bussa, S. Spataro

Politecnico di Torino and INFN Sezione di Torino, **Torino**, Italy
F. Iazzi, A. Lavagno

Università di Trieste and INFN Sezione di Trieste, **Trieste**, Italy
A. Martin

Uppsala Universitet, Institutionen för fysik och astronomi, **Uppsala**, Sweden
A. Akram, H. Calen, W. Ikegami Andersson, T. Johansson, A. Kupsc, P. Marciniewski, M. Papenbrock, J. Regina, K. Schönning, M. Wolke

Instituto de Física Corpuscular, Universidad de Valencia-CSIC, **Valencia**, Spain
J. Diaz

Sardar Patel University, Physics Department, **Vallabh Vidynagar**, India
V. Pothodi Chackara

National Centre for Nuclear Research, **Warsaw**, Poland
A. Chlopik, G. Kesik, D. Melnychuk, J. Tarasiuk, M. Wojciechowski, S. Wronka, B. Zwieglinski

Österreichische Akademie der Wissenschaften, Stefan Meyer Institut für Subatomare Physik, **Wien**, Austria
C. Amsler, P. Bühler, N. Kratochwil, J. Marton, W. Nalti, D. Steinschaden, E. Widmann, S. Zimmermann, J. Zmeskal

Editors:	Malte Albrecht	Email: malte@ep1.ruhr-uni-bochum.de
	Luigi Capozza	Email: lcapozza@uni-mainz.de
	Valery Dormenev	Email: valery.dormenev@exp2.physik.uni-giessen.de
	Thorsten Erlen	Email: therlen@ep1.ruhr-uni-bochum.de
	Holger Flemming	Email: h.flemming@gsi.de
	Christopher Hahn	Email: christopher.l.hahn@physik.uni-giessen.de
	Fritz-Herbert Heinsius	Email: heinsius@ep1.ruhr-uni-bochum.de
	Thomas Held	Email: thomas@ep1.ruhr-uni-bochum.de
	Tobias Holtmann	Email: tholtmann@ep1.ruhr-uni-bochum.de
	Miriam Kümmel	Email: miriamk@ep1.ruhr-uni-bochum.de
	Pawel Marciniewski	Email: pawel.marciniewski@physics.uu.se
	Markus Moritz	Email: markus.moritz@exp2.physik.uni-giessen.de
	Oliver Noll	Email: ernoll@uni-mainz.de
	Viktor Rodin	Email: v.rodin@rug.nl
	Andrey Ryazantsev	Email: andrey.ryazantsev@ihep.ru
	Christoph Schmidt	Email: schmidt@hiskp.uni-bonn.de
	Claudius Schnier	Email: cschnier@ep1.ruhr-uni-bochum.de
	Tobias Seifen	Email: seifen@hiskp.uni-bonn.de
	Tobias Triffterer	Email: tobias@ep1.ruhr-uni-bochum.de
	Hans-Georg Zaunick	Email: hans-georg.zaunick@exp2.physik.uni-giessen.de
Technical Coordinator:	Lars Schmitt	Email: l.schmitt@gsi.de
Deputy:	Anastasios Belias	Email: a.belias@gsi.de
Spokesperson:	Klaus Peters	Email: k.peters@gsi.de
Deputy:	Tord Johansson	Email: tord.johansson@physics.uu.se

Abstract

This document provides an update to the Technical Design Report (TDR) for the Electromagnetic Calorimeter (EMC) of the $\overline{\mathrm{P}}$ANDA Experiment. The original TDR was published in August 2008.

Contents

Executive Summary

This report presents an update to the PANDA EMC Technical Design Reports (TDRs) and reflects the current status of the Target Spectrometer (TS) Electromagnetic Calorimeter (EMC) of the PANDA experiment.

The Anti**p**roton **An**nihilations at **Da**rmstadt (PANDA) experiment will be one of the four flagship experiments at the new international accelerator complex Facility for Antiproton and Ion Research (FAIR) in Darmstadt, Germany. PANDA will perform unique experiments using the high-quality antiproton beam with momenta in the range of 1.5 GeV/c up to 15 GeV/c, stored in the High Energy Storage Ring (HESR) to investigate fundamental questions of hadron physics in the charmed and multi-strange hadron sector and deliver decisive contributions to the open questions of QCD. The scientific program of PANDA includes hadron spectroscopy, in particular the search of exotic states in the charmonium mass region and spectroscopy of multi-strange baryons, investigation of properties of mesons embedded in nuclear matter, nucleon structure, and hypernuclei. The cooled antiproton beam colliding with a fixed proton or nuclear target allows hadron production and formation experiments with a luminosity of up to $2 \times 10^{32}\,\mathrm{cm}^{-2}\,\mathrm{s}^{-1}$ in the fully completed version of the facility. In the modular start version (MSV) the luminosity will be $1 \times 10^{31}\,\mathrm{cm}^{-2}\,\mathrm{s}^{-1}$.

The PANDA experiment ist designed to achieve 4π solid angle coverage, high resolution for tracking, good particle identification, high precision calorimetry, high rate capabilities, versatile readout and event selection. The antiproton beam interacts with a cluster or pellet hydrogen, deuterium or heavy nucleus target. The application of a fixed target at PANDA results in a forward peaking of the reaction products. To ensure a geometrical acceptance close to 4π and a good momentum resolution in a wide range, the chosen setup consists of two spectrometers: the Target Spectrometer (TS) based on a 2 T superconducting solenoid magnet surrounding the interaction point and the Forward Spectrometer (FS) using a large gap 2 T m dipole magnet for momentum analysis of particles emitted at the most forward angles. The FS covers an angular range of $\pm 10^\circ$ in the horizontal plane and $\pm 5^\circ$ in the vertical plane.

The PANDA electromagnetic calorimeter of the TS covers nearly 4π for an efficient reconstruction of complex states. It is complemented in the FS by a shashlyk type sampling calorimeter. Due to the 2 T superconducting magnet of the TS a very compact calorimeter is needed. The maximum expected annual dose of 125 Gy in the most forward region demands radiation hardness. An effective background rejection, especially for complex final state channels, is mandatory. Therefore, the EMC has to provide an excellent spatial and energy resolution over a huge dynamic range from 10 MeV up to 15 GeV.

As scintillator material improved $PbWO_4$ scintillator (PWO-II) was chosen. It provides a small radiation length (0.89 cm), a short decay time of 6.5 ns and a factor two improved light yield compared to $PbWO_4$ scintillator (PWO), as was used in the CMS experiment. To increase the light yield further by about a factor of four, the calorimeter will be operated at a temperature of $-25\,^\circ$C.

The EMC is built as a homogeneous calorimeter in the shape of a barrel closed by two endcaps containing nearly 16 000 PWO-II crystals. The crystal length is 200 mm ensuring coverage of the electromagnetic showers even at the highest energies. Tapering of the crystals varies with the angle to the beam axis and is minimal in the forward endcap. The backward endcap consists of straight crystals.

The crystals are wrapped with a reflective material to optimize light collection and reduce optical crosstalk. To minimize the material budget between the crystals they are are supported by carbon fibre alveoli packs. Theses structures are hold by rear inserts connected to support plates. All parts are surronded by a thermal shielding made of Vacuum Insulation Panels (VIPs). Cooling and temperature stabilization at the operating temperature of $-25\,^\circ$C of the PWO-II crystals and the preamplifiers are realized by a mixture of methanol (60 %) and water (40 %), which is distributed through tubes to the detectors.

The temperature is monitored by specially designed ultrathin platinum resistance sensors placed between the crystals. These and other sensors such as for the humidity of the dry air inside the cooled detectors and the pressure of the cooling liquid are read out by the Temperature and Humidity Monitoring Board for PANDA (THMP) electronics and monitored by the Detector Control System (DCS). A light pulser system monitors the light yield loss of the indvidual crystals, allows for linearity checks

of the electronics chain and serves as a diagnostics tool during setup and PANDA operation. The LED pulser modules mimic the scintallation light pulses of PWO-II over the full dynamic range by means of Liquid Crystal Display (LCD) attenuators, which guarantee a compact design to fit inside the solenoid magnet.

Readout of the PWO-II scintillators is accomplished by two Avalanche Photodiodes (APDs) on each crystal covering an area of $2\,\mathrm{cm}^2$. The very inner part of the forward endcap, which is exposed to high radiation, comprises 768 crystals, each read out by a single Vacuum Photo Tetrode (VPTT). Sitting inside the TS magnet the photo tubes will loose half their gain, which is considered acceptable with respect to the achievable performance, while the APDs are not affected by the solenoid field at all. For the barrel EMC and the backward endcap EMC the APDs are read out by a low-noise and low-power ASIC preamplifier (APFEL). Each ASIC is connected to two APDs and provides two differential outputs with adjustable gain for each channel to achieve a full dynamic range of 10^4. The forward endcap EMC with its higher signal rates and up to 50 % wider dynamic range compared to the barrel EMC features a low-noise and charge-integrated preamplifier with low power consumption based on discrete electronics. The version for reading out the APD is optimized for a gain of $M = 200$, the mechanically shorter version for the VPTT readout is available in three versions, which are adjusted to three different amplifications. The VPTTs were manufactured with different gains and, for an optimal dynamic range, the gains are matched with the corresponding preamplifier gain, the position within the varying magneetic field, and the crystal light output. The gain of the APDs is adjustable over a wide range by the high voltage (HV). Each APDs gain is adjustable by individual HV control boards within the detector.

The signals from the preamplifiers of both endcaps are fed to 64-channel 80 MHz sampling analog to digital converter (SADC) boards with 14 bit resolution. For the forward endcap the boards contain analog shaping input stages with high/low gain splitting. The SADC boards provide two Kintex-7 field programmable gate arrays (FPGAs) for online feature extraction and two small form-factor pluggable (SFP) optical interfaces with 4.8 Gbit/s capability and are housed in dedicated water-cooled crates. The barrel EMC preamplifier signals are read out either by the same type of SADCs or by digitization on the detector with a specially designed Hit Detection ASIC (HDA). The latter case is the preferred option as it minimizes the cables that have to be routed through the magnet. The SADC readout is considered as a backup solution.

The digital data stream is processed within FPGAs on the same board as the analog to digital converters (ADCs). Several filters are applied to recognise pulses with and without pileup, including the pileup pulse. For each pulse the amplitude and the occurance time is determined and sent together with the channel number for further processing to the data concentrator modules. The data concentrator also serves as a distributor of the detector synchronization signals. A module is housed in a single Advanced Mezzanine Card (AMC) and is equipped with 60 optical transceivers and 16 backplane multi-gigabit links, each running at 12 Gbit/s.

The detector modules will be precalibrated with muons from cosmic showers to an accuracy of at least 10 %. Further calibrations will be performed at FZ Jülich for the forward endcap EMC and at Mainzer Mikrotoron (MAMI) for the barrel and backward endcap modules. During operation the EMC will be calibrated in situ with physics events (neutral mesons and electrons).

Several advanced prototypes and first-of-series components were constructed to optimize the mechanical design, the performance and to study the insulation and detector cooling. It was shown, that the required energy resolution of $\sigma_E/E = 1\,\% \oplus 2\,\%/\sqrt{E/\mathrm{GeV}}$ is achievable. A time resolution of below 2 ns can be reached, for energies above 500 MeV a time resolution below 200 ps is feasable.

Construction of the barrel and both endcap EMCs is ongoing and a timely installation inside the PANDA detector can be expected.

This document is structured as follows: To keep the connection to the original PANDA EMC TDR the chapters are organized in the same order and the duplication of content is avoided. The Chap. 1 replaces the original Chap. 2 and gives a current description of the PANDA experiment. The design considerations of the EMC (Chap. 3 EMC TDR) are still valid and are not repeated here.

The selection of PWO-II as the scintillator material and its properties are described in detail in the original Chap. 4. Here in Chap. 2 information on the new crystal manufacturer **Cry**stal **Tur**nov (CRYTUR) and the quality of the crystals is given. The light loss in the scintillator due to the irradiation during data taking cannot be recovered by spontaneous recovery at temperatures of −25 °C. Therefore each PWO-II crystal is equipped with a LED to stimulate the recovery process and to re-

duce the radiation damage.

The photo detectors (original Chap. 4) for the barrel and backward endcap, the large area APDs, are fully described in the EMC TDR. In Chap. 3 consequently only a brief summary of their properties is given and the screening and gain calibration procedure is described in detail. Based on the response of the reviewers of the EMC TDR we have also chosen APDs for the outer 80 % of the forward endcap and vacuum photo detectors only for the area of highest rate and radiation dose. Hamamatsu Photonics K. K. developed Vacuum Photo Tetrodes (VPTTs) with a higher gain than the vacuum phototriodes originally intended. The properties and the screening of the VPTTs are presented in Chap. 3.

The requirements for the readout electronics of a large dynamic range of more than four orders of magnitude and a low threshold demanded specific optimizations in this area. Compared to the Chap. 6 of the EMC TDR the final preamplifiers and further details on digitization and feature extraction are described in Chap. 4. To be able to use the full dynamic range, it is important to optimize the gain of the input signals. For the APDs this can be achieved by varying the operating voltage. Therefore a high voltage regulation system was developed which can adjust the operating voltage of each APD individually. Due to the minimum space available, special care has been taken with the arrangement of the cables (Sec. 4.7). The electronics chapter closes with the Detector Control System (DCS).

For the mechanics and integration (Chap. 7 of the EMC TDR) several changes are notable: The number of crystals for the forward endcap was increased from 3600 to 3856 to have no acceptance hole in the range between the forward endcap and the forward calorimeter of the FS. In the overlap region between the forward endcap and the barrel calorimeter two rings of crystals were added to avoid shower leakage on the side for high energy photons. The design of the backward endcap was completely changed. Compared to that the barrel calorimeter has undergone only minor changes. All design changes are documented in Chap. 5.

As an update to the calibration and monitoring (Chap. 8 EMC TDR) a section on the precalibration of the submodules with muons from cosmic ray showers, a section on the final light pulser monitoring system and a new section on the temperature and humidity monitoring is given in Chap. 6.

For specifics on the simulation please refer to the Chap. 9 of the EMC TDR.

After the EMC TDR was written in 2008 for all three detector systems close to final prototypes were built and have undergone several beam tests. The results are listed in Chap. 7 and replace the original chapter on performance (Chap. 10 EMC TDR).

The Chap. 11 on organization of the original EMC TDR is updated in Chap. 8 where required. This mainly concerns the changes in the participating groups and the change of the crystal producer. The chapter is completed by the status and schedule of the construction.

1 The $\overline{\text{P}}$ANDA Experiment

1.1 The $\overline{\text{P}}$ANDA Scientific Program

The Anti**p**roton **An**nihilations at **Da**rmstadt ($\overline{\text{P}}$ANDA) experiment [1], at the future Facility for Antiproton and Ion Research (FAIR), envisages a physics core program [2] that comprises

- charmonium spectroscopy with precision measurements of mass, width, and decay branches;
- the investigation of states that are assumed to have more exotic configurations like multiquark states, charmed hybrids, and glueballs;
- the search for in-medium modifications of charmed hadrons in nuclear matter;
- the γ-ray spectroscopy of excited states in doubly strange $\Lambda\Lambda$ hypernuclei.

In the charmonium and open-charm regions, many new states have been observed in the last years, that do not match the patterns predicted in those regimes [3]. There are even several states unambiguously being of exotic nature, raising the question about the underlying mechanism to form such kind of states [4].

The production of charmonium and open-charm states in e^+e^- interactions are restricted to initial spin-parities of $J^{PC} = 1^{--}$. This limits the possibility to precisely scan and investigate these resonances in formation reactions. The use of $\bar{p}p$ annihilation does not suffer from this limitation. Combined with the excellent energy resolution of down to about 25 keV, this kind of reactions offer unique opportunities to perform hadron and charmonium spectroscopy in the accessible energy range.

1.2 The FAIR High Energy Storage Ring

The combination of the High Energy Storage Ring (HESR) and $\overline{\text{P}}$ANDA aims at both high reaction rates and high resolution to be able to study rare production processes and small branching ratios. With a design value of 10^{11} stored antiprotons for beam momenta from 1.5 GeV/c to 15 GeV/c and high density targets the anticipated antiproton production rate of $2 \times 10^7\,\text{s}^{-1}$ governs the experiment interaction rate in the order of cycle-averaged $1 \times 10^7\,\text{s}^{-1}$. The stored antiprotons do not have a bunch structure, and with 10 % to 20 % allocated to a barrier bucket, the antiprotons are continuously spread over about 80 % of the HESR circumference.

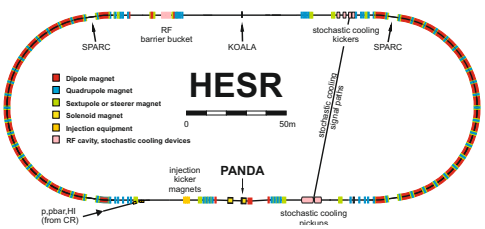

Figure 1.1: Schematic overview of the HESR. The $\overline{\text{P}}$ANDA detector is located at the bottom. Possible locations of the other experiments are indicated at the top. Standard operation has the antiproton injection from the Collector Ring — part of the antiproton production chain at FAIR — from the bottom left, or protons at reversed field polarities.

Two complementary operating modes are planned, named high luminosity mode and high resolution mode. The high luminosity mode with $\Delta p/p = 10^{-4}$, stochastic cooling and a pellet target density of $4 \times 10^{15}\,\text{cm}^{-2}$ will have an average luminosity of up to $\mathcal{L} = 1.6 \times 10^{32}\,\text{cm}^{-2}\,\text{s}^{-1}$. For the high resolution mode $\Delta p/p = 5 \times 10^{-5}$ will be achieved with stochastic cooling and will operate in conjunction with a cluster jet target to limit the energy broadening caused by the target. The cycle-averaged luminosity is expected to be $\mathcal{L} = 1.6 \times 10^{31}\,\text{cm}^{-2}\,\text{s}^{-1}$. The values described here are the design values for the HESR and the $\overline{\text{P}}$ANDA experiment.

In the modularized start version the recuperated experimental storage ring (RESR) will not be available to accumulate the antiprotons. Instead, the accumulation process has to be done with the HESR itself. The absence of the dedicated RESR has the implication that, on one hand, the maximum number of antiprotons is reduced by one order of magnitude to $N_{\text{max}} = 10 \times 10^{10}$ compared to the high luminosity mode. On the other hand the accumulation process, which takes a finite time, cannot be performed in parallel but further worsens the duty cycle (for more detail see [5]). However, since the full version of FAIR is decided to be built, the re-

quirements for detectors of the PANDA experiment have to be set up regarding the original design values.

1.3 The PANDA Experimental Setup

The cut-out of the PANDA setup in Fig. 1.2 shows the detector components. The state of the art design covers nearly 4π of the solid angle for neutral as well as charged particles in a very broad momentum range. It can be divided into the Target Spectrometer (TS) and the Forward Spectrometer (FS) part which is defined by the spectrometer magnet arrangement. The lifetime of the PANDA detector is divided into different phases. Some detector components will not be available when PANDA starts data taking for the first time, but will be installed during subsequent maintenance periods and at later phases of the experiment. The start version of the detector is called the "Day-1" setup.

1.3.1 PANDA Targets

The PANDA Target Spectrometer is designed to allow the installation of different targets. For hydrogen as target material both Cluster Jet Targets and Pellet Targets are being prepared.

An extension of the targets to heavier gases such as deuterium, nitrogen, or argon is planned for complementary studies with nuclear targets. In addition wire or foil targets are used in a dedicated setup for the production of hypernuclei.

1.3.2 PANDA Spectrometer

Micro Vertex Detector The micro vertex detector (MVD) [6] consists of a four layer barrel detector and six detector wheels in the forward direction made from radiation hard silicon pixel and strip sensors. It was optimized for the detection of secondary decay vertices from charmed and strange hadrons as well as for a maximum acceptance close to the interaction point. Moreover transversal momentum resolution is improved compared to a setup without the MVD. It is about 40 cm long and its radius measures from 2.5 cm to 15 cm.

Straw Tube Tracker The straw tube tracker (STT) [7] is a gaseous detector. An assembly of aluminized tubes with diameters of 10 mm is operated at over pressure to make them self supporting. In those a single anode wire is spanned. In total 4636 STT tubes are arranged in 27 layers around the MVD. With a length of 150 cm and an outer radius of 41.8 cm a coordinate resolution of 150 µm in the transversal plane and about 3 mm in the longitudinal direction is achieved.

Forward GEM Detectors Three stations of gas electron multiplier (GEM) detectors are placed between 1.1 m and 1.9 m downstream of the interaction point and are detecting charged particle tracks at polar angles below 22° to extend the acceptance of the STT into forward directions.

Barrel DIRC The barrel detector of internally reflected Cherenkov light (DIRC) in PANDA [8] covers particle identification in the polar angle range of $22° < \theta < 140°$ and is based on the successful BaBar DIRC detector [9]. 1.7 cm thick fused silica slabs are surrounding the beam pipe in a radial distance of 45 cm to 54 cm. As a segmented photon readout Micro-Channel Plate (MCP) Photo Multiplier Tubes (PMTs) were chosen which are by design insensitive to magnetic fields.

Forward Endcap DIRC Particle identification for polar angles between $5° < \theta < 22°$ is performed by the forward endcap disc DIRC detector [10]. The radiator discs have thickness of 2 cm and a radius of up to 110 cm. A sophisticated optical system is attached to the outer rim in order to correct for Cherenkov light dispersion before measuring the photon coordinates with MCP PMTs.

Barrel ToF A time-of-flight (ToF) barrel system [11] is placed outside of the barrel DIRC detector to identify charged particles with a slow velocity and to detect photon conversions in the DIRC detector. In total 1920 scintillator tiles with dimensions of 87 mm × 29.4 mm × 5 mm and silicon PMTs attached to each end of a tile are providing hit information with a time resolution of less than 100 ps. Therefore these are essential in many event time reconstruction algorithms used for the PANDA software triggers. In addition a good spatial resolution is used as an input to the online pattern recognition.

Electromagnetic Calorimeters The PANDA EMC was presented in the original TDR [12] that is updated by this document. It features a geometrically compact design, high count rate capability and excellent energy resolution of 2 % at 1 GeV/c photon momentum. To achieve this goal, lead

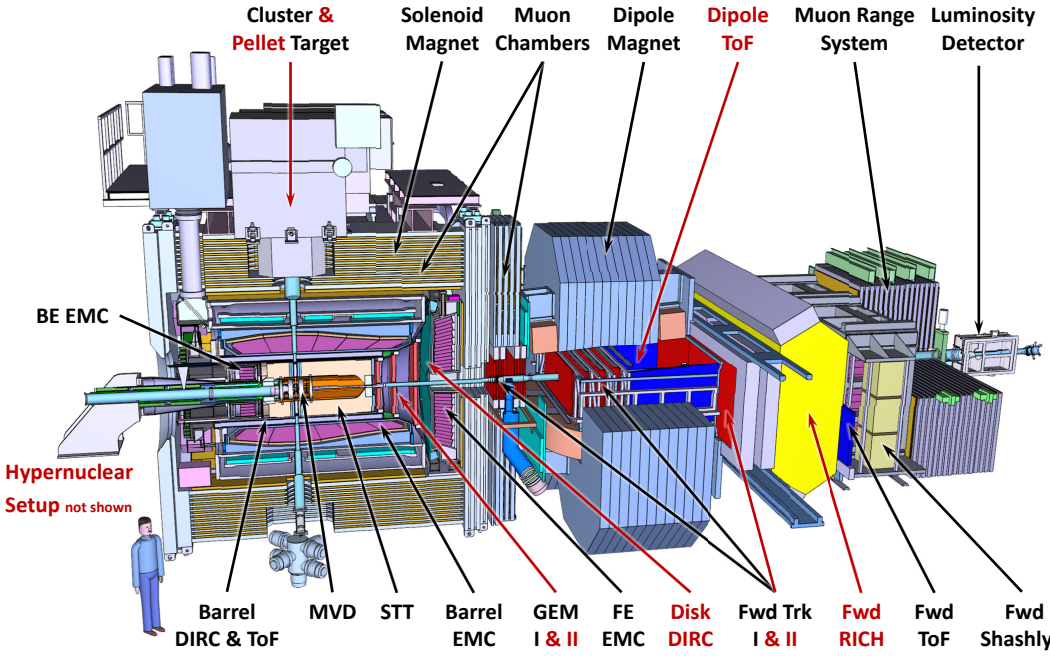

Figure 1.2: Side view of PANDA with the Target Spectrometer (TS) of the left side, and the Forward Spectrometer (FS) starting with the dipole magnet center on the right side. The antiproton beam enters from the left. Detector components labeled in black are part of the Day-1 setup, red labels indicate upgrades for later phases.

tungstate ($PbWO_4$) — cooled down to −25 °C for a higher photon yield — was chosen as a scintillating material. Starting at an inner radius of about 57 cm 11 200 20 cm long crystals with a face area of 2.1 cm × 2.1 cm are arranged to a barrel. In the forward direction 3856 tapered crystals are forming the endcap and the backward direction is covered with about 500 crystals[1] to cover the geometrical acceptance of the TS region.

Muon Detectors The outer layers of PANDA consist of muon detectors [13] made of iron sheets instrumented with aluminum mini drift tubes (MDT). High energetic pions are absorbed while through-going muon tracks can be identified. Moreover in the TS region the iron material is at the same time the magnet yoke for the magnetic field flux return.

Forward Trackers In the FS, the forward trackers (FT) [14] is made of straw tubes arranged in double layers upstream, inside and downstream of the dipole to reconstruct charged particle trajectories in the forward direction.

Forward Particle Identification For the particle identification in the forward region a Ring Imaging Cherenkov Detector (RICH) is planned combined with a ToF system. The RICH detector is designed to consist of a self focusing radiator array [15]. The separation of $\pi/K/p$ tracks would cover a wide range of 2 GeV/c to 15 GeV/c track momentum when implementing two or more consecutive silica aerogel layers with increasing densities as a radiator. Plane lightweight mirrors deflect

1. The backward endcap is — at the time of writing — subject to a redesign, see Sec. 5.3.2.

rings of Cherenkov light out of acceptance which are then sensed by a matrix of PMTs.

The Forward ToF [16] will use slabs made from plastic scintillator and PMTs attached to both ends that are arranged perpendicular to the beam pipe covering a momentum range of up to 2.8 GeV/c for π/K separation and up to 4.7 GeV/c in case of K/p separation.

Forward EMC The forward EMC [17] will consist of 1404 shashlyk-type modules of 55 mm × 55 mm cell size which can achieve a resolution as good as $4\,\%/\sqrt{E}$. An array of lead-scintillator slabs is perforated longitudinally by wavelength shifting fibers.

Luminosity Detector The most downstream detector is the luminosity detector (LMD) [18] which measures the elastically scattered antiprotons at small angles. The LMD is a small tracking station with four layers of High-Voltage Monolithic Active Pixel Sensors covering the full azimuthal angle and polar angles between 3 mrad to 8 mrad.

1.4 $\overline{\text{P}}$ANDA Data Aquisition

Due to the high interaction rate at the $\overline{\text{P}}$ANDA spectrometer the data acquisition (DAQ) [19] will feature a decentralized approach for feature extraction. The complete schematic of the $\overline{\text{P}}$ANDA DAQ system is depicted in Fig. 1.3. It will employ a push architecture where every front end of the setup has a free running and instantaneous readout. It has to be able to extract physical events based on data signatures, called feature extraction. The physically relevant information is processed and sent to data concentrators were the information of several front ends are collected. From here the complete detector information of one HESR burst is transmitted to the event building stage and the compute nodes. The compute nodes employ modern FPGAs that reconstruct all tracks and correlate these with the data from particle identification (PID) detectors. Different physics triggers using cuts on reconstructed variables such as invariant mass distributions or transverse momenta will decide which events contain information relevant to the physics program and are written to disk for offline analysis.

The operation of the $\overline{\text{P}}$ANDA DAQ is synchronized with the synchronization of data acquisition (SODA) net [19] system which is able to provide a common reference time to all components with a precision of 20 ps. It is coupled to the burst structure[2] of the HESR beam and assigns a burst number to each data frame. This way it is possible to assemble a complete event out of the information from individual detector components within the event building network.

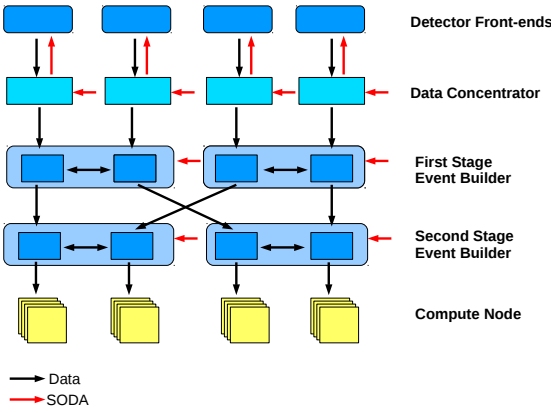

Figure 1.3: Schematic of the $\overline{\text{P}}$ANDA DAQ architecture (based on [20]).

In addition to time synchronization, the SODA link will be used for transmission of DCS information to the detector front ends.

1.5 $\overline{\text{P}}$ANDA Detector Control System

The $\overline{\text{P}}$ANDA Detector Control System (DCS) monitors and operates all the experimental equipment of the $\overline{\text{P}}$ANDA detector [21]. It follows a decentralized approach with one DCS partition for each $\overline{\text{P}}$ANDA subsystem and one supervisory layer that collects the data from all these partitions, archives them and makes them available to the operators on shift.

More details on the $\overline{\text{P}}$ANDA DCS can be found in Sec. 4.8 of this TDR.

1.6 $\overline{\text{P}}$ANDA Infrastructure

The $\overline{\text{P}}$ANDA detector is located in an experimental hall, encased in smaller tunnel-like concrete structure for radiation protection. Most subsystems connect their FEE-components via cables and tubes placed in movable cable ducts to the installations

2. One revolution of an antiproton bunch in the HESR interacting with the target is called burst. 10 bursts are a super-burst.

in the counting house, where three levels are foreseen to accommodate cooling, gas supplies, power supplies, electronics, and worker places. Only subcomponents, where cables must be as short as possible, will place racks or crates directly on the outside of the spectrometer. A detailed account of the PANDA infrastructure can be found at [22].

Bibliography

[1] $\overline{\text{P}}$ANDA Collaboration. Technical Progress Report, FAIR-ESAC/Pbar. 2005. https://panda.gsi.de/oldwww/archive/public/panda_tpr.pdf.

[2] $\overline{\text{P}}$ANDA Collaboration. Physics Performance Report for $\overline{\text{P}}$ANDA: Strong Interaction Studies with Antiprotons. 2009. https://arxiv.org/pdf/0903.3905.pdf.

[3] X. Liu. An overview of XYZ new particles. *Chin. Sci. Bull.*, 59:3815 – 3830, 2014. https://doi.org/10.1007/s11434-014-0407-2.

[4] Yu. S. Kalashnikova et al. Quark and Meson Degrees of Freedom in the $X(3872)$ Charmonium. *Phys. Atom. Nucl.*, 73:1592 – 1611, 2010. https://doi.org/10.1134/S1063778810090127.

[5] K. Götzen. Average Luminosities and Event Rates at $\overline{\text{P}}$ANDA. Report of the PID TAG, March 2009.

[6] $\overline{\text{P}}$ANDA Collaboration. TDR for the $\overline{\text{P}}$ANDA Micro Vertex Detector. 2011. https://panda.gsi.de/publication/re-tdr-2011-001.

[7] $\overline{\text{P}}$ANDA Collaboration. Straw Tube Tracker Technical Design Report. 2012. https://panda.gsi.de/publication/re-tdr-2012-001.

[8] $\overline{\text{P}}$ANDA Collaboration. TDR for the $\overline{\text{P}}$ANDA Barrel DIRC Detector. 2017. https://panda.gsi.de/publication/re-tdr-2016-001.

[9] R. Aleksan et al. Test of a large scale prototype of the DIRC, a Čherenkov imaging detector based on total internal reflection for BaBar at PEP-II. *Nucl. Instrum. Meth. A*, 397(2):261 – 282, 1997. https://doi.org/10.1016/S0168-9002(97)00744-4.

[10] $\overline{\text{P}}$ANDA Collaboration. TDR for the $\overline{\text{P}}$ANDA Endcap Disc DIRC. 2019. https://panda.gsi.de/publication/re-tdr-2018-006.

[11] $\overline{\text{P}}$ANDA Collaboration. TDR for the $\overline{\text{P}}$ANDA Barrel TOF. 2016. https://panda.gsi.de/publication/re-tdr-2016-003.

[12] $\overline{\text{P}}$ANDA Collaboration. Technical Design Report for the $\overline{\text{P}}$ANDA Electromagnetic Calorimeter. 2008. https://panda.gsi.de/publication/re-tdr-2008-001.

[13] $\overline{\text{P}}$ANDA Collaboration. Technical Design Report for the $\overline{\text{P}}$ANDA Muon System. 2013. https://panda.gsi.de/publication/re-tdr-2012-003.

[14] $\overline{\text{P}}$ANDA Collaboration. Technical Design Report for the $\overline{\text{P}}$ANDA Forward Tracker. 2017. https://panda.gsi.de/publication/re-tdr-2017-001.

[15] A.Y. Barnyakov et al. Focusing aerogel RICH (FARICH). *Nucl. Instrum. Meth. A*, 553(1):70 – 75, 2005. https://doi.org/10.1016/j.nima.2005.08.073.

[16] $\overline{\text{P}}$ANDA Collaboration. TDR for $\overline{\text{P}}$ANDA Forward Time of Flight Detector. 2018. https://panda.gsi.de/publication/re-tdr-2016-004.

[17] O. Mineev et al. Photon sandwich detectors with WLS fiber readout. *Nucl. Instrum. Meth. A*, 494(1):362 – 368, 2002. https://doi.org/10.1016/S0168-9002(02)01493-6.

[18] $\overline{\text{P}}$ANDA Collaboration. Technical Design Report for the $\overline{\text{P}}$ANDA Luminosity Detector. 2018. https://panda.gsi.de/publication/re-tdr-2015-001.

[19] $\overline{\text{P}}$ANDA Collaboration. Technical Design Report for the $\overline{\text{P}}$ANDA Data Acquisiton. 2020. (submitted to FAIR for review).

[20] K. Korcyl et al. Modeling event building architecture for the triggerless data acquisiton system for $\overline{\text{P}}$ANDA experiment at the HESR facility at FAIR/GSI. *J. Phys. Conf. Ser.*, 396(012027), 2012. https://doi.org/10.1088/1742-6596/396/1/012027.

[21] $\overline{\text{P}}$ANDA Collaboration. Technical Design Report for the $\overline{\text{P}}$ANDA Detector Control System. 2019. (submitted to FAIR for review).

[22] $\overline{\text{P}}$ANDA Collaboration. Technical Design Report for the $\overline{\text{P}}$ANDA Detector Infrastructure and Installation. 2020. (submitted to FAIR for review).

2 Scintillation Material

2.1 Production Status at BTCP

After the approval of the EMC Technical Design Report (TDR) [1] in 2008 the mass production at the Bogoroditsk Technological Chemical Plant (BTCP) was started. The acceptance tests were performed in close cooperation with the experts of the Electromagnetic Calorimeter of the CMS detector at CERN (CMS-ECAL) exploiting the **A**utomatic **C**rystal Quality **Co**ntrol **S**ystem for PWO crystals (ACCOS) [2] machine, which was adapted to the PWO-II geometry and its specifications. $\overline{\text{P}}$ANDA specification limits, crystal geometries of PWO-II and its properties comparison vs. the lead tungstate material for CMS-ECAL are given in the 2008 EMC TDR. The test measurements of radiation hardness and absolute light yield including cross-checks at low temperature as well as the final analysis were done at Gießen. The optical transmissions were measured longitudinally as well as perpendicularly to the crystal axis in order to control the homogeneity. Fig. 2.1 shows the measured longitudinal transmission values at the relevant wavelengths of 360, 420 and 620 nm, respectively. The figure confirms the consistency of the measurements obtained at each of the three testing locations. All values are well above the specification limits and none of the crystals had to be rejected due to insufficient optical quality. The maximum variation of the absorption edge along the crystal length, which is a sensitive measure of the light yield homogeneity, is determined by the wavelength corresponding to a transmission value of T = 50 % and remains well below $\Delta\lambda \leq 3$ nm.

The significantly improved light yield of PWO-II is documented in Fig. 2.2. The detected number of photoelectrons per MeV deposited energy is determined at room temperature (T = +18 °C) with a standard photomultiplier with fused silica window and bialkali photocathode (Hamamatsu R2059, QE(420 nm) = 21 %). The signal amplitude caused by γ-rays of a ^{137}Cs source (E_γ = 662 keV)) is calibrated with the single–photoelectron (phe) peak.

Only a few samples did not pass the limit of 16 phe/MeV. The further enhanced light yield of the barrel crystals reflects the light collection due to the more tapered crystal shape compared to the nearly straight geometry of the endcap modules. More than 90 % of the light is collected within 100 ns, which even holds when crystals are cooled down to T = −25 °C. The most critical parameter is the change of the longitudinal absorption coefficient dk due to radiation damage. The crystals were irradiated at room temperature at the facility at Radiation Center of Universität Gießen with an integral dose of 30 Gy using a set of ^{60}Co sources. The longitudinal transmissions were measured up to a wavelength of 900 nm delayed by 30 minutes after irradiation in order to exclude fast spontaneous recovery processes. Fig. 2.3 shows the distribution of the dk value at 420 nm and indicates the significant percentage of extremely radiation hard crystals in the tail of the distribution towards lower values. All crystals above the limit of 1.1 m^{-1} were finally rejected. Radiation hardness appears to be the most selective quality parameter. The measurement at Gießen is compared to the data provided by the BTCP using a different irradiation concept.

More than 9000 crystals for the $\overline{\text{P}}$ANDA calorimeters were produced by Czochralski method at BTCP until its shut down in 2011. Crystals were

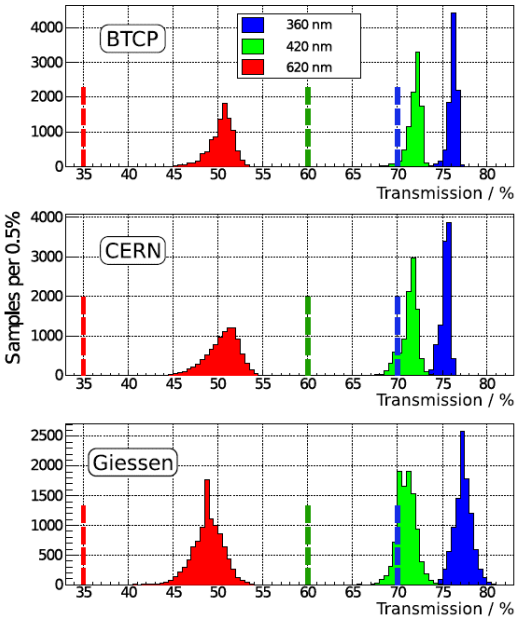

Figure 2.1: The distributions of the longitudinal transmission at three selected wavelengths of PWO-II crystals in $\overline{\text{P}}$ANDA geometry measured at three locations for comparison. Dashed lines mark specification limits.

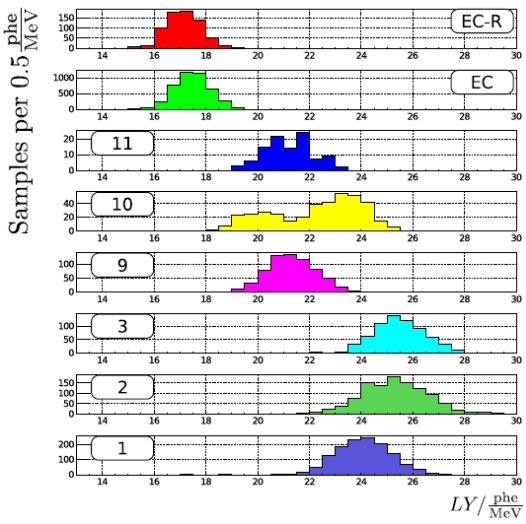

Figure 2.2: The distribution of the light yield measured at T = +18 °C with a photomultiplier tube for PWO-II crystals of 6 different $\overline{\text{P}}$ANDA geometries. The strongly tapered shapes (type 1, 2, 9 and 10) indicate the impact of light focusing. The geometries EC and EC-R are used in the forward and backward endcaps and are only slightly tapered or even rectangular, respectively.

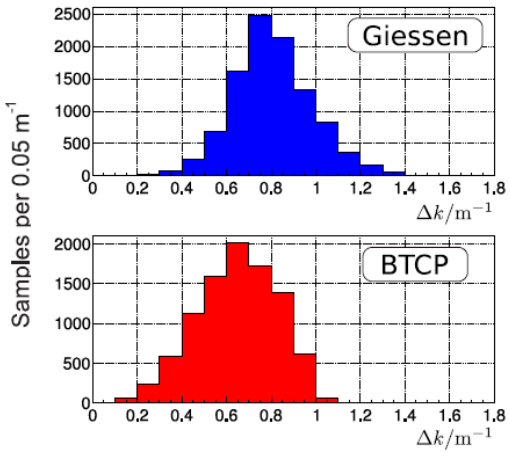

Figure 2.3: Distribution of the radiation induced absorption coefficient dk measured at room temperature for PWO-II crystals. The integral dose amounts to 30 Gy (^{60}Co source). The specification limit was set to $dk \leq 1.1\,\text{m}^{-1}$ determined at the radiation facility at Gießen.

delivered in 10 lots in the period of 2009 – 2010. The crystal production for both Endcaps including spare samples was completed by BTCP [3, 4, 5, 6]. More than half of PWO-II crystals for the Barrel part were still missing when BTCP was closed. Crystals were rejected mainly because dk and light yield values were found outside the specification limits. In total 651 ($< 7\,\%$) crystals had to be rejected.

2.2 Lead Tungstate Crystals produced at SICCAS

Right after the termination of the production of PWO-II crystals at BTCP the research program in collaboration with Shanghai Institute of Ceramics, Chinese Academy of Science (SICCAS) (Shanghai, China) has been reactivated and ran for several years. They use up to now a modified Bridgman technique to grow the crystals and had delivered in the past some smaller fraction of the CMS-ECAL crystals. Over a period of more than 5 years 100 full size crystals (200 mm) were delivered but they never reached a stable condition meeting all relevant quality parameters [4, 6]. The crystals are grown along the c-axis leading to a lower theoretical transmission value at 360 nm. The measured value shows (see Figs. 2.4) an extremely broad distribution and could not be used as one of the quality factors.The results presented in Figs. 2.4, 2.5 and 2.6 contain the complete delivery. For all parameters, the distributions are significantly broader with large tails in both directions. Beside the limitations of the technology, part of the failure might be addressed to strong variations of the quality and the origin of the raw material. A final attempt to use high-quality but pre-mixed material formerly used by BTCP failed as well. Therefore, a continuation of the collaboration was terminated in 2013.

2.3 Production at CRYTUR

The company **Cry**stal **Tur**nov (CRYTUR)[1], Turnov, Czech Republic, has gained good experience in the development and production of different types of inorganic oxide crystals [7] since a long time and has initiated a research program in the middle of 2014 to develop the technology for mass production of lead tungstate crystals [8] based on the Czochralski method. During the first stage series of small samples (1 cm^3) and later rectangular bars (up to 20 mm × 20 mm × 200 mm)

1. CRYTUR spol. s.r.o., https://www.crytur.cz/

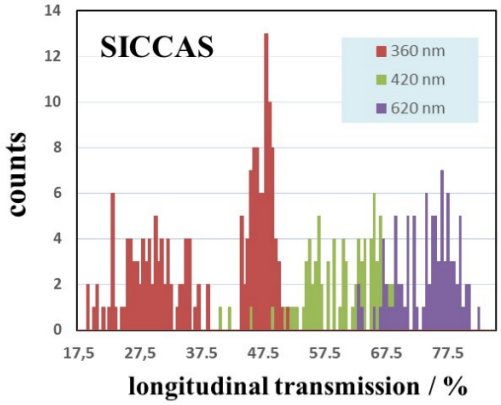

Figure 2.4: Distribution of the longitudinal optical transmissions at three relevant wavelengths measured for full size PWO crystals in PANDA geometry type 11L manufactured by SICCAS.

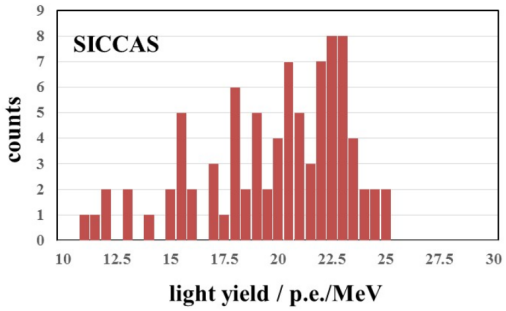

Figure 2.5: Distribution of the light yield of full size crystals provided by SICCAS measured at room temperature with a photomultiplier with bialkali photocathode (QE = 21 %).

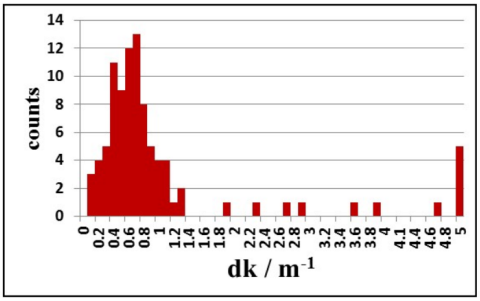

Figure 2.6: Distribution of the radiation induced absorption coefficient for full size crystals provided by SICCAS measured at room temperature. The crystals were irradiated with an integral dose of 30 Gy using a ^{60}Co source.

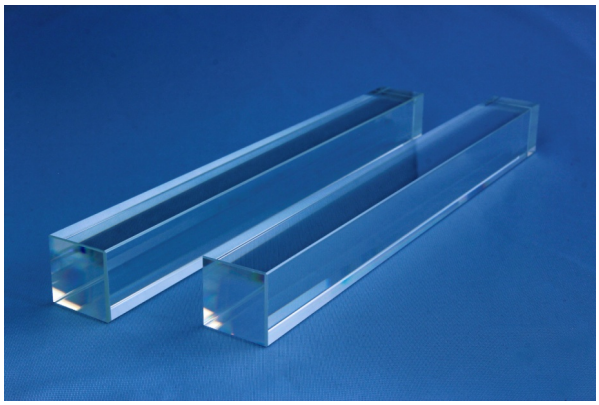

Figure 2.7: Photograph of two tapered PWO-II crystals of PANDA geometry type 11 Left as part of a pre-production lot.

were produced and tested to optimize the growing conditions [5, 6]. The pre-production of crystals in tapered PANDA geometry types was started (see Fig. 2.7) in August 2015. Four in-house designed new furnaces were installed and used for the crystal production including additional equipment for cutting and polishing (see Fig. 2.8 Fig. 2.9). Before crystal delivery the manufacturer CRYTUR certifies the geometry with a 3D laser machine (see Fig. 2.10) and performs cross-checking measurements of the longitudinal optical transmittance and light yield values on the corresponding testing equipments.

In the meantime, additional groups from the university of Prague have joined the PANDA collaboration and provided an additional set-up at the MICROTRON Laboratory at Prague[2] for a prompt inspection of the radiation hardness of the grown ingots. The MT25 facility delivers an electron beam with an energy of up to 20 MeV. The set-up delivers Bremsstrahlung photons by using a radiator to illuminate the samples cut from the top and the bottom of the ingot homogeneously. The typically 1 cm thick PWO-II plates, optically polished on the two larger opposite sides, are slowly rotating during the irradiation. A typical illumination time of 10 minutes at a fixed electron beam intensity allows to simulate the observed damage when irradiated by γ-rays of the strong ^{60}Co source at Gießen accumulating an integral dose of 30 Gy. The measurements of the changes in transmittance are performed immediately after irradiation at the same facility. This installation allows to give an immediate feedback to the manufacturing process.

2. http://www.ujf.cas.cz/en/departments/department-of-accelerators/microtron/

Figure 2.8: Photograph of the installed furnaces at CRYTUR for PWO-II crystal growing.

Figure 2.9: Photograph of the equipment installed at CRYTUR for polishing PWO-II crystals.

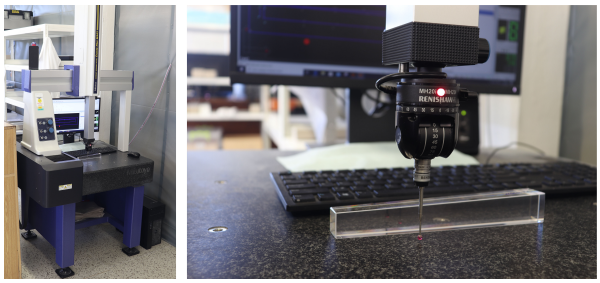

Figure 2.10: Photograph of the 3D machine installed at CRYTUR for the precise measurement of PWO-II crystal dimensions.

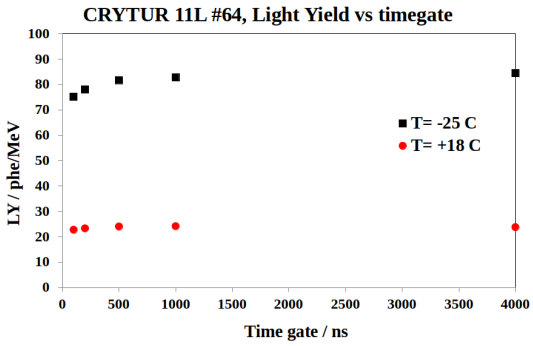

Figure 2.11: Light yield as a function of the integration gate measured at two temperatures for PWO-II sample from CRYTUR delivered as a part of first pre-production lot.

For illustration Figs. 2.11 – 2.12 show the individual performance for a few representative samples. Fig. 2.11 illustrates the light yield measured at two temperatures as a function of the integration gate of the charge sensitive ADC digitizing the direct output of the photomultiplier (Hamamatsu R2059-01). At room temperature more than 94 % of the light are integrated within 100 ns compared to a gate width of 1 µs. This value is slightly reduced to 90.8 % when measured at T = −25 °C. It indicates that slow scintillation components can be neglected and will not have any impact on the rate capability of the electromagnetic calorimeter of $\overline{\text{P}}$ANDA. Fig. 2.12 demonstrates relevant values of the longitudinal transmittance and radiation induced coefficient of three selected crystals. In the short pre-production phase intended for testing and optimization, CRYTUR has established the technology for growing high quality lead tungstate crystals. The described first large crystals showed specifications, which come very close to the parameters achieved for PWO-II developed at BTCP. In this period 192 crystals were produced and quality controlled. Out of the 192 crystals of complete pre-production only 13 had to be rejected in the initial production line primarily due to a dk value exceeding the limit of $1.1\,\mathrm{m}^{-1}$.

2.4 Crystal Quality of Mass Production for the $\overline{\text{P}}$ANDA EMC

The mass-production of crystals of PWO-II quality was started at CRYTUR in 2018. The number of furnaces was increased to 21. Present crystal production rate is of about 50 full-size crystals per month and can be increased by installing additional furnaces. In August 2020, the total amount of PWO-II crystals with $\overline{\text{P}}$ANDA geometries produced by CRYTUR during both the pre-production and the mass production stages passed 530. The following Figs. 2.13 – 2.15 show specification parameters considering all delivered crystals.

No crystal had to be rejected due to lower optical transmittances or light values. The 15 rejected

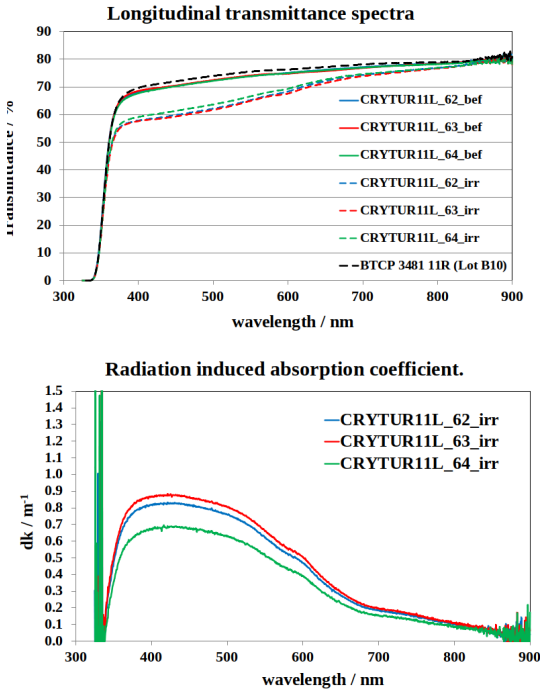

Figure 2.12: (Top) Longitudinal optical transmission as a function of wavelength shown for 3 samples measured before and after irradiation (30 Gy, ^{60}Co) compared to a reference crystal produced by BTCP. (Bottom) Radiation induced absorption coefficient of the same crystal samples due to an integral dose of 30 Gy. The acceptance limit is $dk \leq 1.1\,\mathrm{m}^{-1}$ at a wavelength of 420 nm.

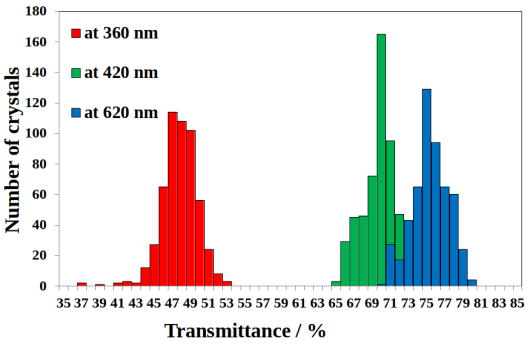

Figure 2.13: Distribution of the longitudinal optical transmissions at three relevant wavelengths measured for full size PWO-II crystals in $\overline{\mathrm{P}}$ANDA geometry types manufactured by CRYTUR.

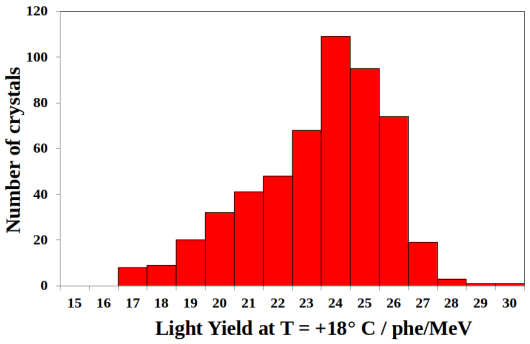

Figure 2.14: Distribution of the light yield of full size crystals provided by CRYTUR measured at room temperature with a photomultiplier with bialkali photocathode (QE = 21 %).

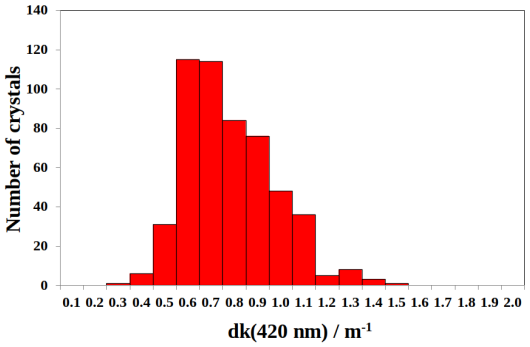

Figure 2.15: Distribution of the radiation induced absorption coefficient for full size crystals provided by CRYTUR measured at room temperature. The crystals were irradiated with an integral dose of 30 Gy using a ^{60}Co source.

exceed the required *dk* value mainly in the very beginning of the pre-production stage or during the burning-in phase of new furnaces.

Table 2.1 summarizes the present status of already delivered or still needed crystals for the Barrel. Both endcaps are already completed. The table contains deliveries from BTCP and CRYTUR as well as some acceptable units produced during the R&D program with SICCAS. Some of the originally rejected crystals from BTCP with parameters close to the limits are considered as spares. Spare crystals are foreseen for instance that any exchange of APDs requires the taking apart of submodules and causes the risk of damaging crystals. It is worth to note that the crystal production for both endcaps and barrel types 1 Left, 1 Right, 2 Right, 3 Right, 9 Left, 9 Right was completed by BTCP with a large amount of spare crystals. As of August 2020 all crystal types needed to complete

two barrel slices were produced and duly accepted as result of CRYTUR mass production. The total amount of PWO-II crystals requested to finish 16 barrel slices including spare units can be evaluated as about 6400. CRYTUR foresees to produce badges of crystals of all required crystal shapes to complete slice by slice.

2.5 Stimulated Recovery of the Radiation Damage in Lead Tungstate Crystals

The operation of inorganic crystalline scintillation materials for detector applications in an environment of strong irradiation requires resistivity to the damage due to ionizing radiation. This problem becomes crucial for electromagnetic calorimetry in high-luminosity hadron accelerator experiments. However, the perfection of the synthetic crystals has physical, technological and economical limits and therefore relies on the search for methods to counteract the radiation damage during the operation of the calorimeter. Point structure defects as well as traps for electrons and holes create a variety of color centers in the crystals with absorption bands in a wide spectral region [9, 10]. After the irradiation stops a spontaneous relaxation of the color centers is taking place via thermo–activation. In fact, this is a thermodynamical process in an open system, which can be further accelerated by injection of energy in an appropriate manner.

There are two processes which are initiated by photons: The ionization of color centers and the transport of the captured electron from a ground state of the color centre to a radiating excited level. The first process (so-called "optical bleaching") depends on the energy width of the conduction band and the location of the ground state of the color center in the forbidden zone. It may be initiated in a wide spectral range from UV to visible light. However, ionization requires in an inefficient manner that the energy of the applied photons is much higher than the thermo-activation energy. The second possible process named "stimulated recovery" is an intra-center resonant transition that can be initiated by photons with an energy even as low as the thermo-activation energy, favorably in the infrared region. In this case, stimulation can even be applied simultaneously with ionizing irradiation, in particular, if the used photo sensor is blind for the chosen wavelength region. As a consequence, the level of the dynamic saturation of the induced optical absorption in the crystal will be reduced. The stimulation

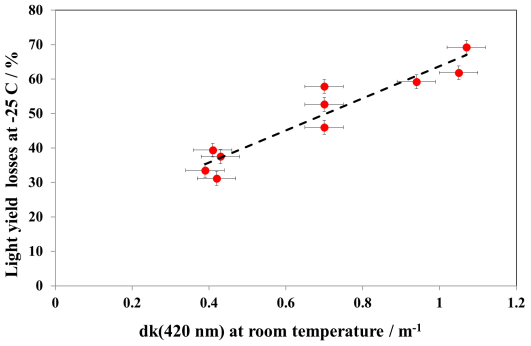

Figure 2.16: Correlation of the relative loss of light yield of cooled PWO-II detectors versus the radiation induced absorption coefficient value at room temperature of investigated crystals. In both cases the integral dose amounts to 30 Gy. The dotted line corresponds to a correlation coefficient of 0.95.

of the recovery becomes effective when two conditions are fulfilled: there is at least one energy level in the center located slightly above the radiating state providing fast recombination and re-trapping processes within the crystal should be strongly suppressed. By variation of the intensity of light one can even control the rate of stimulated recovery.

More relevant for the $\overline{\text{P}}$ANDA EMC application is the behavior at low temperature, which imposes a strong impact on all recovery mechanisms. As investigated in [11, 12], the time constants of the recovery mechanisms become extremely slow at $T = -25\,^{\circ}\text{C}$ in the order of greater than 400 hours. Dominated by the damaging process due to irradiation the light yield deteriorates asymptotically towards a final value which is correlated with the radiation hardness expressed by dk being a measure of the concentration of defect centers in the crystal. Such a correlation for a few accepted crystals is shown in Fig. 2.16 which relates the relative loss of light yield of a cooled detector with the dk value at room temperature. The detector response is measured either with low energy γ-rays or the energy deposition of cosmic muons, respectively. Both values are determined applying an integral dose of 30 Gy.

The most inner part of the forward endcap — corresponding to about 10 % of the modules — has to cope with a dose rate of typically 20 mGy/h for the maximum event rate of 2×10^7 $\overline{\text{p}}$p-annihilations. In the barrel section, radiation damage will be 1 – 2 orders of magnitude lower. Early it was foreseen to operate the $\overline{\text{P}}$ANDA detector including the cooled EMC typically for a period of 6 months and to bring the calorimeter in the second half of the year back to room temperature. In

Table 2.1: Number of PWO-II crystals needed for the PANDA EMC including spare units and summary of all produced crystals of PANDA geometries. The selection is done by crystal types.

Crystal type	Needed amount	Needed amount with spare	Produced by BTCP	Produced by SICCAS	Produced by CRYTUR	Total amount produced	Missing crystals
1	1120	1150	1368			1368	0
2	1280	1310	1142			1142	168
3	1280	1310	705		43	748	562
4	1280	1310	80		82	162	1148
5	1280	1310	78		83	161	1149
6	1280	1310	117		49	166	1144
7	1280	1310	78		83	161	1149
8	640	660	36		51	87	573
9	640	660	692			692	0
10	640	660	416		4	420	240
11	480	490	118	62	120	300	190
Forward Endcap	3856	4400	4400			4400	0
Backward Endcap	640	700	700			700	0
Total	15696	16580	9930	62	515	10507	6323

this case, even keeping the crystals in the dark, relaxation processes are fast and efficient enough to recover the crystals completely during that beam-off period. Detailed studies of the radiation damage of PWO-II crystals have opened up an unexpected option to enhance the recovery by illumination with light [13, 14, 15]. Fig. 2.17 shows examples for illumination with blue light illustrating the change over the entire investigated spectral range.

Fig. 2.18 shows the results for the reduction of the relative light loss achieved with visible light sources centered at emission wavelengths of 464 nm, 525 nm, 639 nm and 860 nm, respectively. For blue light, nearly 90 % of the original signal amplitude was restored within the first 200 minutes already. The used Light-Emitting Diodes (LEDs) have imposed a photon flux of approx. 10^{16} photons/s. These results demonstrate a possible concept if the radiation damage during EMC operation can be either compensated on-line without impact on signal readout or periodically after short shut-downs or breaks in an off-line mode.

It is worth to note that the stimulated recovery of lead tungstate crystals is an effective procedure to improve the radiation resistance of a high-resolution electromagnetic calorimeter. It can be implemented in a wide temperature range down to T = −25 °C, which corresponds to the working conditions of the

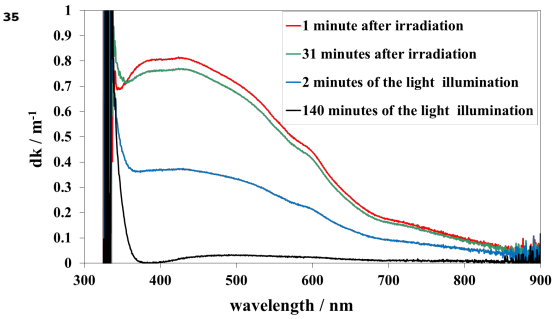

Figure 2.17: Change of the full spectral distribution of the induced absorption coefficient of a PWO-II crystal after irradiation with an integral dose of 30 Gy measured at room temperature. The spectra are measured 1 and 31 minutes after irradiation as well as after additional illumination for 2 and 140 minutes, respectively, with blue light emitted diode (λ_{max} = 464 nm).

PANDA EMC [15, 16, 17]. The recovery processes are more effective in case of illumination with blue light even at a low temperature. However, online recovery could be implemented only for photo detectors with a red edge of quantum efficiency well below 900 nm. The PANDA Collaboration considers as a basic "offline" operating mode during short beam-off phases to recover crystals damage with il-

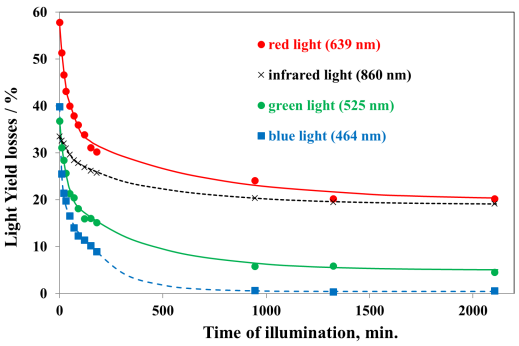

Figure 2.18: Recovery of the loss of the signal amplitude caused by irradiation as a function of the integral duration of illumination using different light sources. All detectors are operated at a temperature of T = −25 °C. The maximum light loss at the beginning reflects the radiation hardness of the individual crystals.

lumination of blue LED light[3].

Bibliography

[1] PANDA Collaboration. Technical Design Report for the PANDA Electromagnetic Calorimeter. 2008. https://panda.gsi.de/publication/re-tdr-2008-001.

[2] E. Auffray et al. Status of PWO crystal production for the electromagnetic calorimeter of CMS and of its construction. *Nucl. Instrum. Meth. A*, 537(1-2):373 – 378, 2005. https://doi.org/10.1016/j.nima.2004.08.046.

[3] V. Dormenev W. Döring T. Eissner M. Korzhik T. Kuske O. Missevitch M. Moritz R.W. Novotny, D. Bremer. The PANDA Electromagnetic Calorimeter – A High-Resolution Detector Based on PWO-II. *IEEE Trans. Nucl. Sci.*, 57(3):1441 – 1446, 2010. https://doi.org/10.1109/TNS.2009.2033913.

[4] V. Dormenev P. Drexler M. Moritz R. W. Novotny R. Schubert T. Eissner, D. A. Bremer. Quality of the $PbWO_4$ Crystals for the PANDA-EMC. *IEEE Nuclear Science Symposium Conference Record (NSS/MIC) 2011*, pages 2095 – 2098, 2011. https://doi.org/10.1109/NSSMIC.2011.6154426.

[5] R. W. Novotny et al. Progress in the Development of the Lead Tungstate Crystals for EM-Calorimetry in High-Energy Physics. *J. Phys. Conf. Ser.*, 928:012031, 2017. https://doi.org/10.1088/1742-6596/928/1/012031.

[6] R. W. Novotny; K.-T. Brinkmann; V. Dormenev; M. Finger; J. Houzvicka; M. Korjik; P. Krist; S. Ochesanu; D. Petrýdes; H.-G. Zaunick. High-Quality Lead Tungstate Crystals for PANDA Produced at CRYTUR. *IEEE Trans. Nucl. Sci.*, 65(8):1998 – 2003, 2018. https://doi.org/10.1109/TNS.2018.2804387.

[7] M. Nikl. Wide band gap scintillation materials: progress in the technology and material understanding. *phys. stat. sol. (a)*, 178(2):595 – 620, 2000. https://doi.org/10.1002/1521-396X(200004)178:2%3C595::AID-PSSA595%3E3.0.CO;2-X.

[8] J. Houzvicka M. Korjik R. W. Novotny A. Borisevich, V. Dormenev. New Start of Lead Tungstate Crystal Production for High-Energy Physics Experiments. *IEEE Trans. Nucl. Sci.*, 63(2):569 – 573, 2016. https://doi.org/10.1109/TNS.2015.2505716.

[9] M. Nikl and K. Nitsch. Radiation induced formation of color centers in $PbWO_4$ single crystals. *J. Appl. Phys.*, 82(11):5758 – 5762, 1997. https://doi.org/10.1063/1.366441.

[10] P. Lecoq A.A. Annenkov, M.V. Korzhik. Lead tungstate scintillation material. *Nucl. Instrum. Meth. A*, 490(1-2):30 – 50, 2002. https://doi.org/10.1016/S0168-9002(02)00916-6.

[11] P. A. Semenov et al. First Study of Radiation Hardness of Lead Tungstate Crystals at Low Temperatures. *Nucl. Instrum. Meth. A*, 582:575 – 580, 2007. https://doi.org/10.1016/j.nima.2007.08.178.

[12] R. W. Novotny et al. Radiation Hardness and Recovery Processes of PWO crystals at −25 °C. *IEEE Trans. Nucl. Sci.*, 55(3):1283 – 1288, 2008. https://doi.org/10.1109/TNS.2008.916062.

[13] V. Dormenev A. Hofstaetter M. Korjik T. Kuske S. Lugert O. Missevitch R.W. Novotny, W.M. Döring. Limitations of the performance of PWO-II crystals due to radiation damage. *IEEE Nuclear Science Symposium Conference Record (NSS/MIC) 2009*, pages 2036 – 2040, 2009. https://doi.org/10.1109/NSSMIC.2009.5402124.

[14] R.W. Novotny A. Borisevich A. Fedorov M. Korjik V. Mechinski O. Missevitch S. Lugert

3. http://www.kingbright.com/attachments/file/psearch/000/00/20160808bak/KA-2810AQBS-D(Ver.8B).pdf

V. Dormenev, T. Kuske. Stimulated recovery of the optical transmission of $PbWO_4$ scintillation crystals for electromagnetic calorimeters after radiation damage. *Nucl. Instrum. Meth. A*, 623(3):1082 – 1085, 2010. https://doi.org/10.1016/j.nima.2010.08.092.

[15] T. Kuske V. Mechinsky V. Dormenev, M. Korjik and R.W. Novotny. Comparison of radiation damage effects in PWO crystals under 150 MeV and 24 GeV high fluence proton irradiation. *IEEE Trans. Nucl. Sci.*, 61(1):501 – 506, 2014. https://doi.org/10.1109/TNS.2013.2275901.

[16] A. Fedorov M. Korjik T. Kuske V. Mechinsky O. Missevitch R. Novotny R. Rusack A. Singovski A. Borisevitch, V. Dormenev. Maintaining low radiation damage of lead tungstate scintillation crystals operating in a high dose rate radiation environment. *IEEE Nuclear Science Symposium Conference Record (NSS/MIC) 2010*, pages 1010 – 1013, 2010. https://doi.org/10.1109/NSSMIC.2010.5873917.

[17] R. Novotny R. Schubert V. Dormenev, T. Kuske. Radiation Damage and Recovery Mechanisms in Cooled $PbWO_4$ Crystals. *IEEE Nuclear Science Symposium Conference Record (NSS/MIC) 2011*, pages 1930 – 1934, 2011. https://doi.org/10.1109/NSSMIC.2011.6154388.

3 Photo Detectors

The detection of the scintillation light of lead tungstate under the given conditions for the PANDA EMC requires excellent photo detectors.

The magnetic field of about 2 T precludes the use of conventional photomultipliers. On the other hand the signal generated by ionization in a PIN photodiode by a traversing charged particle is too large for our applications compared to the corresponding response to scintillation photons. To solve these problems a photosensor insensitive to magnetic fields and with a low response to highly ionizing particles has to be used.

Since the improved $PbWO_4$ scintillator (PWO-II) has a relatively low light yield, the photosensor is required to have internal gain in addition. Due to the increase of the crystal light yield accomplished by cooling the scintillator down to a temperature of $T = -25\,°C$, the used photo detectors have to be radiation hard in this temperature regime.

For the barrel, the backward endcap and the outer region of the forward endcap EMC an Avalanche Photodiode (APD) which has an internal signal amplification in the silicon structure is chosen as photo detector. The threshold of 10 MeV for the lowest photon energies PANDA wants to study requires to maximize the coverage of the readout surface of the crystals, leading to the development of large area APDs of rectangular shape to cover a maximum of the crystal readout surface with two neighboring photo detectors. Furthermore the use of two APDs per crystal offers a number of advantages: Redundancy in case of failure of one APD or failures in the electronics chain, better background suppression and a better signal-to-noise ratio at low energies compared to using only one APD per crystal.

The photon detection in the inner region of the forward endcap EMC has to deal with rates up to 500 kHz and magnetic fields up to 1.2 T. Therefore we have chosen Vacuum Photo Tetrodes (VPTTs) for this region with a diameter of 23.9 mm as photon detectors. The main reasons for this choice are rate capability, radiation hardness, absence of nuclear counter effect and absence of temperature dependence. Standard photomultipliers are excluded due to the magnetic field environment. In contrast to the barrel region, the magnetic field is oriented in the axial direction of the VPTTs and thus makes it feasible to use VPTTs for the inner region of the forward endcap. Vacuum phototetrodes are essentially a photomultiplier tube with only two dynodes and a low field dependence.

3.1 Avalanche Photodiodes

3.1.1 Characteristics

APDs are semiconductor detectors made of silicon, which multiply charge carriers avalanche-like by means of an internal electric field. In cooperation with the Compact Muon Solenoid (CMS) collaboration Hamamatsu Photonics K. K. constructed APDs which were further developed for use at PANDA. The size of the APDs was increased by a factor of four and the format adjusted so that two APDs with a respective size of 14 mm × 6.8 mm fit on the rear face of a PWO-II crystal. This ensures that a large part of the scintillation light can be detected. The front window of the APD is made of epoxy resin to minimize light reflection. The APDs developed for PANDA have an extended temperature range down to −25 °C and are non-magnetic. Other specifications of the type S11048 APDs are given in Table 3.1.

The dark current at the operating temperature of −25 °C is less than 1 nA, which is significantly lower than the dark current at room temperature. Therefore the main source of noise in the electronics chain is due to the large input capacitance of the APD to the preamplifier (about 250 pF). The gain M depends on the operating voltage and temperature and has to be measured for each APD individually. The operating voltage varies within a range of 80 V. This requires grouping of the APDs according to different HV groups, which is described in Sec. 3.1.2.4. For lower temperatures T a lower bias voltage U is needed to reach the same gain. The variation of the voltage depending on the temperature for a fixed gain is $\mathrm{d}U/\mathrm{d}T = 0.81(2)\,\mathrm{V/K}$. The variation of the APD gain M for changes in the bias voltage depends on the gain setting and is shown in figure Fig. 3.1. During operation at PANDA a stable HV supply on the level of $\Delta U = 40\,\mathrm{mV}$ is required in order to have no impact on the energy resolution at the highest energies for a gain of $M = 200$.

Table 3.1: Specifications for the Hamamatsu Photonics S11048 APDs at a temperature of 20 °C.

Parameter	value
Typical quantum efficiency for $M = 1$	70 % to 80 %
Dark current	<40 nA
Terminal capacitance	230 pF to 270 pF
Operating voltage for $M = 100$	365 V to 445 V
Voltage gap break down to operating voltage $M = 100$	>24 V

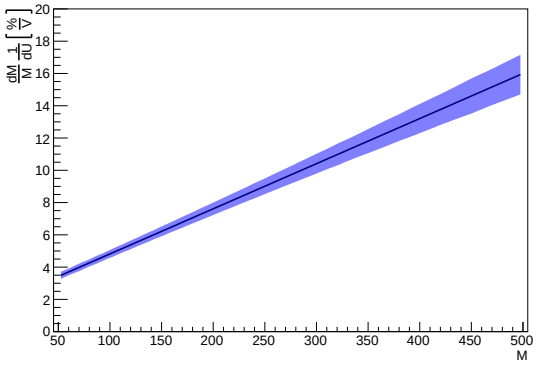

Figure 3.1: Dependence of the relative gain variation per volt on the gain M for the APDs. The blue band shows the 1 σ region of the distribution of all measuered APDs.

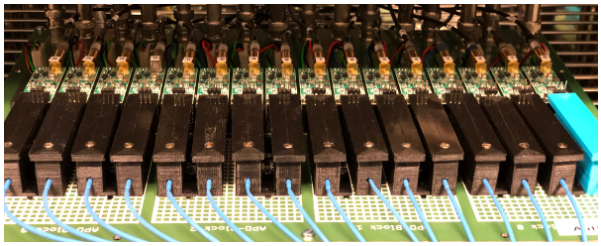

Figure 3.2: Screening setup inside of a climate chamber.

3.1.2 APD Screening and Matching

3.1.2.1 Logistics

The APDs of the $\overline{\text{P}}$ANDA target calorimeter are manufactured and delivered by Hamamatsu (type S11048) to Ruhr-Universität Bochum. After a first screening the APDs are given to Strahlenzentrum Gießen for irradiation and annealing and sent back to Bochum where a second screening takes place. APDs already screened at the Photo Sensor Laboratory of Helmholtzzentrum für Schwerionenforschung GmbH (GSI) are screened at Ruhr-Universität Bochum only once after irradiation and annealing at Justus-Liebig-Universität Gießen.

3.1.2.2 Screening

The APD screening is conducted in climate chambers located at Ruhr-Universität Bochum. Two batches, that is 60 APDs, can be screened in parallel. With an APD screening run duration of about 10 hours the nominal throughput is four batches of APDs per weekday, half of that on weekends.

The screening procedure comprises the recording of alternating current (AC) and direct current (DC) characteristic curves of the APDs at two temperatures, +20 °C and −25 °C.

The screening setup inside each climate chamber (Fig. 3.2) consists of main printed circuit boards (PCBs) with HV and low voltage (LV) connections supplying 16 original $\overline{\text{P}}$ANDA forward endcap preamps (Universität Basel) screwed to the board. The preamps are equipped with sockets accepting the APDs which are suspended in individual plastic mounts for easy mounting and removal. The mounts are equipped with one optical fibre each illuminating the APD. The distance between fibre end face and APD is choosen to achieve a full illumination of the whole photo sensistive area of the APD. One of the 16 channels on each main PCB setup permanently contains a reference APD in order to monitor the intensities of the light sources.

The optical fibres are connected to a light pulser system similar to the ones built for the $\overline{\text{P}}$ANDA target calorimeter (Sec. 6.2.1), modeling the wavelength, pulse shape and intensity of lead tungstate scintillation signals in the $\overline{\text{P}}$ANDA forward endcap EMC, supplemented by a DC operated blue LED. The APD bias voltages are supplied by Iseg HV modules (type EHS F4 10p) as foreseen for the $\overline{\text{P}}$ANDA target electromagnetic calorimeter operation.

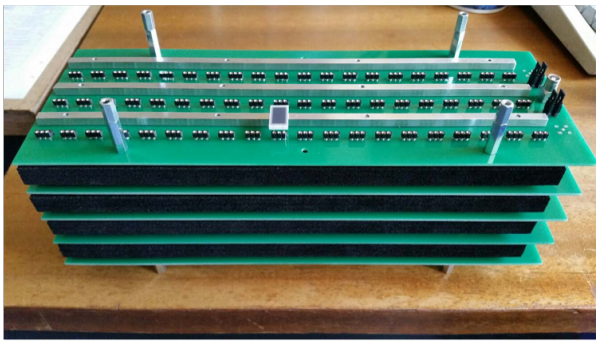

Figure 3.3: PCB stack as used for APD transport, irradiation, and annealing.

3.1.2.3 Exchange of APDs with Strahlenzentrum Gießen

After initial screening the APDs are given to Strahlenzentrum Gießen for irradiation and annealing. The irradiation conditions are a total dose of about 37 Gy, the PANDA full luminosity lifetime dose, applied to the APDs under zero bias (pins shorted). Annealing after irradiation is done at Justus-Liebig-Universität Gießen at a temperature of 80 °C for 48 hours. These treatments are conducted using PCBs equipped with sockets to accept 60 APDs (two batches) each (Fig. 3.3) which are designed for a direct insertion in the irradiation setup at Gießen and are used for transport between Ruhr-Universität Bochum and Justus-Liebig-Universität Gießen. The boards are stackable, secured by screws, for compact and safe shipping. Thus shipping, irradiation, and annealing is done on the PCBs without the need for removing the APDs, thereby saving handling time and keeping stress off the APD contacts.

3.1.2.4 Matching of APDs

In the PANDA target calorimeter radiation damages will occur in the lead tungstate crystals with the consequence that light yield losses will arise during the years of data taking. In order to keep the energy resolution of the calorimeter this will require an increase of the initial APD gain of 200. In the target calorimeter HV adjustment boards will be used. For the forward endcap one HV adjustment board (Sec. 4.6.1) per submodule is foreseen. However, because of the limited voltage adjustment capability of the HV distributor boards, groups of eight similar APDs each are needed for the APD equipped submodule production.

APDs are considered similar if the gain curves (gain vs. bias voltage) behave similar in the relevant region of the initial nominal operation gain since higher gain values are needed as the light yield of the crystals declines.

So the matching criterion was chosen to be the minimum spread s of differences in the necessary bias voltages of APD groups for a gain of 200 and a gain of 300:

$$s = \frac{1}{n-1} \sum_{i,j=0;i<j}^{n-1} ((U_{i,200}-U_{j,200})^2+(U_{i,300}-U_{j,300})^2) \tag{3.1}$$

The matching algorithm is working on data retrieved from the screening. It creates a list of all good APDs, that is APDs with complete data sets and a margin of at least 14 V between its operation voltages for a gain of 200 and a dark current of 10 µA, respectively. From this list suitable pairs are selected until ending up with suitable octets. Sorting this final list with respect to the spread of the octets, submodules will be equipped with the lowest spread octets available at the time of production. The spread of the first 12 groups of APD octets, selected from a pool of 2162 APDs, is in the range of $2.6 \times 10^{-4}\,\mathrm{V}^2 < \mathrm{s} < 4.3 \times 10^{-4}\,\mathrm{V}^2$. This translates to a mean deviation of 21 mV in bias voltages for a gain of 200 and correspondingly a mean gain deviation of the APDs within the worst of the considered suitable APD octets of 0.14 % when supplied by a common high voltage for mean gain of 200.

3.2 Vacuum Photo Tetrodes

3.2.1 Introduction

In the inner region of the forward endcap VPTTs will be used. These are better suited to cope with the extremely high radiation doses and single crystal hit rates that the detectors in the innermost part of the forward endcap will have to withstand. For comparison a single crystal rate of up to 5×10^5/s is expected in the VPTT region and up to 1×10^5/s in the APD region. The maximum liftime dose for APDs is 26 Gy and for VPTTs 230 Gy (10 years data taking at full luminosity).

The VPTTs of the type R11375-MOD were devel-

oped and manufactured especially for the PANDA experiment by the Japanese company Hamamatsu Photonics K. K. The VPTTs consist of an evacuated glass body with a cathode, two dynodes and an anode, which are arranged parallel to the entrance window as shown in Fig. 3.4. In addition, thin aluminum strips are attached to the entrance window in a star shape, which should ensure a faster transport of electrons to the photocathode (see Fig. 3.5).

The function of a VPTT is similar to that of a conventional PMT. A scintillation photon hits the bialkali photocathode, which is vaporized directly onto the inside of the entrance window. The energy absorbed by the cathode leads with a certain probability (quantum efficiency) to the emission of an electron from the cathode due to the photoelectric effect. Photoelectrons are accelerated towards the first dynode consisting of a fine metal mesh. The electrons passing the dynode and the following anode, but some electrons knock out further secondary electrons from the mesh. After the electrons have finally passed them, they hit a massive dynode and knock out further electrons due to their high kinetic energy, which then are accelerated towards the anode.

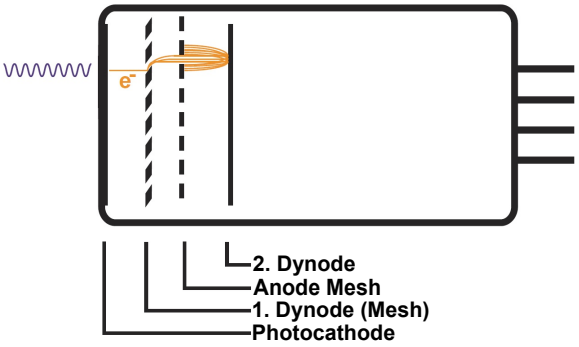

Figure 3.4: Schematic diagram of a VPTT. (based on [1])

The achievable gain of a VPTT is much lower in direct comparison to a conventional photomultiplier, which has a gain factor in the range of $10^5 - 10^8$. However, due to their size and strong magnetic field dependence photomultipliers are not suitable for the use in the PANDA EMC.

3.2.2 Characteristics

For the forward endcap EMC 768 VPTTs are needed. The Hamamatsu R11375-MOD VPTTs have an active area of about 200 mm^2 and a diameter of 23.9 mm so that they match the rear face

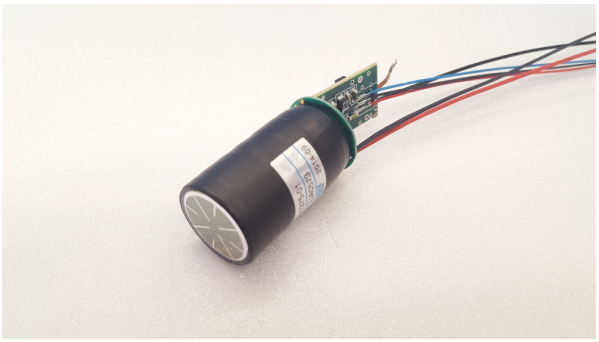

Figure 3.5: Hamamatsu R11375-MOD VPTT. [2]

of the PWO crystals. To stay within the space assigned to the detector the VPTTs are only 40 mm long.

Typically the anode is connected to 750 V, the massive dynode to 450 V, the mesh dynode to 150 V and the cathode to ground. But in the PANDA experiment the VPTTs are operated at a supply voltage of up to 1000 V, which is the maximum recommended value.

The spectral response of the photocathode covers a region from 300 nm to 650 nm with a maximum response at 420 nm. Typical quantum efficiencies of bialkali photocathodes are above 15 %, much less than the quantum effciency of APDs, which are above 65 %. For the Hamamatsu R11375-MOD VPTTs the quantum efficiencies are around 23 %.

The endcap is located close to the door of the solenoid magnet. At the position of the photodetectors the magnetic field varies between 0.94 T and 1.05 T and has a direction between 0° and 3° with respect to the axial direction of the VPTTs. The gain variation under a magnetic field depends on the mesh size of the dynode and the anode.

The dependence of the VPTT quantum efficiency and gain on the temperature has been measured to be small and can be completely neglected compared to the temperature dependence of the light yield (LY) of PWO. VPTTs can be operated in the temperature range from −30 °C to 50 °C.

The capacitance of the VPTT is small compared to the capacitance of the cables connecting to the preamplifiers, such that low noise values can be reached. Typical values are about 22 pF or less. Therefore the connection to the preamplifiers must be kept as short as possible. Also the dark current of < 1 nA is very small compared to the maximum accepted 20 nA of the APDs.

3.2.3 Screening Procedure

In total 900 VPTTs have been delivered (50 pcs. were produced in a preseries for checking parameters and define limits for the final production). The manufacturer determined several parameters for each tube, such as the amplification factor (gain) or the dark current. After arrival the connectors were checked and the properties were remeasured to ensure that all devices meet the specifications and to check the reproducibility of the manufacturer's values.

Gain and dark current The gain and dark current measurements were done at a supply voltage of 750 V and 1000 V to compare the results with the values provided by Hamamatsu and to obtain values for the final operation in the experiment. The anode and cathode current were directly measured with pico-amperemeters, whilst the VPTT was illuminated with constant light (gain) or not illuminated (dark current). To illuminate the VPTT the light of a LED with a wavelength of about 440 nm is used. The LED was chosen because of its similar wavelength to PWO scintillation light.

The measurements have shown that the dark current of all tubes is negligibly small ($\ll 1$ nA), while the manufacturer's values for the gain can be reproduced in the order of a few percent (see Fig. 3.6). None of the tubes had to be returned to Hamamatsu as they all met the minimum gain requirement of 40. VPTTs with a gain of < 40 were part of the preseries. The VPTTs have an average gain of $M_{750\,\mathrm{V}} \approx 53$. By increasing the voltage from 750 V to 1000 V the amplification factor increases by $\sim 20\,\%$. In that case the VPTTs have an average gain of $M_{1000\,\mathrm{V}} \approx 63$ as shown in Fig. 3.7.

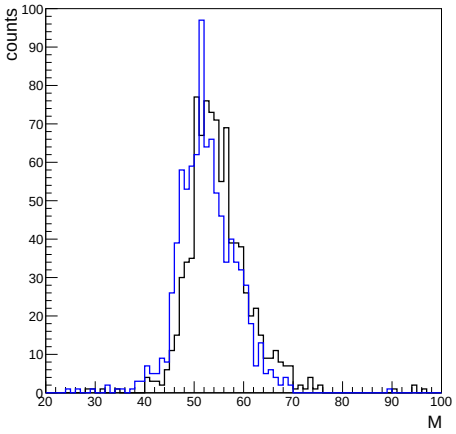

Figure 3.6: Comparison between the gain measured at 750 V (blue) and the gain provided by Hamamatsu (black). (based on [3])

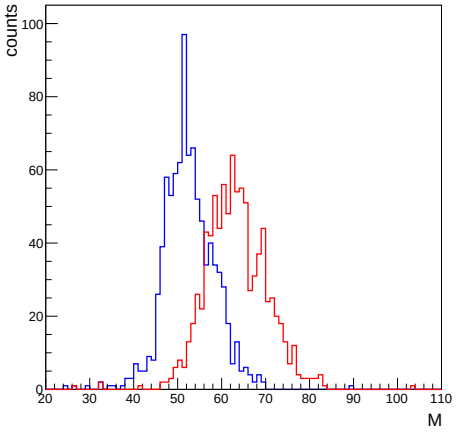

Figure 3.7: Comparison between the gains at 750 V (blue) and at 1000 V (red). (based on [3])

Magnetic field dependence Although the sensitivity of a VPTT to an external magnetic field is significantly smaller than for a full-size PMT, its gain reduction due to the B-field must be considered for its planned usage in the forward endcap. Therefore the VPTT gain dependence was measured in magnetic fields of 0 T to 1.2 T in axial direction. This dependence was determined for all delivered VPTTs. In addition the dependence of the gain reduction on the magnetic field direction relative to the VPTT axis was determined for angles up to 6°.

To study the VPTT signals as a function of strength and angle of the magnetic field, a rotatable magnet was used, which is capable of generating a field of up to 1.6 T in a large volume between the pole shoes (see Fig. 3.8). To measure the gain dependence on the external magnetic field, a test setup was placed inside the gap and the relative change of the gain was determined by illuminating the surface with a pulsed light source (tuned to the emission wavelength of ~420 nm of $PbWO_4$). The light was led via a light guide to a lens/filter system, to illuminate the tube homogeneously. The bias voltage was then varied in the range from 750 V to 1000 V and the magnetic field in a range of 0 T to 1.2 T. Fig. 3.9 shows an example measurement for different magnetic fields normalized to the gain of the VPTT with no magnetic field applied.

The measurement of the gain reduction for a magnetic field oriented perpendicular to the photocathode was done in batches of 15 VPTTs. In every batch one additional reference VPTT was also measured. Normalized to the reference, the gain loss of

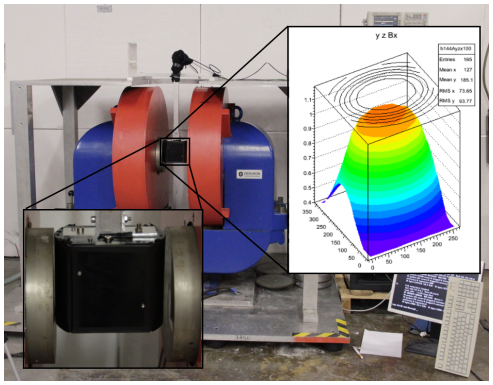

Figure 3.8: Test setup with a rotatable 1.6 T magnet with a large gap for insertion (lower left) of the test cabinet for the VPTT. One the right the field homogeneity is shown.

the VPTTs shows a distribution with a σ/mean of about 5 %. In average the gain of the VPTTs using a voltage of 950 V is reduced to ∼40 % of its original gain if it is placed in a magnetic field of 1 T.

The dependence of the relative gain from the applied external magnetic field for different mounting positions given in terms of the azimuthal angle is shown in Fig. 3.9. The angle was varried up to 6 °. The gain reduction showed no visible difference from the 0° position.

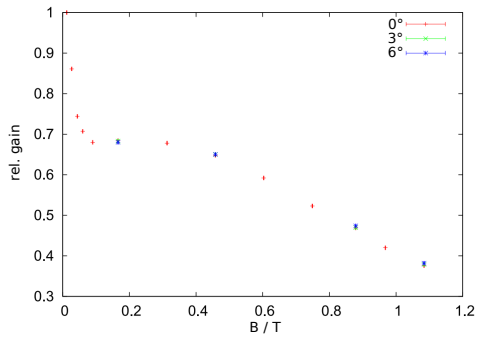

Figure 3.9: Dependence of the relative VPTT gain on the applied external magnetic field. Different mounting positions correspond to different azimuthal angles, which are indicated in the figure by different colors. (based on [4])

3.2.4 VPTT-Matching

As described in Sec. 3.2.2 on average the intrinsic gain of a VPTT is much lower than the gain of an APD. In addition, the range in which the relative gain of the VPTT can be adjusted, is not as large as for the APDs. It can be increased by ∼20 % and the overall gain of the detector module needs to be adjusted before the final assembly. This is done by first matching the VPTTs to the preamplifier and subsequently to the crystal. Thus, a lower gain of a VPTT can be compensated by e. g. a preamplifier with higher gain or a crystal with a higher LY. The parameters of all components necessary for this matching procedure were determined beforehand. Then, a quality factor Q for the expected overall gain can be calculated.

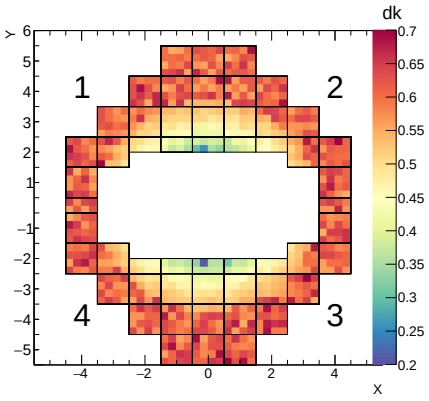

Figure 3.10: Radiation hardness of the VPTT-equipped crystals of the FEC. The plotted value *dk* is inversely proportional to the radiation hardness: a lower value corresponds to a higher radiation hardness.

The detector output signal depends on several variables connected to the crystal (LY), the VPTT (G_0: gain at 950 V, $G(U, B)$: gain dependence on magnetic field and voltage, skb: blue efficiency of the photocathode), and the preamplifier (G_{preamp}: gain), thus defining the quality factor Q:

$$\text{signal} \propto G_0 \cdot G(U,B) \cdot \text{skb} \cdot G_{\text{preamp}} \cdot \text{LY} = \text{Q}. \quad (3.2)$$

The aim of the matching process is to minimize the width of the Q-distribution. The matching algorithms are explained in detail in [4].

As already mentioned on the APD matching procedure, the dose rate varies a lot from the inner to the outer rings. So the crystals, with the largest radiation hardness were placed in the inner Forward Endcap (FEC) region. With decreasing radiation hardness the crystals were placed more to the outer rings (Fig. 3.10). This determined the position of each crystal in the FEC and was the starting point for the matching.

To minimize the quality factor Q the following steps have been done:

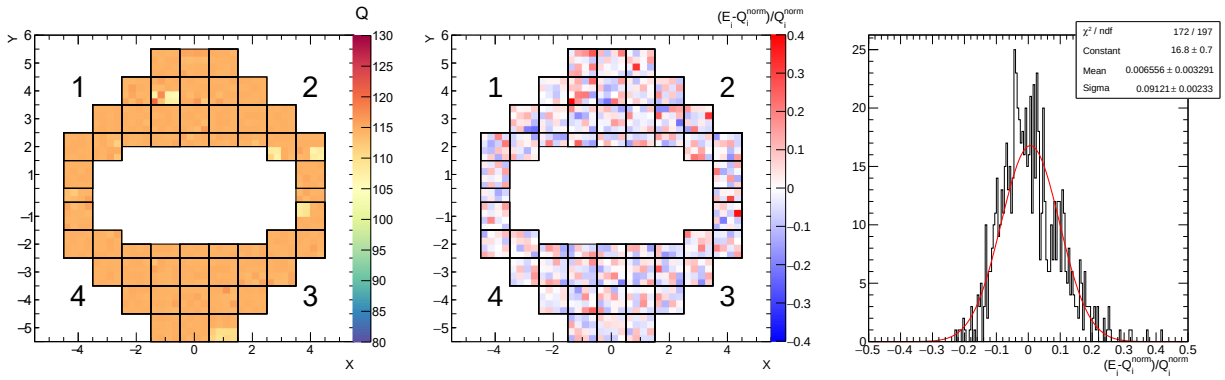

(a) (b) (c)

Figure 3.11: (a) The quality factor Q after the matching. Submodule 1-X1Y4 was produced with a preliminary version of the matching which used the originally specified preamplifier gain; (b) Shows the spatial distribution of the relative deviation of the measured signal (normalized to the mean quality factor) to the expected quality factor from the matching; (c) Distribution of the quantity mentioned before.

Optimize position of VPTT and preamplifier combination Before any matching algorithm was used, the gain variation of the VPTTs at a fixed bias voltage of 950 V was minimized by combining a VPTT with low gain with a preamplifier of higher gain and vice versa (this reduced the variation from $\sigma_{\text{gain}} \sim 12\,\%$ to $\sigma_{\text{gain}} \sim 6\,\%$).

In the next step, the VPTT-preamplifier combination was placed on certain positions inside the FEC (assignment to crystal). The goal in this step was to find an arrangement of the VPTTs where the width of the quality factor distribution is minimal by taking into account the LY of the crystal and the gain reduction of the VPTT in a magnetic field at the placed position. The Hungarian method [5] can be used for this minimization procedure. To employ the Hungarian method one needs to define a cost measure. It is defined by the difference to a target value which should be achieved. This target is the average of the quality factor Eq. 3.2 over all VPTT-preamplifier combinations for an average magnetic field and LY. The cost will then be calculated with the gain reduction of the VPTT at the position and the LY of the assigned crystal.

Optimize compartment of a detector module The Hungarian method resulted in a much narrower width of the quality factor. So far it was not taken into account that the VPTTs were not supplied with an indiviual high voltage. The four detector units (crystal+VPTT+preamplifier) of one compartment are supplied with the same HV. Considering this an additional optimization was performed to reach (1) a minimal difference in the quality factors and (2) a similar slope of the gain-voltage-curve (if an adjustement of the voltage is needed) of the four units in one compartement. The Hungarian method is not suitable for this optimization task, instead the Markov method [6] with simulated annealing [7] was used. All individual values for G_{preamp}, B and LY were taken into account to find an optimal matching.

The quality factor Q after the matching process is depicted in Fig. 3.11a. Nearly all submodules show the same quality factor. The exceptions (especially submodule 1-X1Y4) originate from a preliminary version of the matching, which used the originally specified preamplifier gain values. These turned out to have a much larger spread and somewhat different absolute values than originally specified. Since the glueing of the VPTT to the crystal is irreversible, these submodules could not be rematched. The plots in Fig. 3.11b and Fig. 3.11c show the deviation between the matching, which was done before assembly, and the measured scaling factors (see Sec. 6.1). The width of the distribution of about 9 % (Fig. 3.11c) shows that the agreement with the matching is reasonable.

Bibliography

[1] Michael Leyhe. *Analyse des J/ψ- und $\psi(2S)$-Zerfalls in $\gamma\pi^+\pi^-\eta$ bei BESIII und Entwicklungen zur Auslese des $\overline{\text{P}}$ANDA-EMC*. Dissertation, Ruhr-Universität Bochum, 2013.

https://nbn-resolving.org/urn:nbn:de:hbz:294-38315.

[2] Patrick Musiol. *Analyse der Kanäle $\chi_{c2} \to \pi^+\pi^-/K^+K^-$ in radiativen $\psi(2S)$-Zerfällen bei BESIII und Entwicklung eines Monitorierungssystems für das elektromagnetische Kalorimeter des $\overline{\text{P}}$ANDA-Experimentes.* Dissertation, Ruhr-Universität Bochum, 2018. https://nbn-resolving.org/urn:nbn:de:hbz:294-57322.

[3] Tobias Holtmann. *Suche nach der $Z_c(3900)^{\pm}$-Resonanz in $e^+e^- \to p\overline{n}\pi^- + c.c.$ bei BESIII und Entwicklungen für die Photodetektoren des elektromagnetischen Kalorimeters des $\overline{\text{P}}$ANDA-Experimentes.* Dissertation, Ruhr-Universität Bochum, 2019. https://nbn-resolving.org/urn:nbn:de:hbz:294-68257.

[4] Merlin Rossbach. *Anordnung und Test der Detektor-Submodul-Komponenten für die Vorwärts-Endkappe des $\overline{\text{P}}$ANDA-EMC.* PhD thesis, Rheinische Friedrich-Wilhelms-Universität Bonn, 2019. https://nbn-resolving.org/urn:nbn:de:hbz:5n-55184.

[5] H. W. Kuhn. The Hungarian method for the assignment problem. *Naval Research Logistics Quarterly*, 2(1-2):83–97, 1955. https://doi.org/10.1002/nav.3800020109.

[6] Nicholas Metropolis, Arianna W. Rosenbluth, Marshall N. Rosenbluth, Augusta H. Teller, and Edward Teller. Equation of State Calculations by Fast Computing Machines. *The Journal of Chemical Physics*, 21(6):1087–1092, 1953. https://doi.org/10.1063/1.1699114.

[7] S. Kirkpatrick, C. D. Gelatt, and M. P. Vecchi. Optimization by Simulated Annealing. *Science*, 220(4598):671–680, 1983. http://www.jstor.org/stable/1690046.

4 Electronics

For the PANDA target calorimeter around 500 crystals for the backward endcap, 11 200 crystals for the barrel, distributed within 14 full slices and two reduced slices due to the target pipe and 3856 crystals for the forward endcap have to be read out within a 2 T solenoid. Very individual constraints like space restrictions, needed dynamic range, single detector hit rate or the local strength of the magnetic field lead to the fact that each subsystem demands very individual solutions for the major part of their components. However, two APDs became the common photo sensor for each crystal, except in the innermost region of the forward endcap. Here, the readout has to cope with the highest hit rates of the experiment as a result of the fixed target setup. The weaker magnetic field and the higher mean energies allow to apply VPTTs. To reduce the number of cables, the individual high voltage power supply for all APDs is realized via HV control boards as part of the front- end. Each board serves a dedicated group of APD and is powered by a single HV power supply. The signals of the photo sensors are amplified and shaped with ASICs for PANDA Front-End Electronics (APFELs) or low-noise/low-power-charge preamplifiers (LNPs) in case of the forward endcap. SADCs have been developed as digitization stage for the forward and backward endcap EMC. They are placed as close as possible to the calorimeter volume but outside the cold volume. HitDetection Application Specific Integrated Circuits (ASICs) are currently developed for the digitization of the barrel. They can be placed almost directly behind each APFEL and significantly reduce the amount of cables for the very restricted space between the cold volume of the barrel and the surrounding solenoid. As a backup solution the SADC is available, but requiring signal cable lengths of up to 3.5 m in a very restricted space. The trigger-less concept for the PANDA experiment demands sophisticated feature extraction algorithms which are implemented in FPGAs on the PCBs of the SADCs. They are highly specialized to the specific detector signals, optimized for energy and time resolution and able to recover pile up events. To guarantee a stable operation several parameters like temperature, humidity, current and high voltage of each photo sensor and the individual detector calibration itself (Sec. 6.2.1) to online correct for example for radiation damages between each annealing cycle, is monitored via dedicated custom hardware. All parameters of the calorimter are monitored and controlled through the DCS.

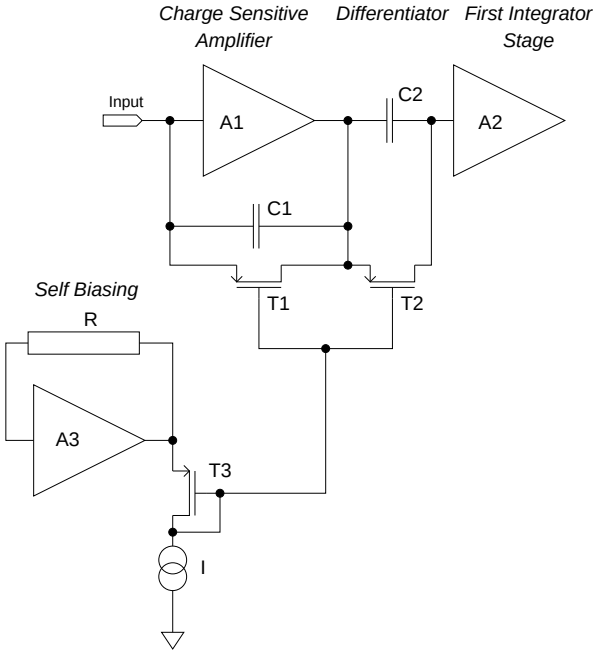

Figure 4.1: Principle diagram of the self-biasing feedback network.

4.1 Preamplifier and Shaper for Barrel and Backward EMC APD Readout

The high compactness of the electromagnetic calorimeter in connection with the required temperature homogenity at low operation temperature makes high demands on space and power consumption. It appears almost mandatory to integrate the preamplifier and shaper on a single chip to fulfill these demands.

For this reason the APFEL-ASIC for the readout of Large Area APDs was developed.

4.1.1 The APFEL-ASIC

Fig. 4.1 shows a principle diagram of the ASIC front end. The circuit of the APFEL is based on well known and established concepts. The input stage is a charge sensitive amplifier (CSA) based on a folded cascode amplifier (A1). To realize the mandatory

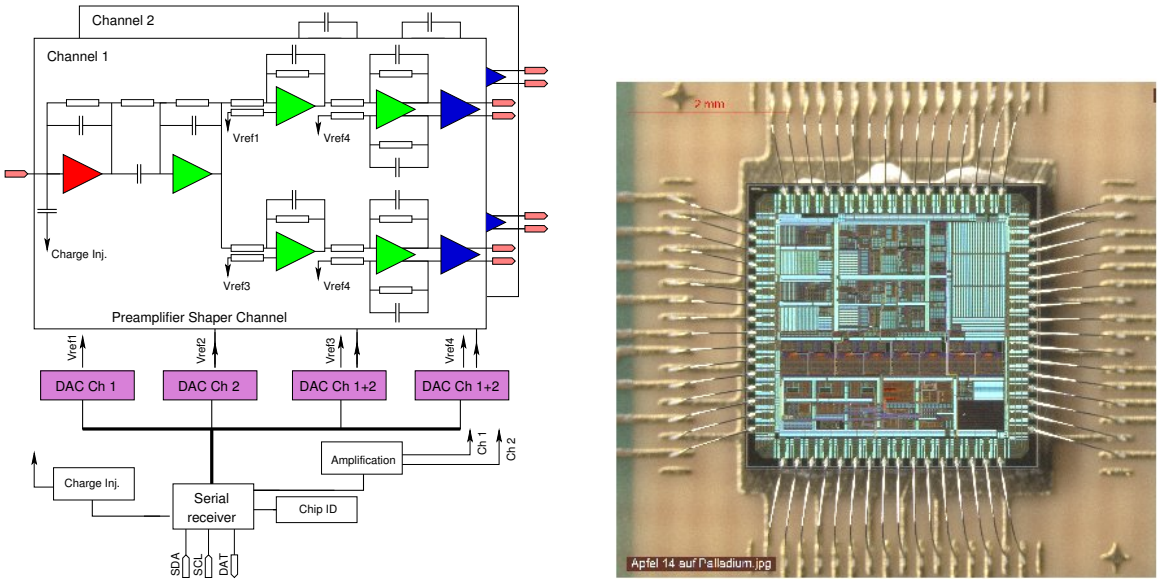

Figure 4.2: Left side: Overall block diagram of the preamplifier and shaper ASIC, Right side: Picture of the prototype preamplifier ASIC.

high resistivity for the feedback resistor a transistor (T1) operating in the subthreshold region is used. Concerning the temperature and process independency a self-biasing technology as described by O'Connor et al. in [1] is realised. As shown in Fig. 4.1 a MOS transistor T3 in diode connection is used together with a current sink to generate the gate source voltage V_{GS} of the feedback transistor T1. The source potential of this MOS diode is fixed by a downscaled version A3 of the preamplifier circuit A1.

The pole which is introduced by the channel resistance of T1 and the capacitance C1 is compensated by transistor T2 in parallel connection to the differentiation capacitance C2. This way a zero is introduced into the transfer function. By choosing the time constants $\tau_2 = \tau_1$ with $\tau_1 = C_1 r_{oT1}$ and $\tau_2 = C_2 r_{oT2}$ any undershoot in the puls shape is eliminated.

The gate of T2 is connected to the same potential as the gate of T1. To ensure that the drain and source potentials of T1, T2 and T3 are equal the amplifiers A2 and A3 are downscaled versions of the input amplifier A1. The amplifier A2 is used as the first stage of a 3rd order integrator.

For the preamplifier design noise consideration played a leading role. The main noise contributer is the input transistor of the Amplifier A1. From noise theory [2] one can see, that the drain source current I_{DS} and the transistor width W are the free parameters to control the transistor noise which decreases with increasing I_{DS} and W. Since at $W \approx 10^4\,\mu\text{m}$ the noise reaches a minimum $W = 12.8\,\text{mm}$ was chosen. A tradeoff between noise performance and the power consumption led to a current of $I_{DS} = 2\,\text{mA}$.

Further parameters which have an impact on the noise performance of the amplifier are the resistance of the feedback resistor realised by T1 and the shaping time. The choice of these parameters is a tradeoff between low noise (large resistance, large shaping time) and the hit rate the preamplifier has to cope with (small resistance, small shaping time). The capacitance C is given by the maximum of the input charge the preamplifier has to deal with.

After the first shaper stage (A2) the signal is split into two paths. A second order integrator stage based on a fully differential operational amplifier follows on each path. A more detailed description of the preamplifier input stage can be found in the original TDR [3] as well as in [4].

A block diagram of the whole APFEL-ASIC is shown in Fig. 4.2 on the left side. On one of the two signal paths a selectable amplification factor of 16 or 32 is realised so this signal path is optimised to measure at the low energy part of the dynamic range with a minimised influence of pick up noise on the connection between preamplifier and ADC. The other path has no additional amplification so it covers the whole upper part of the dynamic range.

After the shaper build up by the differentiator stage and the integrators detector pulses have a semi Gaussian pulse shape with a peaking time of 250 ns.

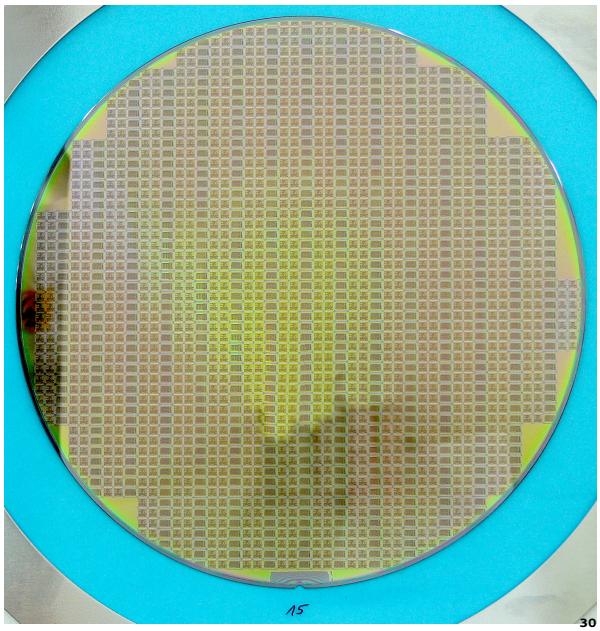

Figure 4.3: Picture of the silicon wafer with APFEL produced by AMS AG.

The shapers are followed by output drivers that can cope with a load of 10 pF parallel to 20 kΩ.

For shaper operation four reference voltages are needed. To guarantee the full dynamic range over a temperature range from −30 °C to +20 °C these reference voltages have to be adjusted. An adjustable voltage reference based on two 10 bit digital to analog converters is implemented on the ASIC to provide this functionality.

A charge injection unit for each channel is implemented on the chip which gives the possibility to inject a defined amount of charge into the preamplifier input for readout electronics monitoring. The amount of charge can be configured with a dynamic of four bits.

To set and read out the adjustable voltage references as well as to set and trigger the charge injection a serial interface of a three wire serial bus is implemented on the integrated circuit. Data transfer has to follow a specific bus protocol which was defined for this circuit. Each transfer consists of 22 bits. After a start signature the first eight bits are used as an address to select a readout chip. The next four bits are used to define a command and the following 10 bits are data bits, e.g. to be written into a DAC register.

The APFEL-ASIC was designed in a 350 nm complementary metal oxide semiconductor (CMOS) technology by AMS AG. After production of several prototypes for development

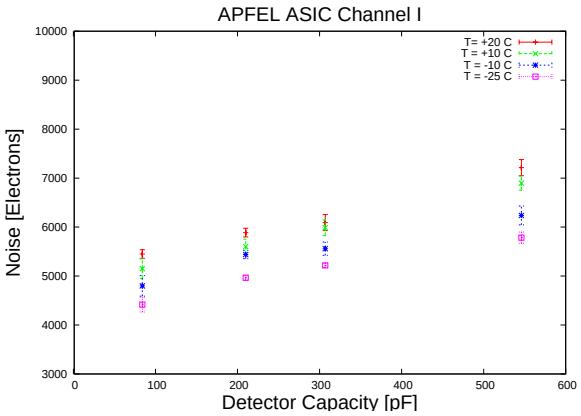

Figure 4.4: Measured noise values of the preamplifier prototype.

and characterisation (shown in Fig. 4.2 on the right side) approximately 18000 chips of the final version APFEL 1.5 were produced in 2015. Fig. 4.3 shows a wafer with roughly 1300 APFEL-ASICs. The chips have been housed in QFN64 packages and are available for the integration in the PANDA detector.

4.1.1.1 Noise, Dynamic Range and Circuit Power Consumption

For specifying the preamplifier prototype over a temperature range from −25 °C to 20 °C the ASIC was mounted on a printed circuit board which can be cooled by a peltier element. To avoid condensation of air humidity the setup is placed in an evacuated chamber. For measurements a voltage step generated by an AWG 510 on a well defined capacitor is used as charge injection. A second well defined capacitor connected parallel to the amplifier input simulates the detector capacitance. The output signals are monitored with a digital oscilloscope type DPO 7254. Serial programming is done with a data timing generator DTG 5078.

For the temperatures −25 °C, −10 °C, 10 °C and 20 °C dynamic range, gain and output noise voltage were measured so the equivalent input noise charge can be calculated. The results for four different detector capacitances are plotted in Fig. 4.4. As expected noise increases linear with the detector capacitance and temperature.

From a linear fit one gets a slope of $S_{\mathrm{ENC}} = 3.30(31)\,e/\mathrm{pF}$ of the equivalent noise charge. The temperature dependency can be described by a temperature coefficient of $S_T = 23.75(31)\,e/\mathrm{K}$.

For an operating temperature of −25 °C the mea-

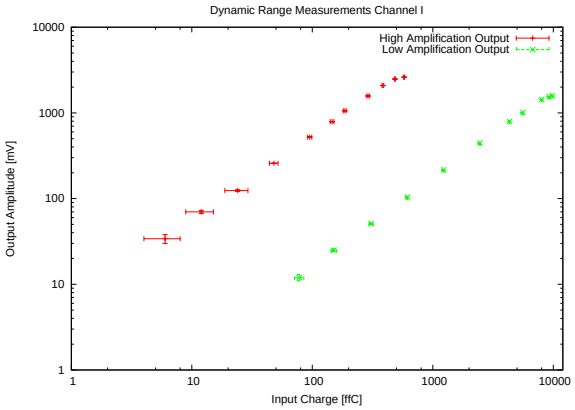

Figure 4.5: Amplification Characteristics of the Preamplifier at −20 °C.

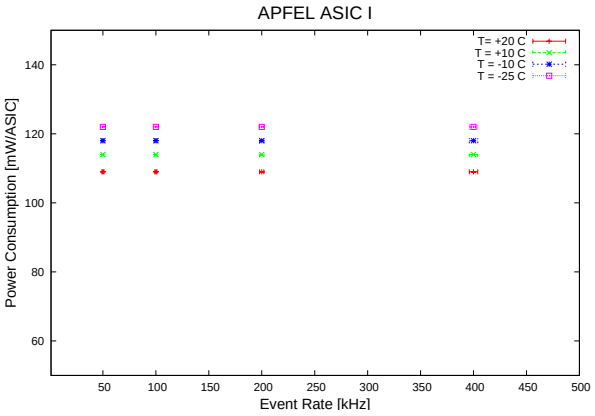

Figure 4.6: Power consumption over temperature.

sured noise of the preamplifier prototype is

$$\mathrm{ENC} = [4234(143) + 3.30(31) \cdot C_{\mathrm{Det}}]\ e$$

so with a detector capacitance of $C_{\mathrm{Det}} = 270\,\mathrm{pF}$ a noise of $\mathrm{ENC} = 5125(165)\,e$ can be expected.

Fig. 4.5 shows the measured characteristics of the integrated preamplifier for the high and the low amplification path. The measurement covers a range from 10 fC to 10 pC input charge. Both paths show an excellent linear behavior with an overlapping range up to 200 fC. Corresponding to the −1 dB compression point definition in RF technology the upper limit here is defined by the input charge where the output voltage is 0.891 times the value expected by a linear fit. For the low amplification path this is 8.5 pC. Together with the measured noise of 0.82 fC this leads to a coverage in dynamic range of 10 366.

In Fig. 4.6 the power consumption dependency of the temperature and event rate is shown. The power consumption increases with decreasing temperature but there is no rate dependency of the power consumption. For an operating temperature of −25 °C the power consumption is 59 mW per channel.

Table 4.1: Measured preamplifier parameters

Parameter			
ENC (−25 °C, 270 pF)	5125	±165	e
Max. input charge	8.5		pC
Dynamic Range	10 366		
Max. Eventrate	350		kHz
Peaking Time	250		ns
Power Consumption (2 Ch., −25 °C)	118		mW

4.1.1.2 Rigid-Flex-PCB

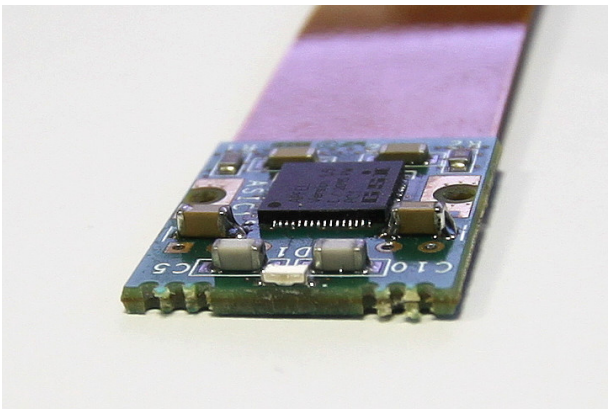

Figure 4.7: The front-end APFEL ASIC mounted on rigid-flex PCB exhibiting the blue recovery LED on it's front edge.

For the integration inside the PANDA detector a rigid-flex-PCB was designed (Fig. 4.7). In addition to the ASIC only a few components had to be placed on the PCB. These are mainly blocking capacitors and the large capacitors to decouple the high voltage bias for the APDs. At the frontside the blue LED is placed to provide sufficient illumination of the crystals for off-line damage recovery (see Sec. 2.5). The APDs will be connected by small connector heads.

On the other side of the flex part a high speed hermaphroditic connector from Samtec is used to connect the rigid-flex-PCB to the backplane described in Sec. 4.6.2 and Sec. 4.6.3. The two APDs attached to the crystals are read out by one APFEL front-end. Each of the two amplifier channels com-

prises two differential analog outputs with a gain ratio between them of nominally 16 (optionally 32) and a differential output swing of ±1 V. As it can be seen in Fig. 4.7 the APFEL-ASIC is housed in a QFN64 package.

4.1.2 Barrel EMC Front-End (FE) Assembly

A precision-milled aluminum-housing encapsulates the rigid part of the ASIC PCB in order to have defined mechanical and thermal contact to the rear inserts and provide an EMI shielding of the most sensitive nodes. The assembly of the entire preamplifier module with ASIC, aluminum capsule, thermal pad and flex cable is shown in Fig. 4.8. The

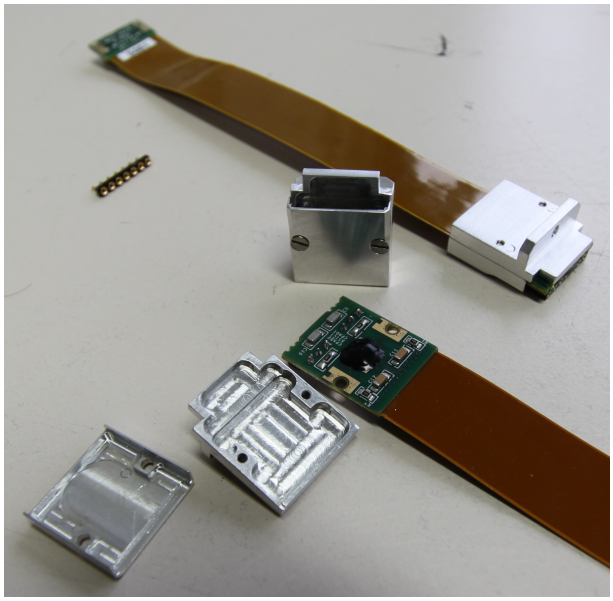

Figure 4.8: Front-End ASIC building block with rigid-flex ASIC-PCB, aluminum housing for heat transport and shielding, The front edge of this block is plugged onto the APDs by means of precision-milled pinheader connector (top left). One assembled front-end block can be seen in the top of the photograph. Note, that for an eficcient heat transfer between ASIC and Al housing, a custom heat pad is added before assembly (not shown here).

mechanical interface of this front-end assembly toward the crystal is defined by a 3D-printed plastic receptacle (Fig. 4.9) which encloses the APDs, ensures a tight placement of all parts and avoids unintended movements of the front-edge pinheader on the APD pins. Additionaly, a small opening in this receptacle is introduced to guide the light of the recovery LED into the crystal through the gap of ≈1 mm between both APDs.

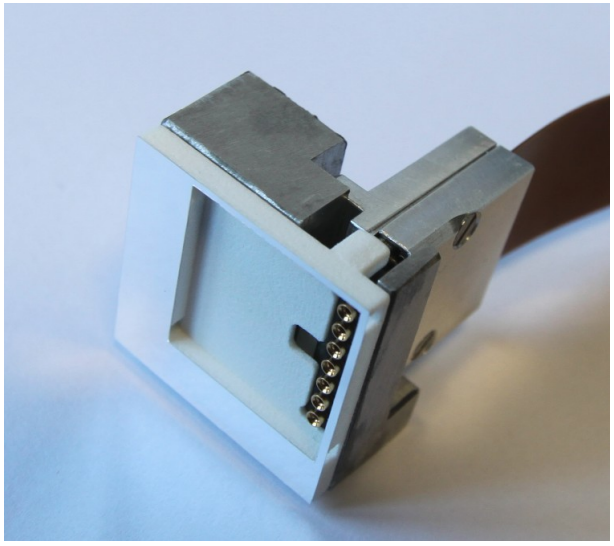

Figure 4.9: Assembled front-end block with plastic capsule on it's front side defining the mechanical interface towards the APD photodetectors and the crystal. Note the small notch right below the APD-interfacing connector which provides a direct path for the recovery light from the on-board LED.

4.1.3 Backward Endcap EMC FE Assembly

As for the barrel EMC, thermal contact, a stable mechanical connection to the APDs and electromagnetic shielding are needed for the APFEL also in the backward EMC. Since the geometry constraints are different, an independent development of the APFEL housing has been undertaken. Also here, precisely milled aluminum elements were designed for holding and encapsulating the ASIC boards and the APDs.

The single components are shown in the sketch at the top of Fig. 4.10. For heat removal from the chip, the PCB is screwed on a bulky heat sink, and a thin Al plate (so-called "ASIC press") is in turn screwed on top of the ASIC. For electrical insulation, a small pad of thermal rubber is inserted between the PCB and the heat sink.

The APDs are held in a 3D-printed plastic case, which is kept in place by two pads located on the back side of the case and fitting two apposite holes in the heat sink. The plastic case has an opening between the two APDs to allow the light from the recovery LED and from the light fiber to enter the crystal (see Sec. 5.3).

The whole construction with heat sink, PCB and APD case is covered with an aluminum capsule, which has approximately the same transverse di-

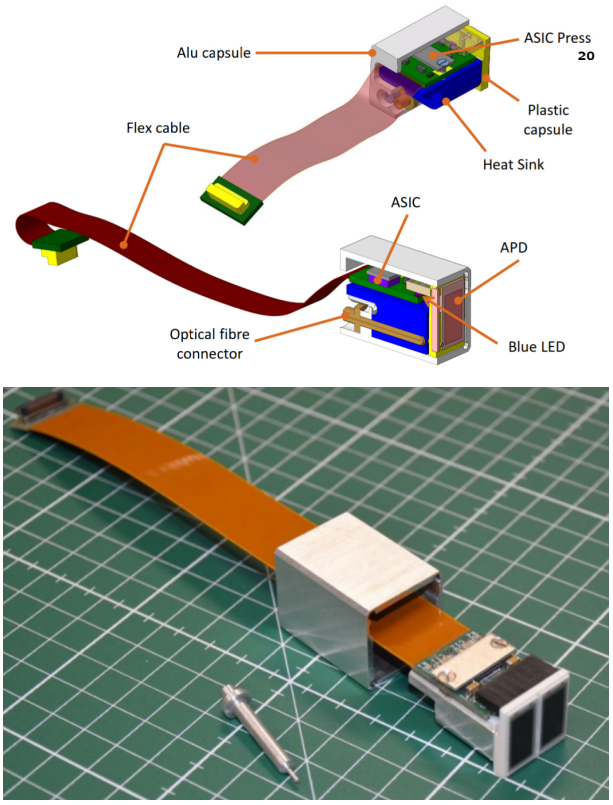

Figure 4.10: Top: sketch of the mechanical components holding the APFEL preamplifier and the APDs in the BWEC. Bottom: picture of a mounted APFEL housing with APDs.

mension of the crystals and is inserted into the carbon fiber alveole together with the crystals. Since these are straight in the BWEC, the shape of the capsule helps keeping the APDs and the APFEL board in place without lateral stresses.

A mounted, open assembly is visible in the bottom picture in Fig. 4.10, together with the optical fiber connector which is inserted into the heat sink from the back side.

4.2 Preamplifier for Forward Endcap EMC Readout

For readout of the photodetector signals in the forward endcap, a charge-integrating LNP has been developed at the Universität Basel. The design, detailed specifications and performance of the preamplifier have been extensively discussed in [3]. Therefore, this section only gives a brief overview of the differences between the prototype version and the versions finally deployed in the forward endcap submodules.

The LNP is directly attached to the anode of the APD / VPTT; this connection between the photo sensor and the preamplifier has to be kept as short as possible. The LNPs are produced in two different geometrical shapes depending on the type of photo sensor, due to the different amount of space that is used up by VPTTs and APDs. Both types are displayed in Fig. 4.11a. In the case of the VPTT units, a second PCB, which carries the passive voltage divider, is used. The voltage divider board (see Fig. 4.11b) was designed to match the outer dimensions of the VPTT and also allows to be mounted in the shortest possible distance from the glass tube. Therefore, it has a round outer shape with a circular opening in the middle, which has a diameter of 7 mm, so that the board can be fitted over the pump port of the tube. The LNP itself is subsequently connected to the voltage divider PCB via two small flexible leads for the connection of the anode and cathode to the tube. High and low voltage supply cables, as well as one coaxial signal cable are connected to each LNP before it is connected to the voltage divider board. A photograph of a VPTT unit at this stage of assembly is shown in Fig. 4.11c.

The gain / amplification of the preamplifiers has been iteratively adapted to match the developments of the photodetectors as well as the subsequent readout chain during the prototyping phase. Finally all LNPs for the usage in connection with APDs were produced with a gain of 0.1 V/pC. Due to the spread in gain of the VPTTs, it was decided to deploy three different versions of LNPs for the VPTT units to compensate part of these differences in signal amplitude. The three VPTT-LNP versions have gains of 0.7 V/pC, 0.82 V/pC and 0.89 V/pC, respectively.

A shrinking tube with a wall thickness of only 150 µm is used to mechanically connect and cover the VPTT with the two PCBs attached to the tube base. The complete volume inside the shrinking tube, which contains the LNP as well as the voltage divider, is finally filled with a two-component silicone based casting compound (Elastosil RT601 A/B) to ensure mechanical stability and electrical isolation as well as protection against liquids. A piece of self-adhesive copper tape is wrapped around the shrinking tube at the position of the preamplifier. The copper tape is equipped with a copper strap which is electrically connected to the ground layer of the LNP to provide electrical shielding. A second shielding layer is created by wrapping the complete unit with self-adhesive aluminum foil. Here, a special type of foil was used, which is certi-

fied to provide a good conductivity also through the adhesive layer, so that an electrical connection to the ground layer of the preamplifier is maintained.

For APD units, the procedure described above is only slightly modified: Since two photo detectors are used in one unit, an additional mechanical component, called *capsule*, is needed for the assembly. These 3D-printed frames made of nylon are designed to accomodate two APDs with a fixed orientation to each other. Additionally, the capsules provide a fixation bar at their rear side, to which two LNPs can be attached. Two APDs are glued into a capsule and connected with very short leads (few mm) to the input soldering points on the respective LNPs, which are fixated on the capsule using M2 nylon screws (see Fig. 4.11d). Each preamplifier is equipped with cables for the high voltage supply lines as well as a coaxial signal cable, while the low voltage supply lines are daisy-chained from one LNP to the second and thus only one set of low voltage cables is needed. Since a proper electrical shielding is absolutely necessary and in the case of APD units enough space is available, a solid aluminum tube with a length of 50 mm is placed around the LNPs. As for the VPTTs, the inner volume of the aluminum tube is filled with Elastosil. The rear end of the aluminum tube is sealed using the self-adhesive aluminum tape described above to provide electrical shielding to the back side.

After a unit has been tested electrically with illumination from a light pulser system, it is labeled with a unique bar code and information such as the tube and preamplifier serial number are stored in a database.

4.3 EMC Digitization

4.3.1 Sampling ADC

4.3.1.1 Technical Design Requirements

The FEE of the EMC register single photon signals with high efficiency and precisely record their amplitude and time of arrival. Due to the large dynamical range of the kinetic energies (up to 15 GeV) and the spread of the energy shower in the EMC it must be possible to merge signals down to 3 MeV. This calls for a dynamical range for the SADC of 14 bits.

Since PANDA will operate in trigger-less mode to ensure high flexibility for physics event selection, the entire DAQ has to run continuously, transmit and pre-process data, and extract hit patterns to be able to provide PID information for online event filtering [3]. For event building and reconstruction, the clocks of all sub-detectors will be synchronized within the SODA framework [5]. The FEE must therefore provide calibration, monitoring and slow control functionality, e. g. setting thresholds or monitoring temperatures.

To minimize cabling bulk, the modules are planned to be placed inside the PANDA detector volume, where they will be exposed to magnetic field of up to 2 T and a non-negligible radiation flux. The design has to meet tight volume constraints and low power consumption demands.

The SADC has been developed by Uppsala University according to the PANDA specifications and contains programmable logic (FPGA), see Fig. 4.12. It is capable to perform signal filtering and extraction of important signal parameters. The processed data are pushed to Data Concentrators via optical links.

4.3.1.2 Specifications

The PANDA SADC is a versatile module and can be adapted to the requirements by selecting hardware components in the assembly process, as well as the functionality is programmable. In particular the sampling rate can be chosen in the range 20..125 MS/s. The analog gain and filtering is flexible and it is possible to configure the device to a single or dual range gain. Therefore it can be used for all parts of the PANDA calorimeter, from the lowest demanding backward and barrel EMC (80 MS/s, single range), through forward EMC (80 MS/s, dual range) and the highest demanding Shashlyk (125 MS/s, single range). The specifications of the PANDA SADC for different hardware configurations are summarized in Table 4.2.

4.3.1.3 SADC Module Construction

The SADC module combines a low-noise amplifier, an analog to digital converter, a digital signal processing part and optical communication interfaces, see Fig. 4.13.

The module is equipped with 64-channel symmetrizing shapers/amplifiers allowing for user defined CR-$(RC)^3$ filter configurations. In configurations with by-passed CR-$(RC)^3$ filter, the input analog stage features over 100 MHz bandwidth. Obtaining a 14-bit dynamic range required by the PANDA experiment was found to be feasible through using a dual-range ADC structure. By fit-

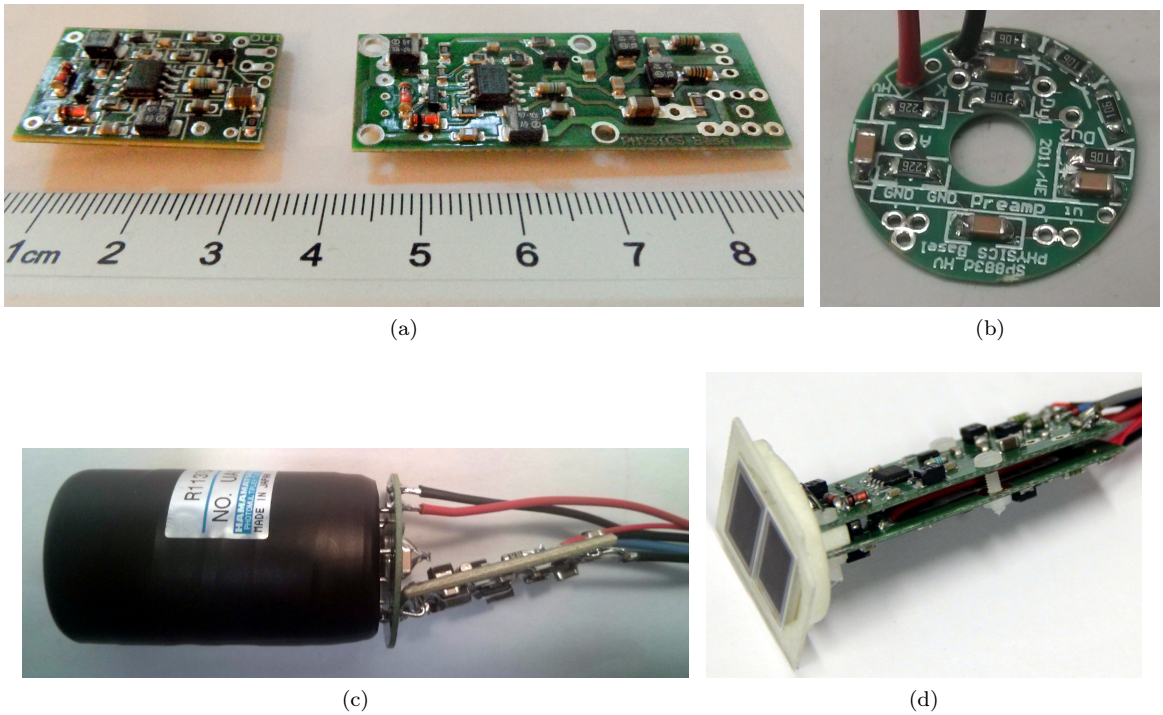

Figure 4.11: (a) Low noise preamplifiers for VPTTs (left) and APDs (right)
(b) Round voltage divider PCB to be mounted directly to the VPTT tube base
(c) VPTT unit with voltage divider and LNP, before sealing
(d) APD unit with two LNPs. The APDs are glued into a nylon capsule.

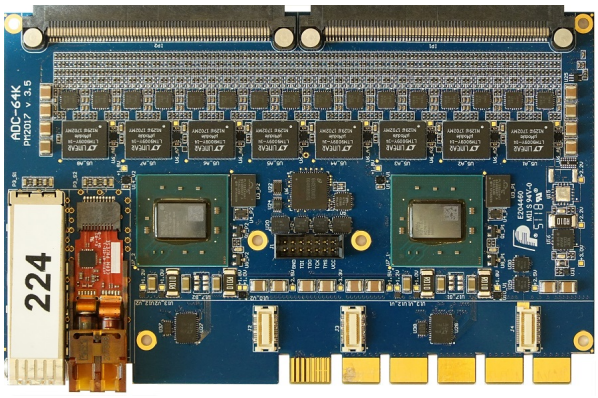

Figure 4.12: $\overline{\text{P}}$ANDA SADC.

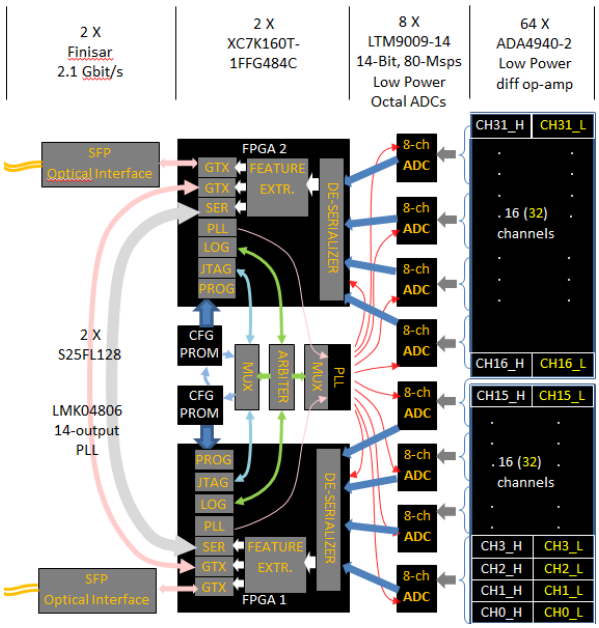

Figure 4.13: Hardware structure of the $\overline{\text{P}}$ANDA ADC.

ting SMD jumpers, a 32-channel dual range configuration can be obtained.

Amplified signals are processed by a set of 8-channel 14-bit, 80 MS/s analog-to-digital converter circuits. Digitized samples of 64 analog signals are sent to 2 FPGAs using 128 LVDS links running at 560 Mbit/s each.

The FPGAs perform signal filtration and extract important signal parameters, such as time of arrival, amplitude and integral including signal pile-up resolution. The firmware is under evaluation [6, 7, 8]. Extracted pulse parameters are pushed to optical links via multi-gigabit transceivers (GTX) running

Table 4.2: Summary of SADC specifications for different subdetectors.

Forward Encap		
Parameter	Low Gain	High Gain
No. of channels	32	32
Gain	0.5	7
Input amplitude	$< \pm 2.2$ V	$< \pm 140$ mV
Noise	1.3 mV	80 µV
Bandwidth	> 100 MHz	> 20 MHz
Sampling Rate	80 MHz	
Barrel and Backward Endcap		
No. of channels	64	
Input voltage	±1 V	
Noise	< 1.0 mV	
Bandwidth	> 100 MHz	
Sampling rate	80 MHz	
Shashlyk		
No. of channels	64	
Input voltage	±1 V	
Noise	< 1.0 mV	
Bandwidth	> 100 MHz	
Sampling rate	125 MHz	
Common features		
Resolution	14 bit	
Amplitude Resolution	< 0.1 %	
Charge Resolution	< 0.1 %	
Linearity	0.6 %	
Data Communication	1 SFP+ 4.8 GBit/s 1 VL 4.8 GBit/s 2 Backplane links 2 GBit/s	
Control	I^2C control SPI monitor JTAG config All Interfaces: 2.5 V or 3.3 V	
Time synchronisation	SODA	
Power	22 W	
Rad-hard-test	5×10^{11} n/cm^2	
Magnetic field test	2 T	
Dimensions	150 mm × 95 mm× 13 mm	

at 2 Gbit/s.

The design can utilize standard SFP/SFP+ transceiver modules as well as VL radiation hard optical transceiver modules from CERN. The two FPGAs on the module are interconnected with a double GTX link, providing data exchange between the FPGAs, hence allowing the module to be operated with only one transceiver. Two additional high-speed (GTX) electrical data links are routed to the backplane.

The ADC module is compliant with the SODA System, for which the reference clock is distributed via a DAQ, using the down-link part of the ADCs optical transceiver. The received reference clock signal is routed out from the FPGAs and processed by a 14-output PLL/jitter cleaner circuit, providing a set of stable clocks for all digitizers as well as for all multi-gigabit transceivers (GTX) inside FPGAs.

A dual FPGA structure and a hardwired arbitration circuit provide routing of the JTAG configuration signals to the FPGAs and control of the reference clock source. This allows for resolving potential communication locks caused by a misconfiguration or a radiation induced damage of the configuration memory contents.

The dimension of 64-channel modules amounts to 100 mm × 150 mm, including the area designated for DC/DC converters. Despite a high channel density, the cross-talk remains below noise. The proximity of specially designed DC/DC converters also does not give any measurable rise to the signal noise. The power consumption amounts to 22 W. This figure is though dependent on the firmware complexity. The modules require efficient cooling, which in the PANDA will be accomplished by liquid-cooled aluminum encapsulations.

Each ADC device contains 4 temperature probes and 32 voltage and current probes for continuous monitoring of the device health. Selected voltages and currents are measured by two slow 16-channel, 16-bit, 7.5 S/s ADCs. Slow ADCs are powered by an external +3.3 V power line. This makes the monitor independent on the device main power. The external power source also serves as a reference voltage, so it is important to keep this voltage at +3.3 V with at least 1 % accuracy. An additional multi-purpose 2-wire interface is provided between the FPGAs and the back plane connector. It can be used for reading FPGA core temperatures, board temperature, setting up front-end detector electronics as well as for announcing SEU events.

4.3.1.4 Firmware Developments

A basic firmware for complete functional tests of all peripheries was developed at the Uppsala University and used during the volume post-production

tests, see Sec. 4.3.1.8. This firmware has become a canvas for further developments, such as a firmware developed at the Universität Bonn, containing UDP cores, which is exceptionally useful for simple readout of smaller experimental setups [9].

The first complete DAQ firmware incorporating the SODAnet protocol was developed in KVI-CART and tested. KVI-CART also developed a radiation damage monitoring firmware [10].

Several further firmware developments concentrated on improving charge and time resolutions [8, 11]. The final firmware is planned to be a compilation of the developed code.

4.3.1.5 Performance Tests

The prototype module was tested in Uppsala and Bochum, using a test setup, which was based on a firmware developed for the Crystal Barrel experiment at the Universität Bonn. The test firmware allowed self-triggering with variable threshold, external trigger and the transmission of full samples with a length of 12.8 µs per channel. The usage of Ethernet with UDP/IP offers a great simplification of the lab setup by sending SADC data to a computer via an Ethernet switch. The obtained performance figures are summarized in Table 4.2.

4.3.1.6 Tests with Detector Setups

Diverse live tests with partial detector setups in beam conditions were also performed.

4.3.1.6.1 Tests with EMC FEC The ADC was used in a detector setup for testing response of EMC Forward End-Cap PWO crystals to photons with energies from 10 MeV to 62 MeV. In the experiment performed at Max Lab III in Lund, 2014, a 3x3 matrix of crystals was equipped with Hamamatsu R11375 VPTT and SP883d signal preamplifiers from the Universität Basel [12] The signals were processed by the Virtex-6 ADC version equipped with 300 ns input shaping filter. The waveform data were transferred to a PC via a VME-based Data Concentrator module (ATLB) [13]. After offline energy reconstruction and applying 1.5 MeV thresholds, the relative energy resolution obtained for photon energies of 11 MeV, 26 MeV, 38 MeV and 62 MeV was found to be fulfilling the Technical Design Report requirements of the PANDA EMC with a safety margin, see Fig. 4.14.

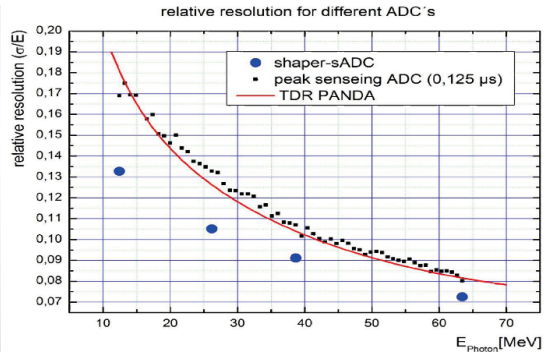

Figure 4.14: Calorimeter energy resolution for low energy photons.

4.3.1.6.2 Tests with EMC BWEC Beam tests with the EMC BWEC prototype at MAMI have been performed between 2014 and 2018 with a test setup consisting of a 4x4 crystal matrix equipped with APDs, APFEL preamplifiers and the PANDA SADC [4]. It was concluded that the typical relative energy resolution amounts to 2.2 % at 1 GeV, fulfilling the TDR criteria (<2.5 %) [8].

4.3.1.7 Irradiation Tests

In order to test the endurance of the ADC in a radiation environment, the SADC was irradiated with a neutron beam at TSL, Uppsala University in June 2016. The purpose of this experiment was to find the cross section of the device for the SEU-induced bit errors and estimate the MTBF of the device when placed inside of the operating PANDA detector.

The neutron beam was produced by directing a 180 MeV proton beam into a full-stop tungsten target. The ADC was first placed at the SUP, perpendicular to the beam which had a diameter of 130 mm. The neutron flux $\phi_n(> 10\,\text{MeV})$ at this position amounted to $5 \times 10^5\,\text{cm/s}^2$ to $1 \times 10^6\,\text{cm/s}^2$ with the energy spectrum as shown in Fig. 4.15.

This experiment was focused on the behavior of FPGA circuits and the most sensitive to radiation. A Xilinx Soft Error Mitigation (SEM) monitor was placed in the FPGAs [14]. After dividing the registered SEU number by beam time and normalizing the result to the neutron flux we have obtained a SEU cross-section:

$$\sigma_{SEU} \approx 7.5 \times 10^{-15}\,\text{cm}$$

per FPGA, giving MTBF of:

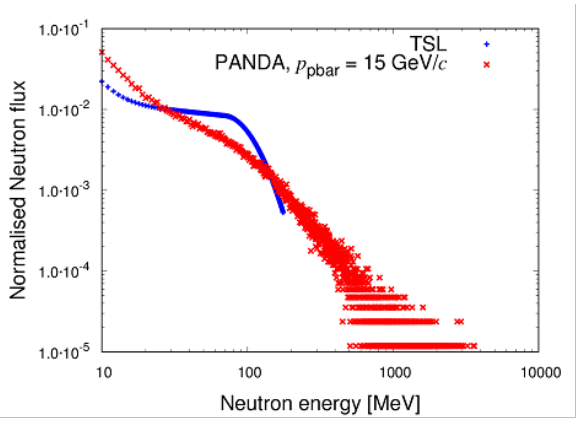

Figure 4.15: Neutron energy spectrum at the TSL (blue) and the anticipated in the $\overline{\text{P}}$ANDA (red).

165(38) h	at	1.5 GeV/c
123(30) h	at	15 GeV/c

With two FPGAs on board of each of 217 SADCs, the Front End EMC predicted MTBF amounts to 17(4) min. During the test no failure in ADC circuits or optical SFP transceivers was observed. During the following irradiation at the CUP the ADC board acquired a dose of 3.6×10^{10}/cm, which according to simulations is comparable with approximately 7.5 years of running the $\overline{\text{P}}$ANDA experiment at a high luminosity. The device was not powered on in this phase. After 1 week radiation relaxation period the board was successfully brought to operation, without observing any degradation of performance.

In November 2016 the ADC board was irradiated with a proton beam delivered by the AGOR cyclotron at KVI-CART, Groningen. The beam was collimated to 120 mm diameter, illuminating a top half of the digitizer board, including one of the FPGAs and SFP optical transceivers.

The total number of impact protons on the device during the proton irradiation session amounted to 1.12×10^{10}/cm equivalent of 6.5 years of detector operation at high luminosity. After the test, the device is still fully functional and no measurable degradation of performance was observed, however only the radiation hard VL transceiver was operational, while a commercial plug-in SFP transceiver got irreveribly damaged at an early stage of the irradiation session. This confirms the need for using radiation hard transceivers for data transfer and control functions at the envisaged location of the SADC modules in the $\overline{\text{P}}$ANDA experiment.

4.3.1.8 Post-production Quality Check

Production of SADC devices was done in 5 lots of 50 pieces each. After each production lot the devices were tested at Uppsala University to ensure production quality.

Tests encompassed full device functionality, including power up test, FPGA programming, ADC performance check, optical interface quality check, flash programming and DAQ test.

In order to facilitate this complex procedure, a dedicated microcontroller-based automatic device tester was built. The tester allows for a controlled power-up sequencing, thus minimizing a risk of severe damages to the tested device in case of malfunction of the power regulating circuitry, generates tests signals for ADC and provides interfaces for the DUT configuration and readout. The tester is equipped with a terminal interface to a PC for control and displaying of test results.

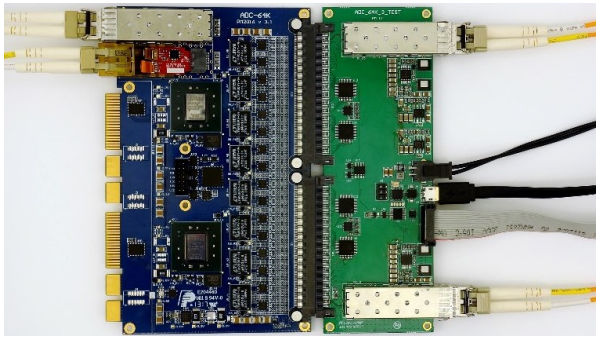

Figure 4.16: Post-production test setup.

The real ADC read-out was accomplished via a ZYNQ-Board, a device constructed for small DAQ systems. The device can receive and transmit data over 4 optical links and provides an interface for a PC [11].

4.3.2 HitDetection ASIC

The described architecture using sampling ADC modules outside the detector for digitising the preamplifier signals requires long cable connections with four differential pairs per crystal from the preamplifier to the ADCs. On one hand this leads to a big cable cross section which is a challenge for the barrel mechanics. On the other hand these long cable include the risk of large pick up noise.

This leads to the idea to integrate the signal digitiser inside the barrel. Therefor a special ASIC called *HitDetection* is under development. HitDetection is an integrated analog transient recorder

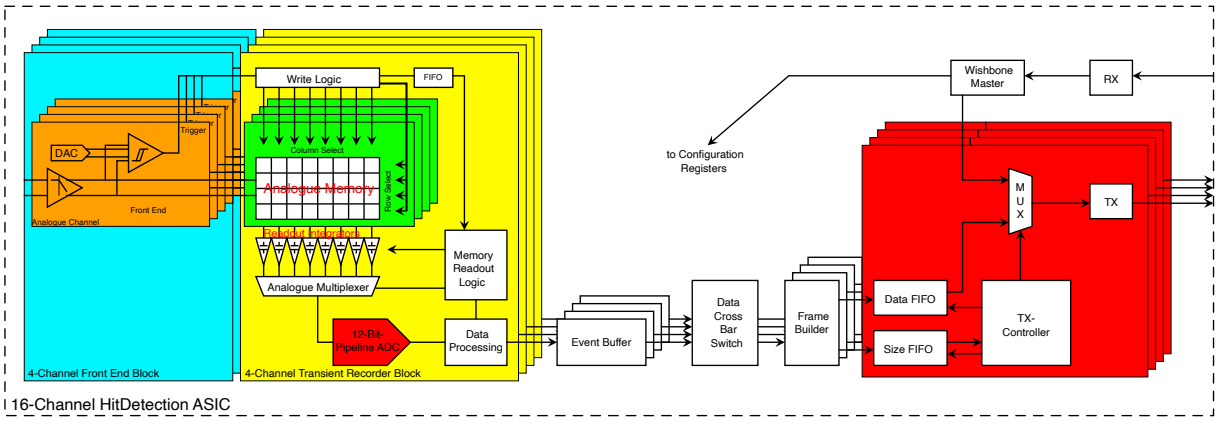

Figure 4.17: Block diagram of the HitDetection ASIC.

with integrated pipeline ADC for digitisation of the recorded transients.

Fig. 4.17 shows a block diagram of the HitDetection ASIC. The incoming signals from the APFEL ASICs are received by the front end unit which consists of an input buffer and a trigger unit. The input buffer is based on a fully differential amplifier which can cope with the high capacitive load of the analog memories capacitor bank. To suppress high frequency noise and interferences and to avoid aliasing the buffer has a configurable low-pass characteristics in the range of 0.7 MHz to 44 MHz.

The trigger unit is used to detect signals from hits in the scintillator crystal. It can be operated in two modes. In leading edge discriminator mode the input signal is compared with a programmable threshold directly. In the differential mode a switched capacitor circuit is used to compare the differentiated input signal with the programmable threshold. This way the trigger unit is not influenced by low frequency interferences like 50 Hz pick up noise.

The output signal of the front end unit is sampled and written into the memory cells of the analog memory as depicted in Fig. 4.18. As long as there is no hit detected the analog values are written into the memory cells of the same row in a cyclic manner as shown in the upper part of Fig. 4.18. The sampling rate is selectable between 0 MS/s and 100 MS/s.

When a hit is detected depicted as red highlighted box in the lower part of Fig. 4.18 a configurable number of further samples called *trigger delay* is written into the current row. Then the row pointer is switched to the next row. The signal transient of the hit is stored in the analog memory for read out and further processing and analog recording is continued in the next row.

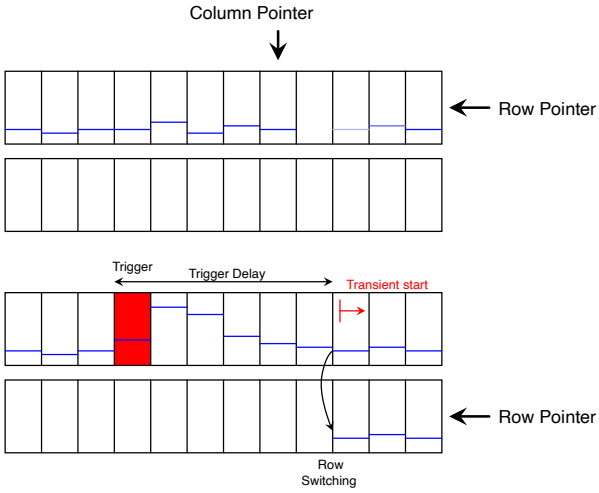

Figure 4.18: Transient recording in the HitDetection Analogue Memory.

The meta information as channel number, memory row and trigger time stamp are written into a FIFO and read out by the *Memory Readout Logic*. This logic controls the readout of a complete row in parallel with a set of 16 read out integrators. The outputs of the integrators are connected to a 12 bit pipeline ADC consecutively by the *Analogue Multiplexer*.

The pipeline ADC converts the analog values with 33 MS/s. The *data processing* unit is able to correct cell to cell variations of the analog memory and extract pulse features on chips. Both processing steps can be disabled individually to make raw data available for the data acquisition. In addition the ADC-Data are combined with meta information like channel number and time stamp.

The analog front ends as well as the transient recorder and digitiser units are combined to four

channel blocks. Four of these four channel blocks are placed on the HitDetection ASIC to provide 16 analog channels.

For communication with the data acquisition serial links based on copper connections with LVDS level are used. These links can be operated with up to 500 Mbit/s. As this might not be sufficient for raw data transport at high event rates the HitDetection ASIC will be equipped with four downstream links in parallel. The number of active links is configurable from one to four. The data coming out of the four four-channel blocks are buffered in event buffers and then distributed to the serial links with a data cross bar switch.

For accessing the internal configuration register of the HitDetection ASIC a Wishbone Bus system[15] is used. A serial receiver is connected via a wishbone master unit to this bus.

4.3.2.1 Status of the Development

The HitDetection ASIC is currently under development in a 180-nm-CMOS technology by UMC. In the past a first four channel prototype was already designed and tested and currently the design of the first 16 channel prototype is ongoing.

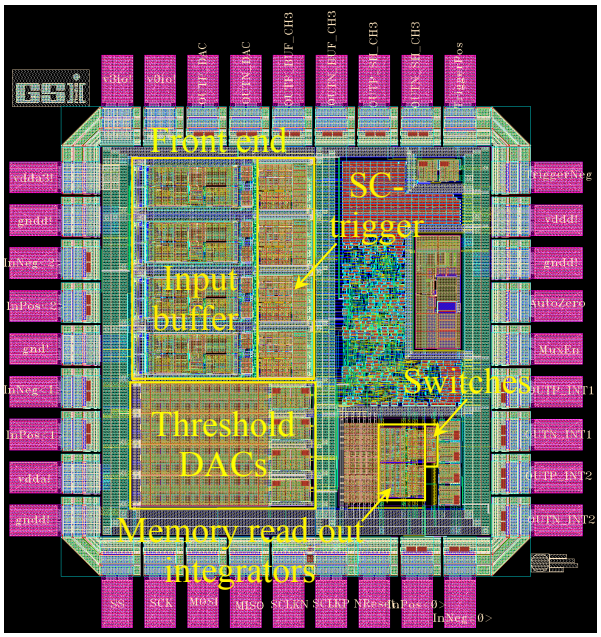

Figure 4.19: Layout of the ASIC with front end test structures

While this report is written two test ASICs with analog components of the HitDetection ASIC are under test. Fig. 4.19 shows the first test chips. It contains a complete four channel block of the front ends including input buffer and switched capacitor trigger unit. The aim of this ASIC is to characterise the isolated analog components in detail. Together with the second test ASIC shown in Fig. 4.20 the complete analog chain can be characterised.

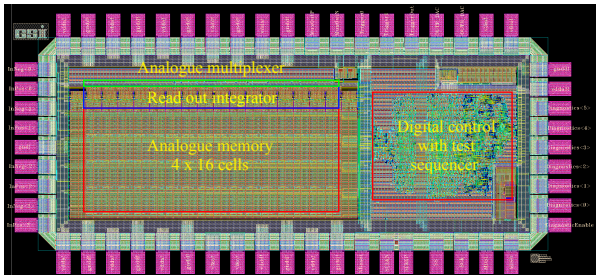

Figure 4.20: Layout of the ASIC with analog memory test structures

In parallel to the tests and characterisation of the analog components the digital backend is under design. At the time of this report the complete digital logic is written as VHDL code and all VHDL entities are simulated in isolated test benches. In the next step groups of logic units and finally the complete chip will be simulated. Then netlist synthesis and place and route will be done.

Assuming a successful test of the analog test ASICs it is planned to tape out the complete 16 channel HitDetection ASIC for an MPW prototyping run mid of December 2020.

4.4 Data Concentrator Module

The Data Concentrator for PANDA is designed to collect data from the PANDA front-end electronics, as well as to distribute detector synchronization signals. The module will be housed in a single AMC board with full size width. The module will feature 60 optical transceivers and 16 backplane multi-gigabit links running at 12 Gbit/s each, see Fig. 4.21. For the EMC the optical transceivers receive the data from the SADC board or via multiplexer boards (Sec. 4.6.2.1) from the HitDetection ASIC and distribute the SODA signals.

In order to maintain high optical link density, the module will be equipped with 12-channel FireFly transmitters and receivers from Samtec. Since the FireFlys are simplex devices, it is necessary to implement one 12-channel FireFly receiver and a 12-channel FireFly transmitter to achieve 12 full duplex channels. Optical fiber pigtails will connect FireFlys with five front panel MPO-type feed-

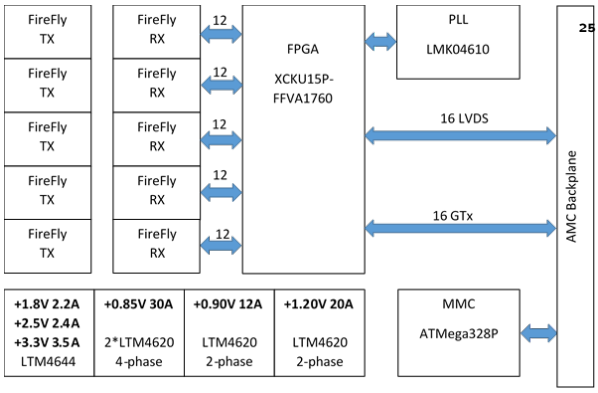

Figure 4.21: Hardware structure of the PANDA Data Concentrator

troughs. The data will be collected, buffered and processed by an on-board Kintex Ultrascale+ FPGA. The FPGA will have a general LVDS connection for "slow" control (up to 2 GB/s) over the AMC bus. In order to support defined latency systems, a stable clock with low phase noise is necessary. The Data Concentrator module will comprise a dual-PLL jitter cleaner and clock distributor LMK04610 from National Semiconducxtor (currently Texas Instrumments). The module will be supplied from 12 V µTCA crate and all necessary internal voltages will be generated by on-board DCDC converters. The estimated power consumption amounts to 60 W, hence the module will need efficient cooling. The voltage turn-on and off sequencing will be controlled by an Atmel microcontroller. For full power control, key voltages and currents will be monitored by a System Monitor located in the on-board FPGA. The first prototype is currently in production and will be available for tests in November 2020. The artwork of the module is shown in Fig. 4.22.

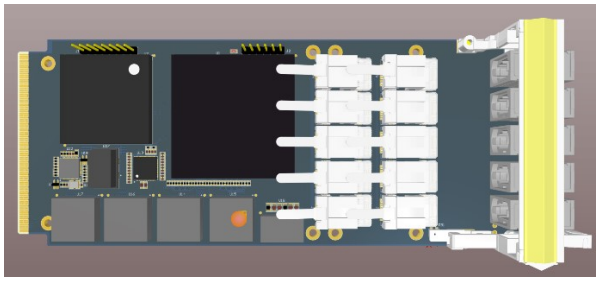

Figure 4.22: Artwork of the PANDA Data Concentrator

The complete readout of the EMC would require 16 of the PANDA data concentrator modules, yet possible data multiplexing rate inside SADC crates for the EMC forward endcap as well as the envisaged use of the HitDetection ASIC may decrease this number.

4.5 Feature Extraction Firmware

The feature extraction for the preamlifier signals for the PANDA EMC is designed to follow the PANDA trigger-less readout concept.

After the transmission of the analog signals via the front-end electronics, the signal will be digitized by the sampling ADC (Sec. 4.3.1) or by the HitDetection ASIC (Sec. 4.3.2) modules. Afterwards, the digital data stream will be processed on the FPGAs, which are located on the PCB of the sampling ADC, or in the data processing unit of the ASIC.

The digital signal processing consists of a signal smoothing by a filter with a finite impulse response, a pulse recognition without an external trigger, a pulse amplitude extraction and a pulse occurrence time determination. Furthermore, the extraction routine is optimized to identify pileup events on the falling edge of the digitized preamlifier pulse.

The outputs of the digital signal processing are so-called hits. A hit consists of the EMC channel information (i.e. APD channel), the extracted amplitude and the occurrence time. The hits, from the different detector channels, are sent to the data concentrator (Sec. 4.4) for further processing.

4.5.1 Barrel and Backward Endcap EMC

In the following, the essential feature extraction methods for the barrel and the backward endcap EMC, optimized for their front-end electronics (Sec. 4.1), are presented. The performance of the methods are demonstrated by both simulations and measurements with beam. For the beam tests, firmware was developed for the FPGAs of the sampling ADC. Finally, the FPGA resource consumption of the current firmware will be addressed.

4.5.1.1 Finite Impulse Response Filtering

A proper signal smoothing is in particular important to extract information of low amplitude pulses. The aim is to suppress undesired frequency components by conserving the pulse shape. Thus, the signal to noise ratio is improved. Consequently, both the lowest single-channel threshold and the relative

energy resolution of the calorimeter is enhanced. A filter with a finite impulse response (FIR) suited the demand for an increase of the signal to noise ratio due to a good adoption of the filter response on the signal structure. Furthermore, a FIR filter does not depend on the output function. Thus, there are no feedback loops, which could lead to a self-excitation of the filtered signal.

The fundamental FIR equation in time-space is:

$$y[n] = \sum_{k=0}^{M} A_k x[n-k] \tag{4.1}$$

with M being the order of the filter. Consequently, there are $M+1$ coefficients needed to calculate one output value. The choice of the coefficients $A_k \in \mathbb{R}$ defines the filter's characteristic. By raising the filter order M, both the damping of undesired frequencies against useful frequencies and the band sharpness improve. The necessary information of the pulse (occurrence time and amplitude) is contained in its rising edge. The full rise time (0 % amplitude to 100 % amplitude) of an APFEL preamplifier pulse is about 300 ns. Consequently, the corresponding signal frequency of the rising edge of the pulse is $f_{\text{signal}} = 1/300\,\text{ns} = 3.3\,\text{MHz}$. By applying the Nyquist theorem it follows an upper pass frequency of $2 \cdot f_{\text{signal}} = 6.6\,\text{MHz}$.

Besides the simple estimation of the pass band of the filter, a study of the spectral density of the full analog readout chain was determined by using an APFEL preamplifier with two biased (380 V) APDs, the backward EMC front-end electronics and the sampling ADC. In Fig. 4.23, the measured spectral density for the different noise contributions is shown. The contribution of the ADC (red) is negligible and is set as reference (0 dB). Moreover, the contribution of the front-end electronics (black) is small. The most dominant contribution comes from the APFEL preamplifier itself with amplitudes above 20 dB for the low gain amplification (blue) and amplitudes above 40 dB for the high gain amplification (green). Unfavorably, the largest contributions are at the same location as the useful signal (0 MHz – 6.6 MHz). The reason is white noise at the input of the amplifier, which also passes the transfer function of the amplifier. Thus, the preamplifier noise has a similar spectral density as the useful signal.

Nevertheless, the filter needs to have a low pass characteristic. Consequently, a pass band between 0 MHz and 1 MHz was chosen. In combination with a wide transition band between 1 MHz and 7.2 MHz, most of the fast frequency components of the useful signal are conserved. The stop band starts closely after the Nyquist frequency (6.6 MHz) at 7.2 MHz. Since the filter has to be implemented on a FPGA, the number of filter coefficients is limited due to FPGA resource considerations. The current FPGA implementation offers a 20 coefficient FIR filter for all 64 ADC channels of the sampling ADC. In Fig. 4.24 the Bode magnitude plot of the current FPGA filter implementation is depicted.

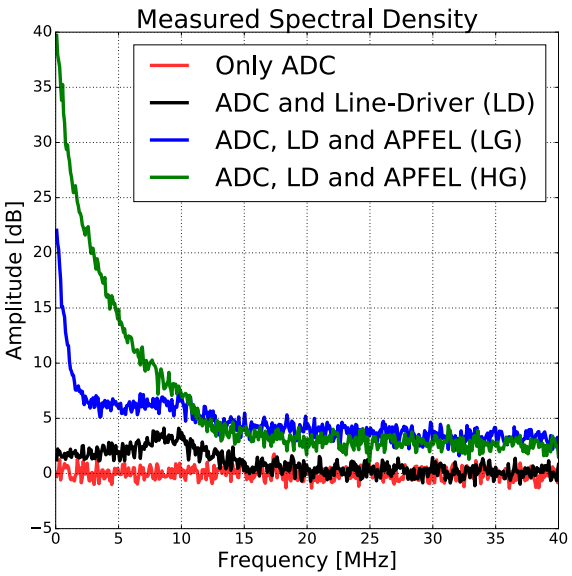

Figure 4.23: The plot shows the measured spectral density of the analog readout chain of the PANDA backward EMC. The noise of the ADC (red) is used as reference (0 dB). Besides the small contribution of the line-driver boards of the front-end electronics, the APFEL preamplifier contributes the most to the spectral density of the noise. Unfavorably, the most dominant noise components are congruent with the time structure of the useful signal. Consequently, a good compromise in terms of the filter characteristic has to be found.

4.5.1.2 Digital Signal Shaping

As mentioned before, the important event information is contained in the rising edge of the pulse. The falling edge of the pulse does not contribute any additional information. Furthermore, the long duration ($\sim$ 1200 ns) of the falling edge (100 % amplitude to 0 % amplitude) of the pulse is rather unfavourable in terms of pileup events. Consequently, a method was developed, which eliminates the falling edge of the pulse. The first step is the discrete derivation $D[i]$ of the signal:

$$D[i] = T[i] - T[i-r] \tag{4.2}$$

with T[i] being samples from the ADC and r being the discrete derivation step width. The second step

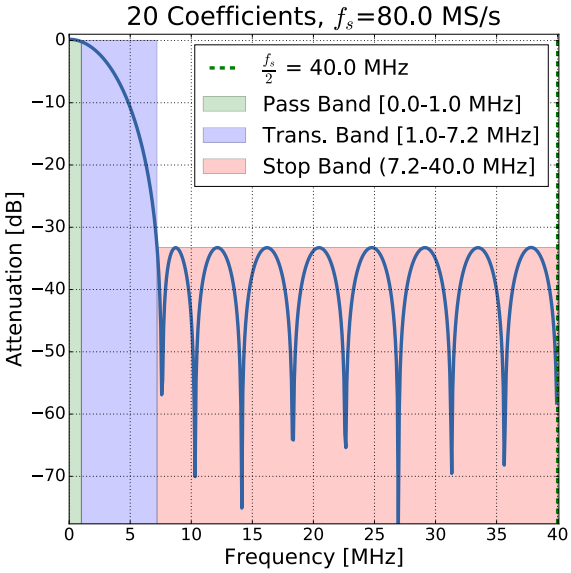

Figure 4.24: The plot shows the Bode amplitude diagram of the current FIR filter implementation on the PANDA sampling ADC. The bands are chosen to conserve the fastest components of the useful signal. Consequently, the damping at the fastest useful signal frequency is less than 4 dB. However, due to the high order ($M = 19$) of the filter, a damping between pass and stop band of more than 33 dB is achieved.

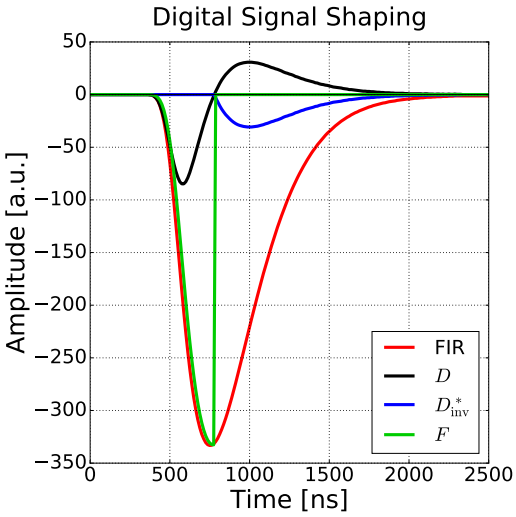

Figure 4.25: The plot shows the components of the digital signal shaping, which is applied to the FIR filtered signal (red). The black curve shows the ordinary discrete derivation of the signal, whereby the blue curve shows the inverted derivation with blocked positive components. The successive integration of the sum of the ordinary derivation and the modified inverse derivation defines the integral function F, which is close to congruent with the FIR curve without falling edge.

is to build the inverse of the derivation by blocking the positive components:

$$D^*_{\mathrm{inv}}[i] = -\Theta(D[i]) \cdot D[i] \tag{4.3}$$

with Θ being the Heaviside function. The sum $D_s = D[i] + D^*_{\mathrm{inv}}[i]$ cancels out the falling edge of the pulse. Finally, the successive integration of D_s and the normalisation by r, returns the original pulse without falling edge:

$$D_s[i] \mapsto \begin{cases} F[i] = F[i-1] + \frac{D_s[i]}{r} & : D_s[i] < 0 \\ F[i] = 0 & : D_s[i] = 0 \end{cases} \tag{4.4}$$

with F being the integration function. In Fig. 4.25 the components of the signal shaping are plotted.

Since the digital signal shaping is basically a derivation with a subsequent integration, the offset (DC) component of the signal is eliminated. Thus, the procedure has a built-in baseline follower. Consequently, the pulse amplitude measurement is reduced to a minimum determination of the integration function (F).

4.5.1.3 Pulse Identification

Digital pulse identification is indispensable for the trigger-less readout concept of the PANDA electromagnetic calorimeter. The digital electronics has to detect APFEL preamplifier pulses autonomously and distinguish them from noise. A proper parameter to characterise a preamplifier pulse is its time under threshold. The time under threshold is the number of samples i_t, while F (Eq. 4.4) is smaller than zero. To enhance the pulse identification even more, an empirical weight function λ_t was developed. The idea is to weight signal structures, which appear like a rising edge of an APFEL preamplifier pulse stronger than other signal structures. The time under threshold condition is included implicitly due to the peak position of λ_t:

$$\lambda(i_t) \mapsto \begin{cases} e^{A_t \cdot i_t} & : i_t \leq P_t \\ M_t \cdot e^{-A_t(i_t - P_t)} & : i_t > P_t \end{cases} \tag{4.5}$$

With P_t being the maximum position and M_t the maximum amplitude of the function. P_t and M_t are connected through the relation $A_t = \frac{log(M_t)}{P_t}$. In Fig. 4.26 an example for a weight function with the parameters $P_t = 28$ and $M_t = 2$ is depicted. A $P_t = 28$ refers to a peak position at 350 ns, which is slightly more than the typical rising time of 300 ns of an APFEL preamplifier pulse. The trigger is set

on the weighted sum:

$$R_t = \sum_{k=0}^{i_k} \lambda_t[k] \cdot F[k] \tag{4.6}$$

If R_t exceeds the threshold ts while F is smaller than zero, the pulse is identified as a hit. There is a threshold ts_L for the APFEL low gain amplification and a threshold ts_H for the APFEL high gain amplification.

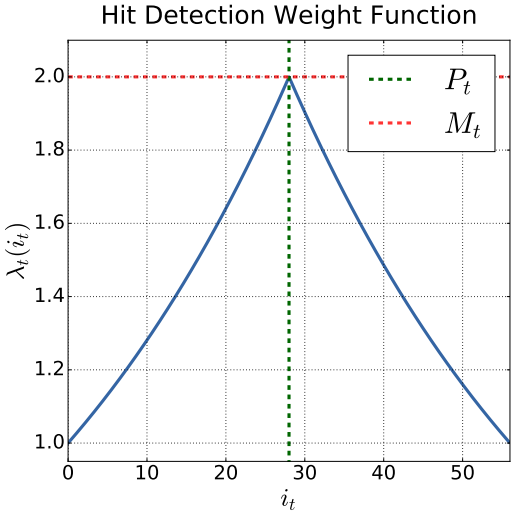

Figure 4.26: The plot shows the empirical weight function, which is applied to the integral function F, to enhance the pulse identification. The idea is to weight signal structures, which appear like the rising edge of an APFEL preamplifier pulse, stronger than other signal structures. The peak position P_t is related to the time under threshold of F. In the example $P_t = 28$ was chosen, which corresponds to 350 ns.

4.5.1.4 Pulse Amplitude Extraction

The minimum of the integration function F (Eq. 4.4) is determined continuously and defines the amplitude of a possible hit. In combination with the pulse identification, described above, the final decision is made. If the pulse identification is positive, the amplitude is transferred to the hit information.

4.5.1.5 Pulse Occurrence Time Determination

The APFEL preamplifier pulse shape can be parameterised by the following function:

$$f(x) = -A \cdot e^{\frac{-N(x-\delta)}{\tau}} \cdot \left(\frac{x-\delta}{\tau}\right)^N, \tag{4.7}$$

with the parameters δ, τ, N and A. The rising time is defined by the parameter τ. Furthermore, the parameter N has an impact on the decay time and A is related to the pulse amplitude. The occurrence time of the pulse is given by the parameter δ. However, the occurrence time δ lies within the baseline noise fluctuations and thus, it is no prominent extraction point. Consequently, the pulse occurrence time determination has to be performed at a characteristic point of the pulse, which is not dominated by noise. Furthermore, the extraction point should not vary with the height of the pulse. The inflexion point of the pulse I meets the requirements and has proven to be a robust extraction point. Hence, the time extraction of the pulse is performed at:

$$T_0 = \delta + I \tag{4.8}$$

with

$$I = \frac{\tau(\sqrt{N}-1)}{\sqrt{N}} \tag{4.9}$$

The time extraction is done by the determination of the zero transition of the second derivative D' (analog to Eq. 4.2) of the FIR smoothed signal (Fig. 4.27).

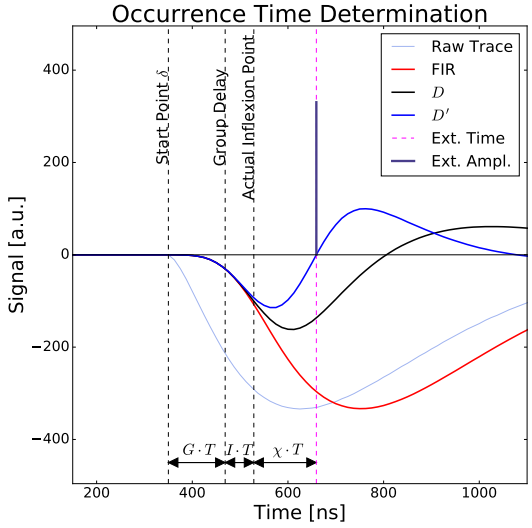

Figure 4.27: The plot illustrates the T_0 determination on the inflexion point of the FIR filtered signal. Due to the group delay G of the filter, the theoretical inflexion point and the discrete derivation, the determined time is shifted compared to the theoretical occurrence time δ. However, the actual time shift is constant for given parameters.

Due to the discrete-time structure of digital data, the time resolution is limited to the time step width

T. For instance, the step width for the ADC data from the sampling ADC is $T = 12.5$ ns (80 MHz sampling frequency). However, improvement is possible with a linear interpolation between two time-discrete values of $D'[i]$:

$$T_0 = i_0 + \frac{D'[i_0]}{D'[i_0] - D'[i_1]} \tag{4.10}$$

with i_0 and i_1, being the samples right before and after the zero transition of $D'[i]$. As a result, the time resolution improves with the number of fragmentation intervals. In the current implementation, the step width of 12.5 ns is fragmented into 64 pieces.

The group delay G of the filter and the numerical derivative induce a shift between theoretical occurrence time and the extracted time. The overall time shift reads:

$$T_{\text{shift}} = T \cdot (G + I + \chi) \tag{4.11}$$

with $G = M/2$ (M is the order of the filter, Eq. 4.1), I the actual inflexion point and χ, which depends on the derivation parameter r. In Fig. 4.27, the different time shift components are shown.

4.5.1.6 Pileup Detection and Correction

The fundamental aim of the digital pulse shaping, which was described above, is the possibility of pileup detection and correction. Depending on the detector rate, different pileup events occur with different probabilities. Four relevant event types can be identified:

1. A second pulse occurs after the decay time of the first pulse, which is not pileup but important to mention for later discussion.

2. A second pulse occurs within the separation limit. Thus, the pulse processing algorithm is not able to separate the pulses.

3. A second pulse occurs after the separation limit but before the first pulse is completely decayed. The pulses can be separated, but the extracted height of the second pulse is attenuated.

4. Two or more additional pulses occur within the time interval of the first pulse. A pulse separation depends on the pulse positions (similar to type 2 and type 3).

In Fig. 4.28 the different pileup types are illustrated. By considering Poisson distributed events, the APFEL preamplifier pulse length of 1500 ns and the occurrence time of secondary pulses the probabilities for the different types at a detector rate of 100 kHz are 86.1 % for type 1, 4.3 % for type 2, 9.5 % for type 3 and finally 1.0 % for type 4.

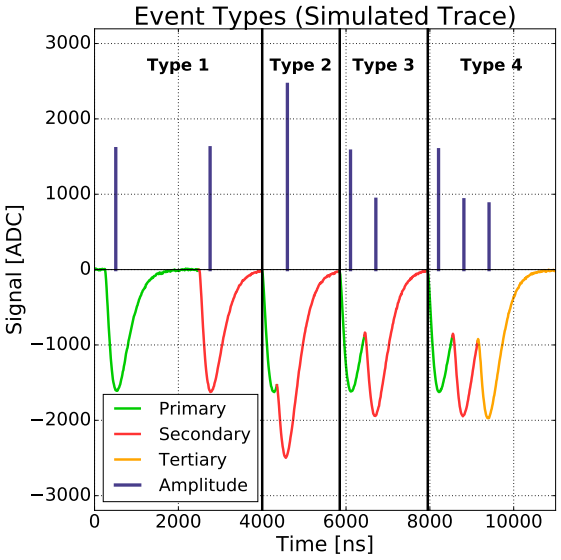

Figure 4.28: Possible event types at high rates.

The current digital signal processing is capable to detect pileup events on the falling edge of the digitised APFEL preamplifier pulse (type 3 events). The minimum time difference between two consecutive pulses depends on both the FIR filter characteristics and the derivation parameter r. A typical value for the minimal time between hits is about 450 ns. Due to the signal superposition of the first and the second pulse, the extracted amplitude of the second pulse is attenuated. Consequently, correction is necessary. The correction factor is a function of the measured amplitude of the primary pulse $H^p_{\text{meas.}}$, the measured amplitude of the second pulse $H^s_{\text{meas.}}$ and the time difference between second and first pulse $\Delta t = T_s - T_p$:

$$H^s_{\text{corr.}} = H^s_{\text{meas.}} \cdot \Sigma(H^p_{\text{meas.}}, H^s_{\text{meas.}}, \Delta t) \tag{4.12}$$

with Σ being the correction function, which can be determined by measurements or simulations. A first attempt to determine the correction function for fixed energies was performed with beam data by utilising the backward EMC prototype (Sec. 7.3). In Fig. 4.29 extracted event amplitudes as a function of the time difference Δt to their previous events for a central crystal at a beam energy of 855 MeV and a detector rate of 110.35 kHz are depicted.

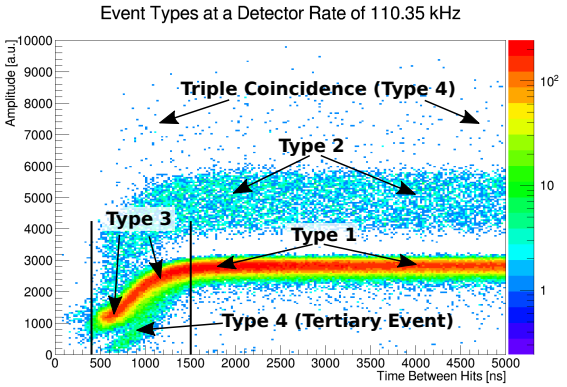

Figure 4.29: Measured pileup amplitude distortion for monochromatic events.

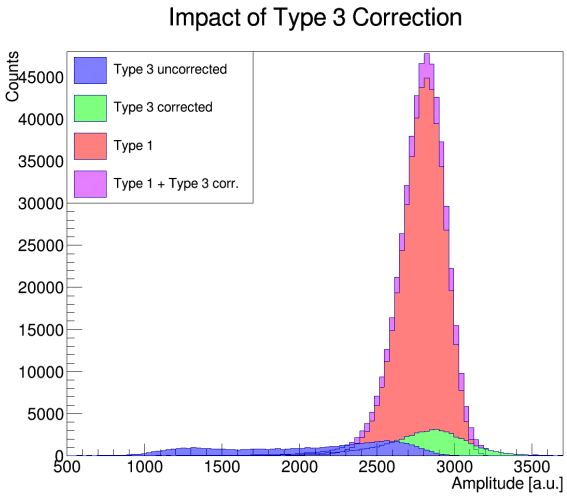

Figure 4.30: Amplitude restoration of type 3 pileup events.

The straight red region shows type 1 events with no amplitude distortion. The broad blue-green region above the red region shows type 2 events. In the case of a monochromatic beam, the amplitudes are about doubled in height compared to type 1 events. Events, with even higher amplitudes than type 2 events, or smaller amplitudes than the amplitudes of the red region, are special cases of type 4 events. The most interesting part of the histogram is the region for time differences lower than the pulse length of 1500 ns. The amplitudes are attenuated due to the superposition of the pulses with the falling edges of the predecessor pulses. By fitting the type 3 region in the histogram with a high order polynomial function, the correction function Σ of Eq. 4.12 can be determined. In Fig. 4.30, the impact of the type 3 amplitude correction is shown for a single crystal spectrum. After applying the correction, the broad blue histogram (type 3 uncorrected) moves towards the type 1 histogram (red). Furthermore, the corrected type 3 histogram (green) is now similarly narrow as the type 1 histogram. By adding the corrected type 3 events to the type 1 events, they are no longer considered as lost events and contribute to the statistics of the measurement. However, the relative energy resolution deteriorates by 0.318(8) %. Depending on the PANDA physics case, it can be chosen between a better energy resolution (ignoring type 3 events) or better statistics (adding corrected type 3 events to type 1 events).

4.5.1.7 Dead Time and Effective Pileup Probability

The dead time of the system was determined with the backward EMC prototype (Sec. 7.3) in combination with a plastic scintillator with a photomultiplier readout in front of the prototype. The duration of photomultiplier pulses is very short (tens of nanoseconds) compared to the duration of calorimeter pulses (1500 ns). Thus, the pileup probability for photomultiplier signals is much lower (<1 % at 100 kHz detector rate) compared to calorimeter pulses (13.9 % at 100 kHz detector rate). Consequently, the pileup losses for the measured rate with the scintillator ($R_{\text{Sci.}}$) can be neglected. The degradation of the measured rate with the calorimeter ($R_{\text{Det.}}$) due to pileup, can be described by

$$R_{\text{Det.}} = R_{\text{Sci.}}(1 - \tau R_{\text{Det.}}) \tag{4.13}$$

with τ being the dead time of the prototype calorimeter. Eq. 4.13 can be rearranged to eliminate the $R_{\text{Det.}}$ dependency on the right side of the equation:

$$R_{\text{Det.}}(R_{\text{Sci.}}, \tau, \epsilon) = \frac{\epsilon \cdot R_{\text{Sci.}}}{1 + \tau \cdot \epsilon \cdot R_{\text{Sci.}}} \tag{4.14}$$

with ϵ being a factor, which is introduced to account for inefficiencies in the scintillator readout. By plotting the prototype rate $R_{\text{Det.}}$ against the scintillator rate $R_{\text{Sci.}}$ and utilising Eq. 4.14 as fit function (Fig. 4.31), the dead time of the PANDA backward calorimeter prototype can be determined to:

$$\tau = 464(13)\,\text{ns}$$

Secondary pulses, which appear within the dead time, can not be distinguished from the primary pulses (type 2 in Fig. 4.28). However, pulses which appear after the dead time can be distinguished. By utilising the amplitude restoration described above, even second pulses, which appear between τ and the

full pulse length (type 3 in Fig. 4.28) can be considered as ordinary pulses. Therefore, according to the Poisson distribution, the effective pileup probability at 100 kHz of the prototype is

$$P_{100\,\mathrm{kHz}} = 4.53(12)\,\%$$

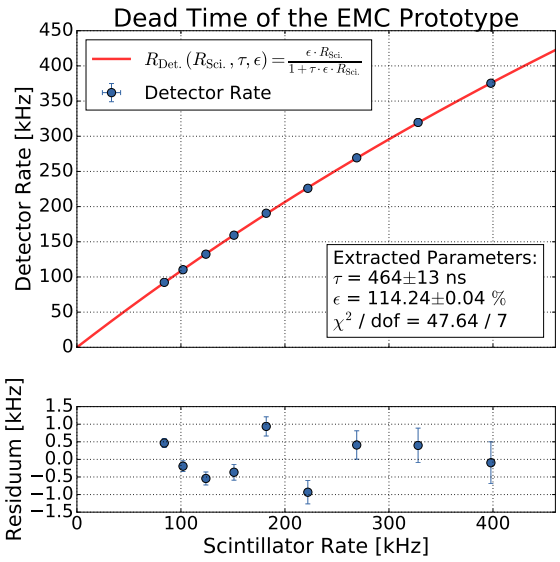

Figure 4.31: Dead time determination of the backward EMC prototype by high rate measurements.

4.5.1.8 Simulation of Signal Processing Algorithms

To develop and test the digital signal processing methods, a software simulation framework was designed. The framework is characterised by the generation of detector signals with realistic noise and the implementation of processing methods by considering digital electronics limitations. Consequently, the output data of the framework are comparable to data recorded with the PANDA calorimeter. All essential detector parameters such as APD gain (M_{APD}), APD quantum efficiency, APD area coverage, crystal light yield, detection thresholds or APFEL preamplifier gain, can be set according to the real detector and the demands on the simulation. For instance the framework reproduces the electronic noise term of the relative energy resolution c. To this end, both detector and simulation input were set to an APD gain of 150 and a hit detection threshold of 2.5 MeV. The analysis of the single APD signals in the APFEL low gain amplification revealed an electronic noise term for the measurement of $c_{\mathrm{meas.}} = 2.16(6)$ MeV and $c_{\mathrm{sim.}} = 2.095(6)$ MeV for the simulation. In Fig. 4.32 the c/E dependency from the energy for both measurement and simulation is shown.

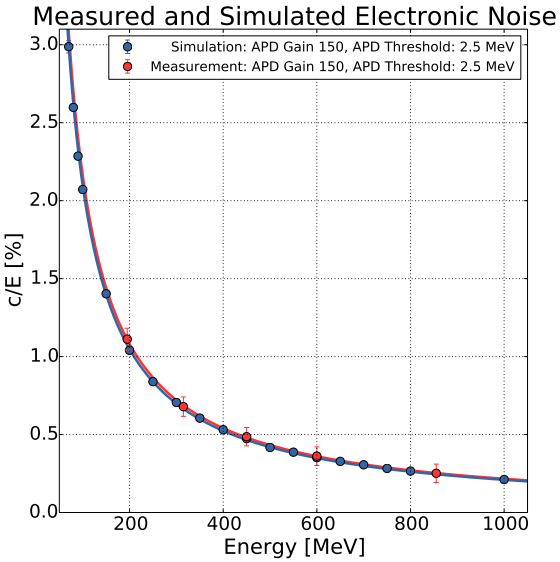

Figure 4.32: Comparison of c/E as a function of the energy for simulated and measured data.

A detailed explanation of the digital signal processing simulation framework can be found in [8].

The simulation framework was utilised for parameter scans to optimise the feature extraction. The parameters r (Sec. 4.5.1.2) and P_t (Sec. 4.5.1.3) were optimised concerning the hit detection efficiency η for 3 MeV events for a hit detection threshold of 2.5 MeV. Best results were achieved for a r value of 4. Furthermore, a P_t value of 22 for the APFEL preamplifier low gain amplification and a P_t value between 27 and 32 for the APFEL preamplifier high gain amplification give the best performance. For the scaling parameter M_t (Sec. 4.5.1.3), a factor of two suits the demand of having a strong separation between useful signals and noise.

After the optimisation, performance tests were done to determine the noise hit rate, the detection efficiency, the time resolution and the non-linearity as a function of the APD gain and other key factors. A detailed description of the different scans and analyses can be found in [8]. The most important results are summarised in Table 4.3. However, at this point the necessity of noise hit reduction through online timestamp comparison should be emphasised. The detection efficiency improves by lowering the detection threshold. Still, at the same time the noise hit rate R_{NHR} increases. Since the data transmission between sampling ADC and data concentrator is limited (558 kHz event rate per ADC channel at the current implementation), a timestamp

comparison between neighbouring APD channels is recommended at the level of the sampling ADC. In contrast to noise hits, true hits are correlated. Consequently, a better noise hit discrimination is possible. In Fig. 4.33 the principle is illustrated for three simulated pulses on the traces of two neighbouring APDs (one crystal). After the comparison of the timestamps, only one noise hit (red) is left on the trace.

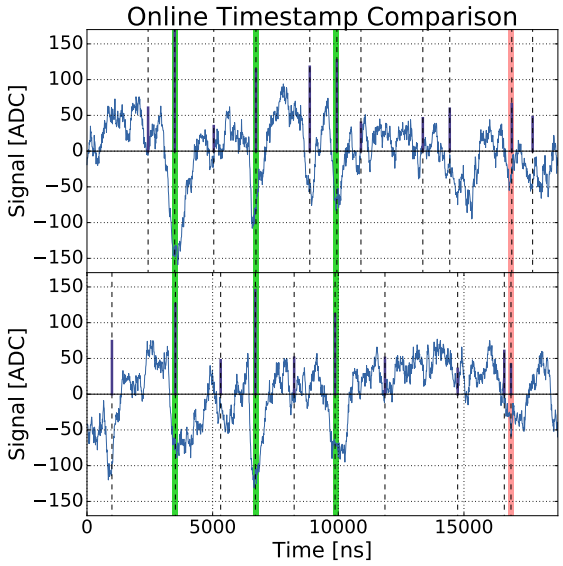

Figure 4.33: Online timestamp comparison.

Depending on the timestamp comparison interval $I_{\text{comp.}}$, the noise hit rate drops by

$$D_{\text{drop}} = 1 - P_\lambda(k)^2 = 1 - \lambda^2 \cdot e^{-2\lambda} \qquad (4.15)$$

with $\lambda = I_{\text{comp.}} \cdot R_{\text{NHR}}$ and $P_\lambda(k)$ being the Poisson distribution with $k = 1$.

4.5.1.9 Firmware Resource Consumption

A test firmware for the FPGAs of the sampling ADC was developed to examine both the presented feature extraction methods and the trigger-less readout concept. The development is based on the firmware, which is used for the crystal barrel experiment in Bonn [16]. At the crystal barrel experiment, a modified version of the PANDA sampling ADC is utilised. However, in contrast to PANDA, an external trigger is used to release the data acquisition. Thus, changes and new developments had to be performed in terms of the data flow. Consequently, the development enables a proof of the capability of the PANDA trigger-less readout concept for the calorimeter for the first time, which includes the full readout chain, the digitisation, the digital signal processing, the refined processing on a data concentrator and the offline analysis on compute nodes. All discussed measurements above (Sec. 4.5.1.6, Sec. 4.5.1.7), were performed by using the test firmware. The current version of the firmware offers a 20 coefficient finite impulse response filter (Sec. 4.5.1.1) for all readout channels, the implementation of all discussed digital signal processing methods and an internal data infrastructure for trigger-less high rate measurements. Thanks to the method of distributed arithmetic [17], the resource consumption of the firmware could be minimised. The firmware occupies 58 % of the available Look-Up-Tables, 52 % of the available flip-flops, 40 % of the available block RAM and 19 % of the available digital signal processing (DSP) slices. Consequently, the firmware occupies roughly 50 % of the sampling ADC FPGA resources and leaves free resources for other algorithms. For instance, the firmware does not yet support baseline monitoring. Furthermore, the resource consumption of the PANDA time distribution system is not yet taken into account. In Fig. 4.34 the utilisation of FPGA resources of the current test firmware is summarised.

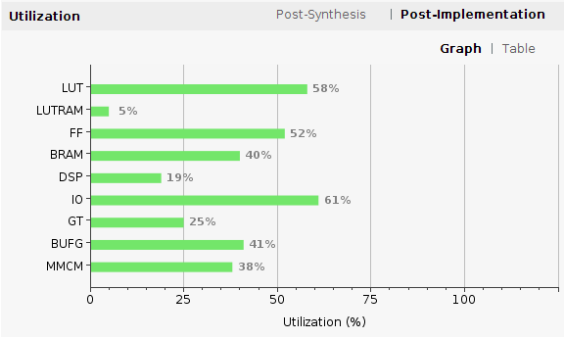

Figure 4.34: Utilisation of FPGA resources for the current test firmware.

4.5.2 Forward Endcap EMC

The feature extraction algorithm for the forward endcap EMC is adjusted to its front-end electronics (Sec. 4.2), which is required to process signals at high interaction rates. Several signal filters are used for efficient signal processing during the feature extraction procedure. As it is explained below, they help to reduce noise levels and pileup occurrence. However, proper parameter setting is important. Thus, Monte-Carlo simulations are done to investigate optimal filter parameters.

Table 4.3: The table summarises the results of the performance test simulations for the digital processing for APFEL preamplifier signals. The simulations were performed for typical APD gains for the PANDA electromagnetic calorimeter. The noise hit rate is shown for a single APD channel for thresholds between 0.5 MeV and 2.5 MeV ("single"). For comparison, the noise hit rate is also given for coincidence measurements with two APDs ("dual"). The detection efficiency is listed for the same threshold interval as the one for the noise hit rate. The values >60 MeV and >500 MeV in the time resolution part refer to pulse heights in units of energy. Similarly, the non-linearity is given for energies lower and higher than 100 MeV.

Parameter	Achieved Value						Unit
APD Gain	150		200		250		-
Preamp. Gain	LG	HG	LG	HG	LG	HG	-
Noise Hit Rate							
2.5 MeV single	331.1(26)	160.9(20)	151.4(20)	38.1(11)	67.9(15)	5.5(4)	kHz
2.5 MeV dual	1.3(26)	0.2(20)	0.1(20)	0.0(11)	0.1(14)	0.0(4)	kHz
1.5 MeV single	875.9(34)	516.9(27)	487.2(29)	308.2(24)	331.4(27)	164.1(20)	kHz
1.5 MeV dual	18.9(34)	4.5(26)	3.8(29)	1.0(24)	1.3(27)	0.2(20)	kHz
1.0 MeV single	1288.0(38)	794.7(29)	1069.1(37)	599.0(28)	722.3(33)	439.8(26)	kHz
1.0 MeV dual	51.1(38)	14.6(28)	31.9(37)	6.8(27)	11.3(33)	2.9(26)	kHz
0.5 MeV single	2203.9(41)	1245.7(33)	1854.7(40)	1063.4(32)	1547.0(40)	926.0(31)	kHz
0.5 MeV dual	177.3(41)	47.0(30)	121.5(40)	31.4(30)	79.8(40)	21.9(29)	kHz
Efficiency	Deposited Energy: 3 MeV						
2.5 MeV	43.0(4)	50.4(5)	43.8(5)	55.3(5)	45.3(5)	58.5(4)	%
1.5 MeV	58.2(5)	65.9(4)	59.2(4)	76.6(4)	62.7(4)	83.9(3)	%
1.0 MeV	63.1(4)	70.6(4)	65.8(4)	80.7(4)	67.2(4)	86.8(3)	%
0.5 MeV	69.3(4)	72.7(4)	69.2(4)	81.6(4)	69.6(4)	87.4(4)	%
Time Resolution							
>60 MeV	4.594(30)	1.717(11)	3.456(22)	1.296(8)	2.729(18)	1.032(7)	ns
>500 MeV	577(4)	219(1)	431(3)	164(1)	345(2)	131(1)	ps
Non-Linearity	Upper Limit						
< 100 MeV	635.12(23)	288.24(179)	138.24(70)	134.80(7)	162.17(7)	103.66(73)	keV
≥ 100 MeV	64.81(3)	41.31(27)	44.90(3)	21.62(27)	44.78(3)	21.05(26)	keV

4.5.2.1 Online Feature Extraction Algorithm

Implementation of the feature extraction algorithm on the FPGA is done in VHDL. More details can be found in [18]. The signal-processing logic is shown as a block diagram in Fig. 4.35. The digitized pulse, i. e. waveform, is guided to parallel branches of the feature extraction.

The Moving Window Deconvolution (MWD) I functional block produces a rectangular shape from the preamplifier pulse. The other branch with the MWD II functional block is used to reduce the pulse length even more in comparison to MWD I. Thus, these two blocks reduce the response time of the detector, which decreases the probability of signal pile-up at high rates. The following Feature-Extraction module (FE) has the same structure for both. Discrete-in-time samples of the digitized waveform are passed through the baseline functional block (Baseline), which restores the correct baseline for precise energy determination. The output of the baseline block is connected to three readout functional blocks, namely to Trigger (Tr), Constant Fraction Timing (CFT) and Moving Average (MA) filter. The MWD functional block provides the time-stamp information. The MA func-

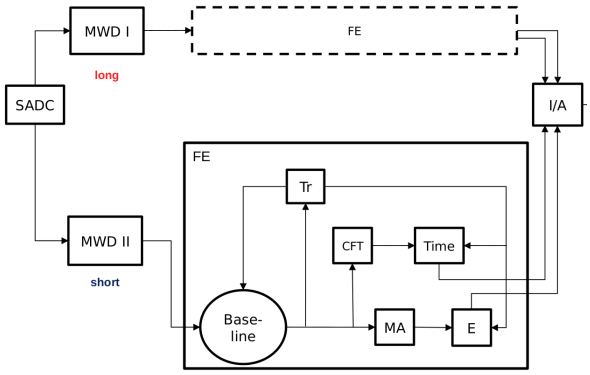

Figure 4.35: The block diagram of the feature extraction algorithm implemented on the FPGA of the sampling ADC.

tional block is used for smoothing and noise reduction leading to precise pulse detection at lower thresholds. If the sample-value is higher than the set threshold in the Tr block, this block sends a command to process the information given by the CFT and MA blocks after each sample from now for the Time-Energy determination in the Time and Energy (E) functional blocks. The Tr block performs not only the detection of the pulse but also its interruption. When the sample-value becomes lower than 1/4 of the threshold value, this block sends a command to stop the time-energy determination. As a result, the time and energy values, extracted from the pulse, are propagated to the last functional block: Pileup Identification and Recovery (I/A). This block is used to estimate the integral/amplitude ratio. If this ratio is bigger than a value set by the user, the output is taken from the parallel branch with a shorter waveform after the MWD block. Received hit data are sent to the data concentrator (Sec. 4.4).

4.5.2.2 MWD and MA Filters

As mentioned above, the MWD filter is used to transform the digitized preamplifier signal to a rectangular shape, which simplifies amplitude detection [19]. It can be understood as some kind of FIR filter but with fixed coefficients. This filter removes the falling exponential edge, thus it reduces the length of the signal. The discrete form of the deconvolution equation is:

$$\mathrm{MWD}_m[n] = x[n] - x[n-m] + \frac{1}{\tau}\sum_{k=n-m}^{n-1} x[k] \tag{4.16}$$

where $x[n]$ is the input value of n^{th} sample, $\mathrm{MWD}_m[n]$ the output value, τ the decay constant and m the length of the MWD filter, which is equal to the output length of the signal, given as the number of sample points. The process of MWD filtering is illustrated in Fig. 4.36.

The MA procedure is another filter for digital signal processing. As explained above, it is used after pulse detection. A number of sample points from the detected input signal is averaged to produce each point of the output signal. This averaging action is applied to remove the high-frequency components, i. e. noise components, in the signal and it can be presented as a low-pass filter. The MA equation for this filter procedure is:

$$\mathrm{MA}[n] = \frac{1}{L}\sum_{j=0}^{L-1} A[n+j] \tag{4.17}$$

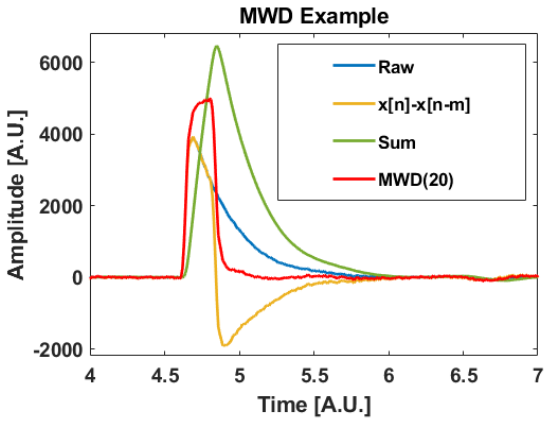

Figure 4.36: The combined graph showing the impact of the different components of the MWD filter, where "Sum" is $\frac{1}{\tau}\sum_{k=n-m}^{n-1} x[k]$.

where L is a number of averaged samples and A their sum. Increasing the number of averaged samples can cause noise suppression. The application of both the aforementioned MWD filter and the MA filter provides the pulse shaping and noise reduction of a digitized preamplifier signal. Modifying the parameters of each filter separately, the obtained pulse shape can vary from triangle ($L \geq m$) to rectangular ($L < m$). The optimal combination is $L = \frac{m}{2}$. The length of the filter plays an important role in the achievement of a better resolution as it will be shown below.

4.5.2.3 Time and Amplitude Extraction

Time extraction procedure is included in the aforementioned CFT block, which performs Constant Fraction Discrimination (CFD)[20]. It is applied to extract the precise time information from the measured signal. A constant-fraction time pick-off is performed by producing a trigger at the zero-crossing level of a bipolar pulse [20], which is created by subtracting an inverted copy of the input pulse from a delayed copy of the same pulse. The inverted copy is attenuated by the constant-fraction coefficient. In our signal processing the CFD is digitally applied to the MWD output:

$$\mathrm{CFD}[n] = \mathrm{MWD}[n] - k \cdot \mathrm{MWD}[n+d] \tag{4.18}$$

where n is the sample number, k is an attenuation coefficient for inverted signal, and d is a delay. The coefficient can be set 1/2 or 1/4 of the pulse amplitude and the delay is set equal to the number of samples in the rising edge. The CFD procedure is shown in Fig. 4.37. The linear interpolation

is used to determine the zero-crossing time. This time stamp is determined to be the local time of the pulse.

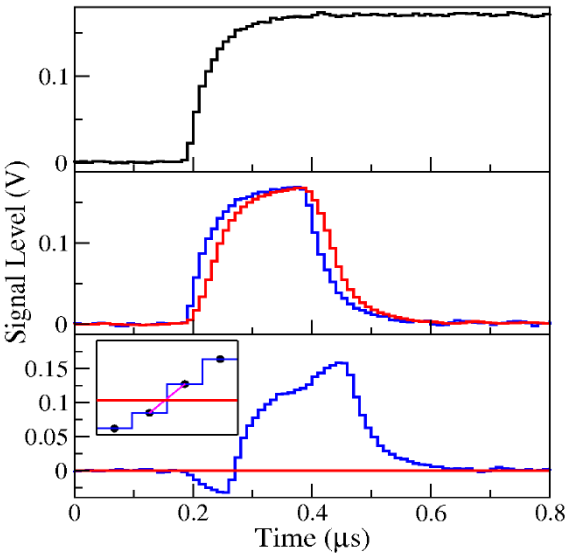

Figure 4.37: The sequence in signal processing to obtain the CFD signal and the time stamp. The raw digitized signal is shown on top (black histogram). In the middle: the resulting MWD (blue histogram) and smoothed MWD (red histogram) pulses; bottom: the CFD signal. Picture is taken from [18].

The amplitude extraction, which is related to the energy deposition in the crystal, takes place after the MA block in the Energy block. The MWD filtering, applied before, simplifies the amplitude extraction for the preamplified signal [21]. The rectangular MWD pulse, smoothed after the moving average procedure, is processed by a simple sample comparison, where the sample with the highest value is defined as the pulse amplitude. The implementation of the MA filter improves the final amplitude resolution, which is shown in Fig. 4.38. Besides the amplitude identification, integral calculation is done in the same Energy functional block for the pileup detection. Once the sample-values are below a quarter of the trigger level, all collected information, such as time, amplitude and integral, is sent to the pileup detection block to determine the pileup occurrence.

4.5.2.4 Pileup Detection and Recovery

The Forward Endcap EMC will be exposed to single-detector hit rates of up to and above $500\,000\,\mathrm{s}^{-1}$ because of high annihilation rates in the phase II, which will lead to pulse overlap cases. To

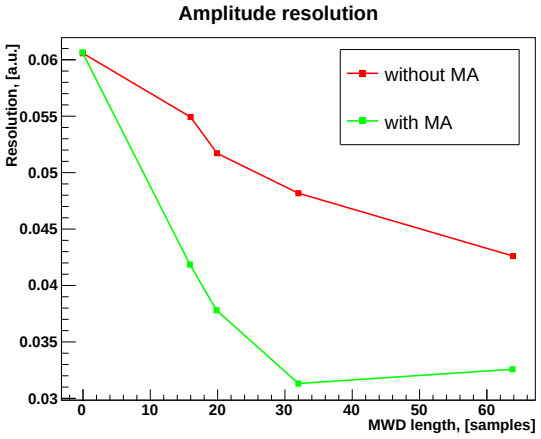

Figure 4.38: The difference in the amplitude resolution if a MA filter is used, which has a length of half of the MWD filter length.

reduce the influence of pileup events on the final measurement results, a pileup detection and recovery algorithm is introduced. As mentioned before, the pulse pileup identification is done by monitoring the integral/amplitude ratio. The estimated pileup identification efficiency is almost 100 % and the false rate of identification is below 1 % [22].

The pileup identification algorithm is implemented on the ADC FPGA. It is based on the assumption of stability of the pulse shape in the complete dynamic range. For a single stable pulse, the I/A ratio is not dependent on amplitude value and it has a saturation level. This fact can be used for pileup detection as shown in Fig. 4.39. In case of pileup, the ratio tends to be greater than the threshold value, which is set as a pileup threshold. One must say that configuration of MWD-MA filters can change this value in both directions. Besides the high interaction rates, the other reason of pileup occurrence is the waveform length. To decrease the influence of this, the aforementioned MWD filter is used. The example of pileup treatment is shown in Fig. 4.40. As it is mentioned above, in case of a pulse exceeding the pileup threshold, the feature extraction algorithm looks at information from the feature-extraction module with the MWD filter that has the shorter integration length and reads out information from this feature-extraction branch. As a consequence, the amplitude resolution becomes worse for a certain pulse amplitude, but it does not have a huge affect in the end, as it will be shown in the next section.

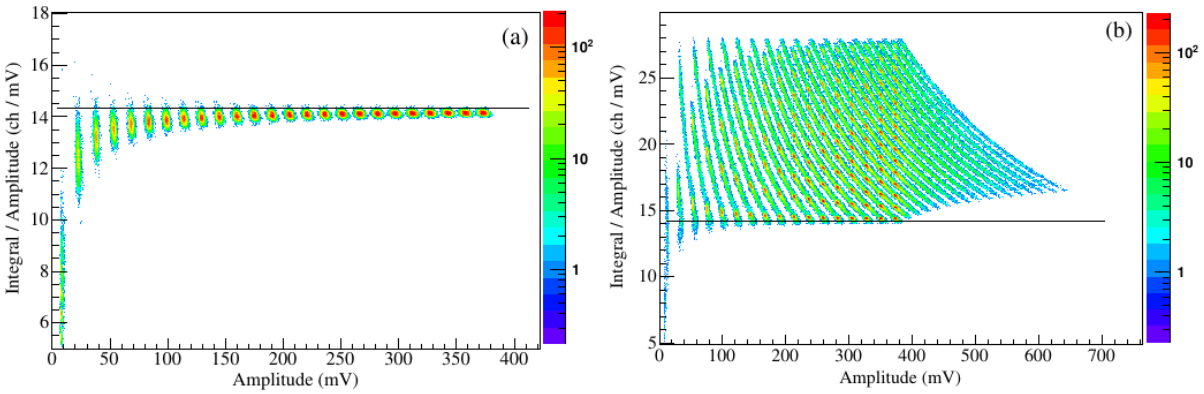

Figure 4.39: The ratio of the pulse integral over the pulse amplitude as a function of the pulse amplitude from simulations: (a) for single pulses only; (b) for pileup pulses only. The horizontal line indicates the pileup identification threshold. Picture is taken from [22].

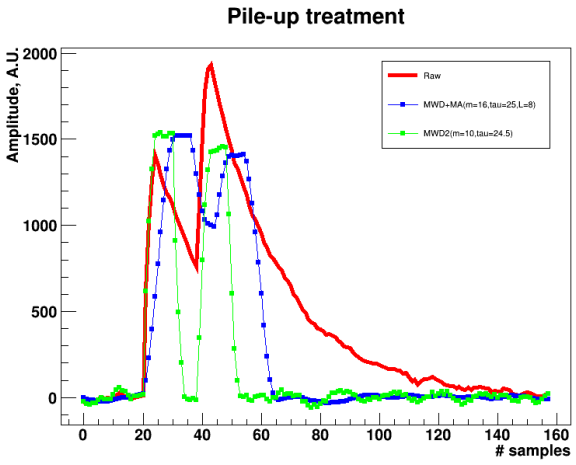

Figure 4.40: An example of pileup occurrence at the Forward Endcap EMC, produced in simulation. The raw waveform with a pileup case (red) is processed by the MWD and MA filters, which recover two separate signals through the MWD shaping.

4.5.2.5 Simulation Studies for Feature Extraction

In order to estimate the efficiency of the feature extraction algorithm, a Monte-Carlo simulation was performed. The signal processing logic was realized as C++ code in the PandaRoot package [23]. In addition, a waveform shape of the preamplifier signal was updated to the current one. For estimation of pileup detection and recovery, a time-based way of simulation was selected where separate events can interfere with each other. The simulation framework was based on gamma rays detected by a EMC Forward Endcap submodule. The number of generated gammas was 10 000, which were one by one ejected into one crystal of the sub-unit. The gamma energy was 1 GeV. First, the interaction rate was set to 1 kHz and later to 500 kHz in order to estimate the final resolution for single pulses and pileup pulses, respectively. Fig. 4.41 shows an example of the reconstructed gamma peak. First,

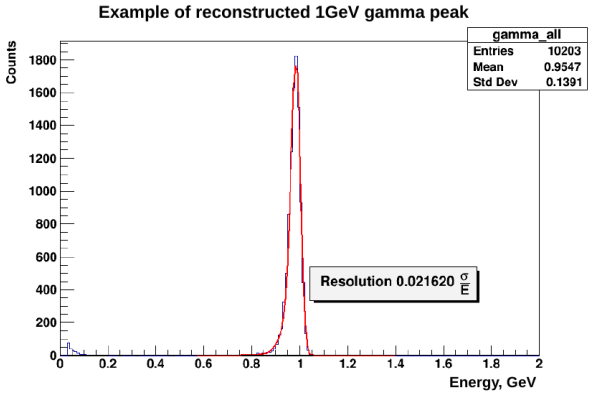

Figure 4.41: An example of the reconstructed gamma peak. Red line shows a Gabler fit function.

the amplitude resolution was investigated for dependence on MWD and MA parameters. It was revealed that the resolution becomes better with longer filters for a stable pulse, which can be produced by a light pulser. Nevertheless, it was not observed for gamma particles because of stochastic processes during their interaction with the scintillation material. The simulation results show that the final resolution of the gamma peak is more dependent on the trigger threshold than on the amplitude resolution. It can be explained by the clusterization, which happens after digitization: the cluster energy resolution is more sensitive to the number of the digitized hits than to the precision of the ampli-

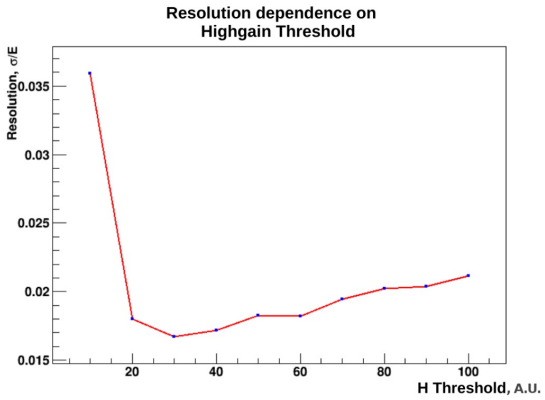

Figure 4.42: Gamma peak resolution as function of the threshold value.

tude determination. However, one has to consider the noise level before the threshold setup to avoid the noise digitization from the baseline oscillations. The final resolution of the gamma peak as a function of the trigger threshold is shown in Fig. 4.42.

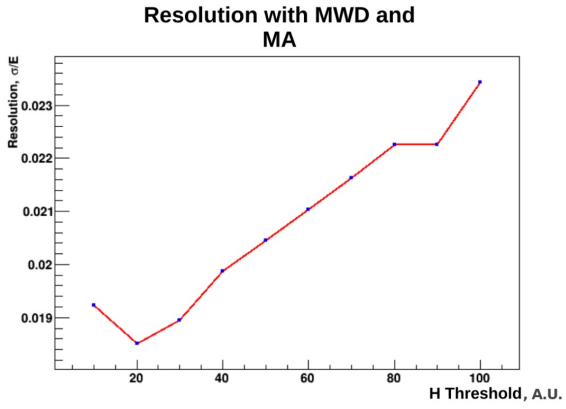

Figure 4.43: Gamma peak resolution as function of the threshold value in case of pileups.

After the finding optimal filter length, it was fixed to estimate the influence of different threshold values in a pileup scenario where the interaction rate is 500 kHz. The result of this is shown in Fig. 4.43. It implies that increasing the filter length is not always the optimal solution, and shorter pulses can lead to a better resolution. Hence, the pileup probability can be also reduced.

4.6 Front-end Electronics Boards

4.6.1 Forward Endcap EMC

In the EMC mainly APDs are used to detect the scintillation light of the crystal. Only in the Forward Endcap two types of photodetectors are used. The inner region at small angles is equipped with VPTTs because of the occurring high event rates, the outer region ($\theta \gtrapprox 12°$) is equipped with APDs as in the other parts of the EMC. To achieve an optimal signal to noise ratio one needs a high amplification as early as possible in the signal chain. The intrinsic gain of the APD can be set by an external bias voltage. In case of a gain of about 200 the relative change is $dM/dU \cdot 1/M \approx 7.6\,\%/\mathrm{V}$ [24]. To set the gain of the APDs with a precision of one percent, a voltage adjustment of $\sim 100\,\mathrm{mV}$ is needed. The gain of an APD may also suffer from radiation damage which makes a readjustment of the voltage necessary to keep the gain constant. Therefore a high voltage adjustment circuit (HV-adjustment-board) has been designed, based on an existing development for the CsI(Tl)-calorimeter of the CBELSA/TAPS-Experiment at ELSA (Bonn) [25]. It allows to adjust the voltage of each APD in a certain range relative to the according input voltage.

Due to the limited space available behind the base plate to which the detector modules are attached, the number of high voltage cables for each detector module was reduced to 4 (2) high voltage supply cables, for the 16 (8) crystals detector modules. For APD detector modules two APDs are attached to each crystal, so one cable supplies voltage to a set of 8 APDs. For VPTT detector modules one cable supplies voltage to 4 VPTTs. Since the gain dependance on the applied bias voltage is only $\sim 0.13\,\%/\mathrm{V}$ for the VPTT photodetectors, an individual voltage adjustment for each of the four VPTTs is not foreseen. Here a proper matching of the crystal (light yield), the preamplifier and the VPTT gain considering also the gain reduction depending on the magnetic field at the specific VPTT position has been performed to ensure a similar performance of the 4 different single crystals in a detector module supplied with the same voltage (see Sec. 3.2.4). For the VPTT detector modules only a PCB forwarding the input voltage to the four VPTTs is used.

Basic Principle Fig. 4.44 shows the schematic of the adjustment circuit. Basically it consists of a current sink, a transistor $Q1$ and a resistor R_S which is

connected to ground at the emitter of the transistor, and an additional resistor R_D.

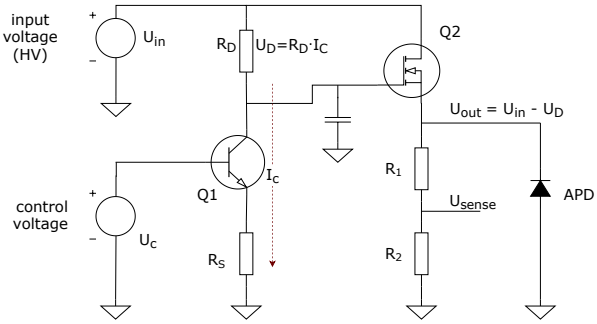

Figure 4.44: Basic schematic of the voltage regulation/adjustment circuit for the forward endcap APDs.

If the control voltage U_C at the base of the transistor $Q1$ is above $\sim 0.6\,V$ the emitter current I_E is given by

$$I_E = \frac{U_C - 0.6V}{R_S}$$

Under normal operating conditions the voltage at the collector ($\sim 400\,V$) is well above the control voltage (0.6 V to 3 V) so the transistor is in amplification mode and the current I_C is given by

$$I_C = h_{FE} \cdot I_B$$

The DC current gain h_{FE} of the selected transistor (PMBTA45) is typically in the order of 100 and the base current I_B in equation

$$I_E = I_B + I_C$$

is negligible and I_C becomes

$$I_C \simeq I_E$$

Thus the current I_C is defined by the emitter current I_E, which is created by the control voltage U_C, and causes a voltage drop U_D across the resistor R_D. Due to the fact that the current is independent of the collector voltage U_{in}, the output voltage becomes:

$$U_{out} = U_{in} - U_D$$

The output voltage U_{out} is then tapped at the collector by a high impedance voltage follower configuration to deliver the output voltage for the next stage, which is fed to the APD and an additional high impedance voltage divider, which will create a sense voltage for an ADC to allow monitoring of the output voltage U_{out}.

The behavior of this high side series regulator circuit was investigated by an LTSpice simulation. Its

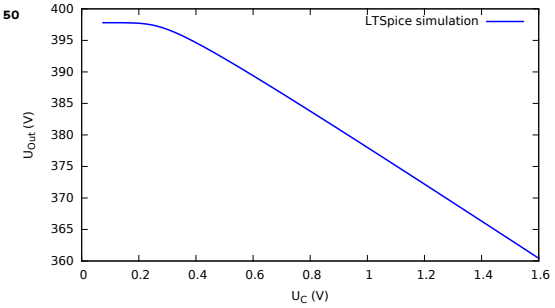

Figure 4.45: LTSpice simulation of the linear HV series regulator output in dependence of the control voltage applied to the current-sinking BJT $Q1$ and values for R_D =10 MΩ and R_S =330 kΩ.

Table 4.4: Component selection of the HV series regulator for the three different EMC parts. The resistors R_D and R_S are matched to the different requirements for the number of APDs supplied by one common HV line and the total allowable spread in APD bias voltages of the connected APDs resulting in different total regulation ranges.

	R_D (MΩ)	R_S (kΩ)	Regulation Range $U_{Out}^{max} - U_{Out}^{min}$ (V)
Barrel EMC	10	330	35
FEC EMC	4.7	820	14
BWEC EMC	100	820	450

result, the output voltage U_{out} in dependence of the control voltage U_C is shown in Fig. 4.45 for an input voltage $U_{in} = 400\,V$. A saturation of the output voltage is observed at low control voltages of $U_C < 0.25\,V$ due to the base-emitter threshold voltage of the current controlling BJT $Q1$. Note that the component values for R_S and R_D determine slope and intercept of this characteristics and were chosen differently in the specific hardware implementations of the three EMC parts. Table 4.4 details the coresponding component selections and the resulting total regulation ranges.

Implementation The amount of change for the input high voltage is set by the control voltage U_C. Fig. 4.46 shows the structure of the voltage generation U_C for the FEC. U_C is mainly given by a voltage divider of an Inter-Integrated Circuit (I^2C) controlled potentiometer with 256 taps (U_p) from a 3 V precision voltage source. The diode D1 is located very close to the transistor Q1 (Fig. 4.44) in the layout of the PCB and it is forward biased in

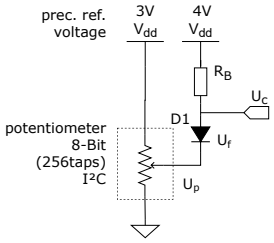

Figure 4.46: Schematic of the circuit for generating the control voltage U_C for the current sink in the FEC.

series with a resistor R_f from an additional precision voltage source, which needs to have at least 3 V plus U_f of D1. The forward voltage of the diode has a very similar temperature dependence to the base-emitter-voltage of the transistor. The control voltage U_C is now the sum of U_p and the forward voltage U_f, which will compensate the temperature dependence of the base-emitter-voltage of the transistor. Tests showed that the remaining temperature coefficient of the output voltage U_{out} is ~6 mV/K.

Fig. 4.47 summarizes the different blocks implemented on the PCB. It is foreseen to monitor not

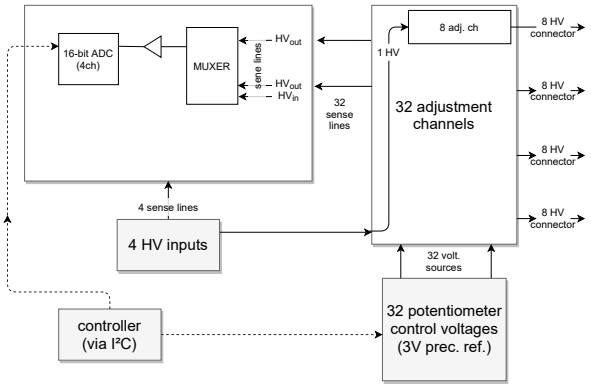

Figure 4.47: Composition of the HV adjustment board for the FWEC APD bias supply.

only the output voltages, but in addition the input high voltages U_{in} are measured. This results in total 32+4 sense lines. These 32 output voltages U_{out} and 4 input voltages U_{in} are routed to five 8-channel analog multiplexers, whose output channel is fed via a buffer and a passive filter into a 16-bit ADC (ADS1115). This ADC has the option to measure the input voltage single ended (versus ground) or differentially to another channel of the ADC and the range of the input can be set in a range from ±0.256 V to ±4.096 V by an internal programmable amplifier. The two 3 V reference voltages (each reference voltage feeds four potentiometer chips) are in addition directly fed to each ADC. By measuring differentially to the scaled down reference voltage one can decrease the input range and this will lead to lower LSB-size, which will minimize the digitization error.

As described in section 5.2, the detector modules are mounted on the base plate. Behind this base plate a usable volume with a height of only 33 mm (see Fig. 4.66 of Sec. 4.7.2) is available. To incorparate the adjustment circuits between the input high voltage lines and the submodule it needs to be placed close to the submodule. A stack of the PCBs onto the patch panel (Sec. 4.7.2) was chosen for optimal usage of the limited space available. This will give a constraint on the shape of the PCB

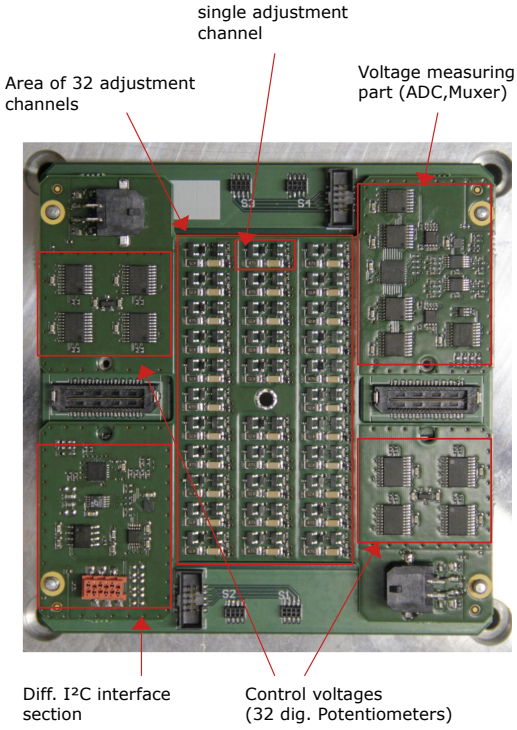

Figure 4.48: HV adjustment board for the FWEC APD bias supply.

and will result in a possible area to incorporate the adjustment circuit and the voltage measurement of ~ 77 cm^2. Fig. 4.49 shows the stack of the patch panel and the HV-board. The different sections and their places on the board are depicted in Fig. 4.48. The biggest area is the central part of the PCB and it is used for the current sink circuits. The top left and bottom right corners of the PCB contain the potentiometers. The remaining two corners contain the I^{2}C interface and the measurement cir-

cuits. Due to the space limitation only voltage but no current measurements are performed in the FEC.

In the design of the PCB, attention has been paid to ensuring that the output voltage picks up as little noise as possible from the I^2C logic signals. The routing of all high voltages, sense voltages and logic signals is distributed over 10 layers, dedicating single layers to one type of trace. To achieve a good separation of the I^2C control lines (data and clock) from the sensitive high voltage lines they are separated by ground layers or power planes to achieve a good separation. Tests showed no visible cross talk of I^2C signals on the analog output signals of the APDs during intense access on the I^2C bus. In addition, the thickness of the board was chosen to be 2 mm to provide the needed stiffness to cope with the mechanical stress on the board due to the cables, while mounting the PCB to the base plate. Fig. 4.49 shows the complete stack of patch panel

Figure 4.49: Test assembly of one detector submodule attached to a small base plate with a HV adjustment board and a patch panel together with signal cables.

and HV-adjustment board mounted on a test base plate cutout to prove the mountability of boards and cables.

Radiation Tests The HV-adjustment boards are located in forward direction, where the radiation dose is significantly higher than in the barrel or backward part of the EMC. To ensure a proper working of the HV-adjustment board, radiation tests were performed at the ^{60}Co-Source of Universität Gießen. The boards were irradiated under operating conditions; the supply voltage was switched on and all channels were operated under high voltage (~ 370 V). The tests were performed with a dose rate of 7.6 Sv/h and an integral dose of 300 Sv was applied. The aim was to investigate whether the components function as expected in the radiation environment and after applying the integral dose. There are two groups of components to consider. One part consists of digital components, which control the adjustment circuit. The other part consists of analog components (transistors, MOSFETs), which adjust the output voltage.

During the irradiation, control over all digital components (I^2C-Switch, I^2C-potentiometer, I^2C-ADC, I^2C-MUXER) was always kept, but an issue regarding the power consumption of these parts was observed. The total current of the supply voltage is ~ 8 mA. During the tests, at an integral dose of about 120 Sv this current started to rise strongly up to ~ 40 mA at the end. As components, causing this major increase, the selected analog multiplexers were identified. For future tests they were replaced by a different type (TMUX1108).

Also the analog part did show some change during irradiation. The transistor is expected to change its parameters due to radiation damage. This results in some drift on the output voltages. A drift of up to ~ 5 V (for an adjustment range of $\sim$40 V) on the output voltages after an integral radiation dose of 300 Sv was observed. Such changes can be compensated by adjusting the HV via the HV-adjustment board, controlling its potentiometers by the controller board.

Controller Board For controlling and monitoring the high voltage boards a controller board has been designed, which serves as a bridge between the DCS and the HV-adjustment boards. The controller board is equipped with a microcontroller (AT90CAN64), which provides an I^2C, a USART- and a CAN-interface. The HV-adjustment boards are connected by differential I^2C to send I^2C commands over a large cable length of up to 3 m and to provide a signal transmission which is less sensitive to electromagnetic interference (EMI). Apart from the differential I^2C signals the cable carries the power lines ($+5$ V) for powering the digital and controlling part of the HV-adjustment boards. The readout data from the controller board is transmitted via CAN to the DCS of the experiment. Furthermore, a serial interface (USART) has also been implemented for easy usage in laboratory or testing environments. For this purpose, a set of SCPI commands was implemented to provide easier access to control the HV-adjustment boards. Up to 16 boards

can be connected to one controller board. Thus, 13 controller boards are required for the entire forward endcap.

4.6.2 Barrel EMC

The four differential output signals per front-end unit (APFEL Rigid-Flex-PCB) are transferred via a 20 cm flex cable through the thermal insulation into the support beam where the Backplane Electronics Board (BPL) are located. Each BPL receives signals from four Front-End ASICs, passes signals for adjusting FE parameters upstream and provides individual adjustments of the APD bias voltages as well as voltage and current monitoring. Currently, two options of signal handling/processing and digitization are foreseen which shape the layout of the BPL units differently. These two options, one with the signal digitization on-board of the BPL, and one with digitization through SADCs located outside of the detector are described in detail in the following sections. The former is considered the default option with the latter as a back-up solution in case technical obstacles appear during the development and evaluation of the HDA final prototype, which is currently not concluded.

4.6.2.1 On-Detector Digitization with the HDA

The BPL units will provide an on-board digitization of sixteen differential analog front-end signals (four crystals per BPL × two APDs per crystal × two different gain outputs per APD channel) with the custom HDA developed specifically for this purpose. The BPL units consist of three layers of electronics boards interconnected by high density board-to-board connectors to a ruggedized triple sandwich block. The bottommost PCB carries the FE ASIC flex connector receptacles, voltage regulators for the front-end electronics (FEE), the HDA digitizer and sensors for environmental monitoring. The topmost PCB contains electronics for the regulation of the individual bias voltages of 8 APDs, one auxiliary custom-made ASIC refered to as Serial Adapter ASIC (SAA) providing several functions to adjust and measure the HV regulator electronics, such as e.g. eight digital-to-analog converters (DACs) and an I^2C master interface. The SAA was designed in a radiation-tolerant submicron process, produced in frame of a Multi-Project-Wafer (MPW) prototyping run, extensively tested and after two iterations finally qualified for the utilization in the PANDA EMC without restrictions. The middle-layer PCB contains connectors for the serial data link to/from the Application Specific Integrated Circuit (ASIC) as well as a voltage regulator and voltage buffering for the BPL on-board electronics. The serial links are organized as cable-assemblies containing eight individually shielded differential pairs terminated through a SAMTEC FireFly connector. With one BPL unit connecting to the DAQ with one of these 8-fold cables, one Barrel EMC slice exhibits 180 data cables routed towards the upstream end of the slice unit to the cable window feedthrough. The serial links from the BPL units (180 per slice segment) are connected to multiplexer boards which are located in upstream direction inside the crates which are foreseen for the SADCs instead in the backup SADC-readout solution. These boards provide 64 front-end-side FireFly connectors, one for each BPL link. The upstream links are implemented through up to four high speed optical Versatile Links which serialize the input data streams. Three of such multiplexer boards are required for the read-out of one slice segment, 48 boards are needed for the entire barrel EMC.

4.6.2.2 Analog Signal Transmission and Off-Detector Digitization (SADC-Option)

The design of the BPL units in case of the backup SADC readout option is slightly different for the signal conditioning and transmission stage as well as for the control interface towards the APFEL FE. The sixteen differential analog signals coming from the APFEL ASICs are, unlike the HDA default option, not fed into an on-board digitizer but driven by a differential buffer (ADA4940) into 16 individually shielded differential 100 Ω cables. The BPL PCB for this readout option is depicted in Fig. 4.50. For this end, the same cable assemblies can be utilized, which are foreseen for the transmission of the HDA digital output links in the default scenario (Sec. 4.6.2.1), but with twice as many cables (16 pairs coresponding to two cables vs. 8 pairs coresponding to one cable per BPL). However, the serial peripheral interface (SPI) bus controlling the SAA and the HV regulators which is provided by the HDA periphery in the default option would not be available and must be fed in externally. Thus, another four differential pairs must be included in the off-detector cabling. The slow-control interface to the APFEL FEs is controlled by the SAA (in opposite to the APFEL interface of the HDA in the default case).

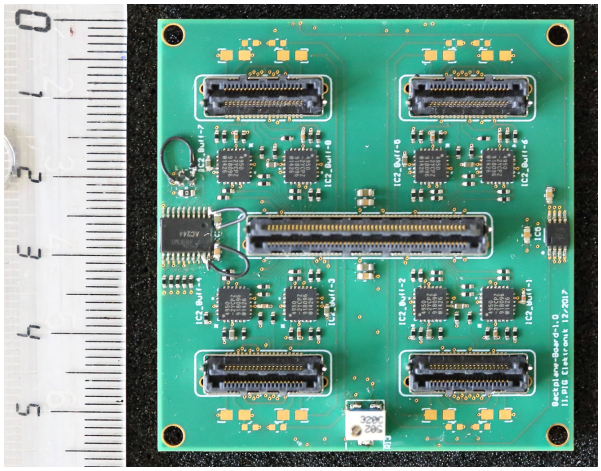

Figure 4.50: BPL buffer board exhibiting connector receptacles for four APFEL ASIC FEs at the edges, eight differential line drivers as well as low-noise voltage regulators (bottom side of the PCB - not shown in this photograph) and logic buffers. The high-density SAMTEC connector in the center of the PCB interfaces up to the middle-layer PCB of the triple-board sandwich.

4.6.2.3 HV Control Board

On each barrel BPL, a total of eight APDs are controlled to guarantee stable operation of the photo sensors. Specifically, the stability of the bias voltage vs. temperature and time is crucial. The linear high voltage high side series regulator, as explained above, is utilized for a single channel to adjust the APD bias voltage for each channel from a common raw high voltage fed into the BPL unit. Each HV regulator is individually controlled via the adjustable current sink formed by the BJT. The BJT's base voltage is supplied by one (out of eight in total) 10-bit DACs of the SAA. The latter interfaces via an on-board SPI bus either to a connector on the interface PCB unit (middle PCB of the BPL sandwich) in case of the SADC readout option or to the HDA ASIC sitting at the digitizer PCB (bottommost PCB of the BPL sandwich), which posseses an SPI master interface for this purpose. The top-layer PCB of the triple readout board sandwich responsible for the HV regulation is shown in Fig. 4.51. Note that the Samtec board-to-board connector interfacing downwards to the middle-layer PCB of the sandwich is mounted on the bottom side of the PCB and therefore not shown in the photograph. The raw HV is provided through the MCX connector on the right-hand side of the PCB. The eight independent regulated bias voltages are routed through the sandwich down to the bottommost BPL PCB where they are supplied to the APFEL FE flex boards.

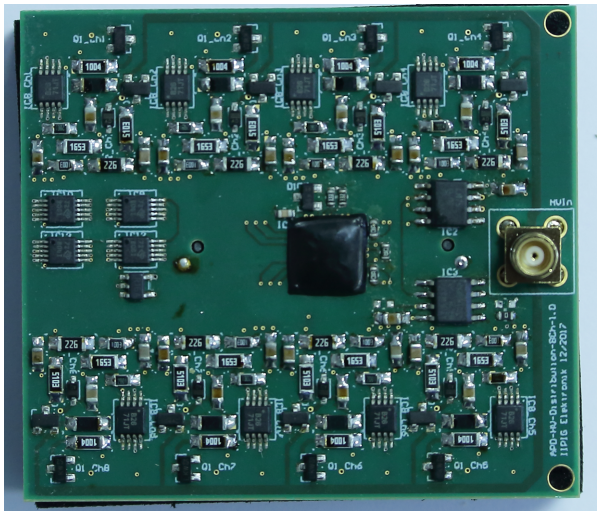

Figure 4.51: High voltage regulation PCB as part of one backplane triple-sandwich unit for the read-out of four crystals. The eight channels contain the HV series regulator, voltage dividers, ADCs for voltage and current monitoring and the SAA ASIC (center of the PCB, covered with a protective coating) providing the eight DAC outputs for the voltage adjustment. The high-density SAMTEC connector in the center of the PCB's bottom side (not visible) interfaces downwards to the middle-layer PCB of the triple-board sandwich.

The simulated and measured response of one HV regulator channel is presented in Fig. 4.52 for an input voltage of $U_{in} = 400\,\mathrm{V}$ for the entire range of settings of the SAA on-board DAC. The mismatch of the curves between simulation and the measurement done with the on-board ADC is attributed to production variations of the mounted resistor R_S which diminishes the available regulation range slightly. Assuming a spread of 10 % in regulation range between boards, a safe range selection of 35 V shall guarantee that the operating points of all eight connected APDs can be adjusted with a safety margin of at least 5 V within the regulation limits.

Prototyping for the HV regulation of the barrel part of the EMC was done by producing several protoype boards with increasing complexity, channel count and functionality. The electronics utilizes the adjustment circuit scheme of Fig. 4.44. In addition to the voltage measurement, the circuit provides the individual APD current measurements. The prototypes consisted of scaled-down 4- and 8-channel versions of the final electronics as shown in

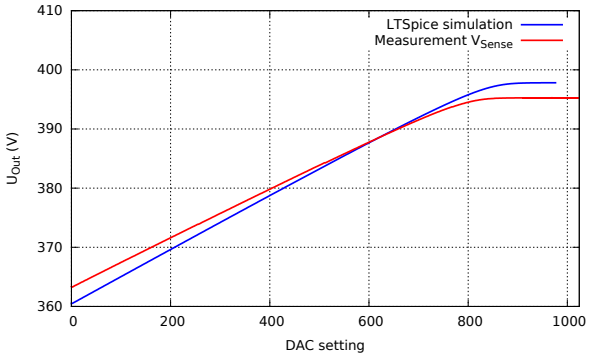

Figure 4.52: Simulated and measured regulation behavior for one channel of the HV regulator at 400 V input voltage over the full SAA on-board DAC range.

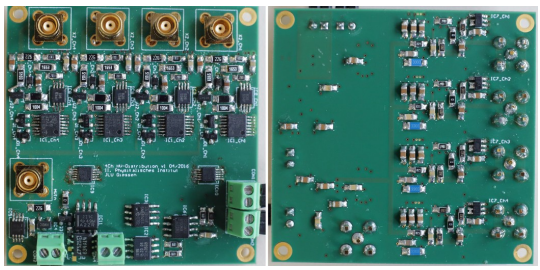

Figure 4.53: Fully mounted 4-channel prototype of the HV regulation electronics, with the raw HV input and four regulated HV channel outputs.

figures Fig. 4.51, Fig. 4.50 and Fig. 4.53. Additional temperature and humidity sensors are mounted on the final PCBs. Irradiation, temperature and time-dependence tests have been carried out with the 4-channel prototype, shown in Fig. 4.53.

The on-board measurement of the ADC were compared to external measurements with a Keithley 2410 sourcemeter. Fig. 4.54 and Fig. 4.55 indicate, that the ADCs of each channel have to be calibrated.

Temperature dependence The temperature dependence of the HV regulator alone was studied. The DAC was set to specific values while the temperature was altered from 25 °C to −25 °C and back in a climate cabinet. The output voltage was observed using the on-board ADC. In Fig. 4.56 the resulting temperature dependence can be estimated to 0.08. . . 0.1 V/°C independent of the DAC setting.

Radiation tests have been performed for proton, neutron and γ radiation. The measurements were conducted by comparing the characteristics of four reference APDs before and after irradiation of the

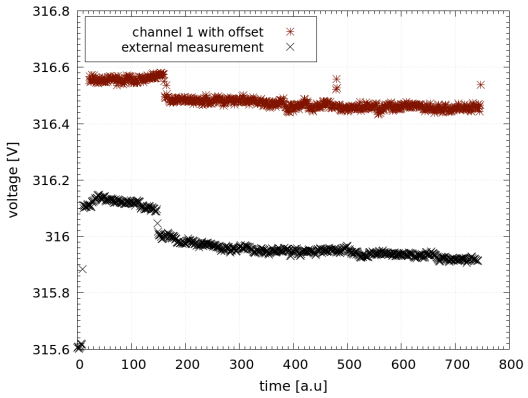

Figure 4.54: Comparison between on-board ADC measurement and external measurement. The general behavior is comparable while some minor deviations occur due to a delay between measurements. The measurement series spans a 60-minute time frame.

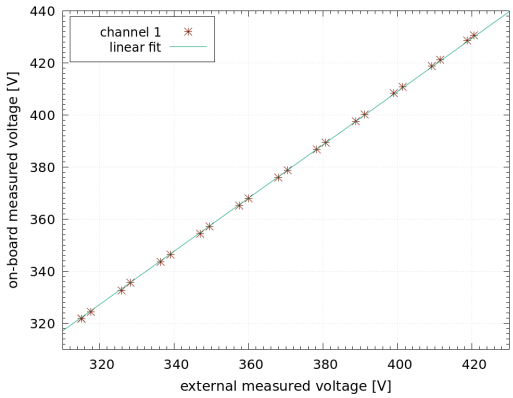

Figure 4.55: Direct comparison between on-board ADC measurement and external measurement of one channel at a full-range sweep of the adjustment DAC.

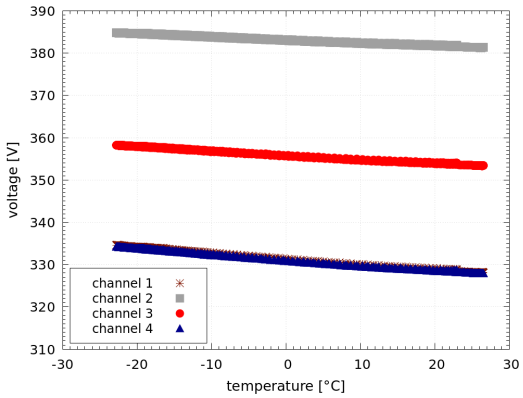

Figure 4.56: Temperature dependence of four channels of the HV regulation electronics. Each channel was kept at a specific DAC setting and the temperature was altered from 25 °C to −25 °C.

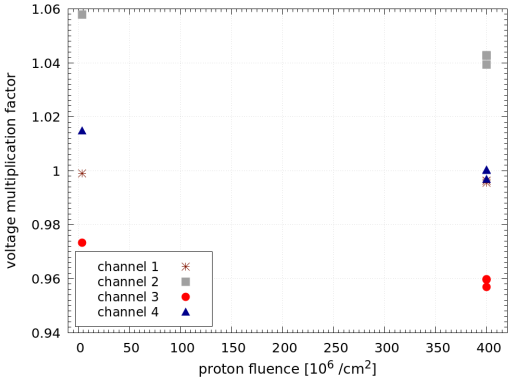

Figure 4.57: Development of the voltage correction factor in dependence of 190 MeV proton fluence.

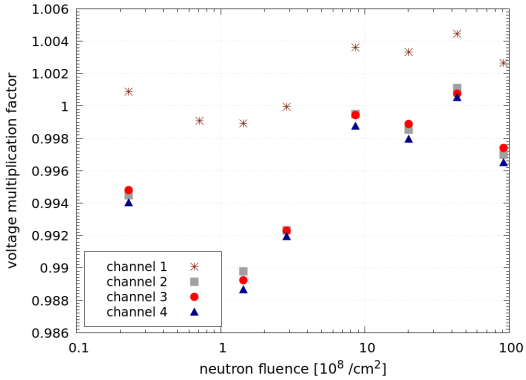

Figure 4.58: Development of the voltage correction factor in dependence of the neutron fluence. Changes are well below 2 %.

PCB using the on-board ADC for current and voltage measurements. To determine the resulting offset and transformation factors, the measured characteristics of the reference APDs were stretched and shifted to match the preirradiated measurements. Thus resulting in two multiplication and two offset coefficients, further details on methology and results can be found in [26]. Thermal annealing was undertaken by heating up the irradiated PCBs to 80 °C for 10 to 12 hours. To study the effect of proton radiation, an exposure with 190 MeV protons was done at the **A**ccélérateur **G**roningen-**Or**say (AGOR) accelerator at KVI/CART (Groningen, Netherlands) with fluences from 4×10^6 p/cm^2 to 4×10^8 p/cm^2 with the 4-channel prototype. The results indicate a shift of the voltage scaling factor within 2 % (Fig. 4.57).

To study the effect of low energetic neutrons a Am-Be neutron source was utilized resulting in an integrated neutron fluence of $2.9 \cdot 10^{10}$ neutrons per cm^2. Fig. 4.58 indicates that low energetic neutrons have little impact on the accuracy of the voltage measurement.

The $\gamma-$irradiation measurements were conducted using a ^{60}Co source at the radiation facility of JLU Giessen (Germany). The influence of an exposure with a total ionizing dose with up to 1000 Gy was studied and results are shown in Fig. 4.59. The results indicate, that below an integrated dose of 150 Gy the changes are less than 3 %. For the barrel EMC the maximum dose for the crystals is expected to be 7 Gy annualy [3].

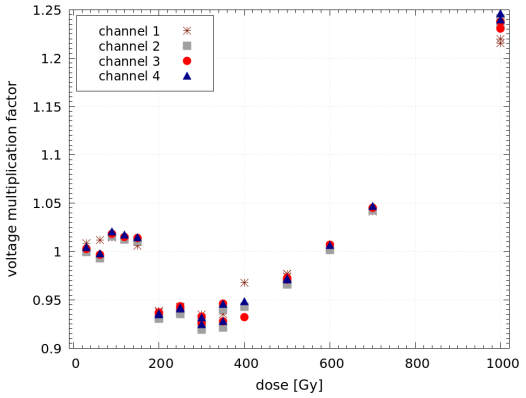

Figure 4.59: Development of the voltage correction factor in dependence of the integrated dose of accumulated γ-radiation.

4.6.3 Backward Endcap EMC

As for the other parts of the EMC and in particular the barrel where the APFEL preamplifier is used, the following electronic services need to be provided for the BWEC by the front-end electronics, situated at the detector:

- readout of the analog output signal from the APFEL,
- power supply and communication for the APFEL,
- HV distribution and control for the APDs,
- four-wire readout of the Pt100 temperature sensors.

In order to have a solution for these tasks, which is suited to the geometrical details of the BWEC (described in Sec. 5.3), specific front-end boards had to be developed independently from the other parts of the EMC. An important aspect to be considered is that the services mentioned above need to be fed

from the outside into the inside of the detector volume, which is cooled at −25 °C. The only outer surface of the BWEC which is available for feeding in the services is the back (upstream) side, i.e. through the mounting plate, which is oriented perpendicularly to the beam direction. Roughly, only the surface covered by the crystals in the transverse plane is available for the service connections.

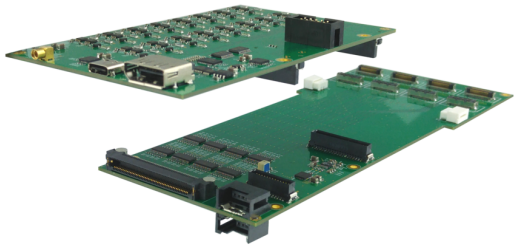

Figure 4.60: BWEC front-end boards.

To minimise the number of connectors involved in the analog signal readout, the solution of a feed-through PCB has been adopted. All connections are passed into the cold volume through these boards, which are air-tightly glued to the aluminum elements connecting the submodules to the mounting plate (Sec. 5.3).

The line driver for the APFEL signals, which need to be sent to the SADC boards over about 10 m of cable, are placed directly on this feed-through PCB, outside of the detector. Therefore, no extra heat source is introduced inside the cold volume.

Since the circuitry for the HV distribution and control requires some space on a PCB, a second board (also referred to as service PCB) has been developed and is stacked on top of the feed-through board outside of the detector volume and takes over the HV regulation and the connections for communication and temperature readout.

The two boards are shown together in Fig. 4.60 and will be described in more detail in the next subsections.

4.6.3.1 Line Driver Board

A picture of the feed-through board is shown in Fig. 4.61. It has an elongated form factor, because it needs to be passed through the mounting plate which has a thickness of 50 mm. The two different widths (visible in the picture) are also motivated by geometrical constraints. The APFEL connectors need to be aligned with the crystals, because of the stiffness of the APFEL board cables. On the other hand, the part traversing the aluminum mounting element needs to be narrower than the total submodule width, to be passed through.

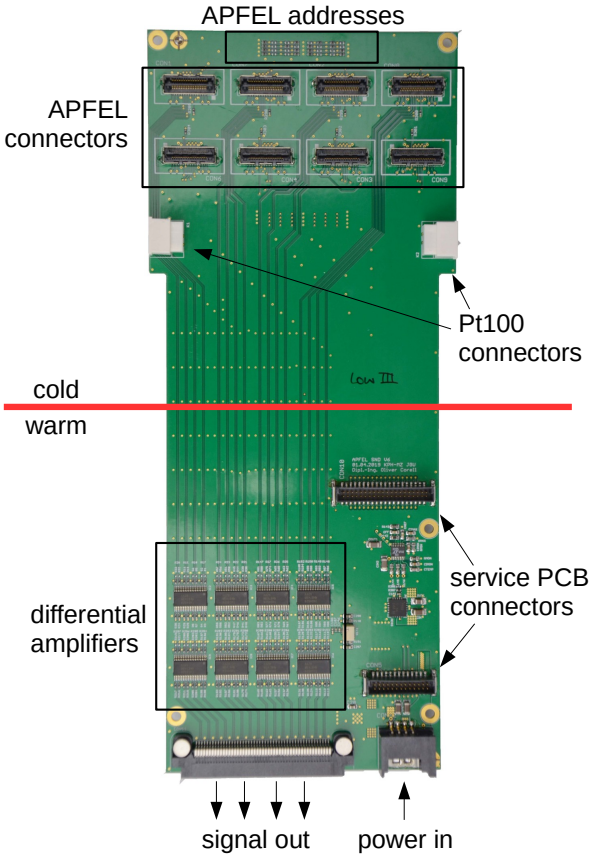

Figure 4.61: BWEC line driver feed-through board.

Inside the cold volume, only passive components are present. In total 8 APFEL boards can be connected to the line driver board. The resistors for coding the geographical addresses of the ASICs (see Sec. 4.1) are located close to the APFEL connectors. Finally, two FPC four-pin connectors for two flat Pt100 temperature sensors are available.

Outside the cold volume, the main components are the differential operational amplifier to boost the APFEL output signals for transmission over long cables. The chosen device, the THS4524 by Texas Instruments, is designed for low power consumption and has a bandwidth of 145 MHz. It has 4 channels and can drive all signals of one APFEL. Thus, there are 8 chips on the board.

The output signals of the amplifiers are accessible through a high density flat connector of type ERF8-

049 by Samtec.

The low voltage supply to both line driver and HV control board is provided through a mini-clamp socket by 3M with 4 contacts. A second socket of the same type is placed on the back of the line driver board, to allow for daisy-chaining the power supply. Three of the four pins are used to power both stacked boards with ±6 V. The fourth pin is used to bias the curing LEDs mounted on the APFEL boards. This way the complete supply circuit of the LEDs can be left open during detector operation.

The HV control board is connected to the line driver board through two board-to-board connectors by ERNI with 26 and 40 contacts, respectively. Through these connectors, the HV supply for the APDs and the control lines for the APFELs are provided. In addition, the four-wire connections from the temperature sensors and the power supply is passed to the service PCB.

The line driver board has been tested and its performance has been proven in prototype tests. In total 100 pieces have been produced at the time of writing. These are needed for mounting the submodules for the FAIR phase 0 endeavour in the first place, but will be also enough for the PANDA backward EMC.

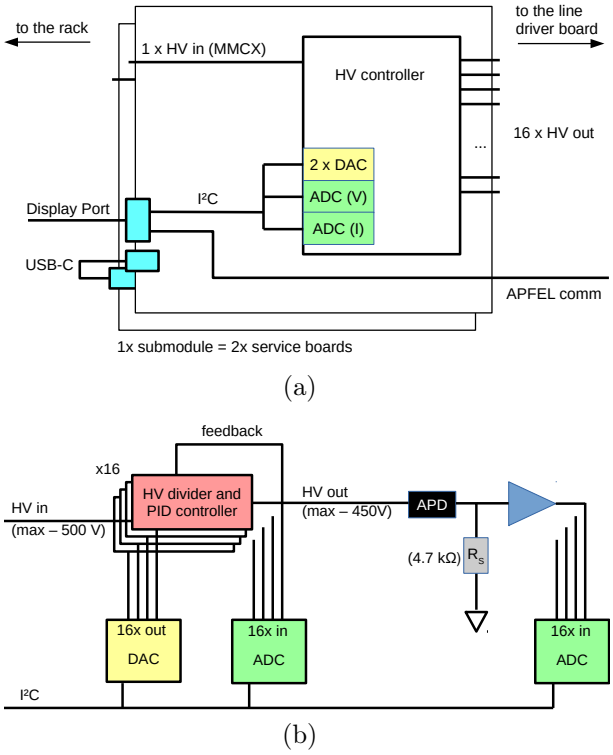

Figure 4.62: (a) Block diagram of the HV control board. (b) Block diagram of the HV controller units.

4.6.3.2 HV Control Board

The functionality of the HV control board and its requirements are the same as for the rest of the EMC and were described above. As for the case of the line drivers, a different development has been undertaken for accommodating the different geometrical constraints.

The functioning concept of the board is depicted as a block diagram in Fig. 4.62-(a). One input HV channel with 500 V is distributed to 16 identical control circuits, which singularly provide 16 APDs with a bias voltage between 0 V and 450 V. These voltages can be controlled via a 16-bit DAC. Output voltages and currents flowing through the APDs are digitised with two 24-bit ADCs. These three devices are controlled through an I^2C interface.

In the block diagram in Fig. 4.62-(b), the functioning idea of one voltage control unit is visualised. The high voltage adjustment occurs in a similar circuit as for the other calorimeter parts (see explanation in Sec. 4.6.1). In addition, the output voltage is fed back into an active proportional–integral–derivative controller, which sets the reference voltage for the adjustment unit. The circuitry for implementing this feature for all channels requires some space on the PCB (as can be seen in Fig. 4.63) and was possible for the BWEC, because of the available space for the front-end boards, which is larger than in the other EMC parts. At variance to the forward and barrel calorimeter, the shunt resistor (4.7 kΩ) for measuring the current is placed on the ground side of the APD.

Concerning the digital communication, the service PCB needs to provide an I^2C interface for the HV control and an APFEL interface, which is a three-wire channel similar to SPI, for the line driver PCB. In order to combine all communication interfaces, i.e. five differential lines, into one single connection for each submodule, and at the same time using a commercial solution, Display Port cables were chosen. Since two boards are used in one submodule, the communication lines are passed forward from the first board, where the Display Port is connected, to the second board through a USB-C cable.

The service PCB is shown in Fig. 4.63. On the left, the voltage control blocks are visible. The connectors for digital communication and HV input (MMCX connector) are placed at the bottom. The four-wire readout for the two Pt100 sensors from the line driver board happens through a box header

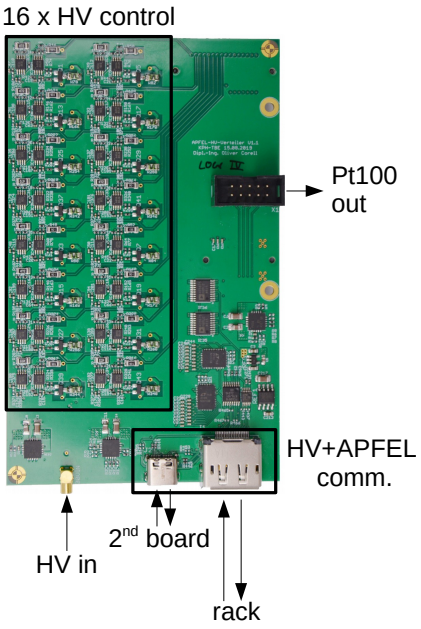

Figure 4.63: BWEC HV control or service PCB.

connector on the right of the picture.

First prototypes of the service PCB have been produced and tested for their basic functionality on a desk test bench. No tests with a prototype detector have been performed yet but are planned. As soon as these are successfully finished, the series production will be started.

4.7 Cables

4.7.1 Barrel EMC

For signal transmission from the BPLs out of the detector volume, 8-fold high-density individually shielded differential pair cables (SAMTEC AWG34 Micro Twinax) with a cross section of 1.4 mm^2 per pair are utilized (Fig. 4.64). The cables are

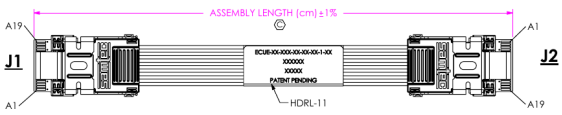

Figure 4.64: Assembly drawing of the SAMTEC ECUE 8 pair cable assembly featuring FireFly connectors [27].

factory-matched with the common FireFly connectors (ECUE family) in assemblies with lengths between 1.5 m and 3.5 m for the connection to the different parts along the slice module. An overview of the relevant technical parameters of the signal cables is given in Table 4.5.

Table 4.5: Specifications of the utilized SAMTEC AWG 34 Micro Twinax data cables (extracted from [28]).

Parameter	Value/Range
Cross section per differential pair	1.4 mm^2
Differential Impedance	100(10) Ω
Insertion loss 3 dB corner frequency	>2.7 GHz
Cross talk to closest pair (f<1 GHz)	<−70 dB

High voltage and low voltage supplies are fed into the barrel slice unit featuring identical cable deployments as in the case of the FW endcap detector. The overall cross section of the cabling for one entire slice module is presented in Table 4.6. Note, that the service feed-through (except cooling and gas services) at the upstream end of the slice support exhibits an aperture of approximately 13 000 mm^2. Low voltage supplies have to take varying voltage drops due to fluctuating power consumptions (6 W per BPL on average) of the BPL units into account. Therefore the cross section for these supply lines was chosen to avoid a voltage drop larger than the allowable voltage regulator drop and was assumed to not exceed 10 % of the nominal value of 6 V.

4.7.2 Forward Endcap EMC

At every submodule mounting position on the base plate, there is a hole to feed through the cables and optical fibers necessary to connect that submodule. The cables are kept as short as possible while maintaining the feasibility of the mounting procedure. On top of this hole a patch panel for distributing the low voltage and analog signal cables of the photodetectors and forwarding the sensor lines is mounted. Through the middle hole of the patch panel, the supply cables for high voltage are fed (see Fig. 4.65). These are attached to the HV-adjustment board from below and this board also serves as a locking for the connectors of the signal cables attached to the patch panel.

The available space for patch panels and cables between the rear side of the base plate and the back plate is only 33 mm, which is shown in Fig. 4.66.

This space must be available for both the adapter boards with connected cables as well as for parts of the air cooling system. In addition, optical fibers are connected to each submodule, which are inserted into the uninsulated volume. This means that there are about 8500 cables and over 15 400

Table 4.6: Cabling budget for one EMC barrel slice module.

Service	Cable Type	Cross Section (mm^2)	Number of Cables	Total Cross Section (mm^2)
High Voltage	H+S Enviroflex 178	2.66	180	609
Low Voltage	copper, flame ret. insulation	50	4	256
Serial Links	AWG34 Micro Twinax bundles (8 pairs)	11.1	180	1998
				2863

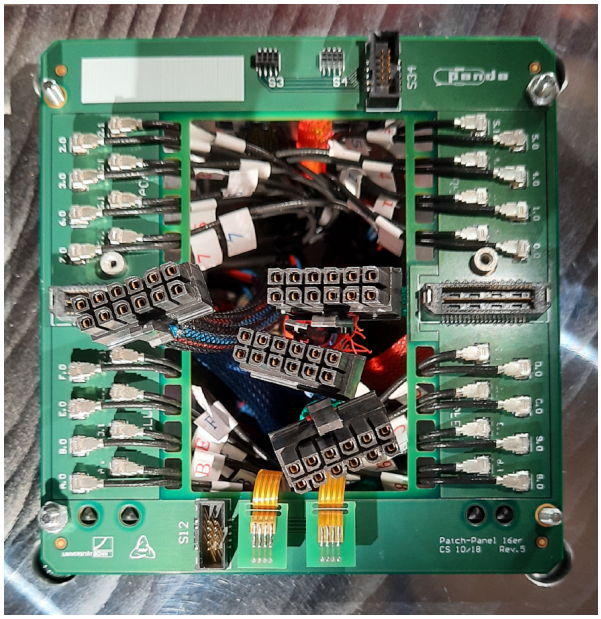

Figure 4.65: Patch panel to adapt the cables from the submodule to the cables leading from inside the cold volume to the outside.

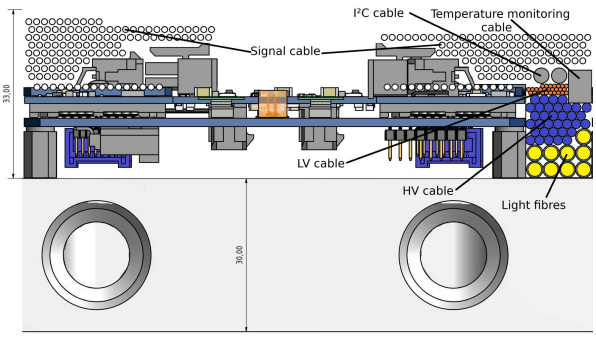

Figure 4.66: Sectional view of wiring harness number 5 shortly before the cable passage guide on the edge of the base plate. An adapter board and a part of the base plate with visible holes is also shown. [29]

optical fibres on the back of the base plate. A detailed routing scheme is necessary to use the available space for all cables and optical fibres to the outside and at the same time to realize the shortest possible cable routes.

The cables used can be found in Table 4.7

Table 4.7: Cable types and number on the base plate per submodule. [29]

Intended use	cable type	VPTT Xtal # per submodule		APD Xtal # per submodule	
		8	16	8	16
Signal cable	Nexans Filotex® 50 VMTX	8	16	16	32
HV cable	Huber+Suhner® Enviroflex	2	4	2	4
LV cable	Kabeltronik UL AWM Style 11027 AWG28/7 FRNC	3	3	3	3
Sensor cable	ribbon cable with 0.5 mm pitch	1	1	1	1
Fiber optic cable	UV 200/220 P28 CeramOptec	32	64	32	64
I^2C	RS Pro ribbon cable twisted AWG 28 grid 1,27(preliminary)	1	1	1	1

The cable routing for HV, LV, optical fibers, sensor cables and signal cables is the same on the base plate, only after being carried out on the frame of the base plate the routing is individually different depending on the cable type. Fig. 4.67 shows the naming scheme of the SADC crates the routing on the base plate and the routing of the signal cables.

6944 signal cables (without spare) lead from the adapter boards to the respective SADCs. The SADC boards are located in racks. There are two different types of racks. Racks with six SADC boards and those that hold 15 boards. Due to the space available within the support frame, the crates with 6 boards are on the top of the frame and the crates with 15 boards are on the side of the frame. Each SADC has 32 channels to read out the photodetectors. A total of twelve crates with 6 boards and ten crates with 15 boards are installed. This leaves 160 SADC channels unoccupied, which corresponds to five spare boards. In order to obtain a clear assignment of SADCs to their respective crates, the SADC crates are numbered consecutively. The numbering is divided into side a and side b and starts at the top of the forward endcap. The top crate with 6 boards on side a is designated Ca1. Subsequently clockwise the second crate is marked Ca2 and so on. On side b the numbering is analogous. Here the top crate with 6 boards is

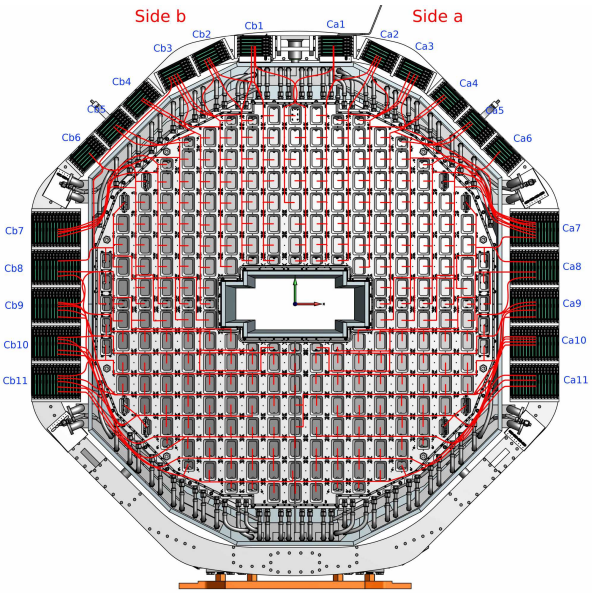

Figure 4.67: Cable routing of the signal cables to the SADCs. [29]

marked Cb1 and counter-clockwise the second crate is marked Cb2 and so on. The routing of the signal cables to the SADCs takes into account that the APDs sitting on one crystal each are connected to different SADCs so that whole channels do not fail if one SADC fails. In addition, the distribution of the VPTTs among the SADCs is as evenly distributed as possible, so that ideally half of the VPTTs are located at inner regions with high rates and outer regions with low rates. Furthermore, only photodetectors of one type are connected per SADC. The assignment scheme is explained in [29].

4.7.3 Backward Endcap EMC

Signal

Because the particular geometrical situation of the BWEC differs from the other parts of the EMC, special solutions for the connections to the detector are needed.

The analog signals from the APFEL preamplifiers are boosted by the FE boards as described in Sec. 4.6.3 and need to be transmitted to the SADC boards, which are situated outside of the spectrometer magnet. The cable length is 10 m.

In order to avoid any transmission interference but at the same time minimize the total cross section of the cables which need to be fed into the spectrometer, a non-standard cable type has been chosen. It is produced by the company Bedea Berkenhoff & Drebes GmbH and it features four singularly shielded twisted pairs. The total outer diameter of the cable including insulation is 3.3 mm.

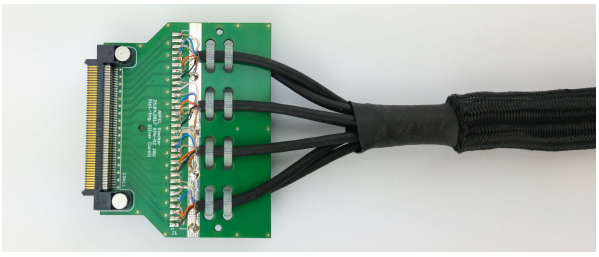

Figure 4.68: BWEC signal cable adapter board.

Since each APFEL has four output channels, one cable per crystal is needed. Therefore, eight cables are needed for one line driver board. These are bundled together within a cable sleeve and the wires are soldered to special adapter boards, which were designed in Mainz. One assembled adapter board with the associated cable bundle is shown in Fig. 4.68. When used, the board is protected by a 3D-printed plastic case.

Communication

Digital communication lines are needed for controlling the APFEL preamplifiers and the HV adjustment. The former works with a three-wires connection similar to SPI, whereas the letter uses the I^2C protocol. Like for the analog signals, this communication lines need to be transmitted to the outside of the detector over 10 m of cable. Therefore a differential transmission with shielded wires is needed. As solution, commercial Display Port cables where adopted, since they contain five differential lines (three for the APFEL communication and two for I^2C). One cable for every 16 crystals is needed, which gives a total of about 30 cables for the whole BWEC.

High Voltage

The HV supply is brought into the detector with 10 m long cables equipped with 51-pin connectors of the S series by REDEL, which was developed for the ATLAS experiment. The cables are quite thick, they have a diameter 13 mm, but each of them provides 16 channels. Thanks to the HV distribution boards described in Sec. 4.6.3.2, only two HV channels from the power supply are needed for each 16-crystal submodule. Therefore, the full detector can be supplied with only four cables.

Other Electrical Connections

Yet to be defined — although uncritical for the detector functioning — are the cables for the low voltage power supply and the temperature readout. The FE boards can be daisy-chained as far as the power supply is concerned. As a consequence, the number of low voltage cables going into the detector will be quite small.

For the temperature readout, around 100 four-wire connections need to be provided. Standard cables and connectors will be used for this purpose.

Light Fibers

One light fiber per crystal needs to be fed into the BWEC. Quartz fibers of 800 µm core diameter are intended to be used for the PANDA experiment (whereas plastic fibers with 1 mm core will be used during the phase 0). They are tied in bundles of 16 fibers each and glued to customized multi-fiber connectors, each of which is connected to one submodule (see Sec. 5.3).

4.8 Detector Control System

4.8.1 Introduction

The PANDA Detector Control System (DCS) has the purpose to monitor and control all the experimental equipment of the PANDA detector. It shall ensure the safe and efficient operation of the PANDA experiment and contribute to the collection of high-quality data[30, 31].

The PANDA DCS consists of the individual DCS partition of each PANDA subsystem and the supervisory layer that is common to all PANDA subsystems. The supervisory layer with the control room Graphical User Interface (GUI) as well as the archive and alarm systems is described in detail in the DCS TDR [30], so this is not repeated here. This document will focus on the DCS partition of the EMC.

The main software used for building the DCS is the Experimental Physics and Industrial Control System (EPICS)[1]. EPICS is used by accelerator centers and physics experiments all around the world and therefore has a large user base, an active development community, and it is proven to work properly[32]. An EPICS-based control system follows a distributed architecture, so there will be many (small) computers running EPICS instead of a large device being a single point of failure. The distributed nature of EPICS and its efficient use of memory and network bandwidth also imply that an EPICS-based DCS is highly scalable.

EPICS is not a monolithic application, but it is a tool set to create an individual control system for a specific detector or accelerator. EPICS has a distributed architecture centered around process variables. "A Process Variable (PV) is a named piece of data associated with the machine (e. g. status, readback, setpoint, parameter)." [32] Every PV has a defined set of attributes like value, timestamp or alarm status. EPICS uses a client/server architecture, with the addition that every server can also act as a client and connect to another server. In the context of EPICS, there are several kinds of servers like Input/Output Controllers (IOCs) and Channel Access (CA) Gateways [33].

4.8.2 Network Structure

The EMC partition of the DCS will have its own subnet within the PANDA experiment IT infrastructure. This subnet will be connected via two gateway computers to other subnets, including the supervisory DCS. The reason for having two gateways is redundancy: One gateway will be the main gateway and the other one is the backup one, ready to jump in immediately if the main gateway should fail.

The EMC subnet connects all devices running EPICS IOCs that monitor and control the equipment of the EMC. Inside this subnet, all PVs of the EMC can be accessed. To allow access from outside the subnet, the gateway computers run a CA gateway, which has an access control list that determines which PVs can be accessed, by whom, and how (read-only or read-write).

Some PVs that refer to expert-only settings will not be available at all from outside the EMC subnet to prevent potentially dangerous changes to these values. The experts responsible for the EMC can log into the EMC gateway via Secure Shell (SSH) and change these parameters from there.

This means that a list of users that have the authority to make such changes to the DCS of the EMC has to be assembled and maintained. Most probably there will be a central user account management within PANDA, so the access rules for the EMC can build upon this and just define a subset of all PANDA accounts to be given permission to access the EMC internal systems. In addition, security techniques like public-key authentication, 2-factor authentication (2FA), and virtual private

1. https://epics-controls.org

networks (VPNs) will be used to prevent unauthorized persons from accessing these systems.

4.8.3 Computing Hardware

In contrast to the DAQ, the DCS has only moderate requirements for computing power. The gateway computers mentioned in Sec. 4.8.2 will therefore be normal, off-the-shelf server hardware. This applies also to other computers that may be necessary for the DCS of the EMC.

In addition, single-board computers like the Raspberry Pi[2] have been widely used during the development of the PANDA EMC [31]. They are also readily available off-the-shelf and their use so far has proven that they have enough computing power to run EPICS and other DCS-related applications.

Nevertheless, there is an issue regarding computers that still requires attention: Operating computers in the radiation environment close to the detector. High-energetic particles like photons can induce bit-flips in the memory or the registers of the processor of a computer which can cause applications and operating systems to perform irregular actions or crash. The solution to this problem is the use of hardware that has been specifically designed to run in radiation environments and thus contains logic to detect and correct such memory errors.

Such hardware is commercially available due to its necessity in the context of autonomous space crafts. There are projects like [34] within FAIR to create a radiation-hard single-board computer similar to the Raspberry Pi, but this hardware is not yet available at the time of writing.

The HV regulation of the APDs (see Sec. 4.6.1) is one example for a component of the EMC where the computer controlling it has to be mounted close to the detector. Other hardware like the HV and LV power supplies will be mounted in a remote location without increased radiation levels, so ordinary hardware can be used to control them.

4.8.4 High Voltage Power Supplies

The EMC uses HV power supplies made by iseg Spezialelektronik GmbH, Radeberg, Germany[3]. Their products follow a modular approach: One crate can host modules with different voltage ranges, measurement precisions and polarities. The individual modules are controlled via the Controller Area Network (CAN) bus and a custom CAN protocol developed by iseg.

iseg offers a dedicated software that communicates with their modules via the CAN bus and is optimized for a minimal latency. There is a device support for EPICS developed within PANDA that connects said iseg software with EPICS. Recent crates from iseg even contain an embedded PC that runs said iseg software and EPICS including the device support, so that only a network cable needs to be connected to integrate such a crate into the DCS. These crates mark an example for the successful cooperation between the PANDA Collaboration and the industry.

The PANDA EMC needs HV to operate the photo detectors (see Chap. 3) and the circuit for operating the blue LED of the LED Pulser (see Sec. 6.2.1). The specifications of the HV modules used for the photo detectors can be found in [35].

Especially the APDs need a stable voltage supply because their gain M depends strongly on their bias voltage U. Under their designated operation conditions in the forward endcap of the PANDA EMC ($M = 200$, $T = -25\,°\mathrm{C}$), the change rate amounts to $dM/dU \cdot 1/M \approx 7.6\,\%/\mathrm{V}$ [24], for the other parts of the EMC, which operate at $M = 150$, this value is slightly smaller. The analysis of the data taken in the lab and during several beamtimes with the EMC prototypes (see Chap. 7) have proven that the HV power supplies made by iseg fulfill the requirements of the PANDA EMC.

The HV modules used for the APDs also provide a very precise current measurement with an accuracy of $\Delta I = \pm(0.01\,\% \cdot I + 4\,\mathrm{nA})$ for currents less than $20\,\mu\mathrm{A}$ [35]. In the forward endcap of the EMC for example, groups of eight APDs will be connected to one HV channel (see Sec. 4.6.1), but nevertheless the current measurement can be used to recognize a problem with one of the APDs and shut them down before permanent damage occurs.

4.8.5 Low Voltage Power Supplies

Several devices within the PANDA EMC need LV, most prominently the preamplifiers (see Sec. 4.1 and Sec. 4.2). The EMC uses power supplies of the PL500 series by W-IE-NE-R Power Electronics GmbH, Burscheid, Germany[4]. The PL500 is a modular series where each group of four channels (one internal module) can have its own specification in form of voltage and current range. One crate can support a power output of up to 3 kW. More tech-

2. https://www.raspberrypi.org/
3. https://iseg-hv.com/
4. http://www.wiener-d.com/

nical details on the PL500 series by W-IE-NE-R can be found in [36].

The PL500 power supplies have an ethernet connector and can be monitored and controlled via the Simple Network Management Protocol (SNMP). There is a standard EPICS device support called "devSnmp" that can connect all sorts of devices that are accessible via SNMP to EPICS [37]; this device support has been successfully used at the prototype for the forward endcap of the EMC (see Sec. 7.2).

There is one connector for a pair of sense wires for each channel and the device supports regulating its output voltage on both the sense wire readout as well as its internal voltage measurement. Indepedent of this selection, both voltage values can be read out via SNMP. Using this, a proper operating voltage at the preamplifiers can be guaranteed although there will be several meters of power cables between the power supplies outside the PANDA detector and the preamplifiers inside the cold volume of the EMC.

4.8.6 Custom Hardware

Several custom devices have been developed for the operation of the EMC. These include the Temperature and Humidity Monitoring Board for PANDA (THMP) used — as the name suggests — for a very precise temperature measurement as well as the monitoring of parameters like humidity and pressure. More information on the THMP can be found as a brief summary in Sec. 6.2.3 and in more detail in Miriam Kümmel's PhD thesis [38]. Another example is the LED Pulser used to monitor the photo detectors and the readout chain (see Sec. 6.2.1).

This custom hardware also has to be connected to the DCS. Both the THMP and the LED Pulser are controlled via the CAN bus. As the whole hardware is custom-made for the PANDA experiment, the software to control the devices also has to be developed within PANDA. This software follows a modular approach:

At the lowest level, there is a C++ library that implements the SocketCAN API [39] of the Linux Kernel. Built upon this library, there is a library for each device that implements the communication protocol of that device. These device-specific libraries use only standard C++ and the aforementioned CAN bus library and are therefore portable to any Linux-compatible device.

At the next level, there is an EPICS device support that connects these libraries to the EPICS core and makes their functionality available to the PANDA DCS. In addition, there are stand-alone applications that can be used to test and calibrate a device without the need for a full DCS stack.

Another custom-made device used in the forward endcap of the PANDA EMC is the HV regulation board mounted behind every APD submodule on the backplate (see Sec. 4.6.1). These boards are used to fine-tune the bias voltage of a group of APDs to make sure their gain is as close to the intended value as possible. These voltage regulators are controlled via the I^2C bus. The other boards mounted inside the cold volume of the forward endcap EMC have only passive components that have nothing that the DCS could monitor or control.

The PANDA barrel EMC also uses a similar method to regulate the bias voltage of the APDs, but the boards are adapted to the mechanical layout of the barrel.

To connect these voltage regulators to the PANDA DCS, a modular approach similar to the one outlined above will be used. There will be a library with minimal dependencies that implements the communication protocol of these components and an EPICS device support that forms the bridge between this library and EPICS.

4.8.7 Graphical User Interface

The Graphical User Interface (GUI) for the EMC DCS will be built using "Phoebus" which is a part of the Control System Studio (CS-Studio) project[5] [30]. Fig. 4.69 shows an example of a CS-Studio GUI made for one of the EMC prototypes.

There will be several GUI parts providing different levels of detail. An interface for the operators on shift in the control room will give a general overview of the status of the EMC. This interface will be integrated with similar overviews for all the other subsystems of PANDA. From this overview one will be able to reach additional interfaces that provide further insight and more details.

The last tier of the EMC DCS GUI are the interfaces for experts that will require authentication to make changes. Read-only access will nevertheless be available to everyone inside the PANDA network. These interfaces will provide access to individual and critical values of the devices — like the set voltage of a single HV channel — where unauthorized changes could be dangerous and cause permanent damage.

5. http://controlsystemstudio.org/index.html

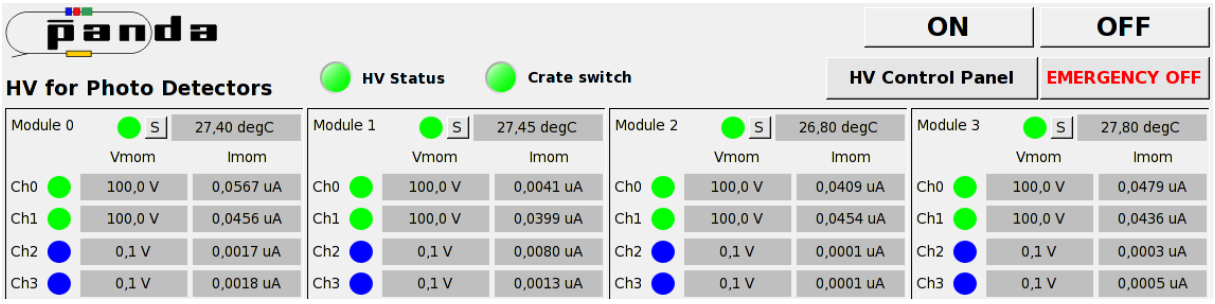

Figure 4.69: Example of a CS-Studio interface from the prototype of the PANDA forward EMC: Excerpt of the detailed HV power supply monitoring screen [40].

4.8.8 Configuration Database

A common configuration database will be established for both the DCS and the FEE. This database will provide a key-value store with a separate configuration namespace for each PANDA subsystem, so that identical parameter names in different subsystems do not cause any problems.

Each PANDA subsystem can define any number of configuration datasets, each dataset will be assigned a unique identifier. Once created, these datasets will be read-only, so that the exact configuration of the PANDA detector during a data-taking run can be reconstructed during analysis. The only way to make changes is to create a new configuration dataset containing the desired changes; this new dataset will receive a new unique identifier. The unique identifier of the configuration dataset used for each PANDA subsystem during a run will be stored in the metadata of that run.

In addition, there will be a list of operation modes common to all PANDA systems; this includes operation modes for both testing and physics. The physics operation modes will e. g. refer to beam characteristics like the beam energy. Each PANDA subsystem can assign one of its configuration datasets to each operation mode so that this configuration dataset is used when the next run beloging to that operation mode is started. The experts of a PANDA subsystem can change these assignments at any time without influencing the other subsystems in any way.

One advantage of this procedure for the EMC is the opportunity to use different high voltage setpoints resulting in different APD gains depending on the beam energy. This makes sure that the full range of the ADCs is usable also with low-energy beams, improving the accuracy of the measurements.

Additional information on the configuration database and its interfaces to various PANDA comoponents can be found in the DCS TDR: [30].

Bibliography

[1] G. Gramegna, Paul O'Connor, P. Rehak, and S. Hart. CMOS preamplifier for low-capacitance detectors. *Nucl. Instrum. Meth. A*, 390:241–250, 1997. https://doi.org/10.1016/S0168-9002(97)00390-2.

[2] Willy M. Sansen and Zhong Yuan Chang. Limits of Low-Noise Performace of Detector Readout Front Ends in CMOS Technology. *IEEE Transactions on Circuits and Systems*, 37:1375–1382, 1990.

[3] PANDA Collaboration. Technical Design Report for the PANDA Electromagnetic Calorimeter. 2008. https://panda.gsi.de/publication/re-tdr-2008-001.

[4] Holger Flemming and Peter Wieczorek. Low noise preamplifier ASIC for the PANDA experiment. *Journal of Instrumentation*, 6:1–8, 2011. https://doi.org/10.1088/1748-0221/6/12/C12055.

[5] Igor Konorov et al. SODA: Time distribution system for the PANDA experiment. pages 1863 – 1865, 2009. https://doi.org/10.1109/NSSMIC.2009.5402172.

[6] G. Tambave et al. Pulse pile-up recovery for the front-end electronics of the PANDA Electromagnetic Calorimeter. *Journal of Instrumentation*, 2012. https://doi.org/10.1088/1748-0221/7/11/P11001.

[7] Markus Preston. *Developments for the FPGA-Based Digitiser in the PANDA Electromagnetic Calorimeters*. PhD thesis, Stockholms universitet, 2020. http://urn.kb.se/resolve?urn=urn:nbn:se:su:diva-179733.

[8] Ernst Johannes Oliver Noll. *Digital Signal Processing for the Measurement of Particle Properties with the PANDA Electromagnetic Calorimeter*. PhD thesis, Johannes-Gutenberg-Universität Mainz, 2020. https://panda.gsi.de/system/files/user_uploads/l.capozza/TH-PHD-2020-005.pdf.

[9] Johannes Müllers and Pawel Marciniewski. Adaption of an FPGA-based Sampling-ADC for the Crystal Barrel Calorimeter. In *TWEPP*, 2017. https://doi.org/10.22323/1.313.0052.

[10] PANDA Collaboration. Technical Design Report for the PANDA Data Acquisiton. 2019. (submitted to FAIR for review).

[11] Markus Preston, Pawel Marciniewski, and Per-Erik Tegnér. FPGA-based algorithms for feature extraction in the PANDA shashlyk calorimeter. *International Conference on Instrumentation For Colliding Beam Physics*, pages 1–10, 2020. https://doi.org/10.1088/1748-0221/15/08/C08011.

[12] I. Keshelashvili et al. Development of Low-Noise / Low-Power Preamplifier for the Readout of Inorganic Scintillators and their Mass Production Test System. *IOP Conference Series*, 587, 2015. https://doi.org/10.1088/1742-6596/587/1/012024.

[13] Pawel Marciniewski et al. A Trigger System Based on Fast Sampling ADCs – Implementation and Tests. In *Nuclear Science Symposium*, 2011. https://doi.org/10.1109/NSSMIC.2011.6154359.

[14] Xilinx Inc. *LogiCORE IP Soft Error Mitigation Controller v4.0*.

[15] OpenCores. Wishbone B4, Wishbone System on Chip (SoC) Interconnection Architecture for Portable IP Cores, 2010. https://opencores.org/cdn/downloads/wbspec_b4.pdf.

[16] Johannes Sebastian Müllers. *An FPGA-based Sampling ADC for the Crystal Barrel Calorimeter*. PhD thesis, Rheinische Friedrich-Wilhelms-Universität Bonn, 2019. https://nbn-resolving.org/urn:nbn:de:hbz:5n-56693.

[17] S. A. White. Applications of distributed arithmetic to digital signal processing: a tutorial review. *IEEE ASSP Magazine*, 6(3):4–19, July 1989. https://doi.org/10.1109/53.29648.

[18] Elmaddin Guliyev. *Verification of a novel calorimeter concept for studies of charmonium states*. PhD thesis, Rijksuniversiteit Groningen, 2011. http://hdl.handle.net/11370/21cc138b-bdde-4fac-9030-1ea566baccc5.

[19] A. Georgiev, W. Gast, and R. M. Lieder. An analog-to-digital conversion based on a moving window deconvolution. *IEEE Trans. Nucl. Sci.*, 41(4):1116–1124, 1994. https://doi.org/10.1109/23.322868.

[20] A. Fallu-Labruyere, Hui Tan, Wolfgang Hennig, and W. Warburton. Time resolution studies using digital constant fraction discrimination. *Nucl. Instrum. Meth. A*, 579:247–251, 08 2007. https://doi.org/10.1016/j.nima.2007.04.048.

[21] A. Georgiev and W. Gast. Digital pulse processing in high resolution, high throughput, gamma-ray spectroscopy. *IEEE Transactions on Nuclear Science*, 40(4):770–779, 1993. https://doi.org/10.1109/23.256659.

[22] G. Tambave, M. Kavatsyuk, E. Guliyev, F. Schreuder, H. Moeini, and H. Löhner. Pulse pile-up recovery for the front-end electronics of the PANDA electromagnetic calorimeter. *Journal of Instrumentation*, 7(11):P11001–P11001, Nov 2012. https://doi.org/10.1088/1748-0221/7/11/p11001.

[23] Stefano Spataro and the PANDA Collaboration. The PandaRoot framework for simulation, reconstruction and analysis. *J. Phys. Conf. Ser.*, 331:032031, 2011. https://doi.org/10.1088/1742-6596/331/3/032031.

[24] Malte Albrecht. *Partial wave analysis of the decay $J/\Psi \to \gamma\omega\omega$ at BESIII and developments for the electromagnetic calorimeter of the PANDA detector*. PhD thesis, Ruhr-Universität Bochum, 2016. https://nbn-resolving.org/urn:nbn:de:hbz:294-49851.

[25] Christian Honisch. *Design, Aufbau und Test einer neuen Ausleseelektronik für das Crystal-Barrel-Kalorimeter*. PhD thesis, Rheinische Friedrich-Wilhelms-Universität Bonn, 2015. https://nbn-resolving.org/urn:nbn:de:hbz:5n-41117.

[26] Christopher Lukas Hahn. *Measurements on the radiation hardness of the high voltage subdistribution prototype of the Electromagnetic Calorimeter for the*

$\overline{\text{P}}$ANDA *Experiment*. Master's thesis, Justus-Liebig-Universität Gießen, 2016. https://www.uni-giessen.de/fbz/fb07/fachgebiete/physik/institute/iipi/arbeitsgruppen/ag-brinkmann/forschung/theses/copy_of_MSc_Thesis_C_Hahn.pdf.

[27] SAMTEC. ECUE-1 Copper FireFly™ Cable Assembly, datasheet, 2019. http://suddendocs.samtec.com/prints/ecue-xx-xxx-xx-xx-xx-1-xx-mkt.pdf.

[28] SAMTEC. 100 Ω, 34 AWG Micro Twinax Cable, datasheet, 2019. http://suddendocs.samtec.com/notesandwhitepapers/ttf-34100-xx-xx_datasheet.pdf.

[29] Claudius Schnier. *Analyse des Zerfalls $\eta_c \to \pi^+\pi^-\eta$ bei BESIII und Entwicklung von Komponenten für das elektromagnetische Kalorimeter des $\overline{\text{P}}$ANDA-Experimentes*. PhD thesis, Ruhr-Universität Bochum, 2019. https://nbn-resolving.org/urn:nbn:de:hbz:294-33806.

[30] $\overline{\text{P}}$ANDA Collaboration. Technical Design Report for the $\overline{\text{P}}$ANDA Detector Control System. (submitted to FAIR for review).

[31] Tobias Triffterer. *Entwicklung von Komponenten für das Detektorsteuersystem des $\overline{\text{P}}$ANDA-Kalorimeters und Studien zur Photoproduktion angeregter η-Mesonen mit dem CB/ELSA-Experiment*. PhD thesis, Ruhr-Universität Bochum, 2016. https://nbn-resolving.org/urn:nbn:de:hbz:294-46682.

[32] John Maclean. Introduction to EPICS. 2014. https://epics.anl.gov/docs/USPAS2014/1-Monday/EPICS_Intro.pdf.

[33] Martin R. Kraimer, Janet B. Anderson, Andrew N. Johnson, W. Eric Norum, Jeffrey O. Hill, Ralph Lange, Benjamin Franksen, Peter Denison, and Michael Davidsaver. EPICS Application Developer's Guide – EPICS Base Release 3.16.2. 2018. https://epics.anl.gov/base/R3-16/2-docs/AppDevGuide/AppDevGuide.html.

[34] J.A. Lucio Martinez and U. Kebschull. The Fault Tolerant Local Monitoring Control Board. In *CBM Progress Report 2017*, page 120. The CBM Collaboration, 2017. https://repository.gsi.de/record/209729/files/CBMProgressReport2017.pdf.

[35] iseg Spezialelektronik GmbH. Technical Documentation: EHS series. 2018. https://iseg-hv.com/files/media/iseg_datasheet_EHS_en_22.pdf.

[36] W-IE-NE-R Power Electronics GmbH. PL512/PL506 Modular Power Supply System – Technical Manual. 2014. https://file.wiener-d.com/documentation/PL506-PL512/Manual_PL512_PL506_00679_A4.pdf.

[37] John Priller. EPICS SNMP Device Support Module. 2019. https://groups.nscl.msu.edu/controls/files/devSnmp.html.

[38] Miriam Kümmel. *Analysis of $J/\Psi \to \phi\eta\eta$ at BESIII and calibration of the temperature monitoring system for the $\overline{\text{P}}$ANDA electromagnetic calorimeter*. PhD thesis, Ruhr-Universität Bochum, 2019. https://nbn-resolving.org/urn:nbn:de:hbz:294-64681.

[39] Oliver Hartkopp, Urs Thuermann, Jan Kizka, Wolfgang Grandegger, Robert Schwebel, Marc Kleine-Budde, Benedikt Spranger, Thomas Gleixner, Andrey Volkov, Matthias Brukner, Klaus Hitschler, Uwe Koppe, Michael Schulze, Pavel Pisa, Sascha Hauer, Sebastian Haas, Markus Plessing, Per Dalen, and Sam Ravnborg. SocketCAN – Controller Area Network. 2020. https://www.kernel.org/doc/Documentation/networking/can.rst.

[40] Tobias Triffterer. Alarm notifications for the $\overline{\text{P}}$ANDA detector control system. 32nd CANU and 9th JCHP-FFE Workshop, Bad Honnef, Germany, 2014.

5 Mechanics and Integration

5.1 Barrel Calorimeter

The crystals of the barrel calorimeter cover the polar angular region from 22° to 140° with an inner radius of 570 mm.

5.1.1 Crystal Geometry and Housing

The basic crystal shape is a tapered parallelepiped. Right angle corners are introduced in order to simplify the computer-aided design (CAD) design, the mechanical manufacturing process and to reduce machining costs. To obtain the barrel geometry with a high granularity, eleven different shapes are designed in two mirrored geometries (Fig. 5.1). The alternating right and left crystals are face to face on their perpendicular faces providing a so called flat-pack configuration which is also used in the CMS calorimeter (Fig. 5.2). The average mass of one crystal is 0.98 kg. The mass range goes from 0.88 kg to 1.05 kg. All given dimensions are nominal with an asymmetric tolerance of $0/-100\,\mu m$.

5.1.1.1 Crystal Arrangement along the Circumference

The cross-section crystal ring arrangement is shown in Fig. 5.3. The edge length of the shown front size of an individual crystal is 21.28 mm, which is close to the Moliere radius of PWO. Each ring is divided into 160 crystals. Taking the gap dimensions into account (see Sec. 5.1.2.1.1), one reaches a radius of 570 mm. The crystals along the rings are grouped by 10 to 16 sectors of 22.5° coverage, depending on the longitudinal position. The design foresees that the crystals are not pointing towards the target position. A tilt of 4° is added on the focal axis of the slice to reduce the dead zone effect. This means that particles originating at the target never pass through gaps between crystals, and therefore always go through a significant part of the crystal material.

5.1.1.2 Longitudinal Crystal Positioning

Crystal positions and their individual geometries along the axis parallel to the beam are shown in Fig. 5.4. In total 71 crystals are divided into 17 groups with 4 crystals of the same size in each and one group of 3 crystals with the same size. The mirror symmetry, with respect to the vertical axis, reduces the number of different crystal shapes in the arrangement from 18 to 11. The lateral sizes of the rear faces (readout side) vary between 24.35 mm and 29.12 mm and the average area is equivalent to a square with 27.3 mm edge length with ±15 % area variation between the 11 types of crystals. The lateral sizes of the front faces vary between 21.17 mm and 22.02 mm. Their average area is equivalent to a square with a lateral length of 21.3 mm. In total 71 crystals are aligned along the beam at the radius of 570 mm.

A tilt angle of 4° is introduced to reduce the dead zone effect. This corresponds to a focus shift of approximately 37 mm downstream. The entire barrel would contain 11 360 crystals without considering the necessary openings for the target pipe. It has a total length of 2466 mm and a volume of $1.3\,m^3$. Fig. 5.5 highlights one slice consisting of 710 crystals from the total barrel volume. In two of the slices 80 crystals each have to be removed to fit the target pipes.

5.1.1.3 Crystal Light Collection

The crystals are wrapped with a reflective material in order to optimize light collection and reduce optical cross talk. The considered material is Specular Film DF2000MA from 3M, commonly called VM2000 in the past, with a thickness of 65 µm. The non-metallic multi layer polymer, was employed for the crystals of the DVCS calorimeter at JLAB and the GLAST calorimeter. In order to achieve a good fitting for each crystal geometry, the individual foils get prefold scratches via a well tuned laser. In order to preserve the excellent energy resolution for the lowest energies, it is not foreseen to correct the longitudinal dependence of the light collection.

5.1.1.4 Carbon Fiber Alveoli

Each crystal will be contained in an individual cell of a carbon fiber alveoli pack in order to avoid any load transfer to the fragile crystals. The crystals are held in place by their rear end. Epoxy pre-impregnated carbon plain weave fabric is precisely molded in custom devices to fabricate alveoli units. 18 devices of different size are necessary to mold alveoli units of 18 types with 2×4 cells (2×3 for crystals type 11). Five units of the same type are

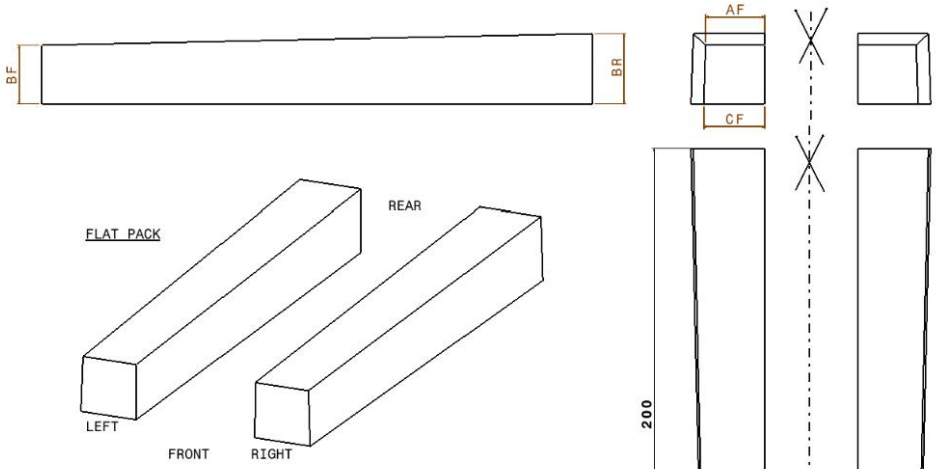

Type	Volume (cm3)	AF (mm)	BF (mm)	CF (mm)	AR (mm)	BR (mm)	CR (mm)	Quantity / slice	
								Left	Right
1	126,86	21,21	21,28	21,27	29,04	28,75	29,12	40	40
2	126,56	21,18	21,28	21,39	28,78	28,75	29,07	40	40
3	125,79	21,17	21,28	21,51	28,36	28,75	28,81	40	40
4	120,85	21,17	21,28	21,60	27,90	27,22	28,45	40	40
5	119,69	21,17	21,28	21,69	27,35	27,22	28,01	40	40
6	118,35	21,19	21,28	21,78	26,72	27,22	27,47	40	40
7	112,9	21,22	21,28	21,86	26,23	25,47	26,99	40	40
8	111,75	21,23	21,28	21,91	25,70	25,47	26,51	20	20
9	110,52	21,23	21,28	21,95	25,14	25,47	26,00	20	20
10	107,01	21,25	21,28	22,00	24,70	24,42	25,56	20	20
11	106,25	21,25	21,28	22,02	24,35	24,42	25,23	15	15

Figure 5.1: The shape of the scintillator crystal and the definition of geometrical parameters. The average crystal corresponds to squares of 21.3 mm for the front face and 27.3 mm for the back face and its mass is 0.98 kg. The final geometry of the crystal is available on EDMS under the reference: Definition of Barrel crystals - 210308.pdf

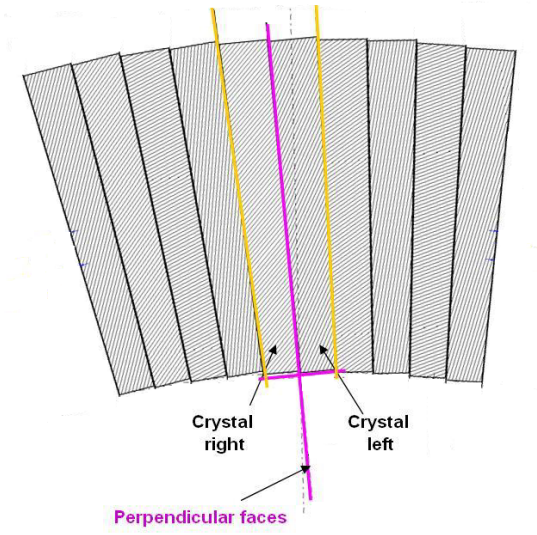

Figure 5.2: Arrangement of crystals across the barrel using the flat-pack configuration.

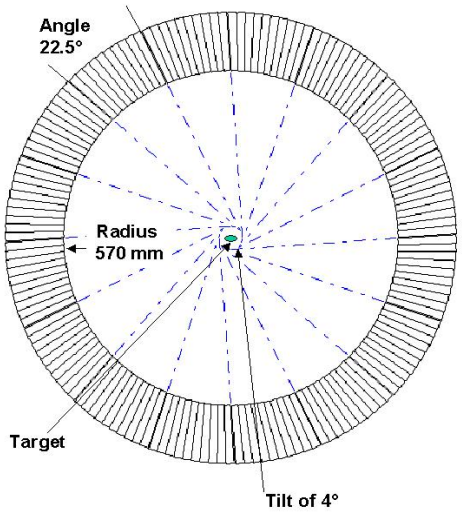

Figure 5.3: Cross section of the barrel calorimeter. The 160 crystals are grouped into 16 sectors.

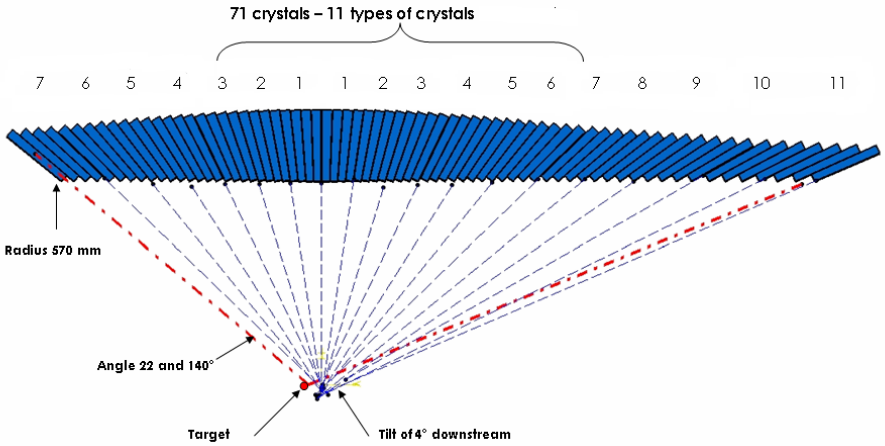

Figure 5.4: Crystal arrangement of the barrel along the beam axis. Positions of the different crystal types are indicated. Due to the mirror symmetry, 11 types are sufficient instead of 18.

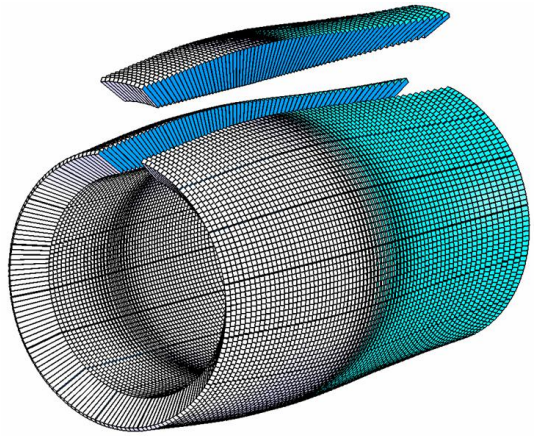

Figure 5.5: View of the total barrel volume with a separated single slice of 710 crystals. A slice covering 1/16 of the barrel volume.

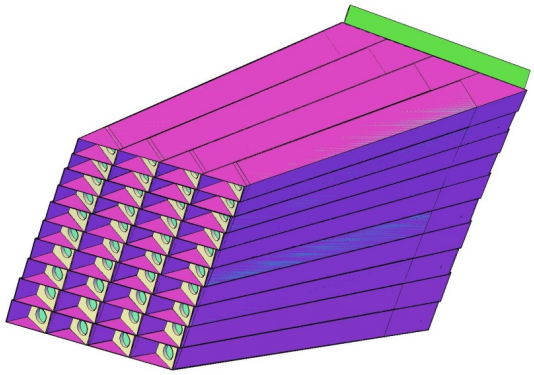

Figure 5.6: Alveoli pack assembled with crystals. View from the front side. Front inserts with mounting holes for the optical fibers of the monitoring system are shown.

glued together to form an alveoli pack with 4×10 or 3×10 cells, respectively. The outer walls of a pack have a thickness of (200 ± 20) µm and the inner ones (400 ± 20) µm.

After insertion of the crystals, aluminum inserts will be glued with epoxy on to the rear side of each alveoli cell. Those inserts represent the interface with the support structures. To prevent longitudinal crystal movement, thin plastic plates (front inserts) are placed in front of the crystals. They will be glued to the walls of each cell. Each front insert has a hole for the light pulser monitoring system (Fig. 5.6).

Temperature cycling tests between $-40\,°C$ and $30\,°C$ were performed to check the reliability of the gluing stressed by the different thermal expansions of the involved materials. Fig. 5.7 shows one of the deformation tests, here in the vertical position. The results of 80 µm horizontally and 10 µm vertically are tolerable and in agreement with analytical calculations.

5.1.2 Barrel EMC Mechanical Structure

The Barrel EMC will operate at $-25\,°C$ in dry air atmosphere inside a solenoid magnet of 2 T with an inner radius of 95 cm and a length of 2.8 m. A thermal screen will surround the main part of each slice dividing the Barrel EMC volume into two regions: cold (inside thermal screen) and warm (out-

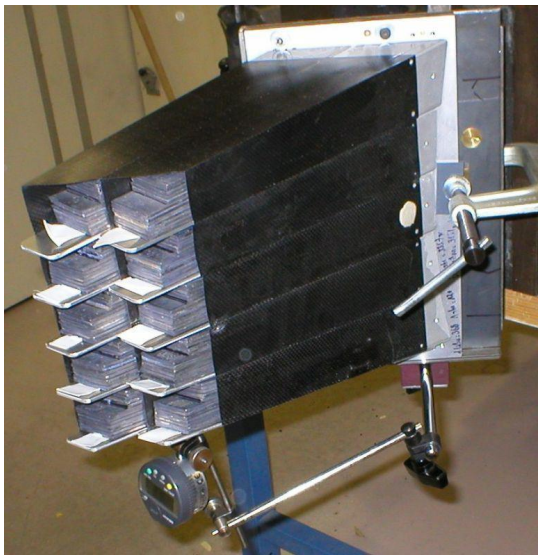

Figure 5.7: Deformation test of carbon alveoli unit with 2×4 cells in vertical position. Here, 10 µm have been measured, compared to 80 µm in the horizontal position.

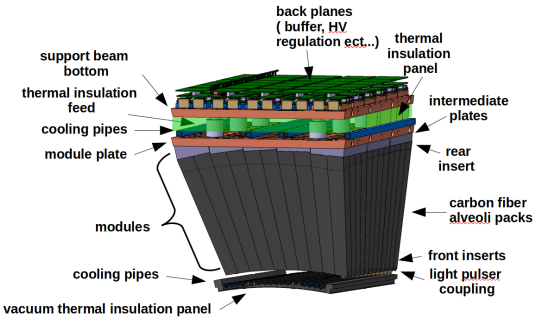

Figure 5.8: Schematic cross section view of the concept for the major components of a slice.

side thermal screen). Fig. 5.8 represents the design principle of one slice with respect to all constraints like mechanic and electronic integration and thermal ones.

5.1.2.1 Mechanical Structure inside Thermal Screen

A modular structure is used to build a slice as shown in Fig. 5.9. Each of the 18 modules contains equal numbers of right and left crystals of the same type. The modules are mounted on 7 different back module plates, forming 7 individual super-modules. Super-module no. 1 contains only one module. Super-modules no. 2 – 6 are built from three different module types. Super-module no. 7

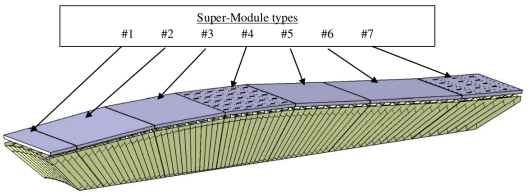

Figure 5.9: Modular structure of a slice.

contains two different modules. The mirror symmetry can be found between super-modules no. 3 and no. 4.

5.1.2.1.1 Distances between Crystals

The distance between two crystals is calculated from the thickness of materials, structure deformation and mechanical tolerances. Fig. 5.10 shows a drawing of the different gaps which will be explained in detail. A conservative concept has been chosen, which can be considered as an upper limit of the expected dead space.

The basic distance between crystals inside an alveoli pack is defined as 0.68 mm and represents the sum of:

- 400 µm, thickness of the carbon wall;
- 130 µm, the doubled thickness of the wrapping material;
- 120 µm, the free gap left for alveoli deformation and temperature sensors (description of sensors is given in Sec. 6.2.2);
- 30 µm, the approximate manufacturing tolerance.

This calculation is based on the nominal dimension of the crystal. There might appear an additional distance of maximum 0.2 mm between two adjacent crystals due to polishing tolerances. Gaps between the identical shapes of 4 crystals in one alveoli pack might introduce an additional lateral spacing up to 350 µm.

Between alveoli packs, the thermal expansion of the mounting plate amounts to approximately 120 µm. For the mounting tolerance 100 µm are considered. Together with the basic distance between crystals of 0.68 mm this adds up to a total value of 0.9 mm. Between modules, a distance varying between 2.4 and 3.3 mm has to be considered. This value takes into account the mounting feasibility and tolerances in the mechanical assembly, and the structure deformations.

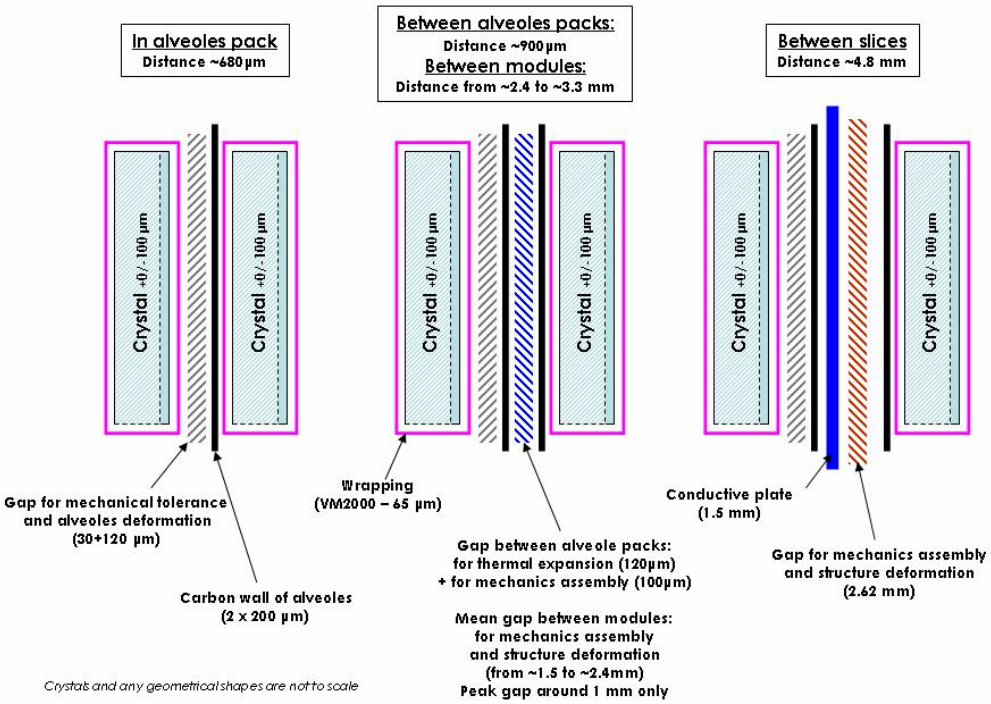

Figure 5.10: Summary of the expected dead space between calorimeter crystals.

Between adjacent slices, there is a thin conductive plate foreseen. The size of the gaps here are not equal. One of them could have a size up to 2.62 mm due to mechanical mounting tolerances caused by the deformation of the whole structure. The other gap could have a size of up to 1.5 mm. The distance between crystals in this area amounts to less than 4.8 mm.

5.1.2.2 Super-Module Structure

The structure of a super-module is shown in Fig. 5.11. The alveoli are produced longer than necessary and get cut (20.0 ± 0.5) mm behind the back face of the crystals. The protruding part is used to glue the aluminum rear inserts to each alveole. The rear inserts fix the crystal position inside the alveoli, to fix the ASIC front end and make the precise connection to the aluminum intermediate plates. The shapes of these inserts are different for each single cell in the alveoli units. In total, 142 $(8 \times 17 + 6)$ different rear insert types are needed.

Intermediate plates are fixed by screws and pins to the eight different inserts of each alveoli unit for precise positioning. Five different shapes of intermediate plates are necessary to create a flat top surface of one module type for the attachment to the aluminum back module plate. Thus, the total number of designs for the intermediate plates is equal to 90 (5×18).

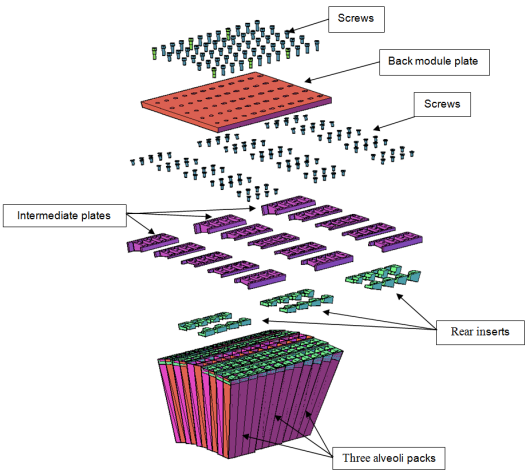

Figure 5.11: Exploded view of super-module. Front inserts, crystals and capsules with APDs are not shown.

The rear inserts and intermediate plates have to fulfill the following requirements:

- The insert never touches directly neither the crystal nor the APD but only the APD covering capsule. This prevents any significant longitu-

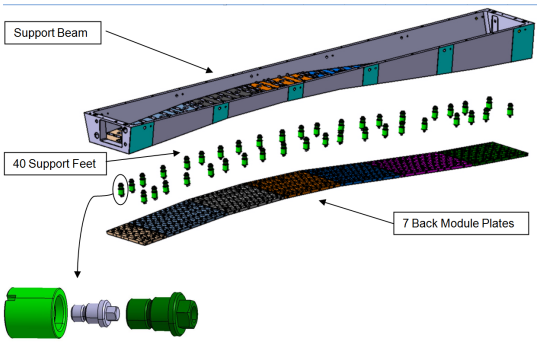

Figure 5.12: Mechanical connection between "cold" super-modules and "warm" support beam with the use of G10 fiberglass support feet of 30 mm length

dinal movement of the crystal inside its cell.

- Enough space has to be provided for the APFEL front-end including its flexible PCBs which are going to the back planes inside the support beam through the openings in the back module plates.
- A good thermal contact for the APFEL to the back module plate has to be provided.

The back module plates have to be machined with good flatness in order to stay within a reference plane even under the weight of the crystals. Their designed thickness is 14 mm. The back module plates are cooled down with the cooling system. Further thermal details are given in Sec. 5.1.5. Each plate is connected to the warm support beam by 30 mm long glass-fiber support feet. Those are designed for low thermal transfer and low deformation as shown in Fig. 5.12.

On the target facing side, the alveoli units are cut in that way, that there is at least 1.5 mm space to the assigned area of the front cooling. A plastic stopper (front insert) of max. 3 mm thickness will be glued on its entire perimeter inside each alveoli cell in front of the crystals. The required tolerance of their external dimensions is $0/-100\,\mu m$.

5.1.2.3 Support Beam and Rings Definition

In one slice of 710 crystals, 18 modules of alveoli packs are grouped together into 7 super modules: 5 super modules of 120 crystals each, 1 super module with 70 and 1 with 40 crystals. The super modules are supported by an aluminum support beam of 2.7 m length with trapezoidal cross section. The internal part of the support beam is used for housing part of the front end (backplanes), readout and

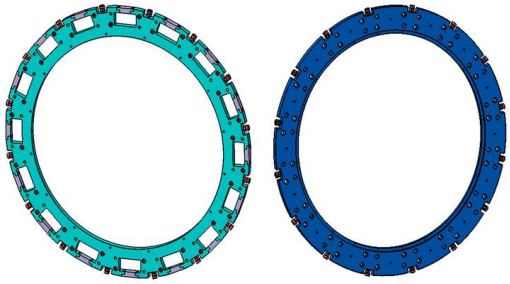

Figure 5.13: Support rings

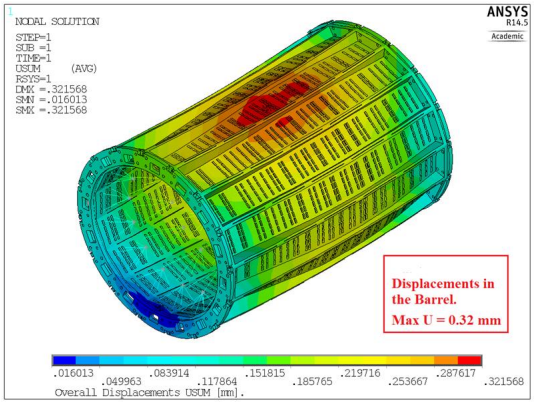

Figure 5.14: Deformation of the fully assembled barrel. All the slices are fixed to each other. For better illustration, only the support beams are shown.

power supply cables. The details about the integration of those services are provided in Sec. 5.1.3. These services are operated at room temperature. Access must be possible by simply opening the cover plate when the barrel is in a maintenance position.

Sixteen support beams are fixed on two support rings of 40 mm thickness at their ends (see Fig. 5.13). Those rings provide an alignment adjustment for the slices. They are made out of stainless steel with sufficient non-magnetic quality. The magnetic quality may have been altered by the machining or the welding process. Therefore a magnet-relieving annealing is foreseen in an oven.

A fixation between neighboring slices is necessary to improve the integrity of the barrel shape. The maximum displacement in the assembled barrel is calculated to be less than 0.4 mm as shown in Fig. 5.14.

5.1.2.4 Adapted Design for the Target

The target system is passing vertically through the calorimeter. Two specially desigend slices with

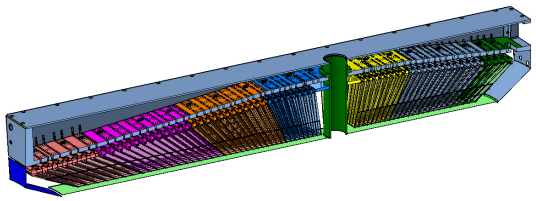

Figure 5.15: Slice with a hollow cylinder for the target pipe. Two central modules are removed.

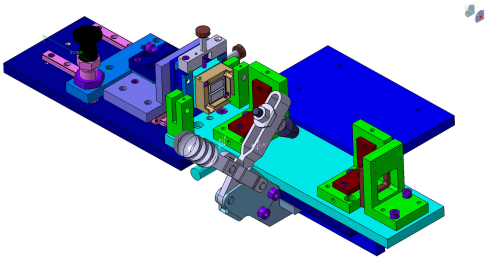

Figure 5.16: Special APD gluing tool for APD alignment, constant pressure during curing process and inspection of the gluing quality.

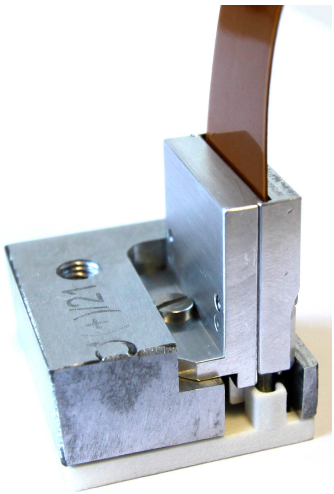

Figure 5.17: APFEL inside aluminum housing with outgoing flexible PCB. The housing is screwed on a rear insert. APDs are located in plastic capsule.

holes for the target pipe are forseen. In each target slice two central modules with 40 crystals will be removed, adding up to 160 crystals removed from the barrel. The mechanics and the thermal shields are modified and a thermally insulated hollow cylinder is added (see Fig. 5.15). In any case, the target tube will not be in contact with the cold area and will be free to move. No special alveoli but a reduction of the alveoli pack with less gluing is needed.

5.1.3 Electronics Integration

Due to the magnetic field, APDs are employed as photosensors (APD details given in Sec. 3.1). Two APDs of $7\,\text{mm} \times 14\,\text{mm}$ each are used and glued on the back face of the crystal by using the silicon adhesive Dow Corning 3145 RTV with special APD-gluing-tools (Fig. 5.16) inside a clean room environment. Through an opening at the crystal face opposing the APD gluing quality is checked for air inclusions or dust particles, which could impair the light collection.

Both APDs are connected to an APFEL with two input channels. Each input channel is split into two different gain stages to cover the full dynamic range of the APD signals. The APFEL provides shaping of the signal to cope with high count rates (detailed description is given in Chap. 4.1). Besides mechanical protection during the mounting process, fixation of the APFEL to the rear inserts and electromagnetic interference protection, a housing is foreseen which provides heat loss dissipation via thermal conduction through the holding structures (Fig. 5.17).

The APFELs are connected to the back plane units through shielded multilayer flexible PCBs. Four APFELs can be connected to each unit. Those units consisting of 3 staggered PCBs, providing services like individual voltage regulation for each APD, signal buffers and environment monitoring. A detailed description of the back plane units is given in Sec. 4.6.2. They will be fixed inside the support beam with back plane adapters (Fig. 5.18). The middle bridge is introduced to avoid overlapping flexible PCBs, especially around their support beam feed troughs, and therefore possible over pressure leakages through the corresponding sealing rings. Furthermore, the back plane adapters will keep the sealing rings in their position (see also Sec. 5.1.5). The transversal space at the support beam bottom level is not sufficient everywhere, especially at the most forward region. By staggering several of a slightly modified version of the adapters the trapezoidal shape of the support beam is taken into account (Fig. 5.19).

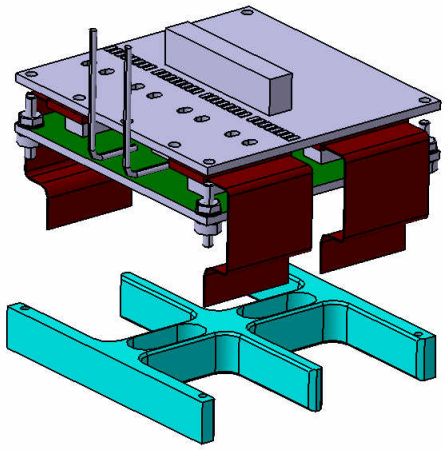

Figure 5.18: Part of the back plane detached from its fixture (backplane adapter) for the support beam and four connected flexible PCBs.

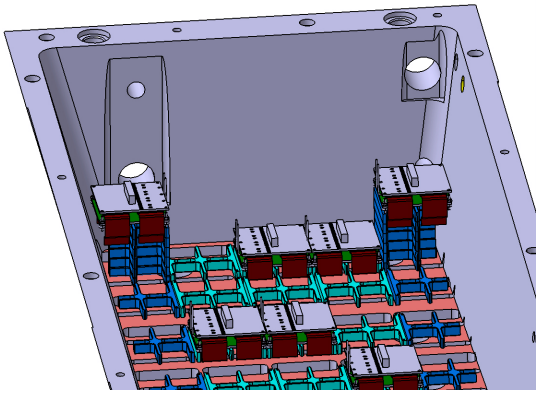

Figure 5.19: Due to the trapezoid shaped support beam, certain back planes have to be mounted at an elevated position by staggering some modified back plane fixtures (dark blue color).

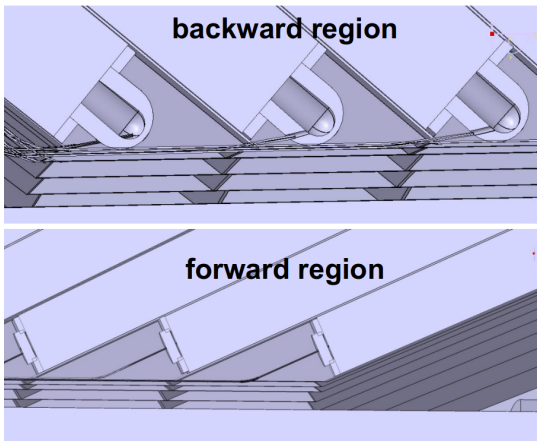

Figure 5.20: Light pulse injection into the crystals for calibration monitoring. A direct coupling to the crystals is only possible in the most forward region, elsewhere light guides are needed.

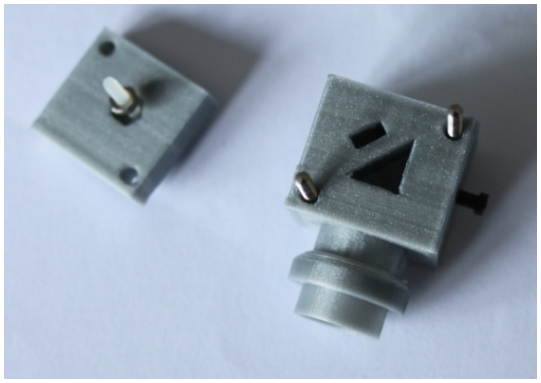

Figure 5.21: Opened first 3D printed light guide prototype as prism retainer. The fiber can be attached at the right hand side. The prototype is not optimized to minimize the material budget.

5.1.4 Light Pulser Monitoring System Integration

For an online correction of detector calibration drifts mainly due to radiation damages inside the crystals and to monitor all components of the read out chain, a stabilized light pulser system is foreseen. A detailed description of the pulser system itself is given in Chap. 6.2. The light pulses are transferred with radiation hard glas fibers (V200/220 P28 CeramOptec, Germany) into the barrel. The pulses are injected into the crystals through their front face. The long term bending radius of the used fibers is limited to 30 mm and there are space restrictions in front of the crystals so the direct optical coupling can only be applied for one third of the crystals in the most forward region. For those, a small plastic cylinder with a borehole for a bunch of fibers, placed inside the front stopper, can be used as connector. All other crystals require light guides (Fig. 5.20) with deflections of 40° and 140° between the fibers and the perpendicular of the crystal front faces. A light guide prototype using a small radiation hard prism is shown in Fig. 5.21.

5.1.5 Thermal Cooling

5.1.5.1 Requirements

By decreasing the operating temperature of the lead tungstate scintillator crystals their light yield

(Photons per MeV) increases. For a fixed voltage the APD photo sensor gain increases at lower temperatures as well. For the crystals it is 2.5 %/°C more light yield and for the APDs 5 %/°C more gain around the operation voltage for a gain of 150. The nominal operating temperature for the EMC is chosen to be −25 °C. The temperature stability requirement for the barrel is given by its modules which have the best performance for the highest expected photons of less than 10 GeV. For the highest energies, the leading part of the energy resolution parameterization is the constant term. The modules with the at least tapered crystals of the barrel will have the smallest value and therefore the best performance at the upper energy range. Their shape and the resulting detector performance is almost identical to the forward endcap ones which have $\frac{\sigma}{E}(10\,\text{GeV}) = 1.15\,\%$ (Fig. 7.8 in Chap. 7.2). With respect to the crystals light yield and APD gain temperature dependence, a temperature stablity of 0.1 °C is required to have no impact on the energy resolution.

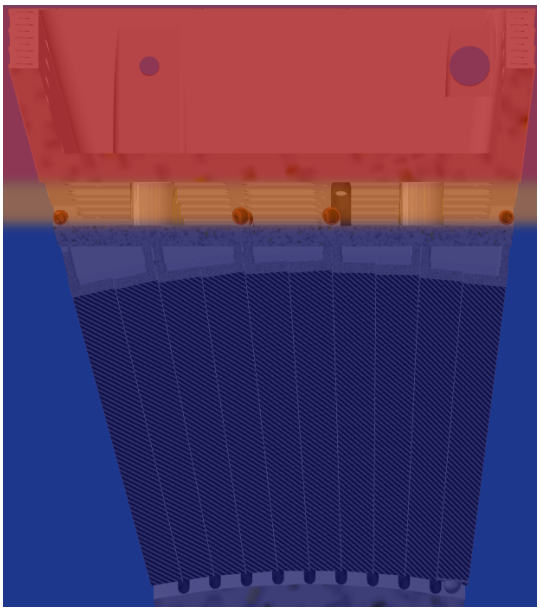

Figure 5.22: CAD-Drawing showing the hot, intermediate and cold volume of each barrel slice.

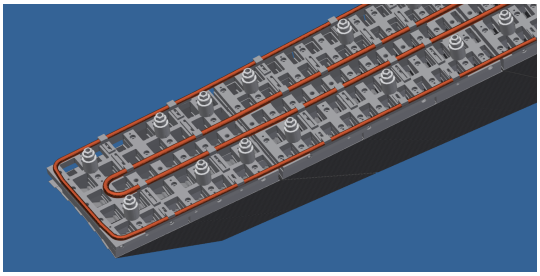

Figure 5.23: CAD-Drawing showing the configuration of cooling pipes.

5.1.5.2 Heat Sources and Transfer

Active heat sources are the electronics and cables in the support beam, as well as the APFELs which are close to APDs and crystals. Heat is also transferred via the mechanical structure, from neighboring detector components and contact surfaces to ambient air. The heat produced by the electronics in the support beam has to be removed to reduce the temperature gradient and to stabilize the temperature for the high voltage supplies. To minimize the heat transfer from the mechanical structure and support beam electronics towards the cold volume further, the super modules are only held in place by G10 fiberglas support feet. The only metal parts connecting support beam and super modules are the traces in the flex PCB cables. The heat load of the APFELs is 59 mW per each of the four channels. They are closest to the temperature sensitive APDs and crystals and packaged into aluminum housing to allow heat transfer to the cooled super module plates. The heat transfer between slices is negligible because they are operating at the same temperature on all close and contact surfaces.

5.1.5.3 Cooling Layout

Each barrel slice is divided into a hot, an intermediate and a cold volume. The hot volume consists of the support beam containing cables and electronics, the intermediate section is for insulation and the cold volume at −25 °C includes the super module plates, APFEL assemblies, APDs and the crystals in their carbon fiber alveoles.

The cooling is provided by circulation of liquid methanol water mixture and supported by cooled dry air to prevent condensation and the buildup of ice inside each slice. The liquid cooling system is designed to operate below atmospheric pressure to prevent leakage. Main copper cooling lines run on top of super module plates, which act as heat sinks. The cooling lines have a circular cross section and there are two separate loops, the inner loop with an outer diameter of 12 mm and the outer loop with an outer diameter of 10 mm. The pipes used have a wall thickness of 1 mm. The outer loop has to be of smaller diameter cross section to accommodate the flexible PCB cables that run perpendicular from each crystal surface.

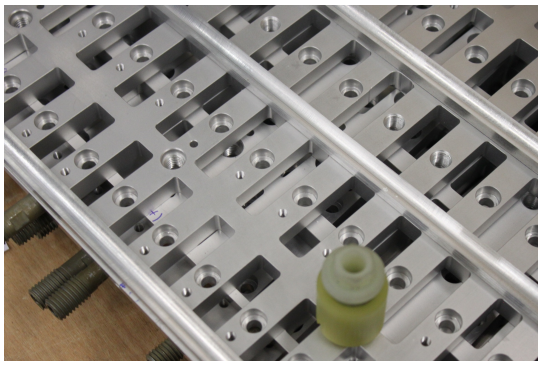

Figure 5.24: Picture showing the half pipe adapter profiles.

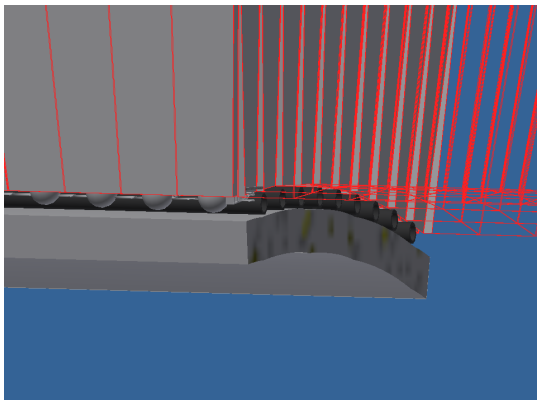

Figure 5.25: Picture showing a half cut view of the front VIP.

Table 5.1: Cooling relevant properties of PWO and CH_3OH+H_2O.

Parameter	PWO	CH_3OH+H_2O
Density	8.28 g/cm^3	0.93 g/cm^3
Specific heat	262 J/kg	3.151 J/kg
Conductivity	3.22 W/(m K)	34.1 W/(m K)

Table 5.2: Material properties of the used insulators

Parameter	VIP	Silicon Foam
Conductivity	0.004 W/(m K)	0.10 W/(m K)

For better thermal conductivity each cooling line is attached on the full length of each super module plate by an aluminum profile. The cooling pipes and profiles are held down via aluminum clamps.

The front cooling consists of 9 plastic pipes with an outer diameter of 6 mm and a wall thickness of 1 mm which run between manifolds on either end of the slice along the crystal front faces. The coolant inlet is in the upstream manifold, and the downstream manifold is connected to a return pipe that runs below the support beam to the shared outlet manifold of main and front cooling. The coolant used is methanol and demineralized water in a 60 to 40 percent mixture, properties can be found in table 5.1. A total flow of 15 L/min of coolant is expected, removing about 730 W of heat per 1 K in temperature difference. In simulations that considered all possible heat sources, the outlet temperature was less than 1 K higher than the inlet temperature. The maximum temperature gradient in the cold volume is 0.8 K.

5.1.5.4 Insulation

To prevent an exchange of air from the hot to the intermediate volume in the slice, each cutout of the support beam is filled with silicon rubber cylinders which seal around the flexible PCB cables. Below the support beam, a one piece silicon foam mat provides insulation between the cold volume and the support beam surface. The underside of the cold volume will be insulated by a commercially available 15 mm VIP. This panel consists of a pressed core of porous material and a vacuum tight membrane. The panel is formed, laminated with the membrane and then evacuated. This panel is formed to follow the inner diameter of the EMC barrel. Simulations showed a heat transfer of 7 W from the ambient air at 25 °C to the cold volume at −25 °C. Material propterties of insulation material can be found in table 5.2.

5.1.6 Integration in the PANDA Target Spectrometer

Fig. 5.26 defines the complete volume of the barrel. The overall dimensions are required for the integration of the neighboring detectors. The total mass is approximately 18 tons composed of 11 tons of crystals and 7 tons of support structure. The services are going out of the slices in the backward area and afterwards through the corners of the octagonal shape of the yoke as shown in Fig. 5.27. A list of services is given in table 5.3.

5.1.7 Assembly of the Slices and the Barrel

The construction of a single slice and the assembly of the complete barrel require a large amount of manpower, installation space and time for testing. The production time is of the order of 3 slices per

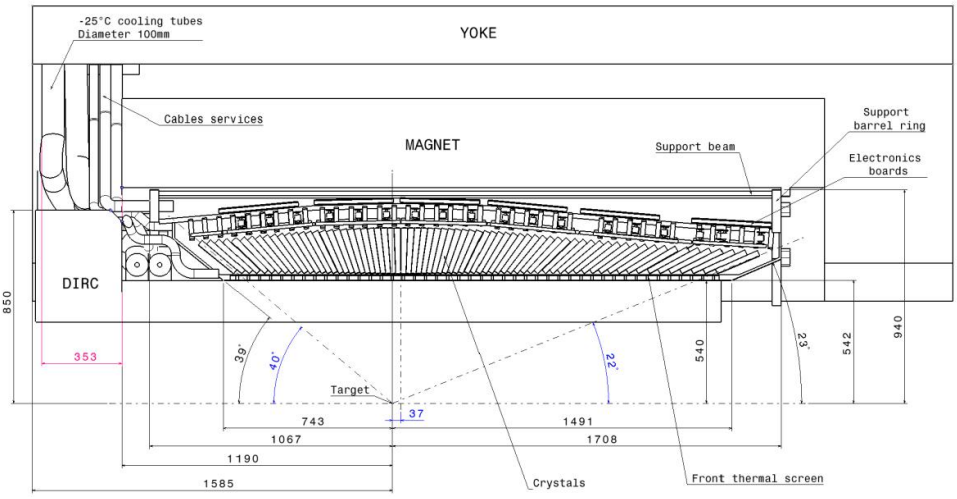

Figure 5.26: Dimensions of one slice.

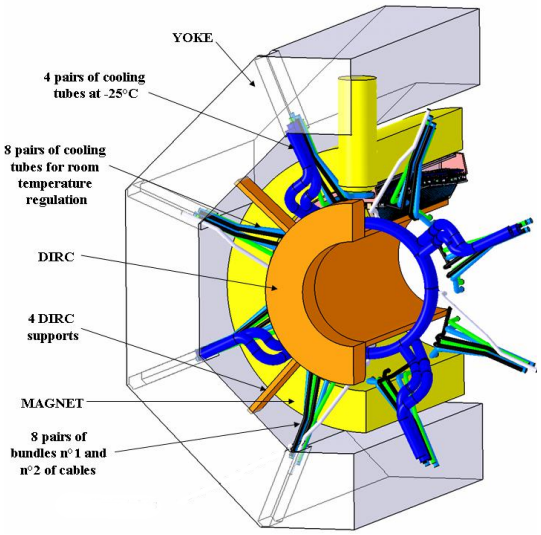

Figure 5.27: Services going outside the barrel into the corners of the octagonal yoke.

Table 5.3: List of services in the backward area.

Service	Detail	Ø(mm)	Qty.
Bundle 1	High/low volt. ADC supply opt. fibers	50	16
Bundle 2	Dry air, humidity temperature sensors opt. fibers	40	16
Tube 1	Water 20 °C	50	16
Tube 2	Coolant −25 °C	105	8

year and will need a good coordination between the different laboratories.

To assemble the Barrel EMC various devices and tools as well as technological components, specific for each operation, have to be designed and manufactured. A sequence of assembly is described in Sec. 5.1.7.1.

5.1.7.1 Slice Assembly Sequence

1. Assembly of modules (18 types)
   - Gluing two screened and matched APDs onto each crystal.
   - Wrapping crystals with reflector foils.
   - Crystals insertion process into alveoli pack including installation of thermal sensors between crystals, installation of APD capsules and gluing of rear and front inserts to the alveoli.
   - Mounting of ASICs to the rear inserts.
   - Mounting of intermediate plates.
   - Testing of electrical connections.
2. Mounting of support feet to the back module plates.
3. Mounting of modules to the back module plates to assemble super modules.
4. Arrangement of super modules in a device for precise positioning of super modules.
5. Mounting of cooling pipes to the dedicated positions on the back module plates.

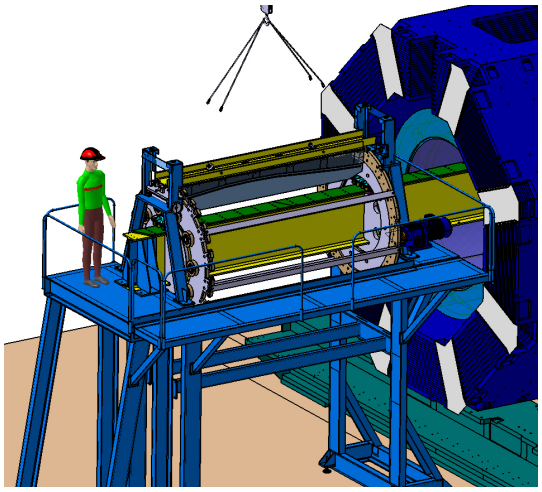

Figure 5.28: Final barrel mounting.

6. Installation of thermal insulating material

7. Mounting of support beam with the use of a technological beam which is necessary for assembling, storage and transportation of each slice as well as for the final barrel assembly.

8. Air sealing of openings in the bottom of the support beam and flexible PCBs passing through.

9. Mounting of back planes inside the support beam, connecting flexible PCBs to the back planes.

10. Transfer the slice to the device allowing rotation around the longitudinal axis for final assembling.

11. Mounting of signal and power supply cables to the electronic boards.

12. Mounting of optical fibers of the monitoring system.

13. Mounting of front thermal shielding with cooling pipe.

5.1.7.2 Final Assembly of the Barrel

Fig. 5.28 presents a sketch of the mounting procedure of the barrel. Each slice is installed one by one between two support rings. A special rolling system with a stable central beam going through the solenoid will be used. Once the barrel is complete, it can be moved to its final position and fixed inside the solenoid of the $\overline{\text{P}}$ANDA detector.

5.2 Forward Endcap

Since the beginning of the development of the forward endcap, the design has been partially changed. In order to facilitate the allocation of the individual components, the forward endcap can be divided into different areas as seen in Fig. 5.29.

View 1: Rear area within the cooled volume, as seen from the interaction point, used for the cable routing from the cooled volume to the uncooled volume. This volume is bounded on one side by a 3 mm thick aluminum plate and on the other side by the base plate. The depth of this area is 33 mm.

View 2: The base plate is mounted with the outer retaining frame. Both the base plate and the outer retaining frame are made of aluminum (AlMgSi1). At twelve, five and seven o'clock, feet are mounted on the holding frame to support the base plate.

View 3: Submodules including brackets. The submodules of the forward endcap each consist of eight or 16 $PbWO_4$ crystals and associated photodetectors. The submodules are mounted on the base plate and have a weight of approx. 20 kg.

View 4: The electronic components are located outside the cooled volume of the forward endcap. These include the light pulsers, the THM$\overline{\text{P}}$s and the SADCs.

View 5: The cooling. The cooling of the forward endcap is divided into four parts. The four cooling components are divided into air cooling, main cooling, side cooling and front cooling.

View 6: Insulation of the forward endcap, which consists of vacuum insulation panels with a coefficient of thermal conductivity of $\lambda \leq 0.005\,\mathrm{W/(m\,K)}$ from va-Q-tec[1].

View 7: The support frame is made of AlMgSi1, both because of the magnetic field in the final operation and to save weight. It is the central support of the forward endcap. [1]

5.2.1 Submodule Structure

Two different sizes and two different types of submodules are used in the forward endcap. This re-

1. https://va-q-tec.com/technologie/vakuumisolationspaneele/

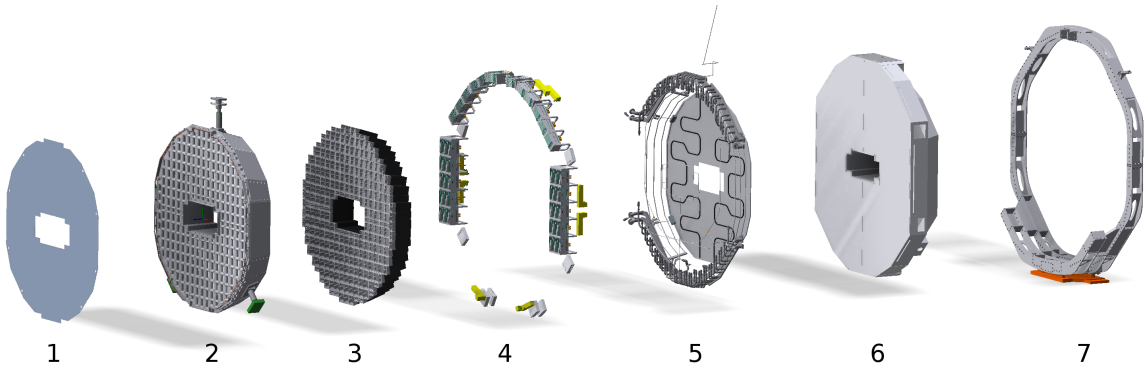

Figure 5.29: Exploded view of the Forward Endcap.

sults in a total of four different submodule variants. On the one hand there are submodules that hold eight photodetector crystal units, and on the other hand there are submodules with 16. Both submodule variants are constructed as APD and VPTT submodules. Since the structure of the different submodules is very similar, as an example in Fig. 5.30 a 16 crystal submodule of APD type is shown.

The shell that holds a submodule together is made of a carbon fiber/resin mixture with a wall thickness of 0.8 mm and is called an alveole. This material is used because of its high stability at low mass loading. The alveoli are closed at the front and have a cross-shaped strut on the inside to increase stability. In each of these four areas there are four photodetector crystal units, which are separated from each other by another cross-shaped strut. A photodetector crystal unit consists of a $PbWO_4$ crystal covered with a reflective foil (DF 2000 MA) to which a photodetector is glued with DowSil3145. The adhesive DowSil3145 is a silicone that vulcanizes at room temperature. For optimal adhesion, the crystals are primed with PR-1200 from DowSil. When gluing photodetectors to the crystals, annealing LEDs are also coupled to the crystals. Flat top LEDs[2] are used for VPTT units and for APD units SMD LEDs[3]. In Fig. 5.30 an APD unit is shown. It consists of two APDs mounted in a capsule, one preamplifier per APD, one annealing LED and a shield made of an aluminum tube. Four APD units are enclosed by an aluminum insert. Four inserts are inserted into an alveole with the photodetector crystal units. The inserts are fabricated such that they can be screwed[4] to the mounting plate and are pressed outwards and thus fixed within the alveole. In addition, an aluminum sleeve with four glued-in optical fibers is inserted into each slot.

The individual submodules are attached to the base plate by means of interface pieces which are screwed to the mounting plate with four screws[5]. The connectors are manufactured individually for the position in which the respective submodule is mounted. Due to the symmetrical design of the forward endcap, each connector geometry is present at least twice, often four times. This allows the end faces of the submodules to be aligned to a point in front of the interaction point. Due to the weight of the submodules of approx. 20 kg, the same Dalmec manipulator arm is used for their assembly, which was already used by the CMS experiment at CERN.

Two APDs and thus two preamplifiers are installed per photodetector unit. The preamplifiers of the APDs must be electrically shielded. For this purpose an aluminum tube is slid over the preamplifiers of each photodetector unit and glued to the capsule. This aluminum tube (EN AW 6060) is 50.0(5) mm long and has a diameter of 22 mm and a wall thickness of 1 mm. For the 3088 APD units, the aluminum tubes were sawn to length and then the grade of the tubes was removed by vibratory grinding. In order to ground the aluminum tubes, ground straps are attached to these tubes, which are later attached to the inserts.

When used in the forward endcap, the ground straps are fixed with blind rivets[6]. This connection is quick and not very susceptible to failure and is also suitable in terms of the strength of the connection [1].

2. Unbranded 3 mm flat top LED $I_F = 20\,mA, U_F = 3.0\,V - 3.6\,V, 460\,nm - 470\,nm$
3. Kingbright 3 mm × 1 mm right angle SMD chip LED lamp
4. DIN912 A4 M4×12
5. DIN912 A4 M4×16
6. ISO 15983 / DIN 7337

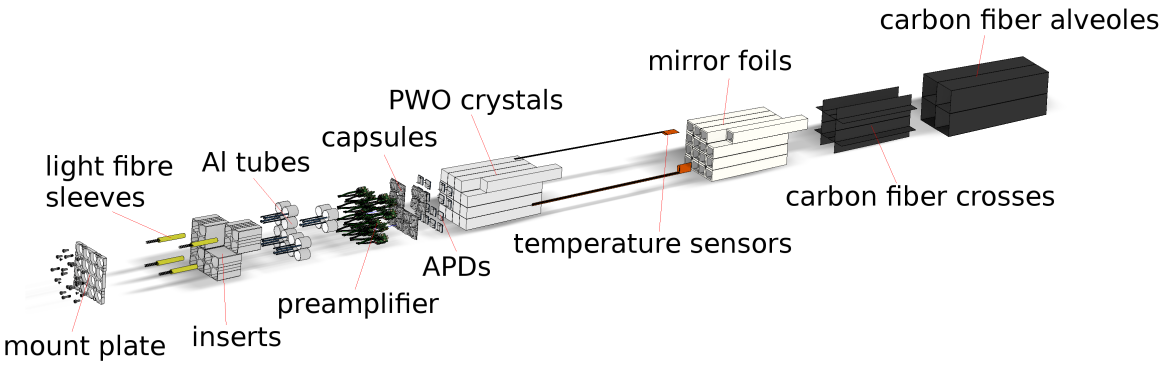

Figure 5.30: Exploded view of an APD submodule. [1]

5.2.2 Arrangement of Electronics

In the forward endcap 10 THMPs are used to read out the temperature and humidity sensors. More information on the THMP can be found as a brief summary in Sec. 6.2.3 and in more detail in Miriam Kümmel's PhD thesis [2]. In order to achieve electromagnetic shielding and to protect the THMPs, they are inserted into aluminum housings. These aluminum housings are adapted KO HL 2 combination housings from Fischer Elektronik GmbH & Co. KG. The temperature sensors are read by a four-wire measurement. The four openings on the top of the housing are cable bushings for the associated ribbon cables.

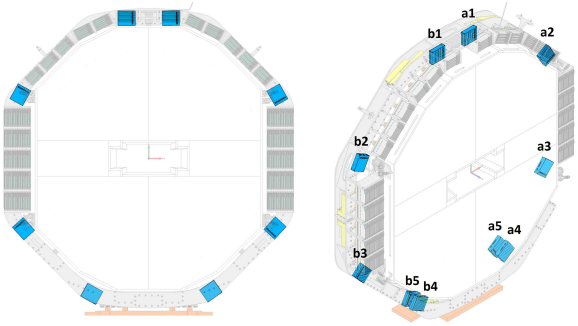

Figure 5.31: Two CAD views of the forward endcap with numbered THMPs highlighted in blue [1].

The THMPs are mounted on the support frame and their positions on the forward endcap are shown in Fig. 5.31. When attaching the THMPs to the support frame, the alignment must be observed so that the side with the adjusted front panel points towards the point of interaction. [1]

The arrangement of the readout electronics of the photodetectors can be found in Sec. 4.7.2.

5.2.3 Light Pulser Monitoring System Integration

To avoid crossing of fibers and cables, the backplate uses the same routing for fibers and cables (see [1]). This is shown in Fig. 5.32.

Beginning at the submodules, the optical fibers are first laid on the backplate before supply cables are routed to the submodules. They are therefore in direct contact with the backplate. The supply cables are mounted on adapter boards, which are mounted on the backplate behind each submodule with stud bolts. Between the studs of two boards there are 12.8 mm space for laying, exactly in the middle between two boards the height of the free space is 13 mm. A strand will never contain more than 544 fibers. [3]

For the forward endcap, ten light pulser modules are required, which are mounted in the support frame. Fig. 5.33 shows the endcap with mounted light pulser modules. After irradiation with a gamma and neutron source with a multiple of the radiation dose expected in 10 years of operation, no impairments of the light pulser were found [3].

Four "I-shaped" modules are mounted in the upper part of the support frame, two of them are in the same position but aligned differently. Six "L-shaped" modules are placed at the sides and the bottom of the support frame, because it is not possible to connect the supply cables at the back as with the "I-shaped" module, but to connect them

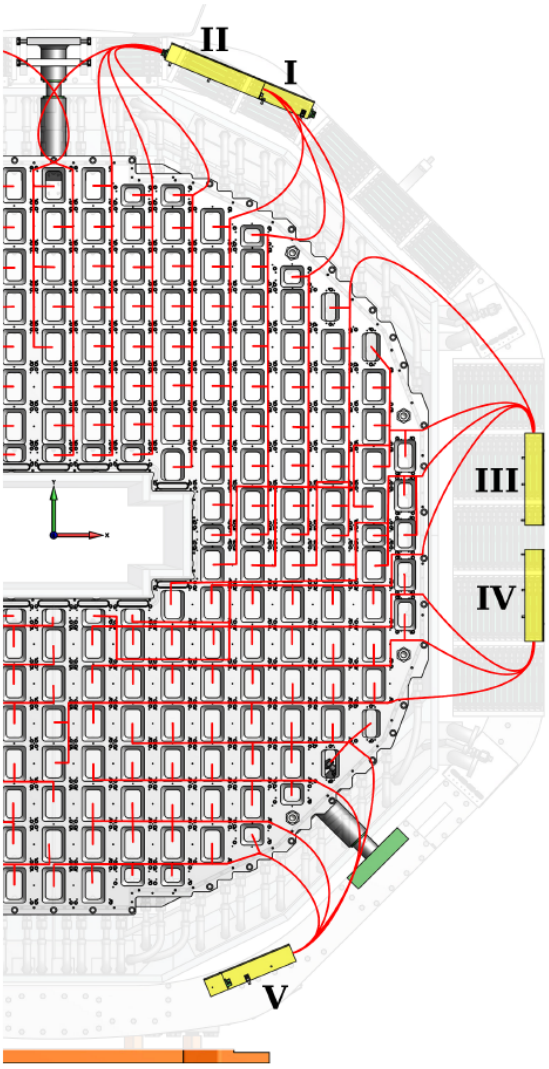

Figure 5.32: Light fiber distribution of the strands on the backplate. You can see only one half of the backplate, since the distribution is symmetrical. The light pulser modules are marked by the roman numbers [3].

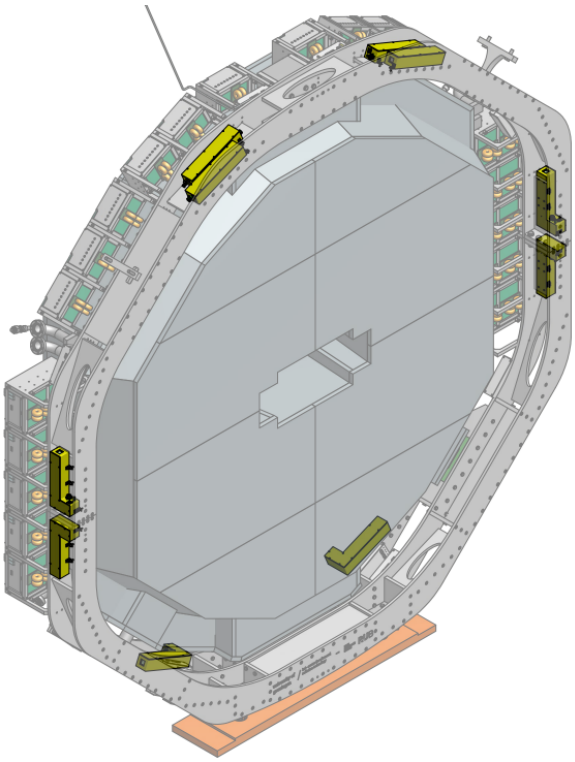

Figure 5.33: The forward endcap of the EMC. The two light pulser module shapes (I + L) are shown in yellow [3].

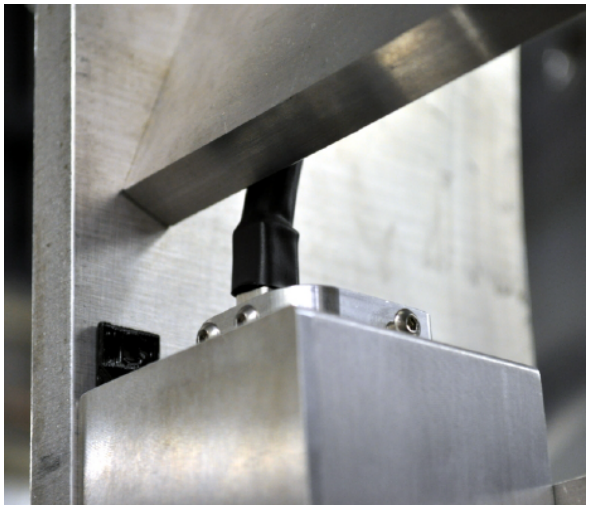

Figure 5.34: Mounting of the fiber strands on light pulser modules in the support frame. The minimum bending radius of the optical fibers is maintained [3].

from the same direction as the fiber strands have to be fed in. The mounting of the fiber strands to the light pulser modules III and IV (see Fig. 5.32) is demanding due to a cross plate in the support frame of the endcap (see Fig. 5.34). The minimum bending radius is not exceeded with mounted fiber strands, but it is not possible to attach and detach the fibre strands if the light pulser module is fixed to the support frame. To achieve this the light pulser module is mounted on the support frame after all fiber strands have been fixed. [3]

In order to separate the electrical ground of the housing of light pulsers and the support frame, not only mounting angles made of polylactide are used, but also, since the housing touches the frame on the bottom and side surfaces, an insulating layer (polyamide) is placed between the housings and the support frame. [3]

5.2.4 Insulation and Cooling

The $\overline{\text{P}}$ANDA EMC is cooled down to −25 °C to improve the light output of the $PbWO_4$ crystals. A coolant pump and a cooling unit are responsible for both endcaps and the barrel area. Both the pump and the cooler are positioned in a recess in the hall floor. A mixture of methanol (60 %) and water (40 %) is used as coolant, which is distributed to the two detectors near the barrel area by a distribution box. [1]

5.2.4.1 Structure of the Thermal Insulation

The complete thermal insulation of the forward endcap, constructed of vacuum insulation panels, has a surface area of 11.2 m^2 and a thickness of 15 mm for the panel before the front cooling and the scintillation crystals and 20 mm for the remaining areas. The design of the insulation is divided into the sections listed in Table 5.4.

Table 5.4: Parts of the thermal insulation of the forward endcap [4].

Part	Area [m^2]	Panel thickness [mm]
Front panel	3.08	15
Back plate	4.29	20
Inner Stiffener ring	0.93	20
Outer Stiffener ring	1.28	20
Side area with feed-throughs	2.35	20
Total	11.93	

In order to reduce the number of direct thermal bridges between the cooled interior of the detector and the exterior to room temperature, the total thickness is achieved at many points of the insulation by overlapping thinner panels with a wall thickness of 10 mm. However, this method is not applicable everywhere. On the one hand, the front panel cannot be made up of several layers, since the minimum producible panel thickness is 10 mm. Thus two layers would exceed the allowed total thickness of 15 mm. On the other hand, panels with multiple bevelled edge surfaces are applied in a non-overlapping manner. Chamfered edge surfaces and panel thicknesses less than 20 mm result in a part of the production-related turned-over lashing surrounding foil resting on the edges of the panels. The combination of the overlapping flap and bevel means that a virtually joint-free connection cannot be guaranteed while maintaining the required angle. Furthermore, no areas are insulated in an overlapping manner, which can be lined with an additional insulating material. This leads to a reduction of production costs, since the additional lining can be carried out with other, cheaper insulating materials. All insulation panels are bonded with the easily applied Sabacontact AAC adhesive from SABA. The adhesive consists of a CR-polymer or neoprene and is characterized by a high temperature resistance. Fig. 5.35 shows a CAD drawing of the front and rear view of the forward endcap and the thermal insulation without further components of the endcap. [4]

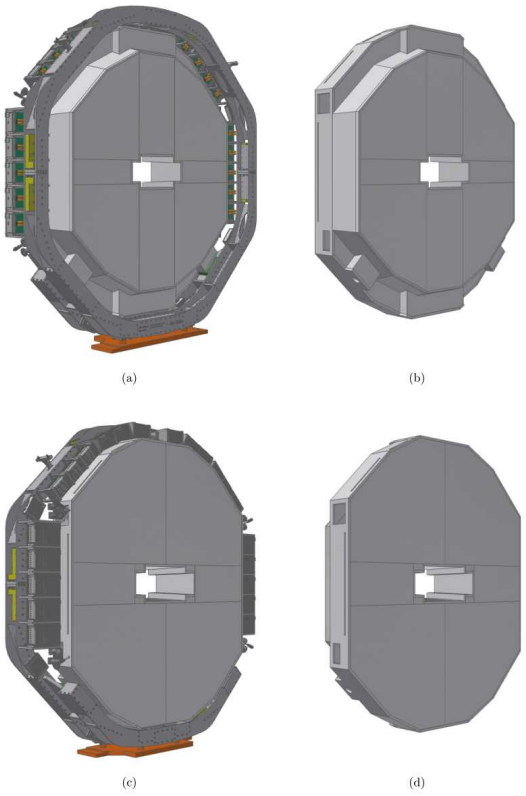

Figure 5.35: Front and rear view of the complete forward endcap (a and c) as well as thermal insulation without further components of the endcap (b and d)[4].

5.2.4.2 Cooling

To reach the operating temperature of −25 °C and to ensure temperature stability a cooling system consisting of four separate cooling circuits is used. These are the main cooling, side cooling, front cooling and air cooling. For the first three cooling systems in the enumeration, a methanol-water mixture will be used with a ratio of 60:40.

5.2.4.2.1 Main cooling The main heat loads of the forward endcap are the cable bushings and the photodetectors or the preamplifiers of the photodetectors near the $PbWO_4$ crystals. The main heat load is removed by the main cooling system. To dissipate this heat load, the base plate, on which the submodules are mounted, has cooling pipes running through it. This is shown in figure Fig. 5.36.

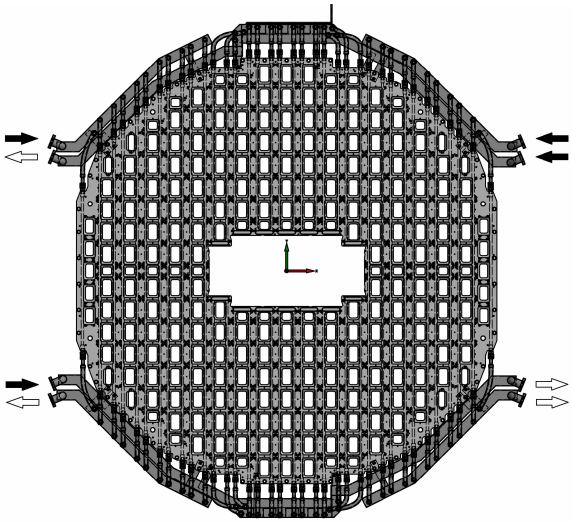

Figure 5.36: Technical view of the base plate of the forward endcap with highlighted internal cooling pipes and connected manifolds. The filled arrows show the direction of the inflowing coolant and the unfilled arrows show the direction of the draining coolant [1].

A total of 36 holes with a diameter of 13 mm pass through the base plate. Flexible metal tubing with an internal diameter of 12.7 mm from Swagelok FJ series connects the 72 fittings to eight stainless steel (304) manifolds. The manifolds are attached to the outer support frame and each has a CF40 port for mounting the coolant supply and return lines. The metal hoses are bolted to two manifolds. In order to reduce possible leaks, this has been changed for the other six, where the end connections of the metal hoses are welded to the main body. Due to the limited space around the base plate, it is not possible to install valves for flow control. As a result, the flow rate per connection depends on the design of the manifold. To ensure that there is sufficient flow per cooling connection to dissipate the heat, a sealing washer with an individual inner diameter is inserted per metal hose at the connection to the base plate. This allows an individual adjustment of the flow per cooling line within the base plate.

5.2.4.2.2 Side cooling The side cooling serves to reduce the temperature gradient in the scintillation crystals and is mounted on the inside of the outer stiffener ring. The stiffener ring forms the outer wall of the cooled area of the forward endcap and connects the equipped backplate with the aluminum front plate of the detector. Since all submodules point to a common point away from the point of interaction, the shape of the ring is a truncated pyramid with a dodecagonal base area. In order to reduce the pressure loss in the cooling lines and at the same time to achieve a homogeneous temperature distribution three top to bottom cooling chambers are installed per half of the detector. Aluminum pipes with an outer diameter of about 9.5 mm or $3/8''$ are used. The corresponding supply lines are located in the upper part and the discharge lines in the lower part of the endcap. The cooling fluid flows thus from top to bottom through the cooling lines. Due to the small space between the submodules and the stiffener ring and to improve the thermal contact between the cooling circuit and the ring recesses for side cooling were milled into the ring. Fig. 5.37 shows the milling for the mounting of the cooling lines.

The diameter of each cutout is 10 mm, the total length of the cut outs depends on their position in the ring and vary between 2.34 m and 2.47 m. The aluminum tubes are shaped so that they touch the ring at every point in the cut outs, which improves the thermal contact. The thermal contact between the cooling pipes and the stiffener ring is further improved by gluing the pipes into the milled recesses with a heat conducting adhesive. In addition, the tubes are pressed to the ring by 30 mm wide and 200 mm long aluminum cross braces. The three cooling lines per half of the ring are connected via a common supply. The homogeneous distribution of the cold methanol-water mixture to the three aluminum pipes are made via distribution boxes, which are installed in the upper and lower area of the stiffener ring (see Fig. 5.38).

5.2.4.2.3 Front cooling The front cooling is located on the inside of the aluminum front panel in front of the submodules. The front cooling serves to dissipate the heat flow, which occurs despite thermal insulation in the front area of the forward endcap and reduction of the temperature gradient along the scintillation crystals. The reversibly attached front insulation consists of 15 mm thick vacuum insulation panels at this point and a base area of $3.08\,m^2$. The total heat flow to be dissipated by the front cooling, taking into account the thermal bridges between the panels and a safety factor of 1.5 is 80.3 W. The front cooling consists of an alu-

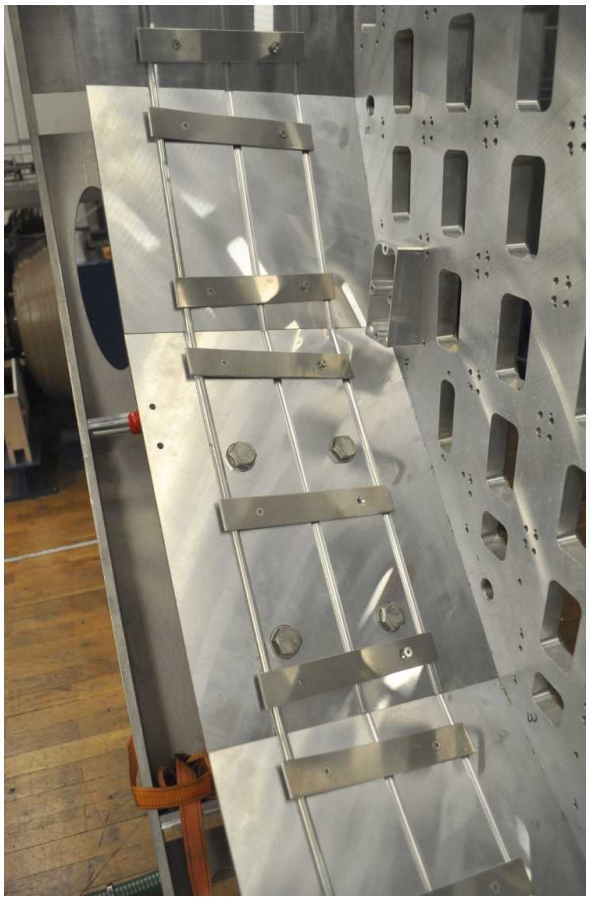

Figure 5.37: Cut outs in the stiffener ring of the forward endcap to accommodate the cooling lines of the side cooling. Left milling with inserted aluminum tube. In the middle and on the right the cut outs are without tubes [4].

minum front panel with plate thickness of 0.8 mm, an aluminum frame with a thickness of about 9 mm at the outer edge of the plate and the pipes used to distribute the coolant, which are attached to the inside of the front panel. The small thickness of the aluminum front panel is a compromise between the lowest possible material allocation and the stability. The dimensions of the front panel are 1.947 m in height and 1.915 m in the width. The standard dimensions of commercially available metal sheets (maximum width of 1.5 m) are smaller than the dimensions of the front panel, therefore the front panel was made of two aluminum plates welded together. To increase the stability of the front panel, an aluminum frame is glued to the front panel in an airtight and moisture-proof manner. This spacer frame additionally serves to compensate for unevenness on the front surface of the stiffener ring for better attachment of the front panel.

For an efficient dissipation of the heat flow and to reduce the temperature gradient within the crystals, the cooling must take place over the entire surface of the aluminum front panel. In order to cool the front panel evenly, the cooling elements of the two circuits are laid in a meandering pattern. The exact course of the line depends on the respective distance between the front surface of a submodule and the front panel. Since all submodules are connected via elbows to a point away from the interaction point, all four corner points of the front surface of a submodule have a different distance to the front panel. Fig. 5.39 shows the distances between the corner points of the front panels of the submodules and the aluminum front panel.

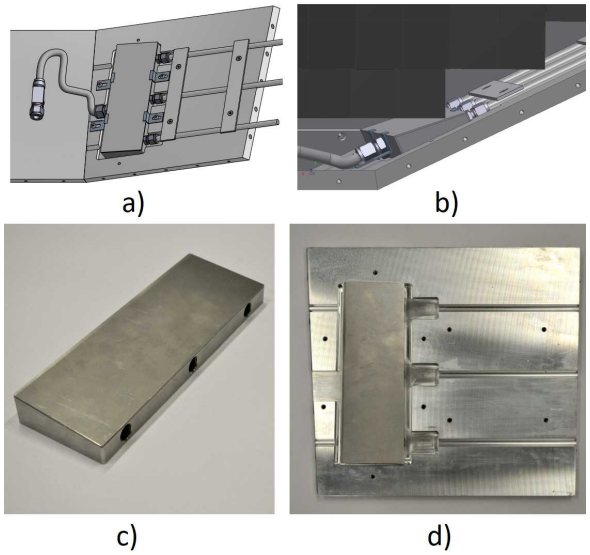

Figure 5.38: a) and b) are CAD-drawings of the distributor box mounted on the stiffener-ring. c) and) are the final distributor box and a machined element of the stiffener ring with milling cut outs. [4]

All distances smaller than 12 mm are marked red, distances between 12 mm and 16 mm are shown in yellow and all distances greater than 16 mm are colored green. The smallest distance of all modules is 11.2 mm, the largest distance is 48.6 mm. The submodules are mounted symmetrically on the forward endcap. The final design considering the above mentioned restrictions for both cooling lines of the front cooling system is shown in Fig. 5.40.

5.2.4.2.4 Air cooling The area near the front and back of the base plate is flushed with dried, cooled compressed air to cool this area and additionally prevent ice formation. The air is cooled by vacuum-insulated tubes and is guided through the magnet to the forward endcap. From there the air is directed to the lower part of the electronics frame.

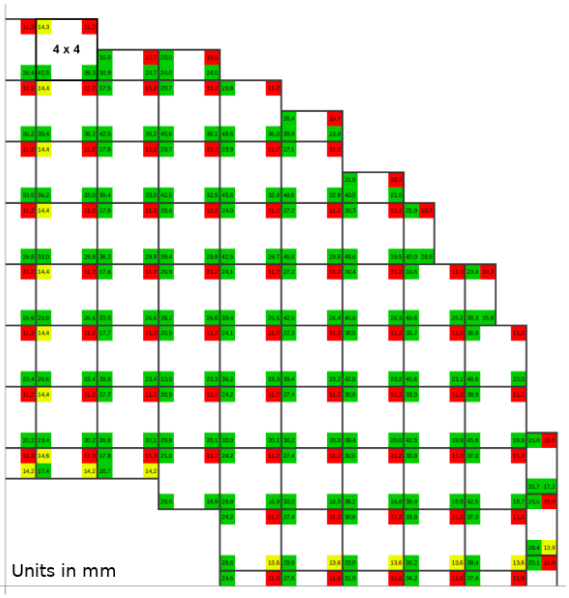

Figure 5.39: Distances between the submodules and the aluminum front panel for a quarter of the forward endcap [4].

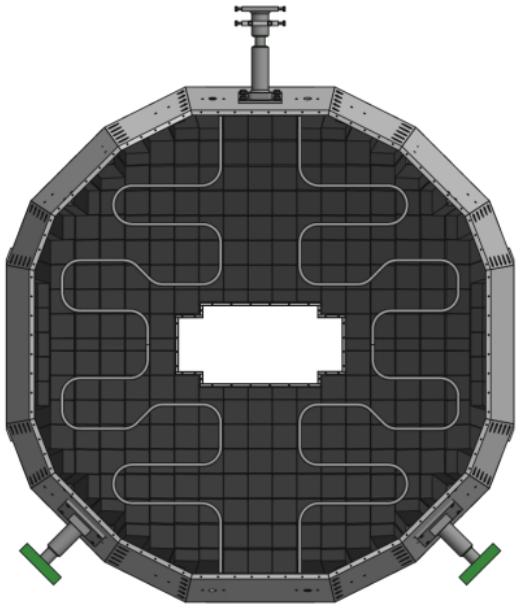

Figure 5.40: CAD drawing of the two final partial circuits of the front cooling with hidden front panel [4].

In the electronics frame there is a feed-through for the air, which is then transferred through a tube to the inner stiffener ring (see Fig. 5.41). The air flow inside the forward endcap is achieved by sealing the four mounting holes of the connectors located in the inner area of the forward endcap. After exiting the electronics frame, the air is directed through the magnet by means of tubes. The selection of the outlet openings in the electronics frame ensures that the inner volume of the forward endcap is flushed with dried air evenly.

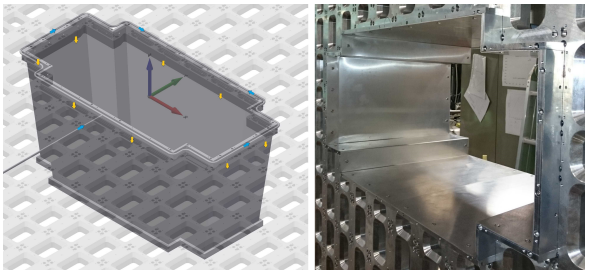

Figure 5.41: Left: Direction of air flow near the inner stiffener ring. The direction of air flow in the supply line is shown in blue. Yellow is the air flow direction through the inner aluminum frame and between base plate and inner stiffener ring. Right: Inner stiffener ring mounted on the base plate. [1].

5.2.5 Submodule Mounting and Tests

For each position of a submodule an aluminum interface piece is used to obtain the desired orientation to a point before the interaction point. Alignment pins are used to ensure exact positioning. This inclined alignment of submodules with respect to the back plate means that submodules mounted at outer positions overlap with submodules mounted at inner positions. Due to the alignment pins, the submodules must be shifted orthogonally to the back plate at least for the last few millimeters. Therefore, the submodules must be mounted starting with the innermost ones and it will not be possible to remove further innermost submodules after completion of the assembly. After mounting the submodules on the back plate of the forward endcap, each submodule must be tested immediately, so that it can be repaired if something does not work properly. Therefore, each submodule is connected to the power supply, readout electronics, and associated DCS components provided by a test stand.

During the assembly process, the submodules are supported by a Dalmec hydraulic manipulator arm, which was used by the CMS collaboration for the assembly of the EMC of the CMS detector (Fig. 5.42, left) and borrowed by the PANDA collaboaration for the assembly of the EMC. [2]

The manipulator arm is able to carry a total load of 50 kg, which includes not only the submodules but also an individual support. Each interface has two holes on its outer side wall. The submodules are

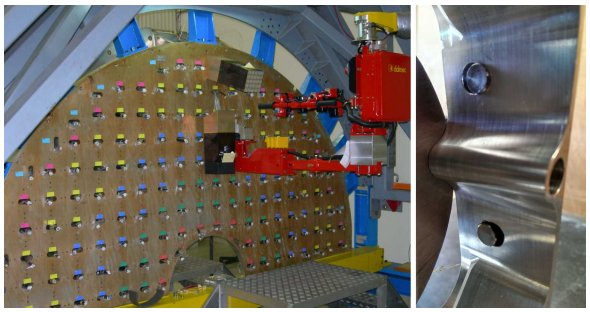

Figure 5.42: (a) Hydraulic manipulator arm used to assemble the endcaps of the electromagnetic calorimeter of the CMS detector (b) Interlocked interface [2].

mounted by means of a holder with two pins, which act as a quick locking system as shown in Fig. 5.42 (right). When the submodule is mounted and attached to the back plate and the weight is released from the holder, it can be easily removed. In addition to the geometrical limitation of the mounting sequence, it is also important to apply the mounting sequence symmetrically to avoid torque. Furthermore, the holder for submodules mounted on the right will be a mirrored version of the holder for submodules mounted on the left. On the side and for horizontally aligned submodules with eight crystals, an adapted holder is again required. With all these considerations in mind, the mounting sequence shown in Fig. 5.43 has been developed. [2]

The forward endcap will be fully tested at the Cooler Synchrotron (COSY), in Jülich before being operated at the HESR at FAIR in Darmstadt. The hall in Darmstadt, in which $\overline{\text{P}}$ANDA will be located, has not yet been built. In order to be able to assemble the forward endcap within the planned time frame, the assembly of the forward endcap will take place with the installation of all submodules in Jülich. Therefore, the complete forward endcap has to be transported from Jülich to Darmstadt once. The expected position of the forward endcap for assembly in Jülich is shown in Fig. 5.44. [1]

The forward endcap requires a secure stand and additional protection against tipping over for both assembly and transport. The transport frame is shown in Fig. 5.45. In addition, to reach the beam height of 2200 mm above the hall floor at COSY, the forward endcap must be raised by about 485 mm. To meet these two requirements, the forward endcap is assembled in a multi-part frame, which can be divided into two components as shown in Fig. 5.46. The construction of the frame was carried out at the Zentralinstitut für Engineering, Elektronik und Analytik (ZEA), subinstitute Engineering und Technologie (ZEA-1), of the research center Jülich. [1]

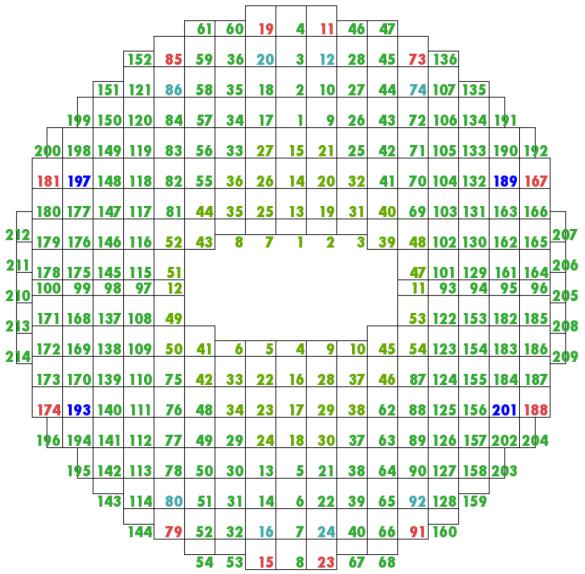

Figure 5.43: Mounting sequence for submodules of the TS EMC forward endcap seen from the IP with VPTT submodules in spring green, APD submodules in green, submodules which cannot be mounted in the naive sequence due to clashes with the outer stiffener ring in red, submodules which therefore must be mounted without alignment pins in teal and submodules which cannot be mounted with the mounting tool marked in blue. [2]

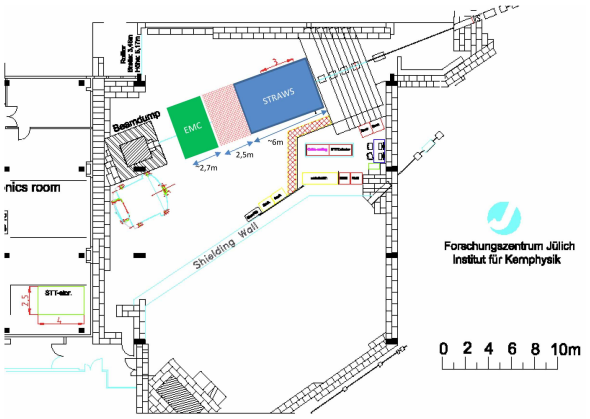

Figure 5.44: Expected position of the forward endcap (green) for mounting at COSY [1].

5.2.6 Integration into $\overline{\text{P}}$ANDA

The space available in the maintenance area in the $\overline{\text{P}}$ANDA hall for the installation of the forward endcap EMC and the connected Disc DIRC is only about 3 meters in downstream direction. The most suitable way to move these detectors into the TS is by lifting and rolling them on short precision rails. Fig. 5.47 shows the device under consideration. The support structure is shown in orange. A carriage

Figure 5.45: Transport frame of the forward endcap.

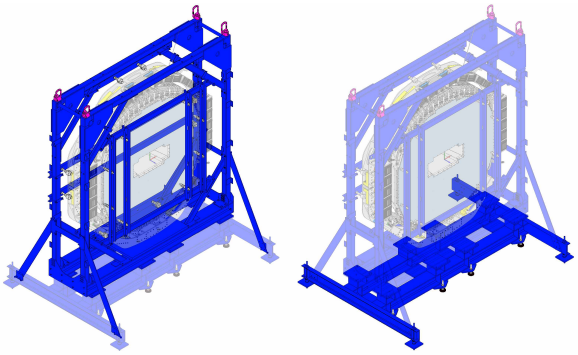

Figure 5.46: Left: Highlighted transport frame for the assembly of the forward endcap in Jülich and for transport to Darmstadt. Right: Highlighted undercarriage for raising the forward endcap in Jülich to the beam height of COSY [1].

(turquoise) will carry the forward endcap EMC and the Disc DIRC. Four cage roller guides (blue) on 2 precision rails (yellow) allow a smooth movement of the carriage. The center of gravity of the moving structure will be in front of the 4 roller guides. The rollers closer to the center of gravity must each carry 55 kN, while the other two carry only 15 kN each, but in the opposite direction. The forward endcap EMC is reloaded from its transport frame onto the wagon. In this position the Disc DIRC will be attached to the forward endcap EMC. A lifting device (marked in magenta) is required to lift the loaded trolley onto the supporting structure. This device is screwed to the top of the trolley and removed. The lifting point must be above the center of gravity. Due to the low friction in the roller guides, the force required to move the loaded trolley is only 300 N. No actuators are required to raise a force of this magnitude. [5]

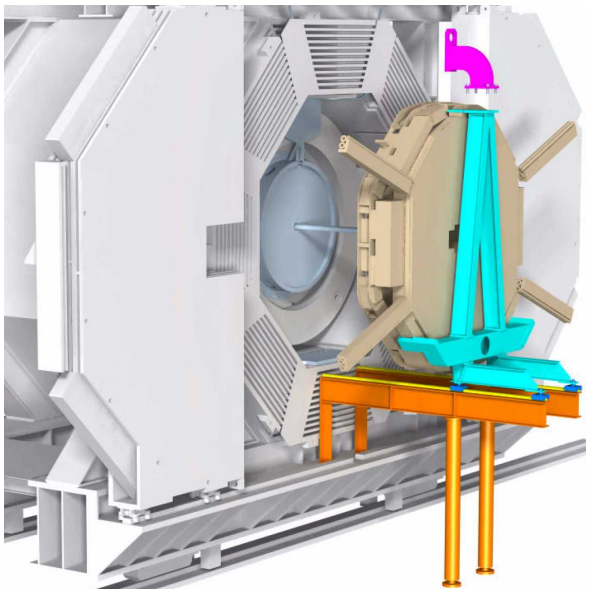

Figure 5.47: Support structure for installation of forward endcap detectors [5].

5.3 Backward Endcap

The BWEC is situated inside the barrel calorimeter at backward scattering angles. It contains about 500 straight crystals, read out with large area APDs, arranged in a ring and oriented parallel to the beam direction. The covered polar angle ranges approximately from 150° to 165°. The exact numbers will depend on the BWEC position along the beam axis, which in turn is determined by the space requirements for the readout electronics of the straw tube tracker, currently work in progress.

Like for the other parts of the EMC, the lead tungstate crystals are organized in submodules. The basic configuration of these is a 4×4 crystal array. Different layouts with some crystals removed from the 4×4 matrix are foreseen for the submodules in the corners and edges of the BWEC, in order to obtain an approximate ring shape.

Each submodule is attached independently through a holding structure to a common mounting plate and has independent signal readout and service connections, i. e. high voltage for the APDs, communication lines to the APFEL preamplifiers, light fibers to the crystals for delivering test pulses and temperature sensor readout.

5.3.1 Submodule Construction

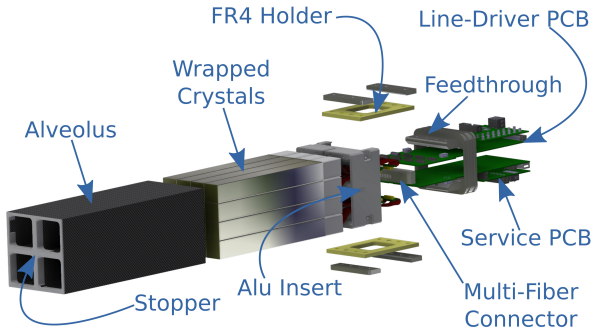

Figure 5.48: Exploded view of a BWEC submodule.

An exploded view of a 16-crystal submodule is shown in Fig. 5.48. The crystals are equipped as described in Sec. 5.3.1.1 and inserted into a carbon fiber alveole (Sec. 5.3.1.2). From the front side, i. e. downstream or towards the interaction point, they are kept in place by a 3D-printed plastic stopper which is glued to the alveole. From the back, the aluminum capsules containing the APDs and APFEL (see Sec. 5.3.1.1) are pressed against the crystals by an aluminum insert, which is also glued to the alveole. The insert is connected via two Fiber-Reinforced Plastic (FRP) plates to another aluminum element, called feed-through.

The feed-through is screwed to the BWEC mounting plate and holds the complete weight of the submodule. It is designed with grooves for two o-rings on the sides, in order to ensure air-tightness between the inside and the outside of the BWEC. It has two holes through which the front-end electronics boards are fed from the outside into the submodule. This way, all the services needed by the submodule stay within the projection of the crystals onto the mounting plate, allowing to mount the submodules very close to one another.

The FRP holders provide thermal insulation between the mounting plate and the insert, which is in thermal contact with the crystals. These holders and the alveoli underwent several stress tests, proving that they can bear the weight of the submodule while staying within acceptable displacements.

The first completely mounted submodule is shown in Fig. 5.49.

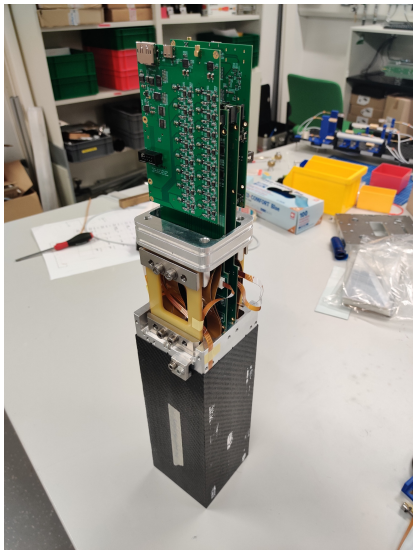

Figure 5.49: The first complete BWEC submodule.

5.3.1.1 Crystal Unit

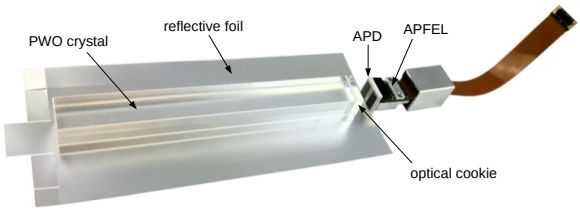

Figure 5.50: Crystal unit for the BWEC.

For the BWEC, only straight crystals are used. They have a length of 200 mm and squared front faces of 24.4 mm side length. Each crystal is equipped like shown in Fig. 5.50. A reflective foil of Daylighting Film DF2000MA by 3M is wrapped around the crystal. The nominal thickness of the foil is 66 µm and its reflectivity above 99 %. The foil is cut and incised beforehand at the position of the foldings with a laser, in order to make the wrapping procedure simpler and to avoid wrinkles or bulges in the foil, due to imprecise cutting or folding.

In the back (upstream) side of the crystal, the foil sheet is left open for coupling the APDs. These are

housed in a 3D-printed plastic case and optically coupled and glued to the crystal with Dow Corning 3145.

The APD case is shaped in such a way that the APD active areas are centered on the crystal face. The distance between the two APDs is fixed by the input connector of the APFEL board. Between them, the case features an opening for allowing the light produced by the annealing LED (mounted on the ASIC board) as well from the optical fiber connector (Sec. 5.3.4) to enter the crystal.

On the back side, the case has two pads to fix its position on an aluminum heat sink, on top of which the APFEL board is screwed. The heat sink was designed as large and massive as possible, to provide both a good electrical connection to ground and a good thermal contact to the cooling. This is important, because the APFEL is the main heat source inside the cooled volume. A hole is drilled through the heat sink for guiding the fiber connector to the crystal surface.

An aluminum capsule is screwed to the heat sink and covers APD case, APFEL board and heat sink. The capsule contributes to the heat conduction and provides electromagnetic shielding for the APDs and the APFEL.

Up to four crystals per submodule are equipped with a flat Pt100 temperature sensor (see Sec. 6.2.2).

5.3.1.2 Carbon Fiber Alveoli

Alveoli of different shapes are needed for the BWEC. However, since the layout of the detector is currently under redesign (see Sec. 5.3.2), the only alveole shape which will certainly enter the final setup is the 4×4 crystal matrix. Since the crystals are straight, the shape of the alveole is a parallelepiped with four holes, each of which houses four crystals in a 2×2 arrangement. The length of the alveole is 262 mm and it has a squared cross section with a side length of 101.1 mm. The aimed wall thickness is 0.40 mm with a tolerance of 0.05 mm. Therefore, the lateral dimensions of one hole, where 2 crystals need to fit, should never be less than 50 mm. This ensures sufficient room for the wrapped crystals to fit into the alveole.

Because of the limited number of needed alveoli, outsourcing their production to an external company was not possible. Therefore, they are manufactured at the Helmholtz Institute in Mainz. The manufacturing procedure consists in shaping pre-cut sheets of epoxy-impregnated carbon fiber (prepreg) sheets into a mold and curing the epoxy resin by baking the mold with the prepreg in an oven for some hours, as detailed in the following.

In Fig. 5.51, some details of the manufacturing procedure are shown. The picture (a) shows the mold, which consists of outer walls and mandrels. These are aluminum bars with a squared cross section of the dimension of the alveole holes. They have a circular perforation along their axis for inserting electrical heaters (Fig. 5.51-(b)), which, during the baking time, are controlled in automatized feed-back mode with the aid of a thermal sensor, to obtain a uniform temperature distribution inside the mold.

After cutting four sheets of prepreg to form the inner walls of the alveole's holes, each of them is wrapped around a mandrel. The mandrels are placed inside the outer mold walls and these are closed. The closed mold is pre-heated in the oven for one hour at 80 °C, in order to start liquefying the resin. Subsequently, the mold is reopened and a fifth prepreg sheet is wrapped around all four mandrels, which are already covered with prepreg. This way, both the inner and the outer walls of the alveole have two layers of prepreg. The wrapped mandrels are then closed anew into the mold, and the main backing is performed for four hours at 120 °C.

About 40 alveoli have been produced at the time of writing, which will be needed for the FAIR phase 0. The achieved tolerance in the lateral outer dimension is about 0.5 mm, and in the wall thicknesses about 60 µm, both within the specifications for $\overline{\text{P}}$ANDA.

5.3.2 Endcap Construction

The construction concept of the BWEC is shown in Fig. 5.52. All submodules are fixed to a common aluminum mounting plate with a thickness of 50 mm. The mounting plate has holes for fixing the submodule feed-throughs as well for the supply lines for the cooling and for the dry air used to keep the inner detector volume free of humidity.

The slots for the feed-through are positioned in order to have a clearance of 1 mm between two submodules. Considering the alveole wall thickness and the clearance within the alveole holes, the maximum distance between two crystals in neighboring submodules stays always below 1.5 mm.

On the inner and outer surfaces of the BWEC ring, cooling shells (Sec. 5.3.3) are fixed to the mounting plate and surround the submodules. Outwards of the cooling shells, VIPs are used for thermally insulating the detector. Finally, this assembly is closed

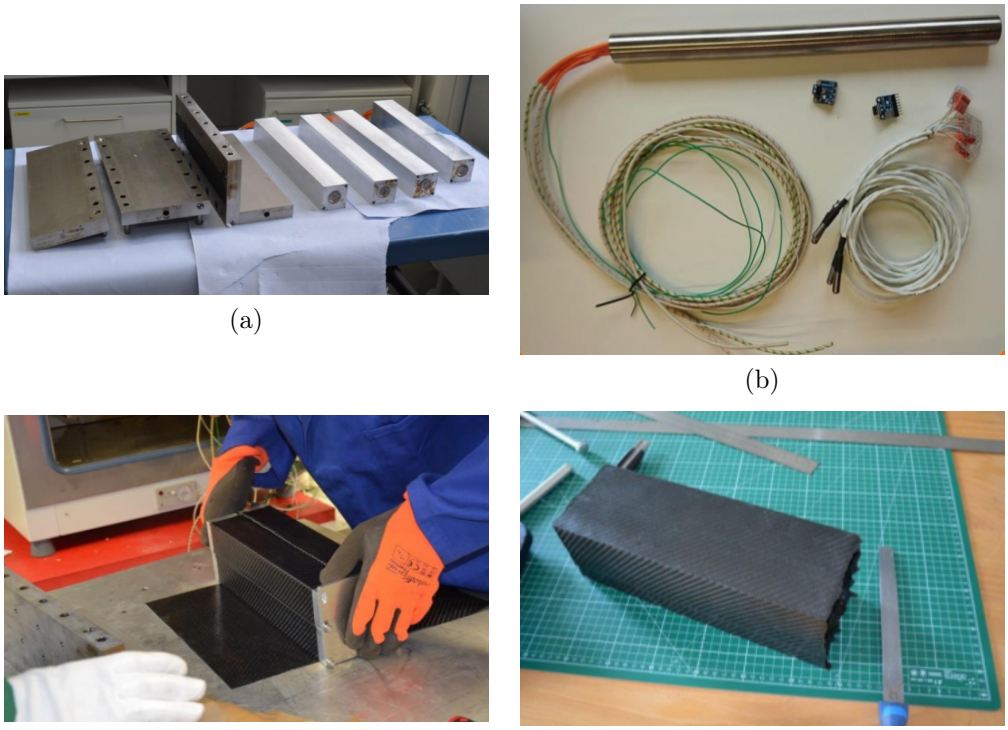

(a) (b) (c) (d)

Figure 5.51: (a) Mold parts for the BWEC alveole production. On the left part of the picture the outer walls of the mold are visible, on the right part the mandrels which define the inner holes. (b) Mandrel heaters to regulate the mold temperature from the inside. (c) Wrapping of the outer prepreg layer before the second backing cycle. (d) Completed alveole before cutting.

completely with an aluminum cover of 2 mm thickness which is also screwed to the mounting plate and provides electromagnetic shielding. Although the exact design of these components needs to be finalized, the overall thickness of these three layers will be about 25 mm.

The current design of the BWEC involves 524 crystals arranged as shown in Fig. 5.53. There are in total 36 submodules, 16 of which are of the basic 4×4 shape. The remaining 20 submodules, on the inner sides and on the corners are of four different shapes.

This layout needs to be re-designed, because the space requirements for the readout cables and service connections of the microvertex detector have increased during the development of that subsystem. Since these services are guided from the inner part of the target spectrometer to the outside through the BWEC central hole, the latter needed to be enlarged. Because of this change, the inner radius of the BWEC outer volume had to be increased from 165 mm to 175 mm. To accommodate this modification a complete layer of crystals needs to be removed and the innermost radius of the crystal ring will be around 200 mm. Consequently, the mounting plate, the cooling shells, the VIP and the outer cover need to be modified accordingly, which is currently an ongoing activity.

5.3.3 Cooling

The BWEC cooling system is divided in four sections, covering the detector from all sides: front, inner, outer and side. The front and inner sides will be covered by a thin aluminum sheet with a braced pipe circuit, minimizing the material budget on the particle path between the target and the crystals. The outer side cooling has 20 mm aluminum plates surrounding the detector. The pipes for the cooling medium are drilled in the plates. On the back side a bent pipe is brought into thermal contact with the aluminum inserts.

This system is currently under development and detailed FEM simulations both for the thermodynamic and the fluidodynamic characterization of the system have been performed. All main heat sources are taken into account in the simulations.

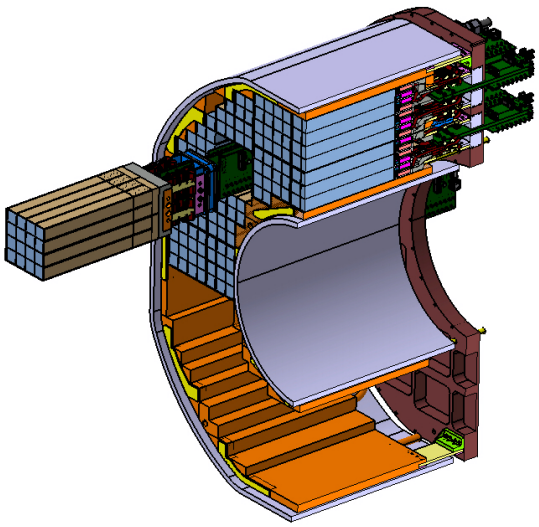

Figure 5.52: BWEC construction concept.

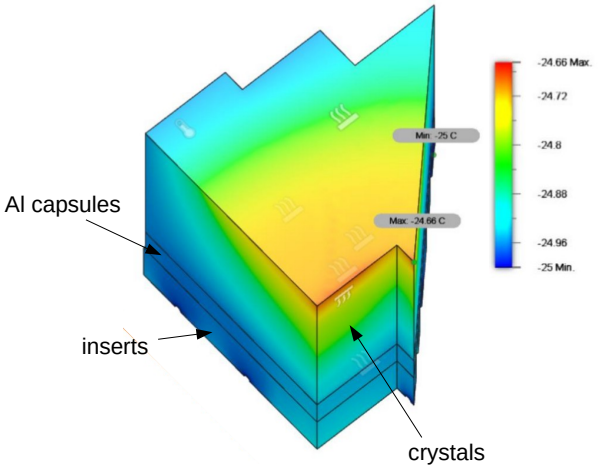

Figure 5.54: Results of a FEM simulation for the BWEC cooling. Only one quarter of the detector was taken into account, which is sufficient for symmetry reasons. In the picture the crystals are facing upwards and are described as one single volume, as well as the aluminum inserts and preamplifier capsules.

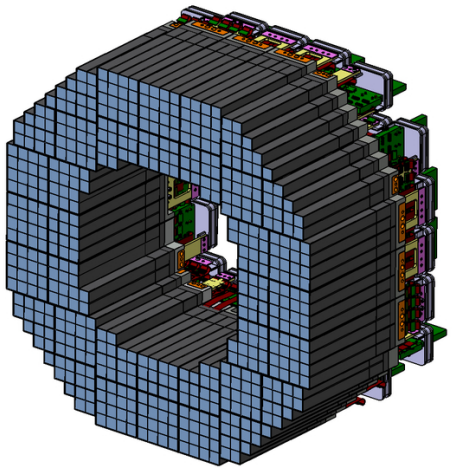

Figure 5.53: Current BWEC layout.

These are the preamplifier inside the cold volume and the heat from the neighboring detector systems, i. e. the front-end electronics of STT and MVD, which enters through the BWEC walls and insulation. The total heat power to be removed is estimated to be around 300 W. According to these studies, the total temperature gradient along the crystals should stay below 0.5 °C. A graphical output from a thermal simulation is shown in Fig. 5.54.

As for the rest of the EMC, the cooling system is operated in leakless mode. The total estimated pressure drop of the system is 330 mbar.

Like in the other EMC parts, temperature monitoring is foreseen for the BWEC by means of very thin Pt100 (see Sec. 6.2.2).

5.3.4 Light Distribution System

In order to test the functionality of the light readout chain and to monitor the level of radiation damage, test light pulses need to be fed into the crystals. Their duration and the wavelength of their light have to be similar to those of a scintillation pulse produced in an electromagnetic shower.

As in the rest of the EMC, the test pulses are generated by a light pulser like described in Sec. 6.2.1. The light pulses are brought into the crystals by means of light guide fibers. At variance to the other calorimeter parts, the fibers in the BWEC will not be one single piece from the source to the crystals. This depends on the fact that, in the maintenance position, the BWEC needs to be moved outside of the spectrometer (as described in Sec. 5.3.5) and therefore every cable and service going into the detector must have the possibility to be disconnected at the level of the mounting plate.

In order to keep the services of the single submodules independent from one another, bundles of 16 fibers (10 m long) will be produced for bringing the light from the pulser to the submodule feed-through holders. From there other fibers will be guided

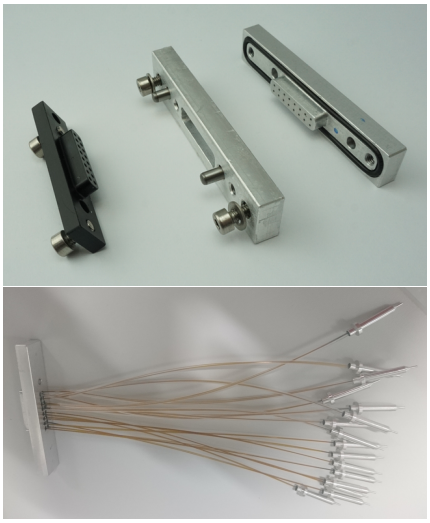

Figure 5.55: Top: multi-fiber connector parts to join the light fibers outside and inside the mounting plate. The middle component will be integrated in a new version of the submodule feed-through (not manufactured yet). The left (inner) and right (outer) connectors are 58 mm and 80 mm long, respectively. Bottom: fiber bundles inside the submodule. For every crystal, 4 quartz fibers (250 mm length, 0.2 mm core diameter) are used to guide the light pulses from the multi-fiber connector to the crystal surface.

through the inner part of the submodules to the individual crystals. The outer fibers and the inner fibers need to be connected properly in order to minimize the light loss at the transition. For this purpose, multi-fiber connectors like the ones shown in Fig. 5.55 have been designed. They are composed of three elements: the middle one is integrated in the submodule feed-through between the front-end electronic boards and keeps the outer and the inner element together. These have 16 holes, inside which the fibers are singularly glued. The holes are drilled on both elements at the same time to ensure a good alignment of the fibers.

In order to couple the fiber to every crystal in a defined way, and facilitating the submodule mounting procedure, the thin aluminum connectors shown on the bottom picture in Fig. 5.55 will be manufactured. The fibers are glued inside them and polished on the tip of the connector. These are inserted into a designated hole in the heat sink (see Sec. 5.3.1.1) and reach the crystal surface on a well defined position.

Several tests were performed for fixing the fiber diameter, in order to have enough light throughput to cover the full signal amplitude range of the readout. Eventually, one fiber per crystal with 0.8 mm core diameter was chosen for the outer segment, and 4 fibers per crystal of 0.2 mm for the inner segment. The choice of thinner fibers for the inside of the submodules is motivated by the shorter minimum bending radius, which is necessary inside the submodule. To compensate for the lower amount of light getting through the thin fibers, 4 of them are used for each crystal.

5.3.5 Integration in $\overline{\text{P}}$ANDA

The BWEC has to be positioned inside the time of flight detector with a tolerance of 1 mm. Its holding structure can be placed only outside of the $\overline{\text{P}}$ANDA solenoid doors. Therefore, a 1.2 m long cantilever arm needs to be used to connect the holding structure with the BWEC, whose weight will be approximately 700 kg.

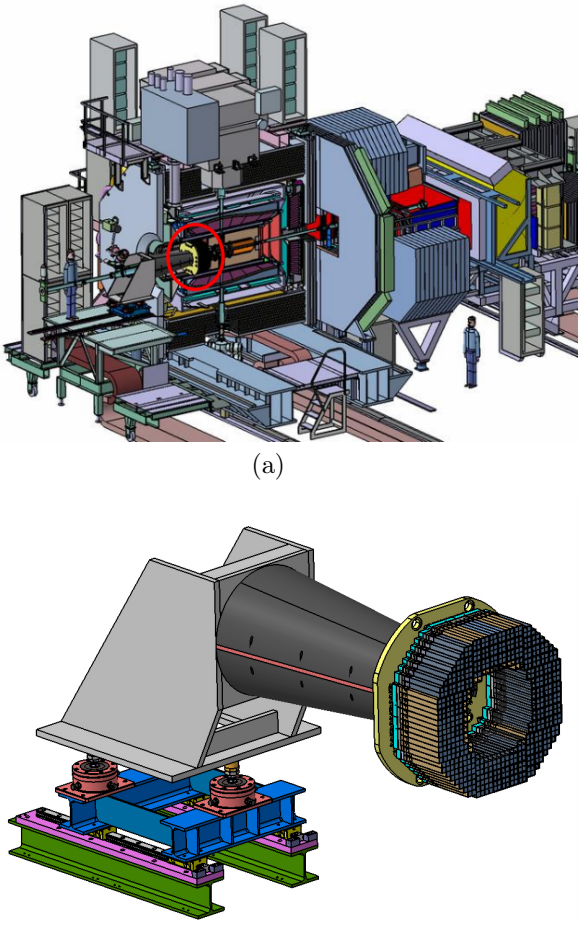

(a)

(b)

Figure 5.56: (a) Visualization of the BWEC inside the $\overline{\text{P}}$ANDA spectrometer together with its holding structure. (b) BWEC on its holding structure.

In Fig. 5.56-(a), the BWEC and its holding structure are shown within the PANDA spectrometer. The holding structure is fixed on an auxiliary platform, which is attached to the outer side of the solenoid magnet doors.

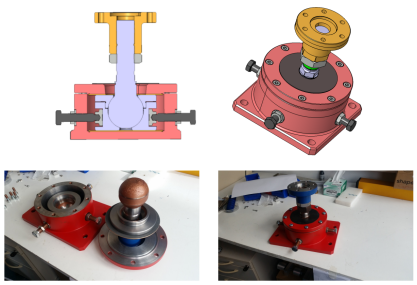

(a)

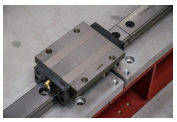

(b)

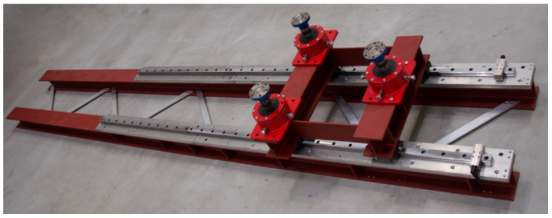

(c)

Figure 5.57: (a) Adjusting feet for precisely aligning the BWEC in all directions. (b) Moving blocks on precision rails. (c) Demonstrator for the complete moving support of the BWEC with rails.

The support structure is shown in Fig. 5.56-(b). The cantilever arm is attached to the mounting plate of the BWEC on the downstream side and on a steel support base of 1.2 m height on the upstream side. The base is fixed to three adjusting feet (Fig. 5.57-(a)), which are a GSI development and allow to adjust the detector in all 6 degrees of freedom. The positioning range in every direction is ±15 mm and the rotation range around every axis is ±5°. The feet can hold a pressure up to 100 kN and a tension of 40 kN. They are mounted on a "trolley" composed of two connected steel beams (in blue in Fig. 5.56-(b)). The trolley is in turn mounted on a rail system consisting of precision rails and moving blocks (Fig. 5.57-(b)) of type SHS-LC-45 by the company THK GmbH. They are specified for tension up to 100 kN and tolerances under this load of about 0.1 mm. The rails are finally installed on steel beams which are fixed to the platform. Fig. 5.56-(c) shows a sample of these rails mounted together with the trolley and the adjusting feet.

In the maintenance position, the auxiliary platform is extended upstream with a mounting platform, on top of which a second segment of rails of 10 m length will be installed. The BWEC needs to be moved on these rails along the whole length of the mounting platform while keeping its transverse position and orientation within the same tolerances specified for the operation position. The transitions between rail segments need therefore to be built with particular care.

Bibliography

[1] Claudius Schnier. *Analyse des Zerfalls $\eta_c \to \pi^+\pi^-\eta$ bei BESIII und Entwicklung von Komponenten für das elektromagnetische Kalorimeter des PANDA-Experimentes.* PhD thesis, Ruhr-Universität Bochum, 2019. https://nbn-resolving.org/urn:nbn:de:hbz:294-33806.

[2] Miriam Kümmel. *Analysis of $J/\psi \to \phi\,\eta\eta$ at BESIII and calibration of the temperature monitoring system for the PANDA electromagnetic calorimeter.* PhD thesis, Ruhr-Universität Bochum, 2019. https://nbn-resolving.org/urn:nbn:de:hbz:294-64681.

[3] Patrick Musiol. *Analyse der Kanäle $\chi_{c2} \to \pi^+\pi^-/K^+K^-$ in radiativen $\psi(2S)$-Zerfällen und Entwicklung eines Monitorierungssystems für das elektromagnetische Kalorimeter des PANDA-Experimentes.* PhD thesis, Ruhr-Universität Bochum, 2018. https://nbn-resolving.org/urn:nbn:de:hbz:294-57322.

[4] Stephan Leiber. *Analyse des Zerfalls $J/\psi \to \omega\pi^+\pi^-$ bei BESIII und Entwicklungen für das Kühlsystem und die thermische Isolierung des PANDA-EMC.* PhD thesis, Ruhr-Universität Bochum, 2018. https://nbn-resolving.org/urn:nbn:de:hbz:294-57457.

[5] PANDA Collaboration. Technical Design Report for the PANDA Detector Infrastructure and Installation. 2020. (submitted to FAIR for review).

6 Calibration and Monitoring

6.1 Precalibration with Cosmic Muons

To achieve the desired energy resolution of the electromagnetic calorimeter of the PANDA experiment a precise calibration is essential. During the experiment, the detector modules can be continuously calibrated using the decay of the π^0 or the η into 2γ. With the precalibration we aim at an accuracy of at least 10 % as seed for the initial calibration. These calibration factors contain the relative difference between the crystals from construction-related fluctuations and will give the best starting calibration for the detector. Furthermore, once the detector modules are installed they can not be easily replaced. Thus, the precalibration also serves as an additional functional test.

As an example, the FEC precalibration measurement will be described in the following section. Similar precalibration measurements will be performed for the slices of the barrel EMC and the modules of the BWEC. The basic principle of the measurements is to fit the results of detailed simulations of the energy depositions of cosmic muons in the test setup to the measured spectra, the resulting scaling factor (α) determining the calibration factor (c).

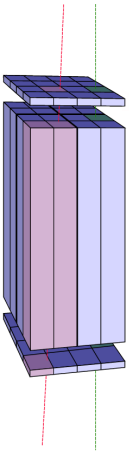

Figure 6.1: Schematic drawing of the 16 detector modules of one alveole with the corresponding trigger scintillators above and below. Two different tracks are shown.

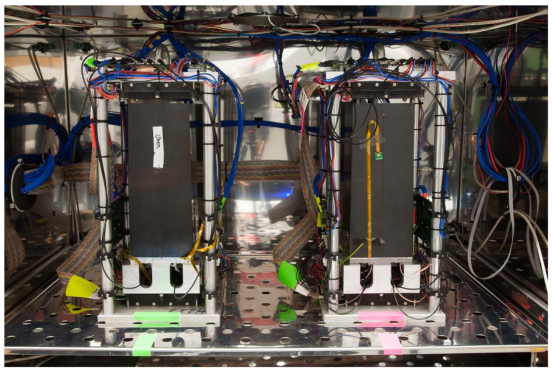

Figure 6.2: Picture of two test and precalibration setups inside one of the two climate chambers.

6.1.1 Forward Endcap Precalibration Setup

The setup of the precalibration measurements for the FEC modules performed in Bonn consists of 16 plastic scintillators placed above the detector modules and 16 plastic scintillators placed below, depicted in Fig. 6.1. The coincidence of the OR of the 16 plastic scintillators above and below acts as a trigger signal for the measurement. Additionally, the hit pattern of the trigger scintillators define the track of the cosmic muon through the PWO crystals, cf. Fig. 6.3.

The scintillation light of a crystal is detected by a VPTT (inner submodules) or two APDs. The resulting electrical signal is shaped by a circuit with similar filter parameters like in the foreseen SADC readout (Sec. 4.3.1) and subsequently digitized by an integrating ADC (Lecroy FERA4300B).

In the PANDA experiment the detector is cooled down to −25 °C in order to increase the light yield of the PWO-II crystals. For the precalibration measurements this is done as well. The measurements are done in a climate chamber which can house two complete setups (stations), cf. Fig. 6.2. The precalibration measurements in Bonn are done with two climate chambers, allowing measurements of four submodules at once.

The climate chambers are cooled down with about 4 K/h to reduce the thermal stress on the detector modules. With a measuring time of about 4 days, a total time of about 120 hours (including setup and cooling time) per precalibration is needed.

A sampled and scaled pulse of a preamplifier signal of an energy deposit of a cosmic muon was fed into

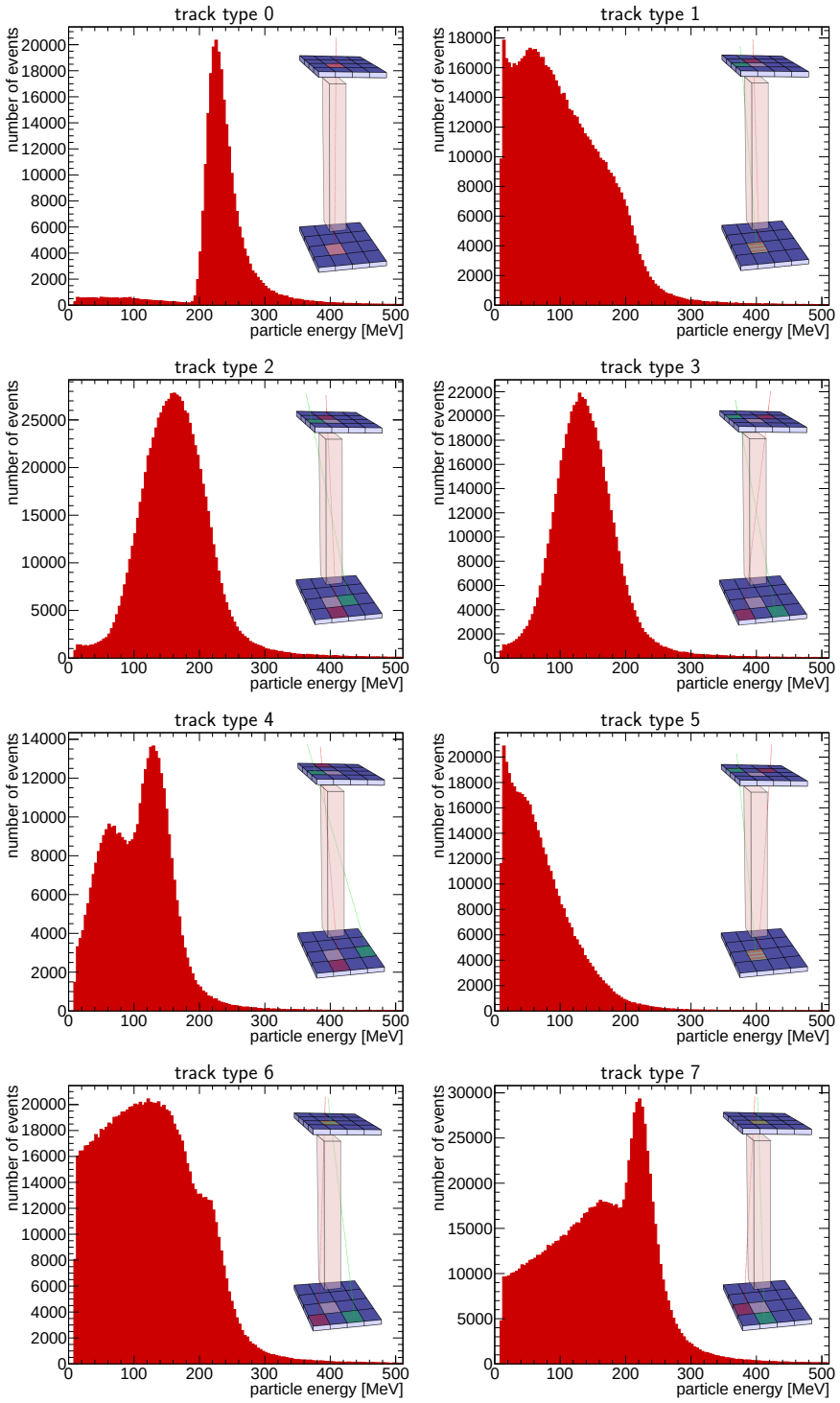

Figure 6.3: Simulated energy spectra for the eight different track types. All track types are defined by the trigger detectors which have seen a signal in coincidence with a detector module. The hit pattern is depicted in the insert. In this example only the hit detector module is shown. Since the upper trigger detectors are closer to the detector modules than those below, track types 1 and 7, as well as 5 and 6, result in different energy spectra.

the signal chain of every channel of all four precalibration stations to get the conversion factor T from ADC channels to mV. This allows to determine the calibration factor c (in MeV/mV) independent of

the measurement station: $c = T/\alpha$, where α is the scaling factor (in ADC channels/MeV).

6.1.2 Analysis

For a precise energy calibration, the exact amount of energy that a cosmic muon deposits in a given crystal is needed. A Monte Carlo simulation employing the Cosmic-ray Shower Library (CRY)[1], provides the deposited energies depending on the energy and direction of the cosmic muon. The simulated energy deposits are shown in Fig. 6.3 together with the corresponding track signature.

The simulated spectra then have to be fitted to the corresponding measured spectra according to $E_{\mathrm{MC}} \cdot \alpha = x_{\mathrm{ADC}}$. Here, E_{MC} is the simulated energy deposit, x_{ADC} the ADC channel of the measured energy deposit, and α the scaling factor (in ADC channels/MeV). The fitting is done by means of a binned Maximum-Likelihood fit. Assuming the number of entries in a given bin to be distributed according to a Poisson distribution, the following likelihood ratio[1] is minimized.

$$-2\ln\frac{\mathcal{L}(y,n)}{\mathcal{L}(n,n)} = 2\sum_i \left(y_i - n_i + n_i \ln\frac{n_i}{y_i}\right), \quad (6.1)$$

where n_i denotes the number of entries in bin i of the measured spectrum and $y_i = \int_{\mathrm{bin}\,i} f(\alpha)$ the number of simulated events in the corresponding energy range. The log-likelihoods of all possible[2] track types are summed up. Compared to just using the straight tracks, this increases the available information for the statistically limited fit. The minimum of the log-likelihood distribution is then determined as follows:

The scaling factor α is varied and the resulting log-likelihood calculated. Fig. 6.4 shows three examples of scaling factors and the log-likelihood distribution. The latter is fitted with a 4^{th} order polynomial to determine the position of the minimum. The uncertainty on the scaling factor is inferred from the position where the minimum value of the log-likelihood ratio increases by 1. With a typical measurement time of about 4 days, the statistical uncertainty is in the order of 1 %.

The analysis method was validated by a Monte Carlo (MC) study, where measured spectra with a known scaling factor α_{gen} were simulated. The determined scaling factor α was then compared to the simulated one. Fig. 6.5 shows the relative deviation of the determined scaling factor for different simulated scaling factors. On average the simulated value can be obtained with an uncertainty of about 1 %. Very small scaling factors (< 4) are an exception. Here the determined value is about 1 % too large. In the measured data, the scaling factors are typically in the order of 5–7.

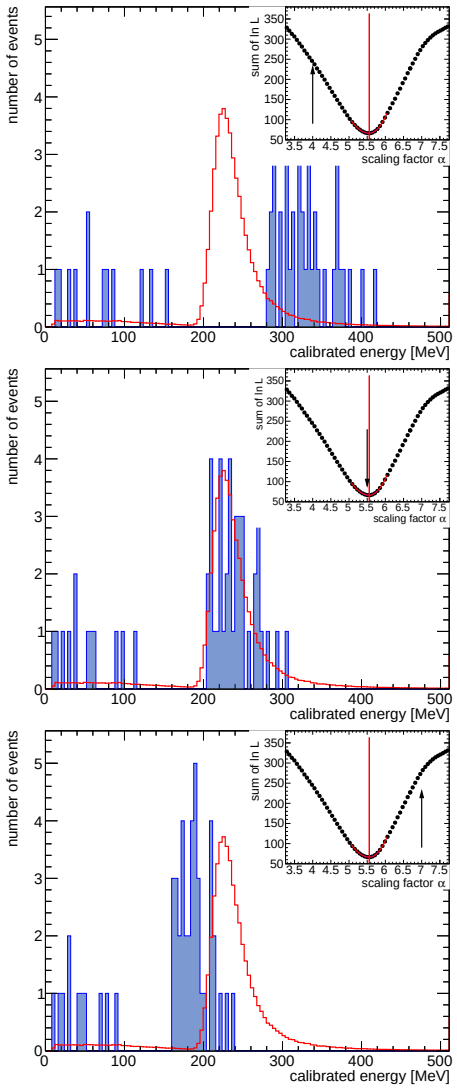

Figure 6.4: Maximum likelihood fit. The scaled measured spectrum for events of track type 0 (measurement time of about 6 d) is shown together with the simulated spectrum (red) for three different scaling factors. The log-likelihood is shown in the insert. The red line marks the minimum. The position of the shown scaling factor on the log-likelihood parabola is indicated with an arrow.

Further details on the precalibration setup and

1. The likelihood ratio follows a χ^2-distribution while having the same minimum as the single likelihood $-\ln\mathcal{L}(y,n)$.

2. Not all track types are possible for all crystal positions. E.g. track types 2 – 4 are not possible for crystals on the corner positions.

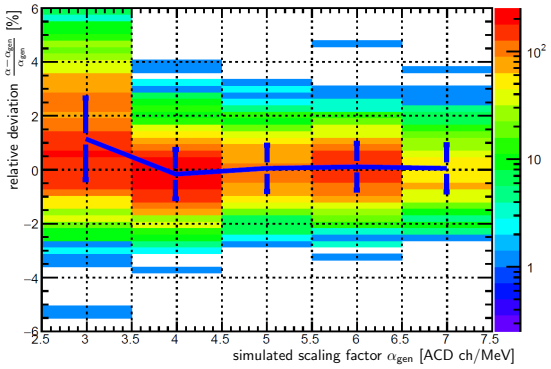

Figure 6.5: Relative deviation of the determined scaling factor to the simulated one for different simulated values. Every entry corresponds to a single scaling factor determination. The blue points mark the mean of the distribution, the error bars show its width (σ of a Gaussian). The statistics of the simulated spectra correspond to about 85 hours of measuring time.

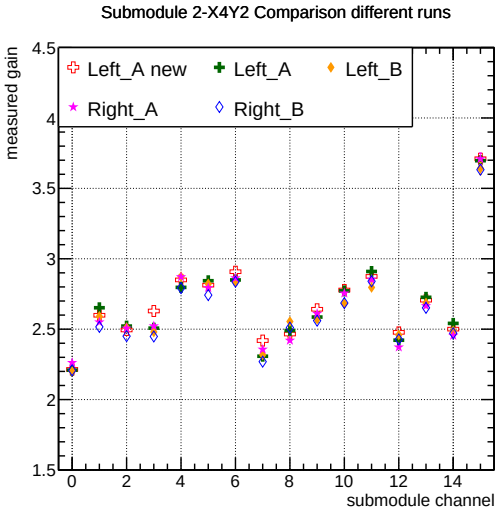

Figure 6.6: The same submodule (2-X4Y2) was measured on all four precalibration stations (Left/Right A/B). The measurement on the first station (Left A) was repeated nearly three months later. All results agree reasonably well.

method can be found in [2].

6.1.3 Results

To investigate systematic effects between the four precalibration stations one submodule, 2-X4Y2, was subsequently measured on all four stations. The results of the calibration factor are shown in Fig. 6.6. The results agree reasonably well with each other. A closer examination reveals systematic differences between the stations of less than 2 %. Additionally, the same submodule was measured in the first station again nearly three months after the first measurement. The determined calibration factors agree very well with each other, confirming the time stability of the precalibration measurements.

The precalibration measurements of the innermost submodules which are read-out via VPTTs, are completed. All submodules are functional and their calibration factors were determined. Together with the maximal voltage output of the preamplifier (2.2 V) the maximal detectable energy can be calculated from the calibration factors and the expected gain reduction in the magnetic field of the final setup (about a factor of 2). The latter was determined for every VPTT in a dedicated measurement in Bonn. Fig. 6.7 shows the maximal detectable energy of each submodule channel on its position in the FEC. The voltages of the VPTTs can only be adjusted in compartments of four. Thus, adjusting the voltage (between 750 V and 1000 V) such that all channels reach the desired energy of 12 GeV results in some channels having a higher maximal detectable energy. The 12 GeV can be reached in all but 11 channels (of 768). Those are just below 12 GeV with the lowest channel having a maximal detectable energy of 11.5 GeV.

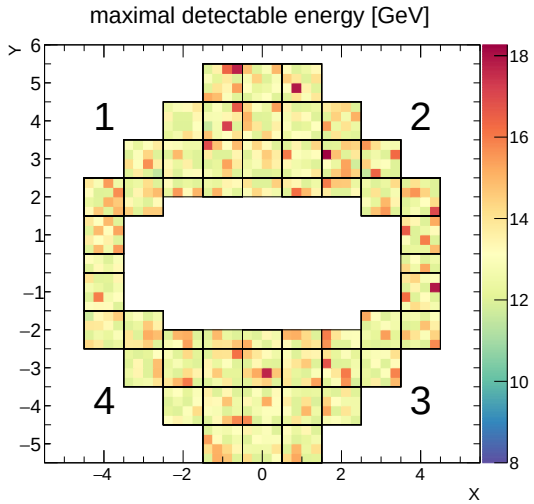

Figure 6.7: Maximal detectable energy of the VPTT-equipped submodules. Every black box marks a submodule with 16 (or 8) crystals. The large numbers indicate the sector of the FEC. The desired maximal energy of about 12 GeV can be reached everywhere.

The precalibration setup was adapted for the APD-equipped submodules, which are subsequently pre-

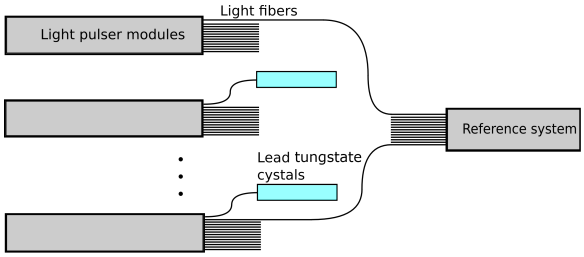

Figure 6.8: Overview of the PANDA calorimeter light pulser system.

calibrated.

6.2 Monitoring

6.2.1 Light Pulser Monitoring System

The light pulser system monitors light transmission losses in the individual crystals of the PANDA target electromagnetic calorimeter [3, 4] and represents a valuable diagnostic tool for the read out electronics linearity and APD gain as well as single channel response checks during assembly of the calorimeter. In the PANDA experiment it allows short term intercalibration in between the regular π^0 calibrations carried out once a day. The light source is designed to mimic the scintillation light of $PbWO_4$ with variable intensity spanning the whole energy equivalent range of 10 MeV up to 12 GeV [5].

6.2.1.1 Overview

The PANDA calorimeter light pulser system is based on several identical pulser units able to feed a maximum of about 500 crystals each by means of an optical fibre distribution system. Accordingly, the forward endcap part of the calorimeter is equipped with ten, the barrel with 32 and the backward endcap with two units.

6.2.1.2 Light Source

The light pulses resembling the $PbWO_4$-scintillation light are generated by blue high power LEDs (type Philips Lumiled Luxeon Rebel). In addition the sytem is able to generate also red and green light pulses in order to be able to distinguish radiation induced transmission losses in the crystals from other sources of degradation in the readout chain.

The blue light pulses are generated by a specifically developed high voltage circuit driven by

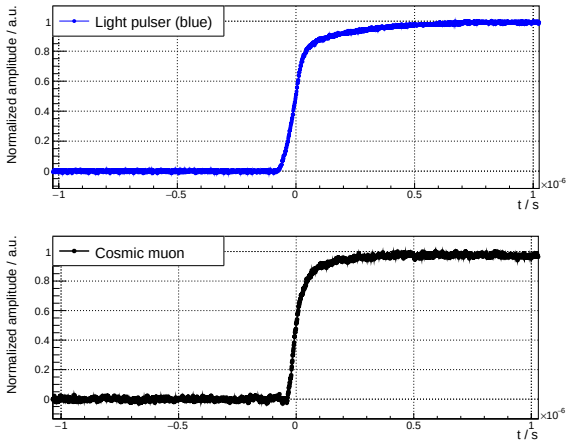

Figure 6.9: Rising edge of VPTT preamp response to a high intensity blue LED pulse (top) compared to the response to a scintillation light pulse (bottom).

Metal-Oxide-Semiconductor Field-Effect Transistor (MOSFET). The resulting pulses are as close as possible to $PbWO_4$ scintillation light pulses allowing proper checks of the complete readout chain from light detection to analog to digital conversion. Resulting output signals of forward endcap calorimeter charge integrating preamplifiers show time constants of about 100 ns rise time and 50 µs decay time as response to both scintillation light and light pulser signals (Fig. 6.9), the decay being determined by the charge integration time constant of the preamplifier.

The red and green LEDs are driven by a low voltage driver circuit each of the Kapustinsky type [6]. While lacking the intensity of the blue LED light that is capable of covering the whole dynamic range of the calorimeter the pulse shape of the green and red light pulses is similarly close to $PbWO_4$-scintillation light in order to be properly treated by the readout electronics as well.

6.2.1.3 Light Mixing and Intensity Variation

Besides the LED light sources the light pulser units contain LED attenuators and light mixing bars: The LED light is coupled via LEDiL LED lenses (Lisa 22° series for Luxeon LEDs) through a pair of 1″ × 1″ LCDs (type FOS, LC-Tec, Sweden) to an acrylic glass bar ($18 \times 18 \times 150\,mm^3$) with 800 grain size sanded entrance face and polished end face. The limited contrast ratio of LCDs, 1:80 for the types used, calls for the usage of a pair in order to safely cover the necessary dynamic range of about 1000 (Fig. 6.10). The resulting intensity variation over the light mixer end face feeding the air

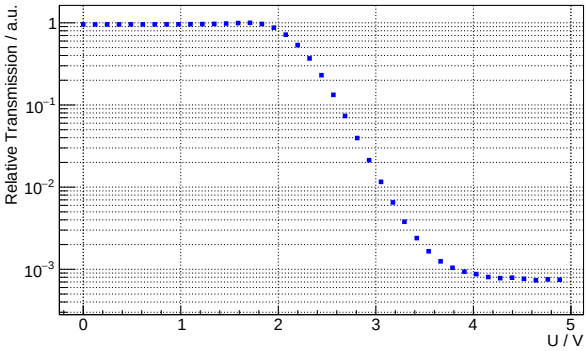

Figure 6.10: Blue light transmittance of an LCD pair as a function of the operating voltage.

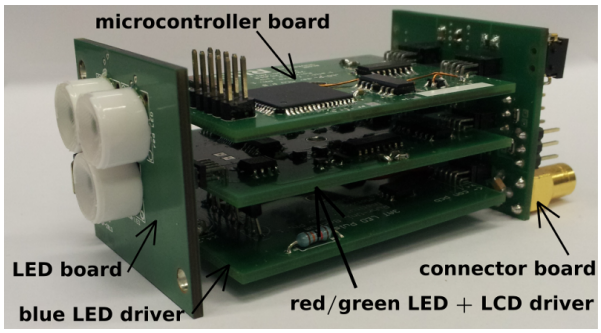

Figure 6.11: LED pulser PCB package.

coupled optical fibres bundles is in the order of 15 % to 25 %. The light intensity profiles are sufficiently stable (RMS of 0.3 %) over a period of 24 hours at medium light intensity.

In order to prevent electrolytic disintegration of the liquid crystals the LCDs need to be driven by square wave pulses rather than DC. The LCD transmittances are determined by the square-wave pulse amplitudes, the maximum being ±5 V in the light pulser system. The LED driver circuits are only triggered once within the positive half cycle of the LCD driving pulses. Furthermore a fixed phase relation between LCD polarization pulses and LED light pulses needs to be ensured, both in order to avoid the occurance of light pulse intensity modulations. Thus a limit for the light pulser repetition frequency is set by the maximum possible driving pulse rate of the LCDs (1 kHz).

6.2.1.4 Control and Electronics

The central control element of the light pulser units is a microcontroller (AT90CAN128-16AU) equipped with all necessary interfaces (SPI, CAN, Joint Test Action Group (JTAG), OneWire) and 128 kB of reprogrammable flash memory. The SPI bus is used for LCD and LED handler communication, CAN bus for external operation and control (pulser frequency, LED color, attenuation), and JTAG for programming the flash memory. Pulse triggers are either gererated internally by the microcontroller or externally received via low voltage differential signaling (LVDS) as being standard operation in the PANDA experiment (Sec. 4.8.6). The square wave pulses for LCD operation are generated by a DAC controlled via SPI by the Micro Controller Unit (MCU) and followed by a driver circuit. Fig. 6.11 shows the light pulser PCB-package consisting of LED, driver, microcontroller, and connector board.

6.2.1.5 Reference System

A time-stable reference for comparison of the individual light pulser unit intensities is necessary if a monitoring of crystal transparancy losses with the desired precision of 0.5 % is required. Thus light of every pulser unit is coupled via optical reference fibres to a photosensor that also detects $LaBr_3(Ce)$ B 380 crystal scintillation light induced by an adjacently placed ^{22}Na source. A VPTT readout unit was chosen as this photosensor because its gain is very stable under temperature or voltage variations. Enclosed in a light tight electrically shielded box it is acting as the reference system by comparing the pulser units intensities with the position of the photo peak in the sodium spectrum. The dynamic of the system allows comparison of all relevant intensities while the pulse shape of the $LaBr_3(Ce)$ scintillations are close enough to the ones of $PbWO_4$ to guarantee proper treatment by the PANDA calorimeter electronics that is used also for the reference system readout.

6.2.2 Ultrathin Platinum Resistance Temperature Sensors for PANDA

Due to spatial limitations and high precision requirements it is not possible to use commercially available temperature sensors to monitor the TS EMC temperature. Therefore, ultrathin platinum resistance temperature sensors have been developed at the Institut für Experimentalphysik I at the Ruhr-Universität Bochum.

In order to ensure an appropriate temperature regulation the temperature sensors thus need to have a precision matching the desired temperature stability of 0.1 °C.

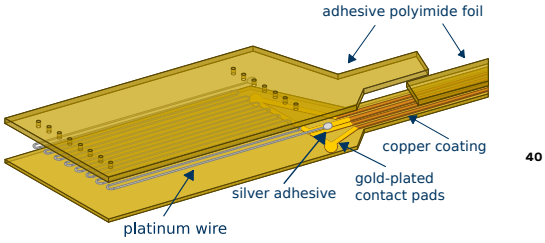

Figure 6.12: Design of a temperature sensor [8].

Besides the requirements on the precision of the temperature sensors there are strict requirements on the dimensions of the sensors, too. Since they are to be placed between the scintillators, they must fit in the tight geometry of the submodules, so their thickness has to be below 150 µm [7]. The width of the sensors must be smaller than 20 mm in order to not extend the width of the crystals.

In the forward endcap part one of these sensors per eight scintillators is foreseen, in the barrel part one sensor per ten crystals and in the backward endcap part one every four crystals, which amounts in total to $482 + 1152 + 131 = 1765$ ultrathin temperature sensors.

6.2.2.1 Design of Ultrathin Platinum Resistance Temperature Sensors

Using the same electronics (THMP, cf. Sec. 6.2.3) to read out both the ultrathin temperature sensors for the PANDA TS EMC as well as commercial Pt100 temperature sensors, it is desirable to obtain similar properties.

A length of approximately 0.5 m platinum wire with a diameter of 25 µm is needed to obtain the desired resistance of 100 Ω at 0 °C.

The platinum is placed in nine loops of approximately 2.7 cm length on the sticky side of self-adhesive polyimide tape. The very thin flexible cable consists of conductor paths etched in 18 µm thick copper layers, which are coated on a 25 µm thick polyimide foil. Figure 6.12 shows the schematic design of such a temperature sensor. To prevent corrosion the conductor paths are covered with another layer of polyimide foil and the contact pads are gold plated.

The platinum wire is electrically connected to the contact pads by a conductive adhesive. Each of the contact pads is connected to two conductor paths. Employing four-wire measurement the influence of the cable resistance and thus the cable length cancels out.

6.2.2.2 Calibration of the Ultrathin Platinum Resistance Temperature Sensors

In order to assess the quality of the produced sensors and to determine the parameters needed to calculate the temperature from the measured resistances, a calibration of each produced sensor is mandatory. For organizational reasons the $482 + 1152 = 1634$ ultrathin temperature sensors for the forward endcap and the barrel part are manufactured and calibrated at Ruhr-Universität Bochum, while the 131 sensors for the backward endcap part are manufactured and calibrated at the Helmholtz Institute in Mainz.

For the Forward Endcap and Barrel Part A circulation thermostat is used to control the temperature during the calibration measurement. A 50:50 methanol-water mixture is circulated through two cooling plates. The temperature sensors are stacked with 0.5 mm thick copper plates in between them and put in a copper box, which is fixated between the two cooling plates as shown in Fig. 6.13. Up to 15 of the ultrathin temperature sensors fit in this box at once. A commercial Pt100 sensor is stored for reference in the bottom and the lid of the box each, which both have a thickness of 5 mm. Since 2019 an improved setup with up to 30 sensors stacked horizontally in a newly designed copper box, which is shown in Fig. 6.14, is in use [8].

For insulation against the environmental temperature the cooling plates are surrounded by a box made of vacuum insulation panels and rigid polymethacrylimid foam [7]. The space between the insulation box and the copper box is filled with styrofoam beads to avoid convection.

Outside of the insulation box, the reference sensors and temperature sensors are connected to a THMP via adapter PCBs. Thus the full setup is as close as possible to the situation in the TS EMC forward endcap, including even the length of the flat ribbon cables between the adapter PCBs and the THMP.

Starting at 20 °C, the set temperatures are decreased in steps of −5 °C down to −30 °C, then increased to +30 °C, and decreased again to +25 °C during a calibration measurement, so that except for the minimum and maximum temperature each temperature is set twice to check for hysteresis effects.

The data for each point consists of a timestamp, the ADC conversions of all 64 THMP readout channels, the THMP board temperature as well as the set temperature and the measured bath tempera-

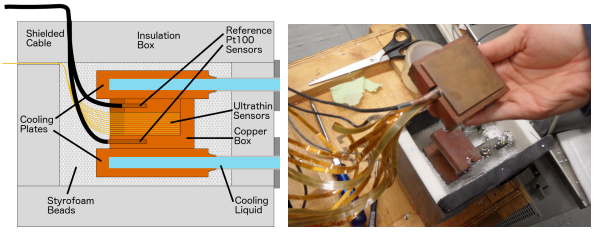

Figure 6.13: Cross-sectional schematic side view of the temperature sensor calibration setup (left) photograph of stacked sensors within the copper box (right).

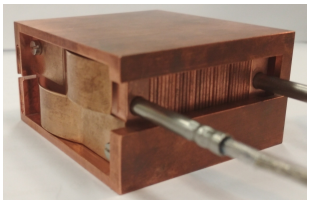

Figure 6.14: New copper box with vertically oriented sensors stacked horizontally.

ture of the thermostat. After reading out the data, a sleep time of ten seconds is passed before reading the next data. The number of points per set temperature is chosen such that a total measurement time of approximately 23 hours results, so that there is enough time to exchange sensors and keep a regular schedule.

All ADC conversions are converted to resistance values according to the THMP̄ calibration parameters of the corresponding readout channel.

The resistances of the reference sensors are converted to temperatures based on the fit of a dedicated reference sensor calibration measurement. The averaged temperature values of the reference sensors are used as reference temperature for the respective data point.

To ensure that the setup is in thermal equilibrium only the last 60 datapoints before a change of the set temperature are considered. After a thorough evaluation of this data a third order polynomial

$$T(R) = a_0 + a_1 R + a_2 R^2 + a_3 R^3$$

is fitted to describe the reference temperature values in dependence of the resistance values of the individual temperature sensors. By comparing calibrations of the same sensor recorded at different dates, the timely stability can also be checked before integration into the TS EMC as shown exemplary for one sensor in Fig. 6.15.

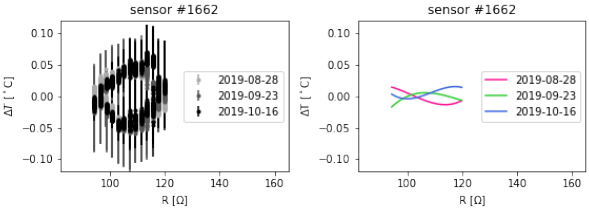

Figure 6.15: Difference of measurement values and calibration fits to the calibration fit mean for all calibration dates.

For the Backward Endcap Part The ultrathin platinum temperature sensors for the backward endcap part of the calorimeter are manufactured at the Helmholtz Institute in Mainz, following a procedure similar to the one used at the Ruhr-Universität Bochum described above. The sensors are tested for functioning after they are manufactured but will be calibrated once they are installed inside the submodules so that they are exposed to the same mechanical conditions they have in the final detector. To that end, three submodules are placed simultaneously in a climate chamber, which was purchased appositely and equipped with a system of 12 class A commercial Pt100 sensors, in order to reconstruct the temperature in every point inside the submodules, including where the flat sensors are positioned. A cooling-heating cycle is performed, where the chamber temperature is set to different values between room temperature and −30 °C. For every set value, after stability has been reached, the temperature profile in the chamber and the resistance of all sensors to be calibrated are measured.

6.2.3 THMP̄

To ensure that no water condenses or ice forms during cooling to the operating temperature of −25 °C, the EMC volume is flushed with dry compressed air. Pressure, humidity and temperature sensors are used to monitor these slowly varying environmental parameters during the cooling process. Custom electronics dedicated to the readout of these sensors have been developed at the Institut für Experimentalphysik I at Ruhr-Universität Bochum.

6.2.3.1 Design of the THMP̄

The Temperature and Humidity Monitoring Board for P̄ANDA (THMP̄) is designed modularly so that besides the resistance temperature sensors also humidity and pressure sensors can be read out. Due to the still comparably high radtiation dose at the

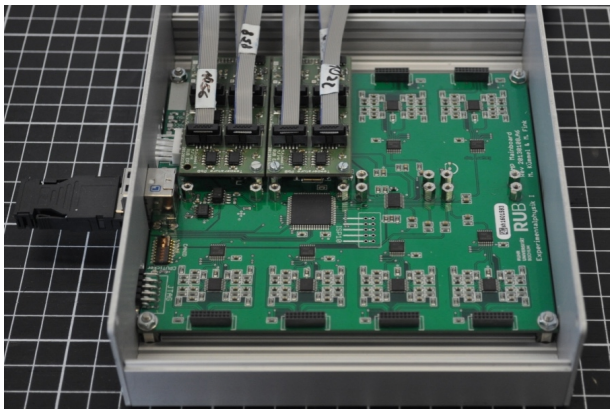

Figure 6.16: Opened THMP̄ case equipped with a mainboard and two PBBs dedicated to temperature sensor readout.

position of the THMP̄s all components have been tested for radiation hardness.

The modular design of the THMP̄ consists of a mainboard to which different kinds of piggy-back boards (PBBs) can be connected. The mainboard is equipped with a microcontroller, an ADC and eight connectors to mount PBBs as the key components. The PBBs have eight input channels which are transferred to an ADC on the mainboard. Hence, up to 64 sensors can be read out in parallel with one THMP̄.

By using different kinds of PBBs, the THMP̄ can read out different kinds of sensors. Two different kinds of PBBs are dedicated to the P̄ANDA TS EMC. The one kind provides 4-wire sensing to read out resistance temperature sensors and the other kind serves for reading out humidity and pressure sensors. Figure 6.16 shows a THMP̄ with two PBBs attached. The THMP̄ uses CAN-bus for communication and for mechanical safety lockable USB-B connectors are used as according connectors.

Mainboard For digitization of analog signals a 8-channel, 14-bit ADC with serial output and an internal reference voltage of $V_{\text{ref}} = 4.096\,\text{V}$ is used. For each PBB one channel is provided. The analog signals of the individual channels of each PBB first pass their respective active low-pass filters before the micro processor routes them via a 1×8 multiplexer through an additional low-pass passive filter to the ADC as depicted in Fig. 6.17 (top). Since the board temperature influences the electronics behavior, the mainboard is equipped with a temperature sensor for monitoring.

In order to identify the boards unambiguously each mainboard and piggy-back board is equipped with a chip, which provides a six byte digital serial number.

PBBs for Humidity and Pressure Sensors The humidity and pressure sensors only need a $+5\,\text{V}$ power supply. The output voltage uses nearly the full range of the ADC so that no amplification of the signals is required. Therefore this PCB only consists of a voltage regulators and eight fuses. The fuses prevent a short-circuit of the humidity sensors due to radiation damage. [9]

PBBs for Temperature Sensors The measurement is based on 4-wire sensing, that means two separate pairs of wires are connected to the respective resistor in parallel. This way the current I through the voltage sensing wires is negligibly small and the voltage drop $U = R \cdot I$ in the current carrying wires is neglectable, so that the line resistance of the wire does not influence the measurement. In order to optimally exploit the ADC input range the sensed voltage drop $U = R \cdot I$ is amplified (gain factor G) and shifted by a reference voltage U_{off} provided by high precision voltage sources. The scheme is shown in Fig. 6.17 (bottom). On the mainboard the voltage drop is digitized, corresponding to a conversion factor $C = \frac{2^{14}}{4.096\,\text{V}} = 4000\,\text{V}^{-1}$, so that the ADC conversion K for a given resistance R is determined by the linear function

$$K(R) = (R \cdot I \cdot G + U_{\text{off}}) \cdot C = n + m \cdot R.$$

6.2.3.2 Calibration of PBBs Dedicated for Temperature Sensors

In order to obtain highly accurate temperature measurements, not only the temperature sensors but also the readout electronics must provide a high precision. The required resolution for the temperature measurement corresponds to a resistance resolution in the order of mΩ resulting in a precision of 10^{-5}. In comparison, the production accuracy of high precision resistors is at least 0.1 %. Thus an individual calibration of all readout channels of the temperature sensor PBBs on the THMP̄ is crucial to obtain the required resolution.

The calibration is realized by measuring the resistances of resistors with well-known values in the appropriate range provided by customized calibration boards. A climate chamber is used to provide different stable temperatures, so that the temperature dependence of the electronics can be measured.

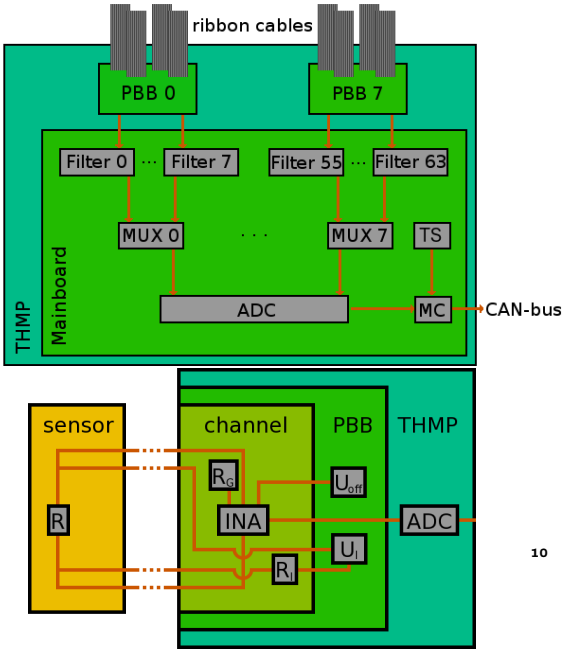

Figure 6.17: Schematic overview of THMP mainboard (top) the PBBs dedicated to the readout of temperature sensors (bottom).

After a thorough evaluation of the recorded data a two-dimensional linear function is fitted to the data

$$K(R, T_{\mathrm{THMP}}) = p_{00} + p_{01} \cdot T_{\mathrm{THMP}} + \ldots + p_{10} \cdot R + p_{11} \cdot T_{\mathrm{THMP}} \cdot R,$$

which describes the ADC conversion in dependence of the resistance and the THMP mainboard temperature and can easily be converted

$$R(K, T_{\mathrm{THMP}}) = \frac{K - (p_{00} + p_{01} \cdot T_{\mathrm{THMP}})}{p_{10} + p_{11} \cdot T_{\mathrm{THMP}}}.$$

to determine the connected resistance from the measured ADC conversion of the respective readout channel and the THMP mainboard temperature.

Evaluating the calibrations of 10 devices with 64 readout channels each, the resistance uncertainty is well be low the design requirement of 7.7 mΩ as shown in Fig. 6.18, which would correspond to a temperature resolution of 0.02 °C.

A more detailed description of the electronics layout, the calibration procedure and corresponding results can be found in the latest thesis covering these topics [8].

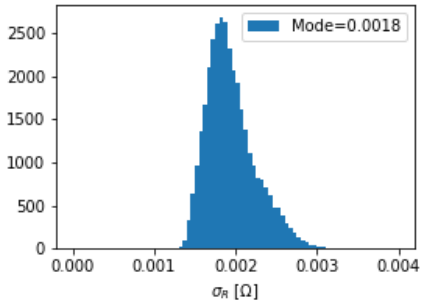

Figure 6.18: Propagated uncertainty of the resistances retrieved from the calibration fits using a sophisticated resistance and temperature uncertainty estimation [8].

Bibliography

[1] Chris Hagmann, David Lange, and Doug Wright. Monte carlo simulation of proton-induced cosmic-ray cascades in the atmosphere. 02 2012. https://nuclear.llnl.gov/simulation/.

[2] Merlin Rossbach. *Anordnung und Test der Detektor-Submodul-Komponenten für die Vorwärts-Endkappe des PANDA-EMC*. PhD thesis, Rheinische Friedrich-Wilhelms-Universität Bonn, 2019. https://nbn-resolving.org/urn:nbn:de:hbz:5n-55184.

[3] V. A. Batarin et al. Study of radiation damage in lead tungstate crystals using intense high-energy beams. *Nucl. Instrum. Meth. A*, 512:488–505, 08 2003. https://doi.org/10.1016/S0168-9002(03)02014-X.

[4] V. A. Batarin et al. Design and performance of LED calibrationsystem prototype for the lead tungstatecrystal calorimeter . *Nucl. Instrum. Meth. A*, 556:94–99, 01 2006. https://doi.org/10.1016/j.nima.2005.10.007.

[5] T. Held et al. An LED/LCD-based Monitoring System for the PANDA Electromagnetic Calorimeter. *subm. to Nucl. Instrum. Meth. A*, 2020.

[6] B. K. Lubsandorzhiev and Y. E. Vyatchin. Studies of "Kapustinsky's" light pulser timing characteristics. *JINST*, 1:T06001, 2006. https://doi.org/10.1088/1748-0221/1/06/T06001.

[7] Jan Schulze. *Analyse des Zerfalls $\chi_{c0} \to K^+K^-\pi^0\pi^0$ bei BESIII und Entwicklung von mechanischen Komponenten für einen Prototypen des PANDA-EMC*. PhD thesis, Ruhr-Universität Bochum, 2012. https://nbn-resolving.org/urn:nbn:de:hbz:294-35247.

[8] Miriam Kümmel. *Analysis of $J/\Psi \to \phi\eta\eta$ at BESIII and calibration of the temperature monitoring system for the $\overline{\text{P}}$ANDA electromagnetic calorimeter*. PhD thesis, Ruhr-Universität Bochum, 2019. https://nbn-resolving.org/urn:nbn:de:hbz:294-64681.

[9] Florian Feldbauer and Patrick Friedel. Report for Temperature and Humidity Monitoring Board for $\overline{\text{P}}$ANDA ($\text{THM}\overline{\text{P}}$). https://panda-wiki.gsi.de/foswiki/pub/EMC/THMP/ThmpReport_Rev1.1.pdf, 2009.

7 Performance

In order to optimize the mechanical design, to fulfill space requirements, to study insulation and detector cooling and to reach an optimum overall performance in particular with respect to the energy resolution certain prototypes have been constructed. Important results and experiences gained with these prototype detectors went into the construction of the target calorimeter and were used to develop and optimize the envisaged assembly procedure. The expected performance of the final subdetectors (endcaps and barrel) is considered to be in close accordance to those measurements since the full scale EMC is comprised of a modular combination of the coresponding prototype-sized units.

7.1 Prototype for the Barrel

For the barrel part of the target spectrometer two prototypes have been constructed containing 60 and 120 crystal units (PROTO60 and PROTO120). The very first prototype PROTO60 was mainly designed to test the performance of the PWO-II crystals with an APD based readout. The properties of PWO-II are given in Chap. 2. The used readout concept differs from the final concept for the Barrel EMC. The most recent prototype PROTO120 was designed with the aim to realize a close to final design of the $\overline{\text{P}}$ANDA barrel EMC.

7.1.1 PROTO60

The prototype consists of a matrix of 60 type-6 PWO-II crystals, arranged similar to the corresponding barrel area of type-6 crystals. At the operation temperature of −25 °C, the crystals are read out with a single 10 mm × 10 mm Hamamatsu APD (S8664-1010SPL) and LNP SP883a [1]. Detailed studies over the full dynamic range at different accelerator facilities using tagged photons, muons or electrons have been successfully conducted. These investigations were about the energy resolution including the impact of the material budget in front of the calorimeter of the other subdetectors [2], the position resolution [3], the time resolution and the position dependent higher order energy correction [4]. The achieved results, especially after certain optimizations including the usage of sampling ADCs [5], are in excellent agreement with the requirements given in the Technical Design Report of the full calorimeter.

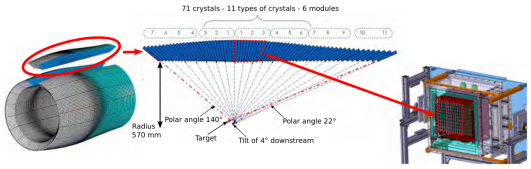

Figure 7.1: The PROTO120 represents a subsection of a barrel slice. It contains 40 PWO-II crystals respectively of type 1, 2 and 3.

7.1.2 PROTO120

The PROTO120 (Fig. 7.1) represents the design of the super module type 4 (see Sec. 5.1). The support beam is replaced by a modified version of the supermoduleplate, with a plastic box on top for housing the backplane PCBs. The gap between the plates is filled with stone wool for thermal insulation. The entrance window of the PROTO120 consists of an evacuated micro porous thermal insulating panel with high thermal insulation properties (Va-Q-Tec, Germany). For the side walls simple foam is used, followed by plastic plates. Meandering copper pipes are attached to the supermoduleplate and to copper sheets between the foam and the side walls of the crystal matrix (Fig. 7.2). The temperature is monitored by several flat temperature sensors (for description see Sec. 6.2.2) placed between the reflector foil and the wall of the alveoles. The whole setup was sealed with silicon glue and flushed with dry nitrogen to avoid water condensation or ice accumulation inside the cooled volume during its operation.

The crystals are read out with two rectangular APDs of the final $\overline{\text{P}}$ANDA version and the preamplifiers are replaced by ASICs for $\overline{\text{P}}$ANDA Front-End Electronics (APFELs). A detailed description of the APFEL is given in Sec. 4.1. The APFELs inside the cold volume are connected via double layer flexcables to an earlier version of the backplane PCBs as descried in Sec. 4.6.2. They are located in the warm volume of the prototype. The signals went through separate buffer boards into SIS 3302 sampling ADC modules [6] with a chosen sampling rate of 50 MHz.

Figure 7.2: Front view of a partly mounted PROTO120 without front thermal insulation panel. The crystals are surrounded by cooling plates and thermal insulation.

The setup was tested at the A2 hall of the MAMI-facility (Germany) with tagged photons in the range of 56 MeV to 770 MeV. A more detailed description of the whole prototype experiment including its analysis can be found in [7] and [8].

The mean value of the tracewise calculated root mean square (rms) noise level of a single APD channel was comparable to a signal of $\mu_{\text{noise}}(\text{rms}) = 0.72\,\text{MeV}$ with a width of $\sigma_{\text{noise}}(\text{rms}) = 0.24\,\text{MeV}$. The mean noise value of the tracewise calculated maximum deviation from the baseline was comparable to a signal of $\mu_{\text{noise}}(\text{max}) = 1.41\,\text{MeV}$ with a width of $\sigma_{\text{noise}}(\text{max}) = 0.42\,\text{MeV}$. Signal filtering algorithms like moving average or band pass have not been used. The detector noise level is almost equivalent to the pure intrinsic noise level of the APFEL which indicates a good shielding and grounding concept for the PROTO120 (Chap. 4.3 in [8]).

The single APD channel threshold was set to $th = \mu_{\text{noise}}(\text{max}) + 3\,\sigma_{\text{noise}}(\text{max}) = 2.7\,\text{MeV}$ for the energy reconstruction. The obtained relative energy resolution of a 3×3 crystal array with centrally impinging photons can be parameterized by

$$\frac{\sigma}{\text{E}} = \sqrt{\left(\frac{2.46\,\%}{\sqrt{\text{E/GeV}}}\right)^2 + \left(\frac{0.16\,\%}{\text{E/GeV}}\right)^2 + 2.32\,\%^2}, \tag{7.1}$$

which is in agreement with the requirements for the $\overline{\text{P}}$ANDA experiment.

7.2 Prototype for the Forward Endcap

A prototype resembling a cutout (see Fig. 7.3a) of the forward endcap comprised of 216 PWO crystals, has been built at the Institut für Experimentalphysik I, Ruhr-Universität Bochum in the past years. Design and construction have been described in detail in [9, 10, 11, 12] before and will just be briefly summarized here. The first calorimeter submodules were built and tested under realistic conditions with this prototype not only in the lab, but also during various test beam times at different accelerators. These submodules were equipped with different types of photo sensors and one goal of the measurements was to select the photo sensor type to be used in the forward endcap. The choice was finally made and after several iterations of improvements to the mechanical parts and electronics components, the first two close-to-final submodules were built.

To perform a final gain matching of the readout chain, two submodules were mounted to the prototype and test beam data at the Elektronen-Stretcher-Anlage (ELSA) accelerator was recorded. The results of all test beam times conducted with the forward endcap prototype are presented in detail in [12] and [13].

The central mechanical component of the prototype is the aluminum backplate, which follows the design of the backplate of the full forward endcap. In total, the prototype can be equipped with 13 full submodules (4×4 crystals) and one half submodule (4×2 crystals). On the front side (upstream), the volume of the prototype is enclosed with a front hull made of aluminum sheets as well as Polyvinyl chloride (PVC) sheets in the region of the central hole for the HESR beam line and the opening towards the forward spectrometer. On the rear side, a frame made of 30 mm thick PVC creates a volume for the routing of light fibers and cables, which is covered by a 3 mm thick aluminum sheet.

A mixture of 60 % methanol and 40 % water is pumped through long vertical holes drilled into the backplate, as well as through polyurethane hoses of 5 mm diameter, which are glued to the inside of the front hull to cool the inner volume of the prototype by external chillers. The aluminum enclosing of the assembly is covered by vacuum insulation panels, as foreseen for the forward endcap, to provide a thermal insulation against ambient temperature.

The complete prototype is mounted in a frame of aluminum profiles with just two rods made of glass

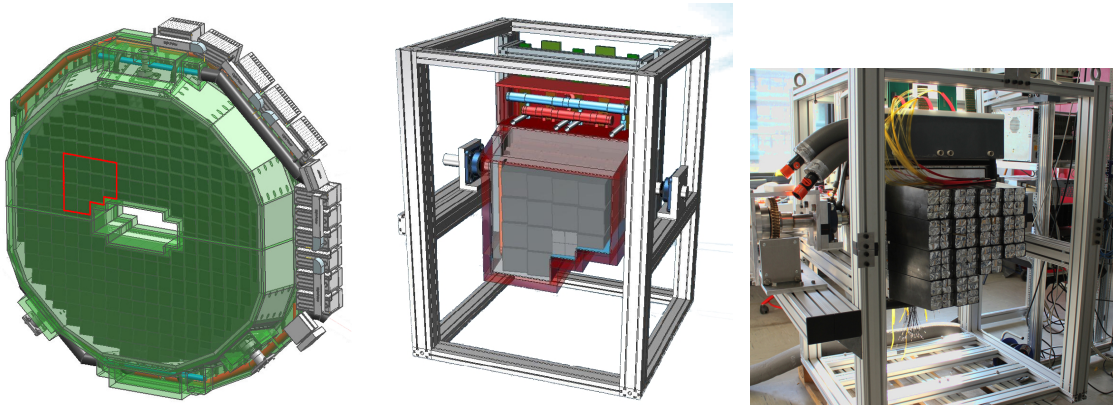

(a) (b) (c)

Figure 7.3: (a) Red: area of the forward endcap resembling the prototype
(b) CAD drawing of the prototype in its holding structure
(c) Photograph of the prototype with all submodules mounted, but with front insulation and shielding removed

fiber reinforced plastic, that are attached to the side faces of the backplate (see Fig. 7.3b). These rods ensure a thermal insulation of the cold backplate from the aluminum frame and enable a rotation of the assembly by a worm drive mounted to the frame, so that the angle of the prototype towards the incoming beam can be adjusted. Furthermore, it is possible to adjust the height of the complete assembly in its frame by moving the bars up or down, to which the bearings that accommodate the plastic rods are mounted. This procedure is, however, only possible if the prototype is opened and a crane is available and thus the adjustments have to be made prior to transportation to an accelerator.

Front and back covers are attached with several screws to the backplate and O-rings between all components ensure an air-tight enclosure of the cold volume. An additional external chiller is used to cool dried pressurized air, with which the cold volume is constantly flushed at a rate of ∼100 L/h. A photograph of the fully equipped prototype before attaching the front hull is shown in Fig. 7.3c. All cables leading to and from the submodules, are led through one of the holes in the backplate and end shortly thereafter. At this point one patch panel PCB per submodule is mounted to the backplate and all cables are connected to it. The patch panel PCBs have been tested at the most recent beam time at the ELSA accelerator; However, they were not available during all previous beam times. A picture of the opened rear side of the prototype is shown for illustration in Fig. 7.4.

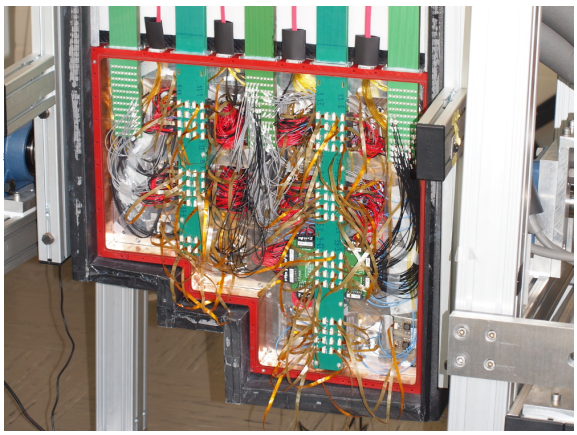

Figure 7.4: Rear view of the opened prototype (vertical green bars are multilayer PCBs).

7.2.1 Overview of Test Beam Times

As many details as possible concerning construction and operation of the prototype were kept in line with the design of the full forward endcap to obtain a realistic test setup. However, several improvements were made over the course of the first four beam times. The first test beam time was conducted at the European Organization for Nuclear Research (CERN) Super Proton Synchrotron (SPS), where positrons with momenta of 10 GeV/c and 15 GeV/c as well as muons with a kinetic energy of 150 GeV were used. Dedicated tracking detectors consisting of a fiber-hodoscope and two silicon strip detector modules were installed in front of the prototype to provide a trigger signal and a precise position measurement for the particles impinging on the prototype crystals. Due to several

issues with the preamplifier gain, the shaper boards and the digitizer modules, the noise and thus the corresponding single crystal threshold were rather high. Shortly after the first beam time, the prototype was installed downstream of the Crystal Barrel detector, which is located at the ELSA accelerator in Bonn. Here, tagged photons were used to measure response and energy resolution of the prototype at three energy points in the range between 1 GeV and 3.1 GeV. Additionally, the rate of the beam photons could be varied at the ELSA facility, so that feasibility studies for the readout of photo detector-preamplifier units at rates comparable to those expected for the innermost crystals of the forward endcap could be performed. After several improvements and modifications of the hardware, an additional test with a beam of tagged photons was performed at the MAMI accelerator. At this beam time the response and the energy resolution for photons in the energy range of 20 – 415 MeV were studied and a single crystal threshold near to the design value was reached for the first time [12]. Since the results regarding the energy resolution at the highest energies were dominated by the partially bad performance of some hardware components, a second beam time at the CERN SPS accelerator was performed after especially the components of the readout chain (shapers, ADCs) were optimized. As a last step, one close-to-final submodule equipped with VPTTs and one equipped with APDs were tested again at the ELSA accelerator, to verify the gain matching of the full readout chain. An overview of all forward endcap prototype test beam times is given in Table 7.1.

7.2.2 Results from Test Beams

7.2.2.1 Noise and Threshold

The best performance regarding energy equivalent noise has been measured for the Vacuum Photo Tetrodes. A mean noise of $\langle\sigma_{\text{Noise}}\rangle_{\text{VPTTs}} = 1.6\,\text{MeV}$ has been determined, which is near the envisaged value of 1 MeV in the Technical Design Report of the EMC [16]. For the APDs a slightly worse value of $\langle\sigma_{\text{Noise}}\rangle_{\text{APDs}} = 2.2\,\text{MeV}$ has been measured.

In order to determine the optimal value for the single crystal energy threshold (E_{thr}), the energy resolution for a 3×3 crystal matrix has been studied in dependence of E_{thr}. For this scan the threshold has been varied in the range of 1 MeV – 15 MeV. Fig. 7.5 shows examples of threshold scans for two different beam energies. The best resolution can be obtained by applying a single crystal threshold of 5 MeV, which corresponds roughly to $3 \cdot \langle\sigma_{\text{Noise}}\rangle_{\text{VPTTs}}$.

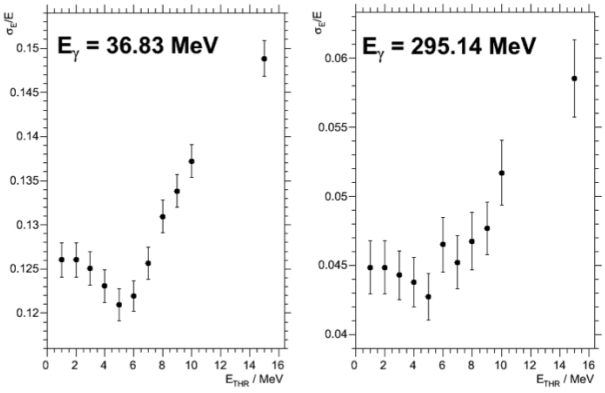

Figure 7.5: Energy resolution vs. applied single crystal threshold shown for two different beam energies (tagged photons, MAMI testbeam). The optimal energy threshold determined by this is $E_{\text{thr}} = 5\,\text{MeV}$ (measured with VPTTs).

7.2.2.2 Energy Resolution

For the PANDA PWO-II crystals about 80 % of the incident energy is deposited in the crystal that is centrally hit by a particle. In order to reconstruct the incident energy, the deposition in many crystals is summed up. For the prototype studies the deposition in symmetrical 3×3 or 5×5 crystal matrices is used. Due to the fact that electromagnetic showers can have asymmetrical shapes and large fluctuations, in the final setup an algorithm will be used to select crystals that contribute to the shower, starting from the crystal with the largest deposition and subsequently moving outwards until crystals are reached, for which the deposition lies below the threshold E_{thr}.

For each beam energy the resolution is determined from a fit to the distribution of the energy sum. This distribution has an asymmetrical shape, which can be described by a Gaussian function with an additional tail towards lower energy deposits. The empirically determined function for this distribution is described in more detail in [17]. The resolution is determined from the width σ_E of the fitted function and the energy of the incident particle E as σ_E/E. The width is defined as $\sigma_E = \text{FWHM}/(2 \cdot \sqrt{2 \ln 2})$. Examples for the energy deposition in the central and surrounding crystals as well as the sum are shown for a low ($E = 295.14\,\text{MeV}$) and a high ($E = 10.0\,\text{GeV}$) beam energy in Fig. 7.6 and Fig. 7.7, respectively.

Table 7.1: List of beam tests with the forward endcap prototype. The test beam times are discussed in detail in [12, 14, 15].

	Beam particles	E_{Beam} or p_{Beam}	Characteristic feature
CERN/SPS	e^+	10, 15 GeV/c	Max. $\overline{\text{P}}$ANDA energy
	μ^+	150 GeV/c	Energy deposit $\approx$ 230 MeV
ELSA/Bonn	Tagged γ	1, 2.1, 3.1 GeV	Rates up to $2 \times 10^{-6}\,\text{s}^{-1}$
MAMI/Mainz	Tagged γ	20 – 415 MeV	Excellent beam energy resolution
CERN/SPS	e^-	5 – 15 GeV/c	Fiber / Si-strip
	$\pi^+, K^+, \bar{p}$	15, 50 GeV/c	Tracking Station
ELSA/Bonn	e^-	1.25, 2.4, 3.2 GeV	Fiber hodoscope

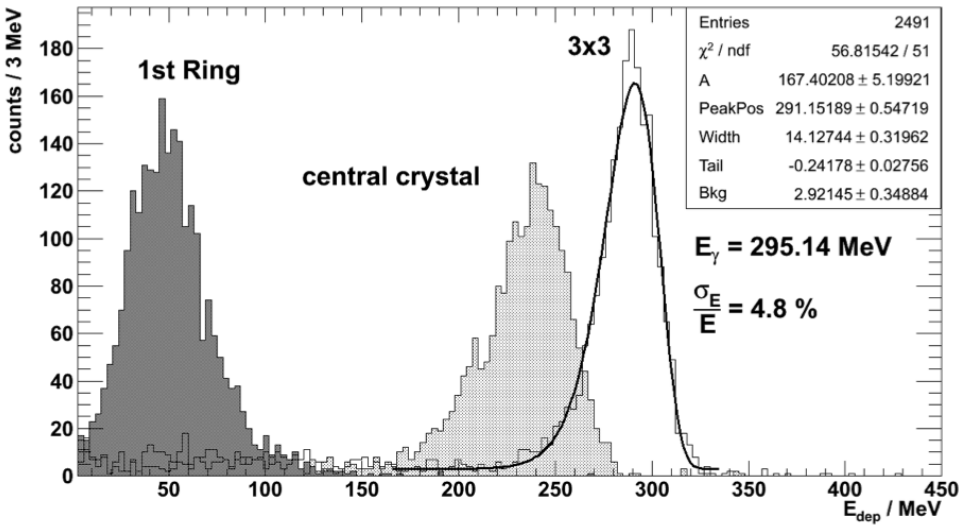

Figure 7.6: Energy deposition in the central crystal, the surrounding ring of crystals and the sum of all nine crystals at a beam energy of $E = 295.14$ MeV. The energy sum has been fitted to obtain the energy resolution (measured with VPTTs).

The resolution has been determined for incident energies in the range of 25 MeV up to 15 GeV for the different photodetector types. All results are summarized in Fig. 7.8 together with the envisaged energy resolution function given in the Technical Design Report [16] (blue curve). For small energies the resolution is slightly worse than the targeted value, while for the highest energies expected in the $\overline{\text{P}}$ANDA experiment the expectations can be met very well. Since only symmetrical crystal matrices were considered here and a simplified version of the feature extraction for the signals was employed, an improvement in performance is expected for the operation of the final detector setup also for the lowest energies.

7.2.2.3 Spatial Resolution

The position resolution of the forward endcap prototype was studied at the CERN testbeam, due to the use of Si-microstrip detectors with a pitch of 50 µm and a fibre hodoscope, that were set up in front of the prototype. The point on the surface of the central crystal, at which a beam particle hit the crystal, can be reconstructed from the information of the tracking detectors as well as from the measured energy depositions in the prototype. A logarithmic weighting method was used to calculate the point of impact from the energy deposition in the crystals. The difference between the point of impact calculated from the energy deposition and tracking detectors, denoted as Δx, shows the spatial resolution (Fig. 7.9). The width of this Gaussian shaped distribution, σ_x, was determined for all four beam energies. The resolution was determined to be $\sigma_x = 1.6$ mm at $E = 5$ GeV (black curve in Fig. 7.9)

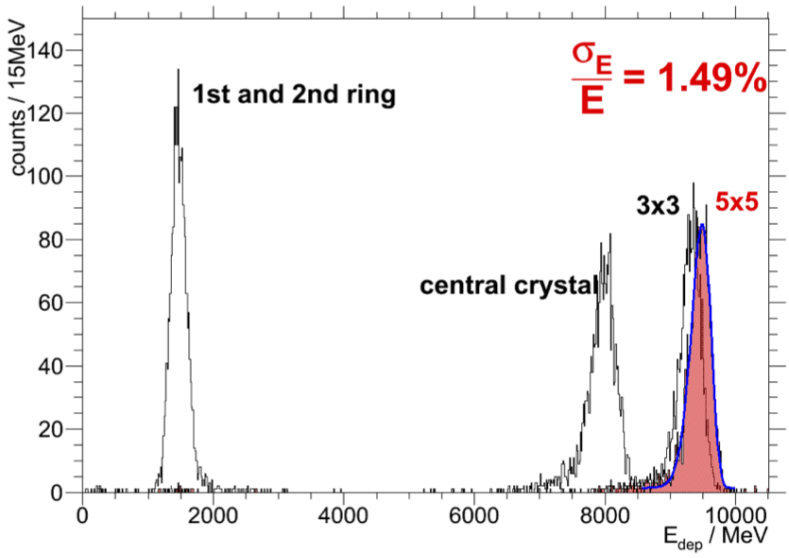

Figure 7.7: Energy deposition in the central crystal, the surrounding two rings of crystals and the sum of all 25 crystals at a beam energy of $E = 10.0\,\text{GeV}$. The energy sum has been fitted to obtain the energy resolution (measured with VPTTs).

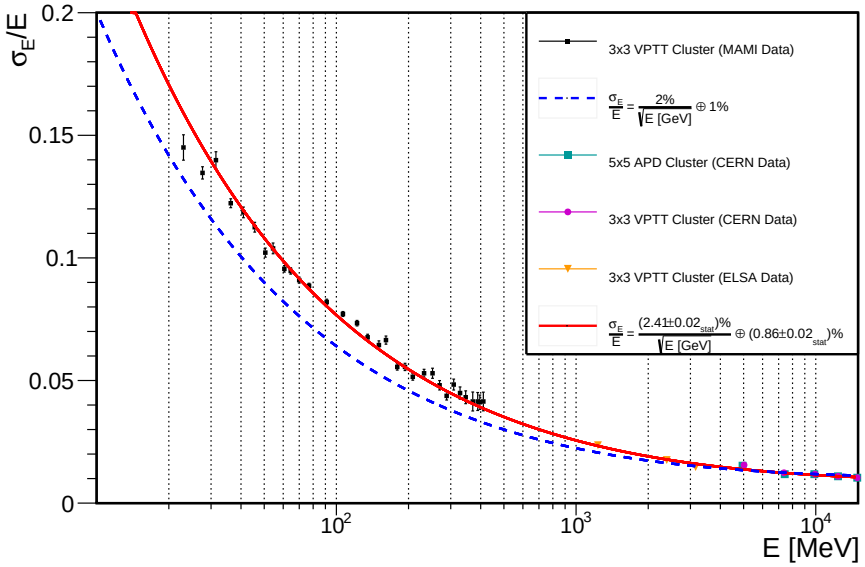

Figure 7.8: Energy resolution as a function of beam energy. The blue curve shows the envisaged energy resolution.

and subsequently decreases to 0.9 mm at an energy of 15 GeV (blue curve). The resolutions for the intermediate energies were measured as $\sigma_x = 1.3\,\text{mm}$ at $E = 7.5\,\text{GeV}$ (red curve) and 1.1 mm at an energy of 10 GeV. These results are in good agreement with the design value for the forward endcap of $\sigma_{x,\text{TDR}} < 3.5\,\text{mm}$. Additionally the dependence of the position resolution from the point of impact along the front face of a crystal has been studied. It was found, that the resolution improves towards the borders of the crystal. In these cases the largest fraction of the energy is deposited in two crystals instead of only the central crystal. This behaviour could also be qualitatively reproduced with Monte Carlo simulations (see Fig. 7.10: red curve: simulation, black: test beam data). Along the front face of the crystal the position resolution is about a factor of three better than the targeted design value for all points that were studied.

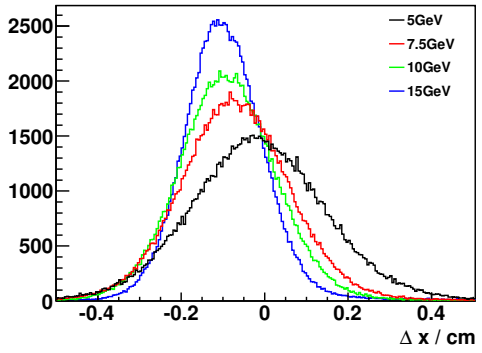

Figure 7.9: Position resolution for different beam energies. The distribution is shifted from the center for higher beam energies due to the non-zero angle between the crystal- and beam-axis.

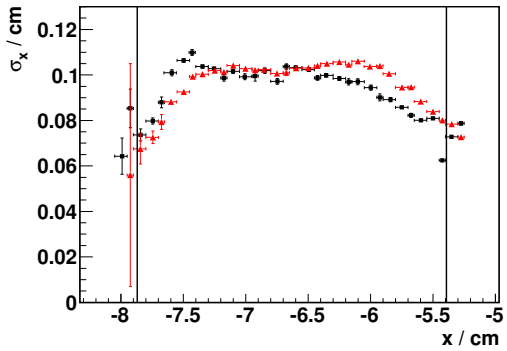

Figure 7.10: Position resolution as a function of the point of impact on the crystal surface for test beam data (black) and Monte Carlo simulation (red). The vertical lines indicate the borders of the central crystal.

7.3 Prototype for the Backward Endcap

As a test bench for all solutions proposed during the development of the BWEC, two 16 crystal prototypes (Proto16) have been built for several purposes. Firstly, it was possible to prove the feasibility of the mechanical construction details, also with emphasis on the development of a mounting procedure for the series production of the submodules. Secondly, the prototype was an ideal environment to develop and test the functionality of all components of the signal readout chain. Thirdly, also all services (e. g. cooling, temperature readout, light pulse distribution, etc.) which are needed for the operation of the EMC could be developed and tested. Finally, the overall detector performance could be investigated and key parameters like the relative energy resolution could be measured with beam tests.

7.3.1 The Prototype Proto16

The Proto16 is a 4×4 crystal array, which is the same arrangement as the basic BWEC submodule. The first version of the prototype was built in 2014 and was since then constantly updated with the new BWEC developments. In 2018, the submodule design underwent a major update, which was necessary for solving service routing issues and for having a more modular BWEC design in view of the use of the detector in an experiment within the FAIR phase 0. For this reason, a new prototype was built following the final submodule design as described in Sec. 5.3. In Fig. 7.11, pictures of the second Proto16 are shown.

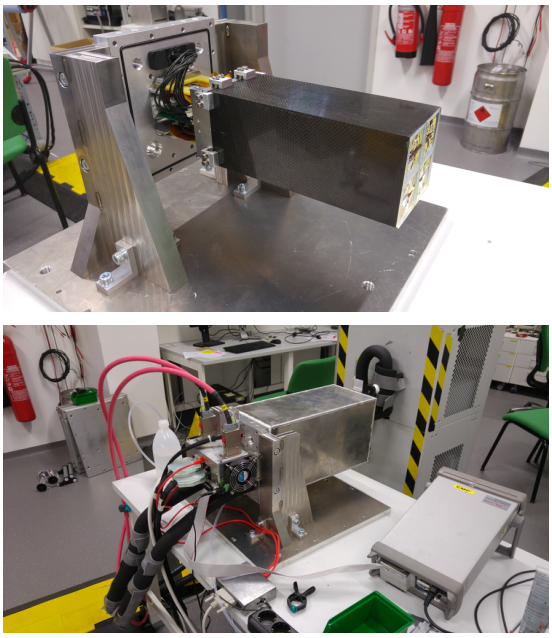

Figure 7.11: Top: the second version of the Proto16. The outer cover, the insulation and the cooling shell are removed to show the detector inside. Bottom: The closed detector with all services connected from the back.

The prototype has an aluminum mounting plate like the BWEC, on which the full weight of the detector is held in cantilever position, and through which all services are fed from the outside into the inner volume.

At variance with the BWEC submodules, the insert is not glued to the alveole, but rather fixed to it with a system of clamps and screws. This allows to disassemble the prototype for maintenance or for updates without breaking the alveole. Likewise, the

APDs are not glued to the crystals, but are optically coupled to them through optical rubber foils of type EJ-560 by Eljen Technology [18] with a thickness of 1.5 mm and cut in squares of 22 mm side.

Readout When the first Proto16 was brought into operation, the PANDA readout system was not fully developed, and could not be used. Still, it was necessary to test the prototype with a readout system based on sampling ADCs. For this reason, many tests were performed using the Multi Branch System (MBS) by GSI together with the FEBEX SADC boards [19]. These have 16 input channels, 14 bit digitization resolution over an input range between −1 V to +1 V, and a sampling rate of 50 MHz. Such specifications are very similar to the PANDA SADC. When this became available, together with the first version of the PANDA readout, running on a TRB board, laboratory and beam tests were performed also with that readout system.

Cooling In order to operate the Proto16 at −25 °C, a cooling shell was built. It consists of 4 copper plates of 2 mm thickness welded together and a pipe circuit soldered on them as shown in Fig. 7.12.

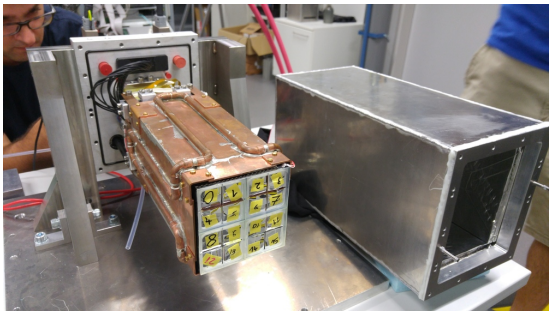

Figure 7.12: Picture of the open Proto16 with the copper cooling shell and outer cover with VIPs (on the right).

The cooling shell is fixed to the aluminum insert so that it covers the alveole from 4 sides, leaving out the front and the back side. The dimensions are chosen in such a way, that the shell almost touches the alveole walls.

For the thermal insulation, a layer of VIPs with a total thickness of 20 mm was inserted between the cooling shell and the external aluminum cover of the prototype.

Ethanol was used as cooling medium, which was cooled with a refrigeration machine of type XT-280 by Lauda GmbH.

To monitor the temperature inside the Proto16 and to perform some temperature profile studies up to 16 flat Pt100 sensors (one per crystal) have been employed.

Monitoring To check the functionality of the readout chain as well to monitor the stability of the detector over longer periods of operation, test light pulses needed to be fed into the crystals. Since the optical fibers used as light guides had to be possibly exchanged during the lifetime of the prototype, plastic fibers were chosen over quartz ones, in order to minimize the costs. To be sure to have a large enough amount of light in the crystals, fibers of 1 mm core were used. For the development phase, it is important to have the possibility to singularly flash light pulses to the individual crystals. Since this is not possible with the PANDA EMC light pulser, a customized pulser was developed at Mainz with 16 different LEDs, singularly coupled with FC/PC connectors [20]. Each LED can be turned on and off, and its bias voltage can be set individually. The chosen LED emits blue light in the wavelength range of the lead tungstate scintillation light. The pulse generation can be triggered with an external logical signal. Provided the trigger signal is fast enough, the rise and fall time of the light pulses are in the order of some nanoseconds.

7.3.2 Beam Tests with Proto16 at MAMI

Several beam tests at the MAMI electron accelerator [21, 22] have been performed during the last years. The duration of the available beam time for each test varied from 48 hours to 5 days, according to the availability of the machine. The first test was performed in 2014 at the A2 facility [23] with high energy tagged photons. This test was quite analogous to those performed with the barrel EMC prototypes and reported in Sec. 7.1. Therefore, it will not be described here. A second series of tests (in 2015, 2016 and 2018) was performed directly with the electron beam at the X1 extraction beam line, where a detector test facility is available. These tests will be described in some detail in the following. Two further beam tests were performed in 2018 at the A1 electron scattering facility [24] within the FAIR phase 0 activity. Since the objective of these tests was rather demonstrating the feasibility of the phase 0 experiment than the characterization of the EMC performance, their description will be also omitted here.

Beam Test Environment The measurements reported here took place at the so-called X1 extraction beam line at MAMI. This beam line is dedicated to providing beam to the X1 synchrotron radiation facility [25], which is located in an experimental hall, adjacent to the accelerator hall B, where the RTM-3 is installed. Between the exit of the RTM and the entrance to the dipole magnet of the X1 facility, a beam pipe segment of about 4 m length can be removed, allowing the electrons from the RTM to exit the vacuum pipe. At that location, a detector test area is available. Here, detector systems can be installed on a movable platform, remotely controllable via step motors, and exposed to the electron beam coming out of the accelerator.

The beam energy can be chosen between 195 MeV and 855 MeV in 15 MeV steps by extracting the electrons from the RTM after a defined number of recirculations. To achieve that, a dipole magnet needs to be moved and placed around the corresponding return beam pipe. After an energy change, the machine needs to be optimized, which limits the maximum number of beam energies which can be set during a beam time. On the positive side, the energy spread of the electrons is about 100 keV and the beam spot has transverse dimensions of less than 1 mm, which offers good conditions for a precise characterization of the detector response.

In order to obtain beam intensities low enough to avoid damages to the detector under test, the laser beam hitting the photocathode at the electron source is switched off and only thermal electrons are emitted from the photocathode and enter the accelerator. A beam shutter at the source can be used to completely turn off the electron beam. By opening the shutter, the beam intensity can be set to have the desired counting rate in the detector.

In Fig. 7.13, pictures from the test area are shown. The prototype was installed on the movable platform with the crystal axis parallel to the beam direction. The platform can be displaced in both directions transverse to the beam. Therefore, all crystals can be moved into the beam, and the entrance position on the crystal front face can be set arbitrarily. During the installation of the prototype on the platform, laser pointers are used to position and align the detector with respect to the nominal beam position. In order to find the actual position of the beam with respect to the crystal matrix, alignment plates have been fixed to the outer box of the prototype. These are painted with a fluorescent paste which allows to see the beam spot when the plate is hit. Since the plates have a well defined position with respect to the crystals, the relative position of the beam with respect to the crystal matrix for any position of the platform can be determined. The accuracy of this alignment procedure is roughly estimated at the order of 1 mm.

During all tests at the X1 facility, a plastic scintillator was installed in front of the prototype calorimeter for tagging the incoming beam electron. The active area of the scintillator counter is larger than the area covered by the crystals in the Proto16 (about $100\times100\,\mathrm{mm}^2$), and its thickness is 20 mm, ensuring a detection efficiency for minimum ionizing particles above 99 %. It is read out via a light guide with a PMT, whose signal is processed with conventional NIM electronics. The PMT pulses are discriminated with a CFD, whose output logic signal can be used in coincidence with signals from the prototype to trigger the data readout. In addition, since the dead time of the scintillator is of the order of some tens of nanoseconds, pile-up losses stay well below 1 % up to electron rates of some hundred kilohertz. Therefore, the measured rate with the scintillator can be used as a reference for studying detection inefficiencies or pile-up losses in the calorimeter.

Data Readout During the beam tests, the MBS readout was used to register data from the prototype event-wise in a triggered mode. On the FEBEX boards, a FPGA processes the digitized signals with a trapezoid filter and discriminates the filtered pulses with a leading edge, producing a logic pulse. This was combined using a coincidence NIM module with the discriminated scintillator signal to obtain a coincidence trigger pulse for starting the data readout.

For every event, signal traces of 1024 samples (20 µm) from all 64 Proto16 output channels were recorded. A ring buffer in the FPGA registers the samples continuously and can be used to save samples obtained before the trigger occurrence. Typically, a time window of 3 to 5 µs before the trigger have been saved, giving the possibility to analyze the complete form of the APFEL pulses offline (and e. g. optimize the digital signal processing algorithms). Since the pulse duration is less than 1.5 µs, more than 10 µs of signal from each channel after every pulse is available for baseline studies.

As an example, the results in Fig. 7.14 show the stability of the baseline position and standard deviation over a time interval of about 36 hours. With the exception of three channels out of 64 which were not working, the rest of the data shows a quite stable detector operation. In addition, the average standard deviation of the baseline σ_{BL} corresponds,

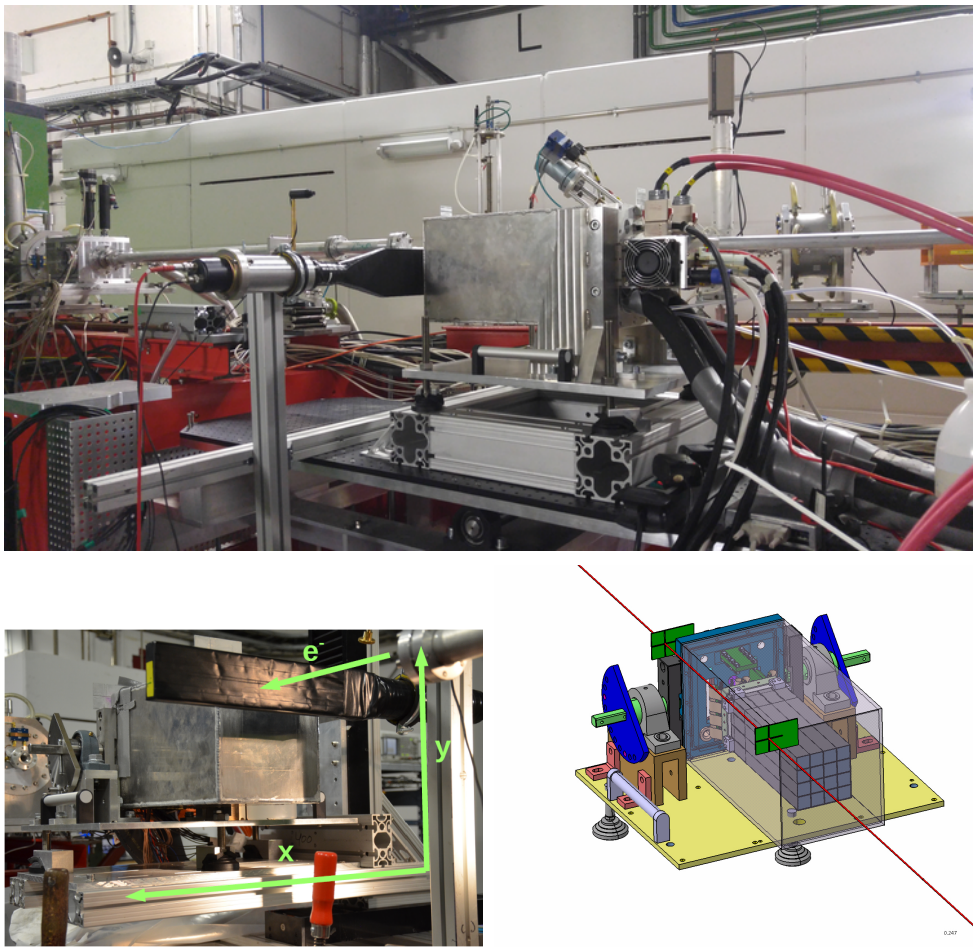

Figure 7.13: Test setup with the Proto16 at the X1 beam line at MAMI. Top: overview of the test stand at the extraction pipe from the RTM-3. Bottom-left: view of the Proto16 and the plastic scintillator from the front (upstream). Bottom-right: sketch of the alignment concept.

for this measurement, to roughly 1.2 MeV for the low gain output and to 0.6 MeV for the high-gain output. Assuming the single channel threshold for the pulse detection needs to be around $3\,\sigma_{\mathrm{BL}}$ (without considering the improvements from the digital signal filtering reported in Sec. 4.5), the 3 MeV threshold claimed in the previous version of this TDR appears feasible.

Response Characterization During all beam tests at the X1 beam line, several beam energies have been used (4 to 6, depending on the beam time duration), and to the least, one energy spectrum was measured with each crystal centered on the beam, to obtain a signal-energy dependence and to determine the relative energy resolution as a function of the incoming beam energy.

For the sake of conciseness, only the results on these two characteristics are reported here, since they bear the most relevant information for the calorimeter operation. They were also among the first results obtained with the Proto16.

In Fig. 7.15, energy spectra measured with 5 different beam energies are shown. Both single crystal spectra and sum spectra are displayed. For the single crystal spectra, the sum of only the signals from the APDs on the crystal which is centered on the beam is histogrammed. For the sum spectra, the signals from a 9 crystal cluster are used.

The signal height from every output channel was extracted analyzing offline the corresponding trace with a simple algorithm, where the baseline is subtracted from the full signal, the pulses are detected applying a simple threshold and the maximum sample value is used as pulse height. This is a very rough procedure and can be improved significantly, using the methods presented in Sec. 4.5, which were not yet developed when the data presented here was

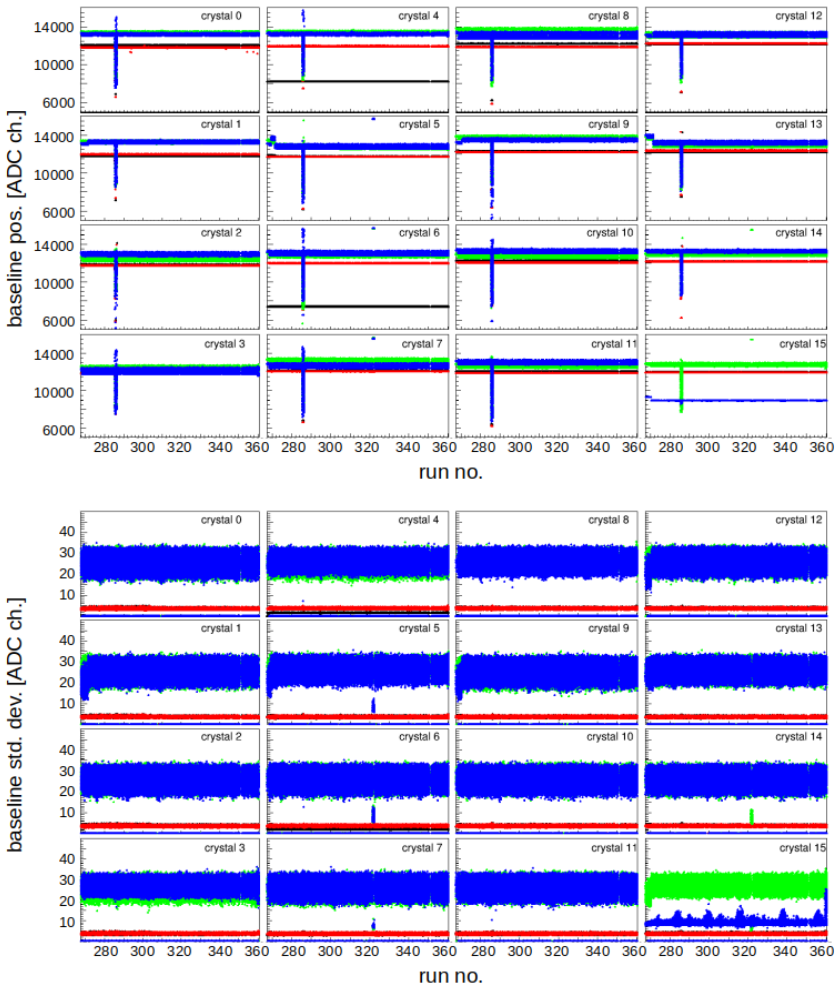

Figure 7.14: Top: scatter plots of the mean baseline position. Each panel corresponds to one crystal with two APDs. The black and red points result from the low-gain outputs, while the blue and green points from the high-gain outputs of the APFEL, respectively. For each event of every run (10^4 events) the baseline value has been calculated over 500 samples. The horizontal position is distributed randomly within a bin corresponding to the run number. The overall time interval spanned by the measurement is about 36 hours. Bottom: scatter plots of the standard deviation of the baseline, obtained analogously to the top plots.

analyzed.

To each of the energy spectra in Fig. 7.15, a fit of a Novosibirsk function was performed [27]. From the fits to the sum spectra, the peak position and the width parameter σ were used for plotting the signal-energy characteristics and the relative energy resolution shown in Fig. 7.16 and 7.17, respectively.

The plot in Fig. 7.16, shows that the response of the prototype has a linear dependence on the incoming energy at least up to 855 MeV, which is roughly the range needed for the BWEC. An important observation to be mentioned is that the five data points were not recorded simultaneously but rather one after another and with some hours of time interval between two successive measurements, and within about 3 days in total. This proves that the detector response is not just linear at a given instant, but it is also stable for operation times of the order of at least several days.

In Fig. 7.17, the results on the relative energy resolution are shown together with the usual three-parameter fit $\sigma_E/E = a \oplus b/\sqrt{E} \oplus c/E$ [26]. The results are in line with the requirements of the previous TDR. The obtained values of a, b and c show that the detector is built and read out according to the specifications. In particular, the value of the electronic noise term c of about 3 MeV is in agreement with the previous estimation based on the

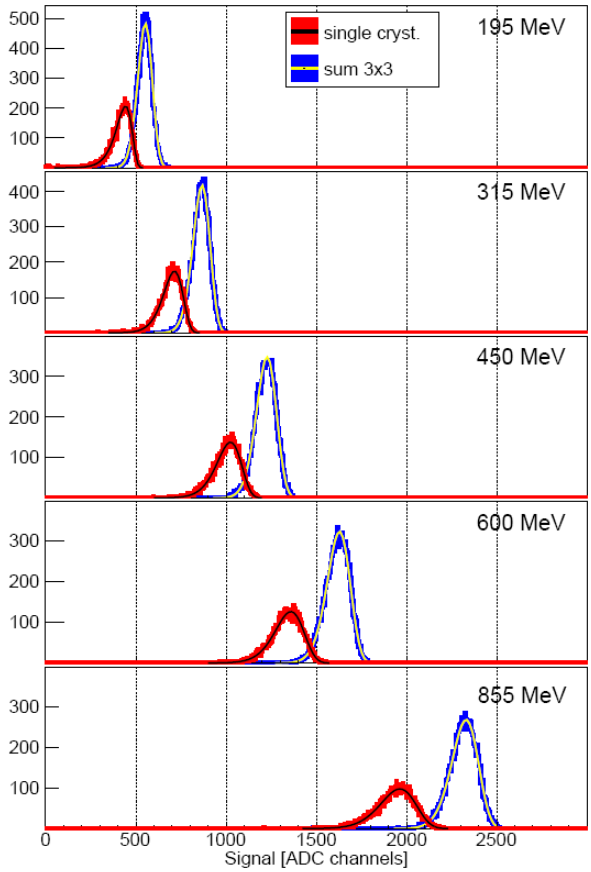

Figure 7.15: Energy spectra measured with the Proto16. For each plot (showing the number of counts as a function of the pulse height), a monoenergetic electron beam was focused on the center of crystal 5. The red spectra are obtained summing only the signals from the APDs in that crystal. For the blue histograms, all signals in a 3×3 matrix around the central crystal were summed. The black and yellow curves represent fits of the Novosibirsk function.

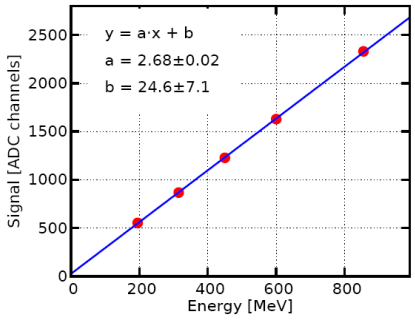

Figure 7.16: Dependence of the total signal recorded in a 3×3 crystal matrix as a function of the incoming electron beam energy. The signal height corresponds to the peak position of the spectra shown in Fig. 7.15, obtained from the Novosibirsk fit.

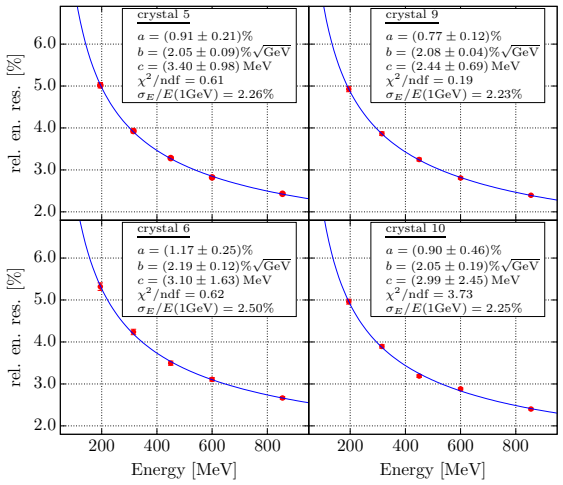

Figure 7.17: Relative energy resolution measured with the Proto16. It is calculated using the σ parameter and the peak position of the Novosibirsk functions shown in Fig. 7.15. Only the results for the four central crystals are shown, around which a 3×3 crystal matrix exists. The curves are fits of the usual parametrization of the relative energy resolution for electromagnetic calorimeters [26].

baseline fluctuations, which were estimated around 1 MeV. Since the signal from 9 crystals are summed for obtaining σ_E/E, and the noise of each readout channel is independent from the others, the 9 noise contributions are expected to add up in quadrature. Therefore, c is expected to be enhanced by a factor $\sqrt{9}$ with respect to the single crystal noise, which is in agreement with the result.

Worth mentioning is also the extrapolated value of σ_E/E to 1 GeV, which should be 2.5% according to the previous TDR. Also this requirement is satisfied by the Proto16.

In addition to these results, several studies have been performed for characterizing the prototype performance. These include:

- Bias voltage scans, where for each centered crystal several APD gains where used, to investigate the impact on the performance.
- Position scans, for studying the detector response as a function of the entrance position into the crystals.
- Angle scans, where the detector was turned around the vertical axis, in order to see the effect of the angle of incidence of the incoming particle on the shower distribution and leak-

ages.

- Event rate scans, to gather information about the pile-up losses and optimize the feature extraction algorithms accordingly.

- The impact position measurement was studied, although with a simplified reconstruction algorithm, which calculates the transverse position as the center of mass of the shower by weighting the crystal center positions in a 3×3 matrix with the signal, i. e. the weights are proportional to the deposited energy. The obtained position resolution for 855 MeV electrons entering in the center of the 9-crystal matrix is about 1 mm.

- The time resolution was also studied. Since the results strongly depend on the time measurement algorithm used, they are presented in detail in Sec. 4.5, where several results obtained using the Proto16 data as input are reported. Applying the feature extraction algorithm offline to the beam test data, values for the time resolution in line with those reported in Table 4.3 were obtained.

The results of all these studies were presented in theses and at PANDA collaboration meetings [20, 28, 29, 30, 31, 32].

Bibliography

[1] W. Erni. Datasheet for discrete Preamplifier for APD Readout, LNP Preamplifer Version SP 883A02. 2008. https://panda-wiki.gsi.de/foswiki/pub/DCS/SupportedHardware/Datasheet_APD_Preamp_SP883a02.pdf.

[2] Markus Moritz. *Measurements and improvements of the response of the PANDA-EMC prototype PROTO 60 to high energetic particles and photons in accelerator experiments*. PhD thesis, Justus-Liebig-Universität Gießen, 2013. http://geb.uni-giessen.de/geb/volltexte/2013/10105.

[3] Daniel Bremer. *Measurements and simulations on position dependencies in the response of single EMC crystals and a prototype for the PANDA EMC*. PhD thesis, Justus-Liebig-Universität Gießen, 2014. http://geb.uni-giessen.de/geb/volltexte/2014/10582.

[4] Tobias Eissner. *The new PWO Crystal Generation and Concepts for the Performance Optimisation of the PANDA EMC*. PhD thesis, Justus-Liebig-Universität Gießen, 2013. http://geb.uni-giessen.de/geb/volltexte/2013/10382.

[5] M. Kavatsyuk, D. Bremer, V. Dormenev, P. Drexler, T. Eissner, W. Erni, E. Guliyev, T. Hennino, B. Krusche, B. Lewandowski, H. Löhner, M. Moritz, R.W. Novotny, K. Peters, J. Pouthas, P. Rosier, M. Steinacher, G. Tambave, and A. Wilms. Performance of the prototype of the electromagnetic calorimeter for PANDA. *Nucl. Inst. Meth. A*, 648(1):77 – 91, 2011. https://doi.org/10.1016/j.nima.2011.06.044.

[6] *SIS3302 8 Channel 100 MS/s 16-bit ADC*. http://www.struck.de/sis3302.htm.

[7] Stefan Diehl. *Optimization of the influence of longitudinal and lateral non-uniformity on the performance of an electromagnetic calorimeter*. PhD thesis, Justus-Liebig-Universität Gießen, 2016. http://geb.uni-giessen.de/geb/volltexte/2016/11998/.

[8] Christoph Rosenbaum. *Optimization of the Front-End electronics of the PANDA barrel EMC*. PhD thesis, Justus-Liebig-Universität Gießen, 2016. http://geb.uni-giessen.de/geb/volltexte/2016/12281.

[9] Jan Schulze. *Analyse des Zerfalls $\chi_{c0} \to K^+K^-\pi^0\pi^0$ bei BESIII und Entwicklung von mechanischen Komponenten für einen Prototypen des PANDA-EMC*. PhD thesis, Ruhr-Universität Bochum, 2012. https://nbn-resolving.org/urn:nbn:de:hbz:294-35247.

[10] J. Becker. *Analyse des Zerfalls $\chi_{cJ} \to K^+K^-\eta$ bei BESIII und Entwicklung des Kühlsystems des Prototypen für das EMC des PANDA-Experiments*. PhD thesis, Ruhr-Universität Bochum, 2012. https://nbn-resolving.org/urn:nbn:de:hbz:294-36868.

[11] Michael Leyhe. *Analyse des J/ψ- und $\psi(2S)$-Zerfalls in $\gamma\pi^+\pi^-\eta$ bei BESIII und Entwicklungen zur Auslese des PANDA-EMC*. PhD thesis, Ruhr-Universität Bochum, 2013. https://nbn-resolving.org/urn:nbn:de:hbz:294-38315.

[12] Malte Albrecht. Aufbau und Analyse der Testmessungen des Proto192 elektromagnetis-

chen Kalorimeters. Master's Thesis, Ruhr-Universität Bochum, 2012.

[13] Malte Albrecht. The Forward Endcap of the Electromagnetic Calorimeter for the PANDA Detector at FAIR. *J. Phys. Conf. Ser.*, 587(1):012050, 2015. https://doi.org/10.1088/1742-6596/587/1/012050.

[14] Markus Kuhlmann. Messungen mit dem Prototypen des PANDA elektromagnetischen Kalorimeters. Master's Thesis, Ruhr-Universität Bochum, 2015.

[15] Malte Albrecht. *Partial wave analysis of the decay $J/\Psi \to \gamma\omega\omega$ at BESIII and developments for the electromagnetic calorimeter of the PANDA detector.* PhD thesis, Ruhr-Universität Bochum, 2016. https://nbn-resolving.org/urn:nbn:de:hbz:294-49851.

[16] PANDA Collaboration. Technical Design Report for the PANDA Electromagnetic Calorimeter. 2008. https://panda.gsi.de/publication/re-tdr-2008-001.

[17] Bernard Aubert et al. Search for decays of B^0 mesons into pairs of charged leptons: $B0 \to e^+e^-$, $B^0 \to \mu^+\mu^-$, $B^0 \to e^\pm\mu^\mp$. *Phys. Rev. Lett.*, 94:221803, 2005. https://doi.org/10.1103/PhysRevLett.94.221803.

[18] Eljen Technology. Silicone rubber optical interface ej-560. https://eljentechnology.com/products/accessories/ej-560.

[19] GSI Helmholtzzentrum für Schwerionenforschung. Multi Branch System (MBS). https://www.gsi.de/work/forschung/experimentelektronik/datenverarbeitung/datenerfassung/mbs.htm.

[20] O. Noll. Prototypentwicklung für die rückwärtige Endkappe des PANDA-Kalorimeters. Master's thesis, Johannes Gutenberg-Universität Mainz, 2014.

[21] H. Herminghaus et al. The Design of a Cascaded 800 MeV Normal Conducting C. W. Race Track Microton. *Nucl. Instrum. Meth.*, 138:1, 1976.

[22] K. H. Kaiser et al. The 1.5 GeV Harmonic Double-Sided Microtron at Mainz University. *Nucl. Instrum. Meth. A*, 593:159–170, 2008. https://doi.org/10.1016/j.nima.2008.05.018.

[23] S.J. Hall et al. A focal plane system for the 855 MeV tagged photon spectrometer at MAMI-B. *Nucl. Instrum. Meth. A*, 368:698–708, 1996. https://doi.org/10.1016/0168-9002(95)00661-3.

[24] K.I. Blomqvist et al. The three-spectrometer facility at the Mainz microtron MAMI. *Nucl. Instrum. Meth. A*, 403:263–301, 1998. https://doi.org/10.1016/S0168-9002(97)01133-9.

[25] W. Lauth et al. Coherent X-rays at MAMI. *Eur. Phys. J. A*, 28S1:185–195, 2006. https://doi.org/10.1140/epja/i2006-09-019-0.

[26] U. Amaldi. Fluctuations in Calorimetry Measurements. *Phys. Scr.*, 23:409–424, 1981.

[27] H. Ikeda et al. A detailed test of the CsI(Tl) calorimeter for BELLE with photon beams of energy between 20 MeV and 5.4 GeV. *Nucl. Instrum. Meth. A*, 441:401 – 426, 2000. https://doi.org/10.1016/S0168-9002(99)00992-4.

[28] M. Deiseroth. Characterization of a Prototype for the Backward End-Cap of the PANDA Electromagnetic Calorimeter. Master's thesis, Johannes Gutenberg-Universität Mainz, 2014.

[29] Ernst Johannes Oliver Noll. *Digital Signal Processing for the Measurement of Particle Properties with the PANDA Electromagnetic Calorimeter.* PhD thesis, Johannes-Gutenberg-Universität Mainz, 2020. https://panda.gsi.de/system/files/user_uploads/l.capozza/TH-PHD-2020-005.pdf.

[30] L. Capozza. Frontend Electronics for the Backward Calorimeter. PANDA DAQ/FEE Meeting, March 2016.

[31] O. Noll. Recent Results with the Backward EMC Prototype. PANDA Collaboration Meeting, September 2016.

[32] L. Capozza. BWEC Status Report. PANDA Collaboration Meeting, November 2018.

8 Organization

The PANDA EMC was presented in the original EMC TDR [1] that is updated by this document. Since the original EMC TDR was presented in 2008, changes concerning the organization arose due to the change of the crystal producer and due to changes in the participating groups. Most parts of the original Chapter 11 are still relevant. Here we concentrate on the major changes.

8.1 Quality Control and Assembly

The main detector components of the target spectrometer EMC are the crystals and the photodetectors. Quality control is organized as a joint effort, as described below. The mechanics and electronics differ between the barrel, forward endcap, and backward endcap EMCs. Therefore the locations of the quality control are divided accordingly. All final drawings are stored in the EDMS database at CERN.

8.1.1 The PWO-II Crystals and the Photodetectors

A large fraction of the 15 556 crystals required were produced by the Bogoroditsk Technological Chemical Plant (BTCP) in Russia. All crystals for the two endcap calorimeters and parts of the barrel calorimeter were produced there. These crystals went through quality control at CERN by a semi-automatic ACCOS machine (automatic crystal quality control system) [2] previously used by the CMS collaboration. After discontinuation of business activities of BTCP, a new producer for the missing 41 % of crystals was found in the Czech Republic. The CRYTUR company proved to be able to produce high quality crystals in the required quantity. The production is pre-tested at CTU in Prague to control the growing process and a complete quality control is carried out at Universität Gießen, including irradiation tests. The crystals for the barrel EMC are stored in Gießen, the ones for the forward endcap EMC in Bochum and the backward endcap EMC crystals in Mainz. The necessary raw material for all the remaining crystals has been purchased and is also stored in Gießen.

The photodetectors, large area Avalanche Photodiodes (APDs) and Vacuum Photo Tetrodes (VPTTs), are manufactured by Hamamatsu Photonics K. K. in Japan. The VPTT sensors are developed by Hamamatsu Photonics K. K. in cooperation with the Universität Bonn. The quality control of the VPTTs was performed in Bochum (gain, dark current) and Bonn (magnetic field measurements) as described in Sec. 3.2. The APD sensors are developed by Hamamatsu Photonics K. K. in cooperation with GSI Darmstadt. The APDs are screened at automated test stations at Ruhr-Universität Bochum and irradiated at the irradiation facility of Universität Gießen. Details can be found in Sec. 3.1.

All the results of the quality control and screening are stored in a database and are used for the optimal allocation for the assembly. This database provides also the operating voltages for the photodetectors.

8.1.2 Barrel EMC

The mechanical parts are produced under supervision of IHEP Protvino. All parts are checked for compliance with specification either at Protvino or at Gießen. The assembly of the slices is carried out in Gießen. Detailed functional tests are conducted during assembly. The slices are connected to the support beam. A crane (2 t, 1.87 m lift height) is available for this purpose in the assembly laboratory in Gießen. All slices are subject to a complete functional test, including tests of the electronics with a light pulser and full tests by measuring cosmic particles. The complete slices will be transferred to a designated interim storage hall, before final transportation to the PANDA-hall, where the final assembly and insertion into the solenoid magnet takes place.

8.1.3 Forward Endcap EMC

The forward endcap EMC is constructed and tested in a cooperation of the groups of the Ruhr-Universität Bochum, the Universität Bonn, the Universität Basel, KVI-CART, Stockholms Universitet and Uppsala Universitet. The forward endcap structure, the crystal dimensions and mechanical components were designed at KVI-CART/University of Groningen. The frame was built under supervision of KVI-CART and assem-

bled in Bochum, while the mechanical components for the submodule structure are manufactured in Bonn. The low-noise/low-power-charge preamplifiers (LNPs) for the VPTT sensors and the LNPs for the APD sensors are designed, fabricated and tested at Universität Basel. The forward endcap design features 214 full-size submodules and 54 half-size submodules consisting of 16 and 8 crystals, respectively. These are assembled in Bochum. Functional tests are carried out at each step during and after the assembly of each submodule. For final tests and a pre-calibration with cosmic muons they are transported to Bonn (Sec. 6.1). The final mounting of submodules into the frame will be done at FZ Jülich, where beam tests are also planned.

8.1.4 Backward Endcap EMC

The backward endcap EMC is developed, constructed and tested at the Universität Mainz/HIM. It consists out of 36 submodules of a variety of shapes. In total about 500 crystals are connected to APD sensors. The APFEL preamplifiers were designed and produced at GSI Darmstadt. The design and manufacturing of the mechanical parts and the electronics boards, as well as the assembly of the submodules and the mounting of the complete detector are done in Universität Mainz/HIM. As with the other detectors, full functional tests are performed after each assembly step. The final detector is subject to beam tests at MAMI.

8.2 Tasks and Responsibilities

The project management is divided into four parts, the EMC coordinator (Fritz-Herbert Heinsius, Ruhr-Universität Bochum), the barrel EMC coordinator (Hans-Georg Zaunick, Justus-Liebig-Universtät Gießen), the forward endcap EMC coordinator (Thomas Held, Ruhr-Universität Bochum) and the backward endcap EMC coordinators (Frank Maas, Luigi Capozza, Johannes-Gutenberg-Universität Mainz). The work and responsibilities are split into several work packages and tasks for the three different parts of the EMC. These are listed along with the coordinating and participating institutes in Table 8.1.

The Orsay group did major contributions to the design of the barrel calorimeter mechanics and the cooling until they left end of 2015 and is thus not listed anymore. The work was taken over by the groups of Protvino, Prague, Gießen and Bochum. The group from Charles Technical University Prague joined PANDA in 2016 and has been contributing to the crystal production and cooling of the EMC ever since. The group from KVI-CART did major contributions to the design of the forward endcap mechanics, cooling and digitization until KVI-CART was terminated end of August 2020. The only remaining part are the developments for the digitization for the forward endcap, which will be taken over by the groups from Bochum, Bonn and Uppsala.

Tasks not listed in the table are the operation of the detector, where all institutes will contribute. The data collection and pre-processing (time-ordering and pre-clustering) on the data concentration level is as well a common task. Most of the work on that part was completed by KVI-CART. The work package for the online and offline software is common to all. Main contributors are groups from China (Institute of High Energy Physics, CAS, Beijing; University of Science and Technology of China, Hefei; Nankai University, Nankai,), Germany (Rheinische Friedrich-Wilhelms-Universität Bonn, Justus-Liebig-Universtät Gießen, Johannes-Gutenberg-Universität Mainz and Helmholtz-Institut Mainz) and Sweden (Uppsala Universitet). Early contributions were from National Centre for Nuclear Research, Warsaw, Poland.

8.2.1 Status and Schedule

At the time of writing this document the production of components for all detectors progressed very well and production readiness reviews have been performed on all three detectors. The current status is briefly described here, followed by the planning for completion of the target spectrometer EMC.

For the *barrel EMC* all the mechanical parts for all slices are complete. These include all the alveoli packs for supporting the 11 200 PWO crystals of the complete barrel EMC. Furthermore, all rear inserts, intermediate plates and front inserts are ready for assembly in Gießen. The first slice is assembled. The preassembly of the second slice started in 2020. The production schedule foresees the assembly of 3 slices per year, given a timely availability of the remaining 6300 crystals. Currently it is foreseen to be ready for installation in 2024. Taking into account a production rate of 120 crystals per month, we will finish by then 12 slices in 3 years and the remaining four slices can be installed at a later stage. However, the details depend on the availability of funds and the overall FAIR construction progress. With sufficient financing, the production of the crystals and the assembly could be accelerated, so that the com-

Table 8.1: Tasks and responsibilities for the realization of the target spectrometer EMC. Participation of former groups and common tasks are specified in the text.

Work Package	Task	Participating (**Coordinating**) Institute
Barrel EMC		**Gießen**
Mechanics	Mechanics	**Protvino**
	Assembly	Gießen, **Protvino**
Crystals	Production and quality control	Bochum, **Gießen**, Mainz, Minsk, Prague, Protvino, Uppsala
Photodetectors	APD screening and irradiation	**Bochum**, Gießen
Electronics	APFEL-ASIC and flex-PCB	Gießen, **GSI**
	Digitization	**Gießen**, GSI, Uppsala
	Cables and power supplies	Bochum, **Gießen**
Cooling system	Design, cooling lines, insulation	**Bochum, Gießen**, Prague
Monitoring and control		**Bochum**, Gießen
Assembly	Detector assembly and test	**Gießen**, Protvino
Forward Endcap EMC		**Bochum**
Mechanics	Alveoli and submodules	**Bonn**
	Support, insulation, cooling lines	**Bochum**
Crystals	Production and quality control	**Bochum**, Gießen
Photodetectors	APD screening and irradiation	**Bochum**, Gießen
	VPTT production and screening	Bochum, **Bonn**
Electronics	LN-preamplifier	**Basel**
	High voltage and low voltage	Basel, **Bochum**
	Cables and electronics	**Bonn**, Bochum
	Digitization	Bochum, Bonn, **Uppsala**
Cooling system	Design, cooling lines, insulation	**Bochum**
Monitoring and control		**Bochum**
Assembly	Assembly and test	Basel, **Bochum**, Bonn, Stockholm, Uppsala
	Cosmic precalibration	**Bonn**
Backward Endcap EMC		**Mainz**
Mechanics		**Mainz**
Crystals	Production and quality control	**Bochum**, Gießen
Photodetectors	APD screening and irradiation	**Bochum**, Gießen, Mainz
Electronics	APFEL-ASIC and flex-PCB	**Mainz**, GSI
	Digitization	**Mainz**, Uppsala
	Cables and power supplies	**Mainz**
Cooling system	Design, cooling lines, insulation	**Mainz**
Monitoring and control		Bochum, **Mainz**
Assembly	Detector assembly and test	**Mainz**

plete EMC could be installed in PANDA in time.

For the *forward endcap EMC* all parts are available. The submodules with the VPTT photodetectors are completely assembled, tested and pre-calibrated. The assembly of the submodules with APD-photodetectors is ongoing in Bochum and will be finished in 2021. The complete assembly will take place at the Forschungszentrum Jülich in 2021-2022. It is foreseen to do complete tests including a calibration with the COSY beam at the COSY-TOF beam area.

The *backward endcap EMC* is part of the FAIR-PHASE 0 program. It will be assembled in 2020/21 and will take part in the measurement of the electromagnetic transition form factor of the π^0 in the space-like region via Primakoff electroproduction at the Mainz Microtron (MAMI) in the A1 experimental hall. The readiness for installation at PANDA is planned for 2023.

Bibliography

[1] PANDA Collaboration. Technical Design Report for the PANDA Electromagnetic Calorimeter. 2008. https://panda.gsi.de/publication/re-tdr-2008-001.

[2] E. Auffray et al. Performance of ACCOS, an Automatic Crystal quality Control System for the PWO crystals of the CMS calorimeter. *Nucl. Instrum. Meth. A*, 456:325 – 341, 2001. https://doi.org/10.1016/S0168-9002(00)00665-3.

Acknowledgements

We acknowledge financial support from

- the Bhabha Atomic Research Centre (BARC) and the Indian Institute of Technology Bombay, India;
- the Bundesministerium für Bildung und Forschung (BMBF), Germany;
- the Carl-Zeiss-Stiftung 21-0563-2.8/122/1 and 21-0563-2.8/131/1, Mainz, Germany;
- the Center for Advanced Radiation Technology (KVI-CART), Groningen, Netherlands;
- the CNRS/IN2P3 and the Université Paris-Sud, France;
- the Czech Ministry (MEYS) grants LM2015049, CZ.02.1.01/0.0/0.0/16 and 013/0001677, Czech Republic;
- the Deutsche Forschungsgemeinschaft (DFG), Germany;
- the Deutscher Akademischer Austauschdienst (DAAD), Germany;
- the European Union's Horizon 2020 research and innovation programme under grant agreement No 824093;
- the Forschungszentrum Jülich, Germany;
- the Gesellschaft für Schwerionenforschung GmbH (GSI), Darmstadt, Germany;
- the Helmholtz-Gemeinschaft Deutscher Forschungszentren (HGF), Germany;
- the INTAS, European Commission funding;
- the Institute of High Energy Physics (IHEP) and the Chinese Academy of Sciences, Beijing, China;
- the Istituto Nazionale di Fisica Nucleare (INFN), Italy;
- the Ministerio de Educación y Ciencia (MEC) under grant FPA2006-12120-C03-02, Spain;
- the Polish Ministry of Science and Higher Education (MNiSW) grant No. 2593/7, PR UE/2012/2, and the National Science Centre (NCN) DEC-2013/09/N/ST2/02180, Poland;
- the State Atomic Energy Corporation Rosatom, National Research Center Kurchatov Institute, Russia;
- the Schweizerischer Nationalfonds zur Förderung der Wissenschaftlichen Forschung (SNF), Switzerland;
- the Science and Technology Facilities Council (STFC), British funding agency, Great Britain;
- the Scientific and Technological Research Council of Turkey (TUBITAK) under the Grant No. 119F094, Turkey;
- the Stefan Meyer Institut für Subatomare Physik and the Österreichische Akademie der Wissenschaften, Wien, Austria;
- the Swedish Research Council and the Knut and Alice Wallenberg Foundation, Sweden.

List of Acronyms

2FA	2-factor authentication
AC	alternating current
ACCOS	**A**utomatic **C**rystal Quality **Co**ntrol **S**ystem for PWO crystals
ADC	analog to digital converter
AGOR	**A**ccélérateur **G**roningen-**Or**say
AMC	Advanced Mezzanine Card
APD	Avalanche Photodiode
APFEL	ASIC for $\overline{\text{P}}$ANDA Front-End Electronics
ASIC	Application Specific Integrated Circuit
BJT	Bipolar Junction Transistor
BPL	Backplane Electronics Board
BTCP	Bogoroditsk Technological Chemical Plant
BWEC	Backward Endcap Calorimeter
CA	Channel Access
CAD	computer-aided design
CAN	Controller Area Network
CERN	European Organization for Nuclear Research
CFD	Computational Fluid Dynamics
CFT	Constant Fraction Timing
CMOS	complementary metal oxide semiconductor
CMS-ECAL	Electromagnetic Calorimeter of the CMS detector at CERN
CMS	Compact Muon Solenoid
COSY	Cooler Synchrotron
CRY	Cosmic-ray Shower Library
CRYTUR	**Cry**stal **Tur**nov
CSA	charge sensitive amplifier
CS-Studio	Control System Studio
CUP	close user position
DAC	digital-to-analog converter
DAQ	data acquisition
DC	direct current
DCS	Detector Control System
DIRC	detector of internally reflected Cherenkov light
DUT	device under test
ELSA	Elektronen-Stretcher-Anlage
EMC	Electromagnetic Calorimeter
EMI	electromagnetic interference
EPICS	Experimental Physics and Industrial Control System
FAIR	Facility for Antiproton and Ion Research
FE	Front-End
FEC	Forward Endcap
FEE	front-end electronics
FEM	Finite Element Model
FIR	finite impulse response
FPC	flexible printed circuit
FPGA	field programmable gate array
FRP	Fiber-Reinforced Plastic
FS	Forward Spectrometer
FT	forward trackers
GEM	gas electron multiplier
GSI	Helmholtzzentrum für Schwerionenforschung GmbH
GUI	Graphical User Interface
HDA	Hit Detection ASIC
HESR	High Energy Storage Ring
HV	high voltage

I^2C	Inter-Integrated Circuit
IOC	Input/Output Controller
JTAG	Joint Test Action Group
KVI-CART	KVI – Center for Advanced Radiation Technology, former Kernfysisch Versneller Instituut
LCD	Liquid Crystal Display
LED	Light-Emitting Diode
LMD	luminosity detector
LNP	low-noise/low-power-charge preamplifier
LSB	least significant bit
LV	low voltage
LVDS	low voltage differential signaling
LY	light yield
MA	Moving Average
MAMI	Mainzer Mikrotoron
MBS	Multi Branch System
MC	Monte Carlo
MCP	Micro-Channel Plate
MCU	Micro Controller Unit
MDT	mini drift tubes
MOSFET	Metal-Oxide-Semiconductor Field-Effect Transistor
MPO	Multi-Fiber Push On
MPW	multi project wafer
MTBF	mean time between failure
µTCA	micro telecommunications computing architecture
MUXER	multiplexer
MVD	micro vertex detector
MWD	Moving Window Deconvolution
NIM	Nuclear Instrumentation and Methods
$\overline{\text{P}}$ANDA	Anti**p**roton **An**nihilations at **Da**rmstadt
PBB	piggy-back board
PCB	printed circuit board
PID	particle identification
PLL	phase locked loop
PMT	Photo Multiplier Tube
PV	Process Variable
PVC	Polyvinyl chloride
PWO	$PbWO_4$ scintillator
PWO-II	improved $PbWO_4$ scintillator
RESR	recuperated experimental storage ring
RICH	Ring Imaging Cherenkov Detector
rms	root mean square
RTM	Race-Track Microtron
SAA	Serial Adapter ASIC
SADC	sampling analog to digital converter
SCPI	Standard Commands for Programmable Instruments
SEU	Single Event Upset
SFP	small form-factor pluggable
SICCAS	Shanghai Institute of Ceramics, Chinese Academy of Science
SMD	Surface Mounted Device
SNMP	Simple Network Management Protocol
SODA	synchronization of data acquisition
SPI	serial peripheral interface
SPS	Super Proton Synchrotron
SSH	Secure Shell
STT	straw tube tracker
SUP	standard user position
TDR	Technical Design Report
THM$\overline{\text{P}}$	Temperature and Humidity Monitoring Board for $\overline{\text{P}}$ANDA
ToF	time-of-flight

TRB	HADES trigger and readout board version 3
TS	Target Spectrometer
TSL	The Svedberg Laboratory
UDP	User Datagram Protocol
UMC	United Microelectronics Corporation
USART	Universal synchronous and asynchronous receiver-transmitter
VHDL	Very High Speed Integrated Circuit Hardware Description Language
VIP	Vacuum Insulation Panel
VL	Versatile Link
VPN	virtual private network
VPTT	Vacuum Photo Tetrode

List of Figures

List of Tables